THÈSE

Pour obtenir le grade de

DOCTEUR DE L'UNIVERSITÉ GRENOBLE ALPES

École doctorale : PHYS - Physique
Spécialité : Physique pour les Sciences du Vivant
Unité de recherche : Laboratoire Interdisciplinaire de Physique

Nouvelles approches expérimentales et théoriques de la diffusion quasi-élastique de neutrons pour l'étude des protéines

New experimental and theoretical approaches to quasi-elastic neutron scattering on proteins.

Présentée par :

Agathe NIDRICHE

Direction de thèse :

Judith PETERS PROFESSEURE DES UNIVERSITES, UNIVERSITE GRENOBLE ALPES	Directrice de thèse
Gérald KNELLER PROFESSEUR DES UNIVERSITES, Université d'Orléans	Co-directeur de thèse

Rapporteurs :

ANDREAS STADLER
SENIOR SCIENTIST, FORSCHUNGSZENTRUM JÜLICH
ARANTXA ARBE
PROFESSEURE, UNIVERSIDAD DEL PAIS VASCO

Thèse soutenue publiquement le **11 décembre 2023**, devant le jury composé de :

ANDREAS STADLER SENIOR SCIENTIST, FORSCHUNGSZENTRUM JÜLICH	Rapporteur
ARANTXA ARBE PROFESSEURE, UNIVERSIDAD DEL PAIS VASCO	Rapporteure
GORAN NILSEN ASSOCIATE PROFESSOR, UNIVERSITY OF STAVANGER	Examinateur
HANS GEISELMANN PROFESSEURE DES UNIVERSITES, UNIVERSITE GRENOBLE ALPES	Président
JEREMY SMITH PROFESSEUR, UT-ORNL CENTER FOR MOLECULAR BIOPHYSICS	Examinateur

Invités :

GERALD KNELLER
PROFESSEUR DES UNIVERSITES, UNIVERSITE D'ORLEANS
ROSS STEWART
SCIENTIST, ISIS FACILITY

Contents

Remerciements

L'aboutissement de ce travail m'a procuré beaucoup de joie et de fierté, et cela n'aurait pas été possible sans les personnes qui m'ont entourée pendant ces trois années.

Je tiens tout d'abord à remercier mes encadrants, Judith Peters et Gerald Kneller, de m'avoir accompagnée tout le long de ce travail de thèse. Cela n'a pas toujours été simple car ce projet démarrait d'une idée ambitieuse : celle d'observer des effets quantiques dans la dynamique des protéines à l'aide d'échanges isotopiques, et avec comme technique la diffusion de neutrons. Face aux difficultés rencontrées et aux résultats étonnants que nous avons obtenus, nous avons persévéré et construit un tout autre projet, non moins intéressant. J'espère que cela ouvrira des portes à l'utilisation de neutrons polarisés pour l'étude des objets biologiques. Cette thèse m'a permis de vraiment réaliser ce qu'était le métier de chercheur : la persévérance et le travail que cela demande au quotidien face aux déconvenues, mais aussi le bonheur de voir progresser son projet et d'appartenir à cette communauté.

Merci Judith pour ton encadrement, tu m'as donné beaucoup de clés pour apprendre à gérer un projet au long terme, notamment concernant la confiance en soi, la communication et l'organisation. J'ai eu aussi la chance que tu me soutiennes lors des moments difficiles. Merci pour les opportunités que tu m'as données de découvrir la communauté scientifique, de présenter mon travail et de voyager par la même occasion. Merci avant tout pour la confiance que tu m'as témoignée dans mon travail et ma rédaction, et en encourageant la publication de résultats inattendus. Je me sens maintenant prête à envisager la suite de ma carrière.

Merci Gerald pour l'apprentissage approfondi de la diffusion de neutrons que j'ai eu auprès de toi, et pour les riches idées que tu partageais régulièrement avec enthousiasme : tu m'as montré que la science, c'est avant tout un état d'esprit. C'était un plaisir d'avoir ces conversations à Soleil.

Merci à Arantxa Arbe et à Andreas Stadler d'avoir accepté de corriger mon manuscrit. Je suis d'autant plus honorée, que votre travail m'a fortement influencée pendant ces trois ans. C'était un plaisir d'échanger avec vous en conférence et lors de la soutenance. Merci de même à Jeremy C. Smith et Hans Geiselman d'avoir fait partie de mon jury de soutenance, tout comme Goran que je remercie aussi de son accueil chaleureux lors de mon expérience sur LET.

Je souhaite aussi remercier mes collègues avec qui j'ai partagé ce temps de travail : Tatsuhito pour ta gentillesse et tes conseils pertinents, Aline pour avoir été mon amie et ma conseillère, Antonio pour ton aide inestimable lors de mon séjour à Lyon et nos pauses cafés, ainsi que Daniele, Christian et Louise. L'environnement de travail de l'équipe de Spectroscopie à l'ILL et de MODI au LiPhy m'ont permis de m'épanouir dans les deux laboratoires.

Cette thèse n'aurait pas été envisageable sans la bourse qui m'a été accordée par le Ministère de l'Enseignement supérieur et de la Recherche, ni sans les temps de faisceaux accordés par l'ILL et ISIS ainsi que le travail considérable effectué par les scientifiques qui gèrent les instruments que nous utilisons. Merci beaucoup à Ross Stewart, Lucile Mangin Thro, Jacques Ollivier, Wolfgang Schmidt, Michael M. Koza et Monica J. Ruiz pour votre aide et votre expertise lors des expériences, mais aussi votre disponibilité pour toutes les questions que je vous ai posées. Je remercie aussi Jean-Marc Zanotti pour nos discussions concernant ses pratiques pour la préparation d'échantillons.

De même, notre travail repose avant tout sur nos échantillons, que nous devons à Martine Moulin (Deuteration Lab) et Philippe Oger (INSA Lyon). Merci Martine pour le temps que tu as dédié à m'aider en 2023 pour la préparation de la protéine, et Elisabetta Boeri pour l'accès à la plateforme de Mass Spectroscopy de l'IBS et pour l'analyse des données.

J'exprime aussi ma reconnaissance à mon comité de suivi de thèse constitué de Peter Fouquet et de Bahram Houchmandzadeh, vos conseils m'ont permis de repartir chaque année avec de nouvelles idées.

Je remercie Skandar Basrour pour l'opportunité qu'il m'a donnée d'enseigner à Polytech Grenoble, et pour m'avoir formée et donné confiance face à une salle de classe. Cela a été une belle expérience grâce à notre petite équipe pédagogique : merci Simon, Gaëtan et

Nathis, j'ai beaucoup appris et rigolé avec vous.
Evidemment une bonne thèse nécessite un environnement favorable, et Grenoble était la ville idéale pour cela. Je remercie d'abord mes amis du LiPhy qui m'ont accueillie : je me suis tout de suite sentie chez moi. Merci à Andrea, Adrien, Louisa, Laila, Alexandre, Maike, Saranath, Wanda, Caroline, Cecile, Camille, Nachi, Valentin, Emrys, Winfried, Markus... Pour ces merveilleux moments, j'aurais aimé plus profiter de nos parties de foot ou des déjeuners au soleil. C'est grâce à vous, ainsi qu'à mes collocs Pauline et Majd, que 2020-2021 a été une très bonne année malgré tout.
Bien sûr, je remercie aussi les amis que je me suis faits à l'ILL et je ne manquerai pas de continuer à venir aux Stammtisch : Arianna, Ronja, Lucas, Rasmus, Maddie, Gabrielli, Milos, Himanshu, Vlad, Riccardo, Laura, Jason, Valentin... C'était un plaisir de partager tout cela avec vous.
J'ai eu la chance de continuer à fréquenter des copains de Strasbourg et d'agrandir ce cercle : merci Thibs, Lucas, Max, Paul, Corentin et Prune pour les répets et les soirées jam, j'ai découvert le plaisir de jouer en groupe grâce à vous. Evidemment il fallait notre autre Thibs et Antoine pour être au complet, ainsi que Solenn pour les soirées jeux. Sans oublier Moran, tu resteras à jamais dans nos cœurs. J'ai eu la chance de découvrir tes qualités incroyables : ton courage, ton optimisme, ta force et ta générosité.
Je remercie évidemment les copains du groupe rando, et les copains à distance : merci Waz, RMGX, Alex et Quentin pour nos weekends ensemble, ainsi que Simon, Marie et Marion.

Evidemment, je dois tout cela à ma famille, qui a cru en moi et m'a toujours encouragée pendant mes études. La maison était un havre de paix qui me permettait de me resourcer auprès des personnes les plus importantes pour moi. Certains n'ont d'ailleurs jamais attendu que j'ai fini cette thèse pour m'appeler "docteur". Merci aussi pour les fous rires que j'ai eus (en cachette) pendant la soutenance. Je pense aussi à mes papis qui sont partis pendant ces trois ans et qui me manquent, vous auriez été fiers de moi.
Mes dernières pensées vont à Hugo, ces années ont été avant tout marquées par notre rencontre et toute la joie que tu m'as apportée. Je te remercie pour ton soutien inébranlable, ta bonne humeur, et tout l'amour que tu as mis dans notre couple.

Abstract

In English :

Proteins undergo dynamics that span several orders of magnitude in time, englobing the femtosecond to microsecond timescale, which can be investigated with neutron scattering techniques. Among spectroscopy techniques, neutron scattering is a valuable tool to study the self-dynamics of hydrogens in proteins and understand conformational relaxation and diffusion at the atomic scale. However, neutron scattering is not just a probe for self-diffusion, but also encodes collective dynamics through its division into an incoherent (self) and coherent (self and collective) contribution, which cannot be separated with conventional neutron scattering techniques, although it is stated that coherent scattering is negligible in those hydrogen-rich systems. The advent of neutron polarisation set-ups for the Time-Of-Flight (TOF) technique, with enough resolution to resolve ps-scale motions, it is an opportunity to investigate both contributions and shed light on the importance of considering collective motions arising from the protein and its hydration water. Therefore, we investigate the dynamics of a protonated Green Fluorescent Protein (pGFP) and its per-deuterated counterpart (dGFP) in powder state and hydrated in D_2O with the help of polarised neutrons and new theoretical approaches adapted to the study of complex systems with self-similar dynamics. First and foremost, this PhD work focuses on the structural information held by polarised diffraction to assess the impact of both contributions, and permits us to understand the extent of D/H exchange between the atmosphere and the hydration shell of the protein. This is then pushed forward with a dynamical study at the ps-scale with polarised quasielastic scattering, which highlights the strong impact of coherent scattering arising from hydration water D-bond network relaxation

in both deuterated and protonated GFP. Consequently, a similar study performed with unpolarised elastic and quasielastic neutron scattering permits us to conclude the study by comparing polarised and conventional QENS. Many questions are then raised concerning usual assumptions, shattered by our investigations, that are made in the frame of incoherent neutron scattering applied to biomolecules, including reflexions on a quantum formalism of scattering functions.

En français :

La dynamique des protéines hydratées s'étend sur plusieurs décades, comprenant des gammes de temps allant de la femtoseconde à la picoseconde qui sont accessibles à la diffusion de neutrons. La diffusion de neutron est un excellent outil pour étudier la dynamique moyennée des noyaux d'hydrogènes dans un échantillon, afin de comprendre les phénomènes de diffusion et de relaxation prenant place à l'échelle atomique. Cependant, la diffusion de neutrons ne sonde pas uniquement la diffusion de noyaux isolées mais comprend aussi des effets collectifs, de par sa division en une partie incohérente (self) et une partie cohérente (self et collective) qui ne sont pas séparables par les techniques de spectroscopie de neutron conventionnelles, même s'il est souvent argumenté que la diffusion cohérente est négligeable dans ces systèmes riches en noyaux d'hydrogène. L'émergence d'un système de polarisation de neutrons pour la diffusion à temps de vol (TOF), avec une résolution suffisante pour étudier la dynamique à l'échelle de la picoseconde, est une opportunité pour explorer l'apport de ces deux contributions, afin de mettre en lumière l'impact non négligeable de la dynamique collective provenant à la fois de la protéine et de son eau d'hydratation. Dans ce but, nous étudions la dynamique de poudres hydratées d'une protéine fluorescente verte protonnée (pGFP) et de sa version deutérée (dGFP) par diffusion de neutrons polarisés. Nous utilisons pour cela une approche théorique adaptée à l'étude de systèmes complexes au comportement auto-similaire. En premier lieu, ce manuscrit présente l'information structurelle obtenue par diffraction de neutrons polarisés, afin d'évaluer l'impact des deux contributions et de nous permettre de comprendre l'étendue des échanges deutérium/hydrogène ayant lieu à l'interface entre la couche d'hydratation de la protéine et l'atmosphère. Nous poursuivons avec une étude de la dynamique des deux protéines à l'échelle de la picoseconde par spectroscopie de neutron polarisés à temps de vol. Cela nous permet de souligner l'impact de la diffusion

cohérente dans le signal, qui provient de la relaxation collective du réseau de liaisons hydrogène formé par l'eau d'hydratation deutérée de la protéine. L'étude de la diffusion élastique et quasi-élastique de neutrons non polarisés nous permet de conclure en comparant diffusion polarisée et non polarisée. A la lumière de ces nouveaux résultats, de nombreuses questions émergent concernant les hypothèses habituellement formulées en diffusion incohérente de molécules biologiques. Cela implique notamment une réflexion sur le formalisme quantique des fonctions de diffusion appliqué aux biomolécules.

Abbreviations and Acronyms

Table of abbreviation and acronyms used in the manuscript.

Technical abbreviations and acronyms	
coh	Coherent
dGFP/pGFP	deuterated and protonated Green Fluorescent Protein
ESF	Elastic scattering factor
ECSF	Elastic coherent scattering factor
EISF	Elastic incoherent scattering factor
FBD	Fractional Brownian Dynamics
FTIR	Fourier Transformed Infra-Red spectroscopy
FWHM	Full-Width at Half-Maximum
HWHM	Half-Width at Half-Maximum
IBS	Institut de Biologie Structurale
ILL	Institut Laue Langevin
inc	Incoherent
LAMP	Large-Array Manipulation Program
LDL/HDL	Low Density Liquid/High Density Liquid
Mantid	Manipulation and Analysis Toolkit for Instrumentation Data
ML	Mittag Leffler function
MSD	Mean Squared Displacements
MD	Molecular Dynamics
NMR	Nuclear Magnetic Resonance
NSE	Neutron Spin Echo
OU/FOU	Orstein Uhlenbeck /Fractional Ornstein Uhlenbeck
PA	Polarisation Analysis
PDB	Protein Data Bank
QENS	Quasielastic neutron scattering
RMSD	Root-Mean-Square Deviation
SANS	Small angle scattering
zpf	Zero point fluctuations
Proteins	
DMPA	Dimyristoyl l-α-phosphatidic acid
GFP	Green Fluorescent Protein
Lys	Lysozyme
Mgb	Myoglobin
PGK	Phosphoglycerate kinase
SNase	Staphylococcal nuclease

Definitions of physical values used in the manuscript

Physical values and constants	
k_B	Boltzmann constant, $k_B = 1.380\ 10^{-23}$ JK^{-1}
β	$\beta = \frac{1}{k_B T}$, J^{-1}
$\hbar$	The reduced Planck constant, $6.626\ 10^{-34}/2\pi$ Js
u	Unified atomic unit, $1,660\ 10^{27}$ kg
Avogradro's constant Na	$Na = 6.022\ 10^{23}$
Electron volt eV	$1.602\ 10^{-19}$ J

Introduction

Proteins are functional chains of amino acids, defined by a hierarchical structure undergoing fluctuating or actively driven motions. They arise at the sub-Angström scale up to large amplitudes spanning the whole protein, while stretching from about 10 fs to several seconds. In this large panel of dynamics that reveals self-similarity in time [1], neutron scattering is an ideal method to probe directly the motions of hydrogen atoms in proteins from vibrational stretching or bending ($\approx$ fs-ps) [2] to amino acid side-chains fluctuations ($\approx$ ps-ns), global protein diffusion in its environment [3] or inter-domain motions ($\approx$ ns-μs) [4]. Even the shortest motions in time and scale are paramount to explain functional modes [5]. These dynamics are also intrinsically dependent on the protein's environment. The impact of temperature [6], pressure [7], crowding [8], weak interactions in the cellular environment [9] etc., are also assessed by neutron scattering.

Proteins were long thought as rigid molecules: this dynamic vision is rather recent, and the existence of conformational fluctuations was indeed brought by Lakovitz and Weber [10] in 1973 with fluorescence quenching by molecular oxygen, and was accepted among the crystallography community around 1980 [11]. Currently, the demonstration of the impact of quantum effects at physiological conditions despite thermal noise brings as well a new conception of the dynamics of biological systems. For instance, it explains enhanced rates between donnor and acceptance states of some enzymes, that are unravelled by primary or secondary kinetic isotope effects that require a quantum formulation based on tunnelling to explain the intensity of isotope effects [12]. It is also reported that in the first step of photosynthesis, the coherence of excitons (electron-hole pairs) would explain how they find the most efficient path to the reaction center [13], and coherence has also

been held as an explanation of birds' sensitivity to the earth's magnetic field [14]. As highlighted by J.C.Brookes in Ref. [15], all those phenomena have in common that they rely on a system based on a protein and a smaller interacting particle, requiring to express the rate of events with Fermi's golden rule formalism.

Hence, our project started with the idea of probing quantum-effects in the internal dynamics of proteins with neutron scattering. To this end, two isotopic forms of the same Green-Fluorescent Protein (GFP) in powder-state were produced and hydrated in D_2O with a hydration level $h = 0.4$ g protein/g D_2O, in order to minimise at most any contribution from the protein's environment. Indeed, neutrons are very sensitive to hydrogen isotopes: neutrons are the perfect probe for averaged dynamics of single hydrogen nuclei in a protonated protein, and to a lower extent of deuterium nuclei in a per-deuterated protein [16].

We also aimed at working with a new formalism developed by G.Kneller. He expresses incoherent neutron scattering from transition probabilities which imply the system wavefunctions [17], instead of using Van-Hove correlation functions formalism [18], hence proposing a whole new quantum-based understanding of neutron scattering in complex systems. It identifies with a sort of Franck-Condon principle [19], where scattering functions write with transition probabilities determined from the overlap of the system's wavefunctions upon energy change $\hbar\omega$ and upon momentum transfer $\hbar Q$ when the neutron "kicks" the sample.

In that sense, a set of elastic ($\Delta E \approx 80$ μeV), quasielastic ($E_i \approx 1meV$) and inelastic neutron ($E_i < 200$ meV) scattering data had been measured by Judith Peters on IN5 (ILL) [20] with the two protein samples. The goal was to investigate isotope effects in zero-point fluctuations, small conformational fluctuations and vibrations in the protein sample. However, our first attempts to understand experiments raised unexpected results: mean squared displacements suggested extremely large amplitude of motions for deuterium in the deuterated protein (dGFP) with respect to hydrogen in the protonated protein (pGFP), although we expected a slow-down and increased confinement. Furthermore, it did not vanish with cross section weighted subtraction of the hydration water. Similarly, quasielastic scattering data suggested fast motions arising from dGFP internal dynamics, at odds with the slow dynamics of pGFP. Indeed, it became clear that we were facing a mix of different information that we could not easily discriminate. It especially raised concerns about the impact of coherent scattering in our samples. Therefore, after

a year we instead decided to dig this essential question in order to continue our initial project.

Indeed, scattering functions, yielding structural and dynamical information weighted by cross-section factors accounting for the interaction between the probe (neutron) and the scattering particle (nucleus), is a sum of cross-terms corresponding to different nuclei and self-terms corresponding to single nuclei. Thus, one can write scattering functions as the sum of an incoherent scattering term, comprising only self-terms weighted with "incoherent" scattering lengths, and a coherent scattering term, comprising both self terms and all the cross-terms weighted with "coherent" scattering lengths [21]. Hence, coherent scattering corresponds to collective information.
Indeed, biological samples are composed of about 50% of hydrogen nuclei which are uniformly distributed in the protein. It raises the assumption that due to the large incoherent scattering cross section of hydrogen with respect to the incoherent or coherent cross sections of all other nuclei, what we probe with time-of-flight and backscattering spectroscopy are the average motions of single hydrogen nuclei in the sample. Another usual assumption is that deuteration of the hydration layer around the protein ensures that only the protein is visible during neutron scattering experiments. It is very convenient in the sense that most available models are built for single particle motions [22, 23]. For coherent scattering involving collective terms, a theory adapted to complex system dynamics is almost non-existent, especially on the space and time scales probing local slow relaxation phenomena.

When we adressed this issue, direct assessment of the impact of coherent scattering in proteins was scarce, although studies implying fully deuterated proteins in D_2O had already been performed and invoked that coherent scattering is preponderant in those samples [24, 25, 26]. Indeed, performing neutron scattering with a polarised neutron beam where one spin projection is scattered and analysed is the only way to unambiguously separate both incoherent and coherent terms [27, 28, 29]. However, the use of such techniques for soft matter is quite recent [30, 31, 32]: most experiments are usually performed with an unpolarised beam where all information is mixed. Polarised neutron scattering for proteins was basically limited to diffraction applied to myoglobin and C-phycocyanin by Gaspar et al [33]. In this study, authors show that coherent scattering is non-negligible in biomolecules. Furthermore, they also demonstrate a significant impact of deuterated water with strong Q-dependence. However, no information concerning per-deuterated

protein in D_2O was available, so we decided to perform our own polarised diffraction on IN12 and D7 (ILL) [34, 35]. Again, we faced startling results concerning the ratio of coherent scattering.

Step by step, the project ended-up concerning almost this single question: what is the impact of coherent scattering in the scattering signal corresponding to protein dynamics, in the energy-range and Q-range that is usually associated to purely incoherent contribution ? Having at hand two isotopic forms of the protein was indeed a great opportunity to answer this essential question that requires systematic studies with model systems. However, the simple "static" picture offered by diffraction does not raise any information concerning the dynamics of the system. At that time, we fortunately came across the work of Arbe et al [32]: they studied D_2O with polarised quasielastic neutron scattering (QENS) and disclosed that in this liquid, both incoherent and coherent contributions have very distinct timescales which fuse for Q large enough. Hence, we decided to perform QENS experiments at LET (ISIS) [36] to directly probe coherent and incoherent dynamics separately. Eventually, the more information we got, the more hints there were concerning a high role of hydration water in our sample dynamics, increasing the complexity of our study. All our finding were questioning usual assumptions, as well as highlighting the importance of choosing the right Q-range to discriminate unwanted collective contributions. Hence, we present here the first study of protein dynamics based on coherent and incoherent separation. We interpret scattering functions with a minimalist model for a collective variable diffusing in a rugged harmonic potential in the frame of fractional Brownian dynamics [37, 38, 39, 40, 41, 42]. We present the outline of the manuscript as follows :

Chapter 1 recalls neutron theory with a highlight on the partial differential cross section obtained from a polarised beam. It presents the minimalist model used for both incoherent and coherent scattering, and a state-of-the art on coherent neutron spectroscopy experiments carried-out so far in soft matter.

Chapter 2 presents neutron scattering experimental methods and the description of our instrumental set-ups. It also introduces our data reduction and analysis, with the spotlight on our analysis in time domain and our handling of polarised data. It also presents the sample production and preparation, as well as the protein structure used for calculations in Chapter 3.

Chapter 3 focuses on the information brought by polarised neutron diffraction studies, and how it can be completed by static structure factor calculations to infer information

on the sample's coherent contribution. It permits to get new insights on the timescale of D/H exchanges in the hydration layer of a protein.

Chapter 4 goes beyond the scope of structural information and provides an analysis of separated incoherent and coherent dynamical information at the picosecond timescale with polarised QENS. It especially highlights the coherent contribution of hydration water in both versions of the protein. We draw parallels with works from other neutron-scattering communities.

Chapter 5 proposes a comparison of aforementioned results with non-polarised data, while **Chapter 6** entails a discussion on elastic scattering in complex systems, with a focus on the search for quantum-effects in elastic scattering and a reflexion on the non-elastic contribution present in elastic scans.

Remark: in the manuscript, the term "collective" refers to terms arising strictly from different nuclei, but we sometimes also extend the term to coherent scattering.

CHAPTER 1

Principles of neutron scattering

1.1 The neutron, a probe to understand the dynamics and structure in matter

In 1932, Chadwick discovers the existence of a neutral particle by bombarding a beryllium target with alpha radiation, which mass should be close to the proton's mass [43]. Its specificity is a high penetration into matter, contrary to high-energy photons that interact strongly with the atom's electron cloud : this lead to a strong interest into neutron-matter interaction.

Eversince, neutrons produced in nuclear reactors (Institut Laue-Langevin) or in spallation sources (ISIS facility) have proved to be a strong probe to investigate both structure and dynamics in condensed matter.
The velocity of produced neutrons follows a Maxwell law, and the further use of moderators enables to modify their velocity and therefore their range of energy of interaction with the sample. Hence, it makes it possible to probe diffusion phenomena occuring at small energy-exchange ($\approx$ meV) with cold neutrons, as well as characterizing vibrations and phonon emission or absorption phenomena (energy $\gg k_B T$) with thermal neutrons.
The neutron properties are at the origin of their interest for matter-matter interactions.

- Its mass $m = 1.675e^{-27}$ kg confers the neutron a De Broglie wavelength $\lambda = \frac{h}{p}$

that scales close to the inter-atomic distance, thus permitting diffraction studies. As a consequence the neutron goes slowly from one atom to another compared to the typical timescale of relaxation in the sample : time-resolved information can be probed with neutrons. This negligible mass explains that the neutron is tackled both as a wave and a particle in the frame of wave-particle duality.

- The coupling of the neutron spin $s = \frac{1}{2}$ with the nuclear spin defines the amplitude of the nuclei cross section. It yields a non-trivial expression of the cross section as a function of the atomic number, which is illustrated by the strong incoherent cross section of hydrogen while high-energy photon based techniques are barely sensitive to light atoms. It yields both an incoherent and a coherent cross sections for each nucleus which enable to separate respectively individual from collective phenomena. Moreover, it enables magnetic studies : its magnetic moment $\mu_n = 1.913\mu_N$ implies magnetic dipole-dipole interactions with surrounding unpaired electrons.

- The neutron's neutrality implies that electrostatic interactions are negligible and that only nuclear interaction prevails, permitting its high penetration into matter.

The kinetic energy of an incoming neutron is equal to :

$$\boxed{E = \frac{\hbar^2 k^2}{2m}}. \tag{1-1}$$

For a typical cold neutron experiment with a $\lambda = 5$ Å wavelength, it corresponds to a velocity of $v = 792$ ms^{-1} and an energy of $E = 3.2$ meV.

A neutron experiment consists in bombarding a sample in crystal, liquid or powder state for instance. A typical neutron beam at ILL is of the order of a few cm^2 with a neutron flux of about 10^5 to 10^{10} neutron/cm^2/s.
The incoming beam is characterised by its flux Φ_0, the neutron's initial energy E and its initial momentum $\mathbf{k}$ which is a vector holding the information of the incident neutron direction. Upon interaction, neutrons can be either absorbed or scattered. Scattered neutrons exit the sample with an energy E' and a momentum **k'**. A neutron spectroscopy experiment consists in measuring the response of the system to the perturbation caused by the neutron probe.

Measuring both the energy and the scattering angle of the scattered neutron is enough to retrieve both E' and **k'** information. Therefore a typical neutron measurement consists in

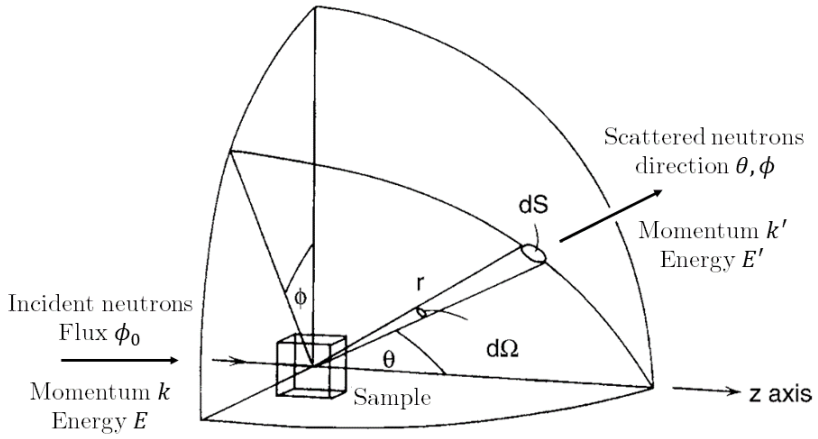

Figure 1-1: Schematics of a neutron scattering experiment, adapted from [44].

counting the number of neutrons escaping the target per second in a solid angle $d\Omega$ defined in directions θ and ϕ in spherical coordinates, with an energy comprised between E' and $E' + dE'$. This quantity, the **double differential cross section**, is the master equation for neutron scattering, which depends on the energy exchange ΔE of the neutron, with ω its pulsation

$$\boxed{\Delta E = \hbar\omega}, \tag{1-2}$$

and on the momentum transfer of the neutron $\mathbf{Q}$

$$\boxed{\mathbf{Q} = \mathbf{k}' - \mathbf{k}}. \tag{1-3}$$

The derivation of the double differential cross section and the further application of classical or quantum-based models to derive physical parameters of the sample's structure or dynamics are the foundations of neutron scattering.

Generally speaking, the goal of spectroscopy is to induce information on the sample's dynamics and structure from its interaction with a probe, be it photons or light particles of matter. The probe's characteristics determine its interactions with the sample, and therefore the extent of available information on the sample : space and energy ranges that can be probed, whether it yields bulk or interface information... The derivation of the double-differential cross section in section 1.2 requires to express a point-like inter-

action potential $\hat{V}$ specific to the neutron-nucleus interaction, the Fermi pseudo-potential.

Why is it interesting to probe biological samples with neutrons ? Briefly, it yields information on the average dynamics of hydrogen nuclei at very short time and space scales with spatial resolution, while causing little damage to the sample. This last aspect is paramount because proteins have to be studied in their native state, and the required amount of sample to carry-out spectroscopy experiments on proteins is about ≈ 100 mg, which is hard and time-consuming to produce. As will be discussed in the instrumental section, neutron spectroscopy techniques are able to span timescales from the fs to almost the μs, for space-scales ranging from covalent bonds to inter-molecular structures.

In the manuscript we mainly focus on the dynamics of samples studied by **Time-Of-Flight** (TOF) neutron spectroscopy, an instrumental technique that relates the neutron's energy to its travelling time from the sample to the detector.

1.2 Derivation of scattering functions

This section concerns the derivation of scattering functions, using Refs. [45, 46, 47, 21]. The reader is partially referred to the appendix to ease the reading of this section.
In the following section, we introduce the target's Hamiltonian $\hat{H}_m$. The sample is composed of N nuclei at thermal equilibrium and characterized by eigenvectors $|m\rangle$ and eigenvalues E_m corresponding to its initial state before scattering, and eigenvectors $|m'\rangle$ and eigenvalues $E_{m'}$ corresponding to its final state.
The neutron probe, on the other hand, is characterized by eigenvectors $|k\rangle$ and $|k'\rangle$ and eigenvalues E_k and $E_{k'}$ corresponding respectively to its initial and final states, defined by Hamiltonian $\hat{H}_k$.
The scattering Hamiltonian, corresponding to the coupling of the probe and the sample, writes $\hat{H}_c$. We denote operators with a hat $\hat{}$, and vectors in bold.

Let us consider that the initial state of the neutron $|k\rangle$ is fixed. The double differential cross section $\left(\frac{d\sigma^2}{\mathbf{d\Omega} dE}\right)_{m,m'}$ restricted to processes in which the sample goes from state

$|m\rangle$ to state $|m'\rangle$ is expressed according to :

$$\boxed{\left(\frac{d\sigma^2}{\mathbf{d\Omega}dE}\right)_{m,m'} = \frac{1}{\Phi_0}\frac{W_{m\otimes k\to m'\otimes \mathbf{k'}}}{d\mathbf{\Omega}dE}}. \tag{1-4}$$

Indeed, $W_{m\otimes\mathbf{k}\to m'\otimes\mathbf{k'}}$ corresponds to the number of transitions of the system from initial state $|m\rangle \otimes |k\rangle$ of the total system to its continuum final state $|m'\rangle \otimes |k'\rangle$ per time unit, per solid angle $d\Omega$ with final energy in E,$E + dE$ (this is homogeneous to a flux). It is divided by the incoming neutron flux, Φ_0.

This is defined such that the total double differential cross section (our master equation) is summed over all initial $|m\rangle$ and final $|m'\rangle$ states of the sample :

$$\left(\frac{d\sigma^2}{\mathbf{d\Omega}dE}\right) = \sum_m \sum_{m'} P_m \left(\frac{d\sigma^2}{\mathbf{d\Omega}dE}\right)_{m,m'}. \tag{1-5}$$

With P_m the probability of the sample to be in initial state $|m\rangle$.

Integration of this quantity yields the cross section σ, which is homogeneous to a surface and is a measure of the effective size of the nucleus as seen by the neutron.

$$\sigma = \int dE \int d\mathbf{\Omega} \left(\frac{d\sigma^2}{\mathbf{d\Omega}dE}\right). \tag{1-6}$$

Getting back to Equation 1-6, the transition rate $W_{m\otimes\mathbf{k}\to m'\otimes\mathbf{k'}}$ from initial state $i \equiv m\otimes\mathbf{k}$ is determined using Fermi's Golden Rule, supposing that the final state $f \equiv m' \otimes \mathbf{k'}$ is a continuum and that the pertubative Hamiltonian $\hat{H}_c$ for the coupling of the neutron and the probe is weak and time-independent. The whole derivation is available in the appendix, section 6.5

$$W_{i\to f} \underset{L\to\infty}{=} \frac{L^3}{\hbar^3}\frac{mk'}{(2\pi)^2} dE d\mathbf{\Omega} |\langle f|\hat{H}_c|i\rangle|^2 \delta(E_f - E_i), \tag{1-7}$$

Where m is the mass of the neutron, and L is the size of the box where the wavefunctions of the neutron are normalised, which tends to ∞. The incident wavefunction of the neutron is linear, and the scattered wavefunction is spherical due to the spherical symmetry of the coupling Hamiltonian, and arrives linear to the detectors due to the large distance betwen the sample and the detectors with respect to the size of the sample.

Hence, $\hat{H}_c$ is a point-like Hamiltonian standing for the nuclear interaction of the neutron and the total system composed of N nuclei. Each nucleus j interacts with the neutron

with the empirical Fermi pseudo-potential $\hat{V}_j = \frac{2\pi\hbar^2}{m} b_j \delta(\hat{r} - \hat{R}_j)$ introduced in 1936 [48, 49]

$$\hat{H}_c = \sum_j^N \frac{2\pi\hbar^2}{m} b_j \delta(\hat{r} - \hat{R}_j). \tag{1-8}$$

$\hat{R}_j$ is the position operator of nucleus j at time 0, and b_j, **the bound scattering length of nucleus** j, is a complex value which measures the amplitude of interaction with the neutron. These are tabulated values for a single fixed nucleus, where a positive value for b denotes a repulsive interaction. The real part of the scattering length corresponds to scattering of the neutron, while its imaginary part denotes the absorption of the neutron.

Replacing Equation 1-8 and Equation 1-7 in Equation 1-4 yields the following expression for the partial differential cross section for an initial state m and a final state m' for the sample

$$\begin{aligned} &\left(\frac{d\sigma^2}{\mathbf{d\Omega} dE}\right)_{m,m'} = \frac{W_{i\to f}}{\Phi_0 d\mathbf{\Omega} dE} \\ &= \frac{k'}{k} \sum_j \sum_l \langle m| b_j^* \exp\left(-i\mathbf{Q}\hat{R}_j\right) |m'\rangle \langle m'| b_l \exp\left(i\mathbf{Q}\hat{R}_l\right) |m\rangle \delta(E_f - E_i), \end{aligned} \tag{1-9}$$

where k and k' are the norms of the initial and final momentums of the neutron. Detailed presentation of the significance and origin of the coupling Hamiltonian, as well as aditional steps to the calculations, are presented in the appendix, section 6.5.
Now, to obtain the master equation we return to Equation 1-5 : we sum the partial differential cross sections on all initial and final state, considering that initially the sample is at equilibrium and follows the Boltzmann distribution. Detailed calculations are performed in the appendix, section 6.5.

$$\begin{aligned} &\left(\frac{d\sigma^2}{\mathbf{d\Omega} dE}\right) = \sum_m \sum_{m'} P_m \left(\frac{d\sigma^2}{\mathbf{d\Omega} dE}\right)_{m,m'} \\ &= \frac{1}{2\pi\hbar} \frac{k'}{k} \sum_{\alpha=1}^N \sum_{\beta=1}^N \int_{-\infty}^{\infty} \left(\sum_{j=1}^{N_\alpha} \sum_{l=1}^{N_\beta} \langle b_{\alpha,j}^* b_{\alpha,l} \exp\left(-i\mathbf{Q}\hat{R}_{\alpha,j}(0)\right) \exp\left(i\mathbf{Q}\hat{R}_{\beta,l}(t)\right) \rangle \right) \exp(-i\omega t) dt. \end{aligned} \tag{1-10}$$

At the cost of simplicity we express the sum on atomic types α and β, which appears useful for the development of scattering cross sections in the case of polarised and unpolarised beams.

1.3 Introduce coherent and incoherent scattering for a polarised and a non-polarised beam

The goal of this section is to explain how scattering functions are obtained in case of a polarised beam where the spin projection is non-random. It appeared essential to us regarding the scarce information available on polarisation analysis applied to non-magnetic materials. We define coherent and incoherent scattering contributions, and how linear combinations of spin-flip and non spin-flip partial differential cross section permit to experimentally separate them.

1.3.1 The scattering length operator

Equation 1-10 standing for the double differential cross section is now fairly simplified and involves the position operators of nuclei in the sample. However, in order to reach an expression where probe and sample information is uncoupled, we need to get scattering lengths out of the thermal average.

However, until now we have neglected the impact of the spin states of both the nuclei and the neutron in the Golden Fermi Rule. We trade b for an operator $\hat{b}$ depending on both the neutron's spin operator $\frac{1}{2}\hat{\sigma}$ and the nucleus spin operator $\hat{I}$. This is now taken into account, such that $\hat{H}_c$ writes :

$$\hat{H}_c = \sum_j^N \frac{2\pi\hbar^2}{m} \hat{b}_j \delta(\hat{r} - \hat{R}_j), \tag{1-11}$$

and

$$\boxed{\hat{b} = A + B\hat{\sigma}\hat{I}.} \tag{1-12}$$

A and B are complex constants.

What is the interest of such a representation ? Once $\hat{b}$ will be expressed as a function of both $\hat{I}$ and $\hat{\sigma}$, it will be possible to project it on the neutron's states to express the double differential cross section in case of a polarised beam (determined initial and final states of the neutron) and an unpolarised neutron beam (random initial states of the neutron, unanalysed final states of the neutron).

Explicit the scattering length operator Let us denote I the spin angular momentum of a single nucleus, and $s = \frac{1}{2}$ the spin angular momentum of the neutron.
We express the coupled {neutron,nucleus} system in the adequate base $|+\rangle$ and $|-\rangle$ constructed with Clebsch-Gordan coefficients from the uncoupled base. The coupled spin operator $\hat{S}$ is equal to

$$\hat{S} = \hat{I} + \frac{1}{2}\hat{\sigma}, \tag{1-13}$$

and verifies $\hat{S}\,|\pm\rangle = S^{\pm}\,|\pm\rangle$. There are thus only two degenerated allowed spin states in the coupled system

$$S^{+}\,|+\rangle = (I + \frac{1}{2})\,|+\rangle\,,\;\; S^{-}\,|-\rangle = (I - \frac{1}{2})\,|-\rangle\,. \tag{1-14}$$

Both states correspond respectively to scattering lengths b^+ and b^-, which are both a measure of the interaction potential Equation A-9 and of the scattering amplitude. The latter is the Fourier transform of the Fermi pseudo-potential. b^+ and b^- are estimated experimentally from scattering of a bound nucleus and are isotope-specific. They are listed in Ref. [23].
Therefore, the scattering length operator $\hat{b}$ verifies :

$$\hat{b}\,|+\rangle = b^{+}\,|+\rangle\,,\;\; \hat{b}\,|-\rangle = b^{-}\,|-\rangle\,. \tag{1-15}$$

Since spin operators verify $\hat{I}^2\,|\pm\rangle = I(I+1)\,|\pm\rangle$ and $\hat{\sigma}^2\,|\pm\rangle = 2(\frac{1}{2}(\frac{1}{2}+1))\,|\pm\rangle$, using

$$\hat{S}^2 = \frac{1}{4}\hat{\sigma}^2 + \hat{I}^2 + \hat{\sigma}\hat{I}, \tag{1-16}$$

yields an expression for the spin coupling operator $\hat{\sigma}\hat{I}$ contained in $\hat{b} = A + \frac{1}{2}B\hat{\sigma}\hat{I}$. Solving Equation 1-15 by projecting $\hat{S}^2$ on $|+\rangle$ and $|-\rangle$ and using Equation 1-12 yields :

$$\boxed{\begin{aligned} A &= \frac{(I+1)b^{+} + Ib^{-}}{2I+1} \\ B &= \frac{(b^{+} - b^{-})}{2I+1} \end{aligned}}\,. \tag{1-17}$$

We now have an expression for $\hat{b}$ operator, Equation 1-12, expressed from b^+ and b^- tabulated values.

1.3.2 Assumptions and simplifications for a protein sample

Spin average Introducing a spin-dependence of the scattering length operator $\hat{b}$ implies that the state of the whole system, as featured in the Golden Rule, includes now the spin-state of the neutron, denoted $|\sigma\rangle$ and the spin-state of the nucleus, denoted $|I\rangle$ in the thermal average. This average on spin and sample states is denoted by horizontal bar over the averaged quantities. Formally this should be expressed, as for any operator $\hat{A}$, using $\overline{\hat{A}} = Tr(\hat{A}\hat{\rho})$ with $\hat{\rho}$ the density matrix for neutron and nuclear spin states. However, it will not be necessary : we assume that **in a protein sample, the lack of magnetic order implies that nuclear spins are randomly oriented**, so that for nuclear-spin average applied to the nuclear spin operator $\hat{I}$, in cartesian coordinates:

$$\overline{\hat{I}_{x,y,z}} = 0, \quad \overline{\hat{I}^2_{x,y,z}} = \frac{1}{3}I(I+1),$$

While the same holds for the neutron's spin operator $\hat{\sigma}$ **in the case of an unpolarised beam** :

$$\overline{\hat{\sigma}_{x,y,z}} = 0, \quad \overline{\frac{1}{2}\hat{\sigma}^2_{x,y,z}} = \sigma(\sigma+1), \tag{1-18}$$

Isotope average We shall also introduce the mean over isotope states. However, we suppose that in our study, the distribution of isotopes for other nuclei than H (that is, C,N,O,S) are negligible, and that we treat explicitly hydrogen separately from deuterium when estimating the neutron polarised cross sections.

Expression for the general case The most general expression for the double-differential cross section should write in the style of Equation 1-10 :

$$\left(\frac{d\sigma^2}{\mathbf{d\Omega}dE}\right) = \frac{1}{2\pi\hbar}\frac{k'}{k}\sum_{\alpha=1}^{N}\sum_{\beta=1}^{N} \int_{-\infty}^{\infty}\left(\sum_{j=1}^{N_\alpha}\sum_{i=1}^{N_\beta}\frac{}{\langle \exp\Big(-i\mathbf{Q}\hat{R}_{\alpha,i}(0)\Big)\hat{b}_{\alpha,i}(0)^\dagger\hat{b}_{\beta,j}(t)\exp\Big(i\mathbf{Q}\hat{R}_{\beta,j}(t)\Big)\rangle}\right)\exp(-i\omega t)dt. \tag{1-19}$$

In the case of a protein sample, the formula for the double-differential scattering cross section is drastically simplified : there is no dynamic coupling between positions and scattering properties of the nuclei, implying that the time-dependent operator $\hat{b}(t)$ can be replaced by its value $\hat{b}$ at $t = 0$. There is also no position dependence of operator $\hat{b}$, so that we can extract it from the thermal average.

It yields the following equation :

$$\boxed{\left(\frac{d\sigma^2}{\mathbf{d\Omega}dE}\right) = \frac{1}{2\pi\hbar}\frac{k'}{k}\sum_{\alpha=1}^{N}\sum_{\beta=1}^{N} \int_{-\infty}^{\infty}\left(\sum_{j=1}^{N_\alpha}\sum_{i=1}^{N_\beta}\overline{\hat{b}^\dagger_{\alpha,i}\hat{b}_{\beta,j}}\langle\exp\left(-i\mathbf{Q}\hat{R}_{\alpha,i}(0)\right)\exp\left(i\mathbf{Q}\hat{R}_{\beta,j}(t)\right)\rangle\right)\exp(-i\omega t)dt} \quad (1\text{-}20)$$

$\hat{b}$ is the scattering length operator and $\hat{b}^\dagger$ its adjoint operator. The bar stands only for neutron and nuclear spin averages.

We will introduce the derivation of the double differential cross section for two different cases :

- **A non polarised beam**. The neutron beam is produced by the nuclear or spallation source with the same amount of projected spins up ($\uparrow$, $s = \frac{1}{2}$) and down ($\downarrow$, $s = -\frac{1}{2}$).
- **The beam is polarised** by means of neutron optics techniques section 2.1.2, so that the incoming beam is composed only of spin up neutrons ($\uparrow$) or spin down neutrons ($\downarrow$) depending on the polarisation technique.

1.3.3 Scattering from an unpolarised neutron beam

In a classical neutron experiment, the beam arrives to the sample unpolarised, which means that the neutrons spins are randomly distributed. It is the default set-up in neutron spectroscopy experiments.
We express the average of scattering lengths operators :

$$\begin{aligned}\overline{\hat{b}^\dagger_{\alpha,j}\hat{b}_{\beta,l}} &\underbrace{=}_{\text{Equation 1-12, } \overline{\hat{\sigma}\hat{I}_{\alpha/\beta,j/l}}=0} \overline{A^*_{\alpha,j}A_{\beta,l} + \frac{1}{4}\hat{I}_{\alpha,j}\hat{I}_{\beta,l}B^*_{\alpha,j}B_{\beta,l}} \\ &\underbrace{=}_{\overline{\hat{I}_{\alpha,j}\hat{I}_{\beta,l}}=0} A^*_\alpha A_\beta + \frac{1}{4}\delta_{jl}I_\alpha(I_\alpha+1)|B_\alpha|^2.\end{aligned} \quad (1\text{-}21)$$

The last equivalence is due to the lack of correlation between the spin states of two different nuclei j and l. Please note, for the calculations, that the spin operator is a hermitian operator ($\hat{\sigma}^\dagger = \hat{\sigma}$, $\hat{I}^\dagger = \hat{I}$).

Therefore the expression for the average of the scattering length operator is composed of a term $A^*_\alpha A_\beta$ that holds for all pairs of nuclei where $j = l$ and $j \neq l$, and one term $\frac{1}{4}\delta_{\alpha\beta} I_\alpha (I_\alpha + 1)|B_\alpha|^2$ that holds only for pairs of the same nucleus where $j = l$.

This leads to a somehow natural decomposition of the double-differential cross section into two contributions corresponding to those weights. Let us introduce the following notations.

$$\boxed{\begin{cases} b_{\mathrm{coh},\alpha} = A_\alpha \\ b_{\mathrm{inc},\alpha} = \sqrt{\frac{1}{4} I_\alpha (I_\alpha + 1)|B_\alpha|^2} \end{cases}}. \tag{1-22}$$

Which are directly expressed from the tabulated eigenfunctions b^+ and b^- of the scattering length operator. We then write :

$$\boxed{\overline{\hat{b}^\dagger_{\alpha,j} \hat{b}_{\beta,l}} = b^*_{coh,\alpha} b_{coh,\beta} + \delta_{jl} |b_{inc,\alpha}|^2}. \tag{1-23}$$

So we can split the double differential scattering cross section Equation 1-20 into two contributions :

- A **coherent term** summed over all pairs of atoms, displaying both **"self-terms"** ($j = l$) and **"distinct-terms"** ($j \neq l$). This term encodes **interference effects**.
- An **incoherent term**, corresponding only to "self-terms" ($i = j$). This term **does not display interference effects**.

How can we understand this splitting into two contributions, and what is the interest behind it ?

Meaning of incoherent and coherent scattering lengths

The physical meaning can be retrieved for the scattering of single bound nuclei. Let us write b as a complex value rather than an operator. We introduce again the scattering lengths b^+ and b^- corresponding to the two available spin states of the whole system.
In the case of a non-polarised sample, the neutron and nucleus spin states are randomly distributed such that all projections of the total spin $\hat{S}\,|+\rangle$ are equivalently probable, so that $|+\rangle$ is degenerated $m^+ = 2S^+ + 1 = 2I + 2$ times and $|-\rangle$ is degenerated $m^+ = 2S^- + 1 = 2I$ times, see Equation 1-14. It raises the following means for b and b^2 values :

$$\begin{aligned}\overline{b} &= \frac{m^+b^+ + m^-b^-}{m^+ + m^-} = \frac{(I+1)b^+ + Ib^-}{2I+1} \\ \overline{b^2} &= \frac{(I+1)\left(b^+\right)^2 + I\left(b^-\right)^2}{2I+1}.\end{aligned} \tag{1-24}$$

Direct comparison yields that term A in the scattering length operator $\hat{b}$ (Equation 1-17), is equal to $\overline{b}$ (Equation 1-24). That is, $b_{coh} = \overline{b}$, Equation 1-24. The same way, calculations lead to $b_{inc} = \sqrt{\overline{b^2} - \overline{b}^2}$, using eq Equation 1-22, Equation 1-17 and Equation 1-24.

$$\boxed{\begin{cases} b_{coh} = \overline{b} \\ b_{inc} = \sqrt{\overline{b^2} - \overline{b}^2} \end{cases}}. \tag{1-25}$$

For a mono-atomic sample with fixed nuclei, we introduce

$$\sigma_{\text{inc}} = 4\pi|b_{inc}|^2, \;\; \sigma_{coh} = 4\pi|b_{\text{coh}}|^2. \tag{1-26}$$

The incoherent and coherent cross sections, respectively. The coherent contribution reflects the structural dynamics of the atoms in the scattering system, and the incoherent contribution results from single-atom contributions. Therefore, the coherent scattering contribution is weighted by the spin-average of the scattering lengths b^+ and b^- of a nucleus, while the incoherent scattering contribution is weighted by their mean-square deviation.

It is now useful to introduce the calculation of incoherent and coherent cross sections in the case of ^{1}H and ^{2}H (deuterium) in Table 1-I. The large hydrogen incoherent cross section is therefore both a consequence of the strong discrepancy between the scattering lengths b^+ and b^- corresponding to the two accessible spin states, but also to the gap between degeneracies $m\pm$ of the two spin states. It introduce a large variation in the scattering amplitudes of a nucleus seen by the neutron, which is exactly what incoherent scattering probes.

Table 1-I: Calculations of hydrogen and deuterium coherent and incoherent scattering lengths and cross sections.

	$_1$H (hydrogen)	$_2$H (deuterium)
Spin	$\frac{1}{2}$	1
Scattering lengths	$b^- = -47.4$ fm, $b^+ = 10.4$ fm	$b^- = 1.0$ fm, $b^+ = 9.5$ fm
Occurrences	$n^- = 1$, $n^+ = 3$	$n^- = 2$, $n^+ = 4$
$\langle b \rangle$, $\langle b^2 \rangle$	$\langle b \rangle$ =−3.7 fm, $\langle b^2 \rangle$ =6.5 barn	$\langle b \rangle$ =−6.7 fm , $\langle b^2 \rangle$ =0.60 barn
b_{coh}, [23]	−3.7 fm	6.67 fm
b_{inc}, [23]	25.27 fm	4.04 fm
σ_{coh}, [23]	1.76 barn	5.60 barn
σ_{inc}, [23]	80.27 barn	2.05 barn

We emphasize the following remarks :

- The difference between the spins of two isotopes, especially for hydrogen and deuterium (table Table 1-II), makes it a powerful tool for contrast when performing partial or total isotopic change.

- Scattering lengths are tabulated for the bound states of a nucleus and are given in Table 1-II for the nuclei composing biological systems. Let us notice that if the nucleus is free, $b_{\text{free}} = \frac{M}{M+m} b_{\text{bound}}$, with m the neutron's mass and M the nucleus mass. Therefore the bound state assumption holds better for heavy nuclei.

- The imaginary part of the scattering length corresponding to absorption is negligible for nuclei in biomolecules, therefore we consider that for any nucleus i in our protein sample, we have $b_i^* = b_i$.

- Contrary to X-Rays, for which b scales with the square of the atomic number, the distribution of scattering lengths for neutron scattering (both incoherent and coherent) is erratic with respect the atomic number, see Figure 1-2. This is therefore a strong complementary method to other spectroscopy techniques, especially for hydrogen-rich samples.

Why separate both contributions ? Large coherent or incoherent scattering lengths in a sample will respectively favour information arising from different nuclei (useful for diffraction, small angle scattering, the study of collective dynamics and phonons...) or favour information arising from single nuclei (useful to study mean-square displacements, self-dynamics, vibrations...).

Table 1-II: List of scattering lengths and cross sections for the most abundant atoms in proteins [23].

	b_{coh} [fm]	b_{inc} [fm]	σ_{coh} [barns]	σ_{inc} [barns]	σ_{abs} [barns]	% in pGFP
H	-3.7	25.27	1.76	80.27	0.33	0
D	6.67	4.04	5.60	2.05	0.00	49
C	6.65	0.00	5.55	0.00	0.00	32
N	9.36	2.0	11.01	0.5	1.9	9
O	5.80	0.00	4.23	0.00	0.00	10
S	2.85	0.00	1.01	0.00	0.53	0
Al	3.45	0.256	1.495	0.00	0.231	
V	-0.402	6.35	5.08	0.018	5.08	

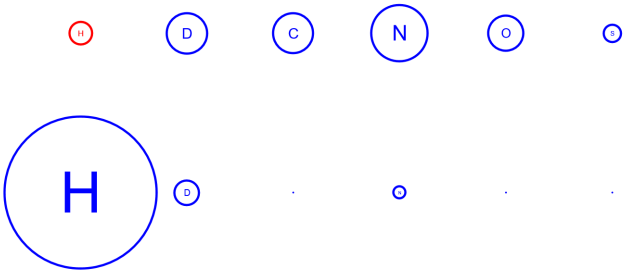

Figure 1-2: Representation of the incoherent and coherent cross sections of nuclei present in Table 1-II. $\sigma_{\mathrm{H,coh}}$ is in red to denote its coherent negative scattering length, corresponding to an attractive Fermi-potential.

Hence, next section will focus on how a fully polarised beam permits to separate easily both contributions.

1.3.4 Scattering from a polarised neutron beam

In the case of a polarised neutron beam, the initial $|\sigma\rangle$ and final $|\sigma'\rangle$ spins of the neutron are produced and analysed such that they are projected upon one spin-state ($\uparrow$ or $\downarrow$); Therefore, the double-differential cross section obtained is **partial on the neutron's spin** :

$$\left(\frac{d\sigma^2}{\mathbf{d\Omega}dE}\right)_{\sigma\to\sigma'} = \frac{1}{2\pi\hbar}\frac{k'}{k}\sum_{\alpha=1}^{N}\sum_{\beta=1}^{N}$$
$$\int_{-\infty}^{\infty}\left(\sum_{j=1}^{N_\alpha}\sum_{l=1}^{N_\beta}\underbrace{\overline{\langle\sigma|\,\hat{b}^\dagger_{\alpha,j}\,|\sigma'\rangle\,\langle\sigma'|\,\hat{b}_{\beta,l}\,|\sigma\rangle}}_{\text{No magnetic order}}\langle\exp\Big(-i\mathbf{Q}\hat{R}_{\alpha,j}(0)\Big)\exp\Big(i\mathbf{Q}\hat{R}_{\beta,l}(t)\Big)\rangle\right)\exp(-i\omega t)dt. \tag{1-27}$$

Where the horizontal bar stands now only for the nuclear spin average.
Now, we need to evaluate the matrix element $\overline{\langle\sigma|\,\hat{b}\,|\sigma'\rangle}$ for each neutron initial and final states. Let us denote $|u\rangle$ the spin-up state ($\uparrow$) and $|v\rangle$ the spin-down state ($\downarrow$).
It is performed from the expression of the scattering length operator ([Equation 1-12]), by using the Pauli matrices properties in cartesian coordinates :

$$\hat{\sigma}_x\,|u\rangle = v,\quad \hat{\sigma}_y\,|u\rangle = iv,\quad \hat{\sigma}_z\,|u\rangle = u\quad \hat{\sigma}_x\,|v\rangle = u,\quad \hat{\sigma}_y\,|v\rangle = -iu,\quad \hat{\sigma}_z\,|v\rangle = -v,$$

and by developing the scalar product $\hat{\sigma}\hat{I}$, such that for any $\{\sigma,\sigma'\}$ in $\{|u\rangle\,,|v\rangle\}$: $\langle\sigma'|\,\hat{b}\,|\sigma\rangle = \langle\sigma'|\,A + \frac{1}{2}B\left(\hat{\sigma}_x\hat{I}_x + \hat{\sigma}_y\hat{I}_y + \hat{\sigma}_z\hat{I}_z\right)|\sigma\rangle$.

It yields :

$$\text{Non spin-flip (nsf)} : \begin{cases} \langle u|\,\hat{b}\,|u\rangle = A + \dfrac{1}{2}B\hat{I}_z & (\uparrow\uparrow) \\ \langle v|\,\hat{b}\,|v\rangle = A - \dfrac{1}{2}B\hat{I}_z & (\downarrow\downarrow) \end{cases} \tag{1-28}$$

$$\text{Spin-flip (sf)} : \begin{cases} \langle v|\,\hat{b}\,|u\rangle = \dfrac{1}{2}B\left(\hat{I}_x + i\hat{I}_y\right) & (\downarrow\uparrow) \\ \langle u|\,\hat{b}\,|v\rangle = \dfrac{1}{2}B\left(\hat{I}_x - i\hat{I}_y\right) & (\uparrow\downarrow). \end{cases} \tag{1-29}$$

$\langle u|u\rangle$ and $\langle v|v\rangle$ denote a **non spin-flip** event (the spin of the neutron has not changed upon scattering), while $\langle u|v\rangle$ and $\langle v|u\rangle$ denote a **spin-flip** event. We can already guess from formula that for a non-magnetic sample, where nuclear spins are disordered, the cross sections for spin flip events are both equivalent, and the same stands for non spin-flip events : we require only two measurements to reach the whole information in longitudinal

polarisation analysis (one spin projection axis long z).

We remind that, since the nuclear spins are randomly oriented :

$$\overline{\hat{I}_{x,y,z}} = 0, \quad \overline{\hat{I}^2_{x,y,z}} = \frac{1}{3}I(I+1),$$

We now treat the spin-flip and non-spin flip derivations of the nuclear spin average of the scattering length operator introduced in the partial scattering cross section, Equation 1-27 :

- The **non-spin-flip** case. We do the calculations for spin-up $|u\rangle$ polarization, however the same result holds for spin-down $|v\rangle$ polarisation.

$$\begin{aligned}\overline{\langle u|\,\hat{b}^\dagger_{\alpha,j}\,|u\rangle\,\langle u|\,\hat{b}_{\beta,l}\,|u\rangle} &= \overline{A^*_{\alpha,i}A_{\beta,j} + \frac{1}{2}A^*B\hat{I}_{z,\beta,j} + \frac{1}{2}AB^*\hat{I}_{z,\alpha,l} + \frac{1}{4}B^*_{\alpha,l}B_{\beta,j}\hat{I}_{z,\alpha,l}\hat{I}_{z,\beta,j}} \\ &= A^*_\alpha A_\beta + \delta_{\alpha,\beta}\frac{1}{3}\left(\frac{1}{4}|B_\alpha|^2 I_\alpha(I_\alpha+1)\right).\end{aligned}$$

  Since $\overline{\hat{I}_{\alpha,i}\hat{I}_{\beta,j}} = 0$ if $i \neq j$. Comparing to Equation 1-22 we retrieve

$$\boxed{\overline{\langle\sigma|\,\hat{b}^\dagger_{\alpha,j}\,|\sigma'\rangle\,\langle\sigma'|\,\hat{b}_{\beta,l}\,|\sigma\rangle}_{\text{non spin-flip}} = b^*_{coh,\alpha}b_{coh,\beta} + \delta_{\alpha,\beta}\frac{1}{3}b^2_{inc,\alpha}}. \tag{1-30}$$

- The **spin-flip** case. We do the calculations for spin-up $|u\rangle$ polarised neutrons, analysed for final spin down $|v\rangle$ neutrons, however the same result holds for $|v\rangle \to |u\rangle$ polarisation.

$$\begin{aligned}\overline{\langle u|\,\hat{b}^\dagger_{\alpha,j}\,|v\rangle\,\langle v|\,\hat{b}_{\beta,l}\,|u\rangle} &= \overline{\frac{1}{4}B^*_{\alpha,j}B_{\beta,l}(\hat{I}_{x,\alpha,j} + i\hat{I}_{y,\beta,l})(\hat{I}_{x,\alpha,j} - i\hat{I}_{y,\beta,l})} \\ &= \frac{1}{4}|B_\alpha|^2\frac{2}{3}I_\alpha(I_\alpha+1).\end{aligned}$$

  The same result holds for spin flip from spin-down $|v\rangle$ to spin-up $|u\rangle$. Comparing to equation [Equation 1-22] we retrieve that :

$$\boxed{\overline{\langle\sigma|\,\hat{b}^\dagger_{\alpha,j}\,|\sigma'\rangle\,\langle\sigma'|\,\hat{b}_{\beta,l}\,|\sigma\rangle}_{\text{spin-flip}} = \delta_{\alpha,\beta}\frac{2}{3}b^2_{inc,\alpha}}. \tag{1-31}$$

Finally, the implication concerning cross sections is obtained fromEquation 1-30 and Equa-

tion 1-31 used in Equation 1-27

$$\begin{cases} \left(\frac{d\sigma^2}{\mathbf{d\Omega}dE}\right)_{\text{coherent}} = \left(\frac{d\sigma^2}{\mathbf{d\Omega}dE}\right)_{\text{non spin flip}} - \frac{1}{2}\left(\frac{d\sigma^2}{\mathbf{d\Omega}dE}\right)_{\text{spin flip}} \\ \left(\frac{d\sigma^2}{\mathbf{d\Omega}dE}\right)_{\text{incoherent}} = \frac{3}{2}\left(\frac{d\sigma^2}{\mathbf{d\Omega}dE}\right)_{\text{spin flip}} \end{cases}. \tag{1-32}$$

Remark : Beam polarisation permits separation of contributions, but nuclear polarisation is also a feasible contrast agent. Polarised beam could perhaps benefit one day from a resurgence of interest in dynamic nuclear polarization (DNP) at low temperature ($T \approx 1K$) for the study of biomolecules [50, 51], which improves contrast and decreases the intensity of incoherent scattering through polarisation of hydrogen and deuterium nuclei from paramagnetic centers spread in the sample.

1.3.5 Scattering functions and properties

The double differential cross section is the quantity that is directly probed instrumentally. For the sake of simplicity, we englobe all atomic pairs under subscripts j and k and do not sum on each nucleus type anymore, but on the total number of nuclei N.

$$\left(\frac{d\sigma^2}{\mathbf{d\Omega}dE}\right) = \underbrace{\frac{k'}{k}\frac{1}{2\pi\hbar}\int_{-\infty}^{\infty}\left(\sum_{j=1}^{N}\sum_{k=1}^{N}\Gamma_{j,k}\langle\exp\left(-i\mathbf{Q}\hat{R}_j(0)\right)\exp\left(i\mathbf{Q}\hat{R}_k(t)\right)\rangle\right)\exp(-i\omega t)dt}_{NS(\mathbf{Q},\omega)}. \tag{1-33}$$

With

$$\Gamma_{j,k} = \left(b^*_{coh,j}b_{coh,k} + \delta_{jk}|b_{inc,j}|^2\right), \tag{1-34}$$

in the case of an unpolarised beam. We introduce the **dynamical structure factor** $S(Q,\omega)$, with N the total number of atoms in the target. This function is directly a probe of the sample's dynamics and does not explicitly depend on the momentum of the neutron.

From this function, two other functions can be deduced using Fourier Transforms, since **r** and **Q** are quantum conjugate variables : **the intermediate scattering function** $F(\mathbf{Q},t)$ and **the time-dependent pair-correlation function** $G(\mathbf{r},t)$.

$$S(\mathbf{Q},\omega) = \frac{1}{2\pi}\int_{-\infty}^{+\infty} dt\, F(\mathbf{Q},t)\exp(-i\omega t),$$
$$G(\mathbf{r},t) = \frac{1}{(2\pi)^3}\int_{-\infty}^{+\infty} d\mathbf{Q}\; F(\mathbf{Q},t)\exp(-i\mathbf{Q}r). \tag{1-35}$$

Figure 1-3 displays how the three functions relate in the case of a simple exponential decay for the intermediate scattering function.

The three functions are paramount : $S(\mathbf{Q},\omega)$ is probed with most instruments, $F(\mathbf{Q},t)$ is

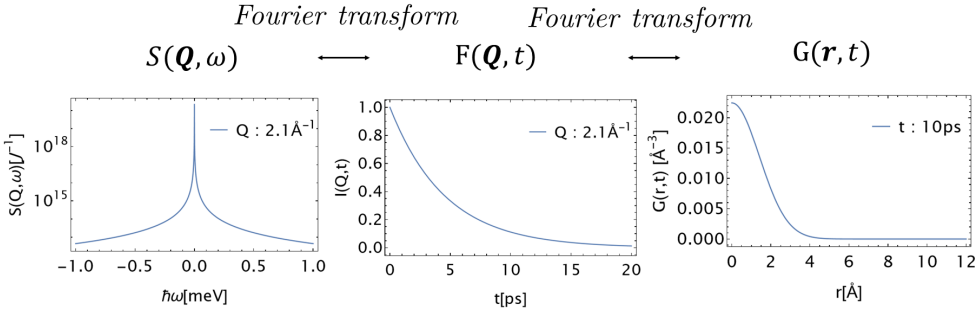

Figure 1-3: Examples of the three scattering functions obtained by Fourier transform, in the case of a single exponential decay with diffusion constant $D = 0.05\text{Å}^2\text{ps}^{-1}$.

probed with the neutron spin-echo technique, and $F(\mathbf{Q},t)$ and $G(r,t)$ are more convenient to build models for relaxation and diffusion of nuclei. Our model presented in section 1.4 is built from the intermediate scattering function $F(\mathbf{Q},t)$.

The classical limit

It is very important to notice that time-dependent position operators $\hat{R}(t)$ do not commute with each others. It is obvious from Heisenberg representation, Equation A-17 : the Hamiltonian $\hat{H}$ is a function of $\hat{p}$, the momentum of the nucleus, which does not commute with the position operator.
They do commute at two conditions :

- At t=0.
- In the classical limit ($\hbar \to 0$) $\hat{R}(t)$ are no longer quantum operators but simply space coordinates. It corresponds indeed to the condition $\frac{\hbar^2 Q^2}{2M} \ll |\hbar\omega|$ (the recoil energy of the neutron is negligible compared to the energy exchanged from/to the neutron by the system) [21].

In the classical limit, $S(\mathbf{Q},\omega)$ and $G(\mathbf{Q},t)$ are real and even functions. For disodered systems, it also applies to $I(\mathbf{Q},t)$ [52].

In the general (quantum) case, in the frame of a Boltzmann distribution of energy levels in the nucleus, the dynamical structure factor for energy loss and gain, are related by the detailed balance (where **Q** reversal is supposed to have no effect in our isotropic sample) :

$$S(\mathbf{Q}, -\omega) = \exp(-\beta\hbar\omega)S(\mathbf{Q}, \omega). \tag{1-36}$$

It means that the probability that enery exchange occurs from the neutron to the nucleus is lower by $\exp(-\hbar\omega\beta)$ compared to the nucleus→neutron energy exchange.
It implies that, as well, the intermediate scattering function is non symmetric :

$$F(\mathbf{Q}, -t) = F(\mathbf{Q}, t + i\hbar\beta), \tag{1-37}$$

which is taken into account when adapting the quantum-correlation function to our classical model, subsection 2.2.4.

Neutron scattering spectra in proteins

Proteins are complex systems with a quasi-continuum of accessible energy levels. However we usually distinguish 3 different regimes of scattering, their energy scales are presented in Figure 1-4.

- **Elastic scattering** : it corresponds to $\Delta E = 0$, there is no detectable energy exchange between the sample and the neutron. However, this is dependent on the instrument's resolution : all non-resolved energy exchanges for which neutrons are too fast to be detected appear as elastic scattering. Hence, it experimentally appears as a broadened peak around $\hbar\omega = 0$ in the shape of the instrument's resolution.
  Typical information : measurements of Mean-Squared Displacements (MSD), geometry of confinement of diffusing particles.

- **Quasielastic scattering (QENS)**: it corresponds to small energy exchange ($\approx$ sub-meV) both sides of the elastic peak. It equivalently correspond to slow dynamics of nuclei submitted to stochastic forces. Statistical physics provides models to relate the shape of the spectrum as a function of **Q** and ω to macroscopic properties of the sample.
  Typical information : characteristic times of diffusion and relaxation in the sample (translational, rotational).

- **Inelastic scattering ($\gg$ meV)** : it probes collective excitations (phonons) and vibrations. An advantage with respect to other spectrocopy techniques is the lack of selection rules.

  Typical information : densities of vibrational states, dispersion relations of acoustic and optical phonons...

Neutron scattering is therefore a strong probe for dynamics in materials due to this large accessible energy range. In this manuscript, we are mainly concerned with sub-meV processes (elastic scattering and QENS).

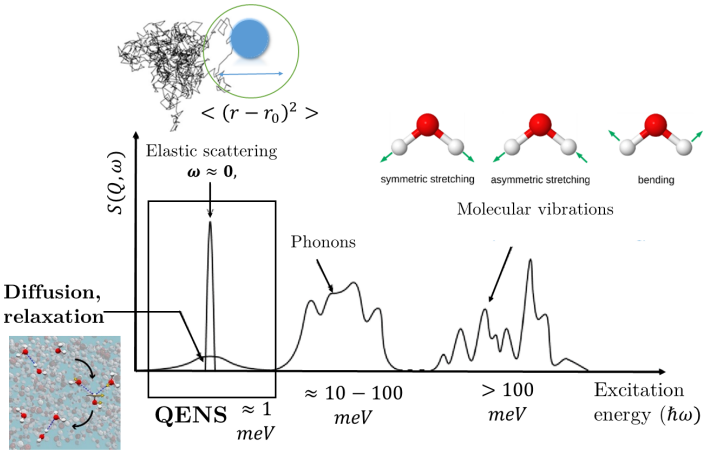

Figure 1-4: Schematics of the excitations in the sample at the atomic scale, observable with neutron scattering, as a function of energy exchange. Adapted from [53, 54, 55, 56].

1.4 Introduction of a model for the neutron scattering intermediate function to encompass both self and collective dynamics in proteins

This section relies on the formalism introduced by Kneller et al in [37, 38] that he and collaborators further applied to protein dynamics [39, 40, 42] and confined water [57]. Ref. [42] proposes a pedagogical introduction to the model in the case of a multi-domain protein, where both following models are used describe the dynamics of hydrogens.

1.4.1 A model for the autocorrelation of a dynamic variable in the frame of fractional brownian dynamics (FBD)

In this section we introduce the solution for the normalised auto-correlation function $\phi(t)$

$$\phi(t) = \frac{\langle x(0)^* x(t)\rangle}{\langle x(0)^* x(0)\rangle}, \tag{1-38}$$

of a complex dynamic variable x subject to a Fractional Ornstein Uhlenbeck process (FOU), where the autocorrelation is defined as

$$\langle x(0)x(t)\rangle = \int\int dx_0 dx P(x,t;x_0,0)x_0 x. \tag{1-39}$$

$P(x,t;x_0,0) = P(x,t|x_0,0)P(x_0,0)$ is the joint probability of variables $x(t)$ and $x(0)$. * is the complex conjugate.

The Ornstein-Uhlenbeck (OU) Process

The Ornstein Uhlenbeck process models nuclei confined in space, via a quadratic potential $V(x) = \frac{K}{2}x^2$ acting as an external force on the nucleus [58].
It means that $P(x,t) \equiv P(x,t|x_0,t_0)$, the transition probability density of x to move from x_0 at time t_0 to x at time t, can be solved with the Fokker-Planck equation [59, 60] :

$$\begin{aligned} &\frac{\partial P(x,t)}{\partial t} = \mathcal{L}_{FP} P(x,t), \\ &\text{where } \mathcal{L}_{FP} = -\frac{\partial}{\partial x}a_1(x) + \frac{1}{2}\frac{\partial^2}{\partial x^2}a_2(x), \end{aligned} \tag{1-40}$$

with drift coefficient $a_1(x) = -\eta x$ such that η is an inverse relaxation time and the fluctuation coefficient $a_2(x) = 2D$ with D the diffusion coefficient. The fluctuation-dissipation theorem states $\frac{D}{\eta} = \frac{k_B T}{K} = \langle x^2\rangle_{eq}$, with $\langle x^2\rangle_{eq}$ the mean-square displacements at equilibrium. Initial conditions imply that $P(x,0) = \delta(x - x_0)$.
The solution to such a process is simply an exponential decay with relaxation time η, such that the transition density probability of x follows a Gaussian distribution with standard-deviation $\sqrt{D/\eta}$ [61]:

$$P(x,t) = \sqrt{\frac{\eta}{2\pi D}}\exp\left(-\frac{\eta x^2}{2D}\right), \tag{1-41}$$

$$\phi(t) = \exp(-\eta t). \tag{1-42}$$

The Fractional Ornstein-Uhlenbeck (FOU) Process

The Fractional Ornstein-Uhlenbeck (FOU) process brings in memory effects [62, 63]. It is necessary in order to get non-exponential decays of the relaxation function, as are probed in proteins due to their heterogeneous behaviour [64]. It is furthermore required to model a more "adequate" environment for the dynamic variable : a walk in a rugged harmonic potential [65] where the effective stiffness is the one of the OU process, but series of local minima are encountered and are reminiscent of the picture of the protein energy landscape [66, 67]. The "fractional" aspect comes from the introduction of fractional derivatives [68] in the Fokker Planck equation, Equation 1-40 :

$$\frac{\partial P(x,t)}{\partial t} = \tilde{\tau}^{1-\alpha}\ {}_0D_t^{1-\alpha}\mathcal{L}_{FP}P(x,t), \tag{1-43}$$

where ${}_0D_t^{1-\alpha} = \frac{d}{dt}\int_0^t d\tau \frac{(t-\tau)^{\alpha-1}}{\Gamma(\alpha)} f(\tau)$, defined for an arbitrary function f (here, $\mathcal{L}_{FP}P(x,t)$), is the Riemann-Liouville fractional derivative of order $1-\alpha$ with respect to t. Γ is the Gamma function and $\tilde{\tau}^{1-\alpha}$ is a scale factor to preserve dimensionality.
In this case, the solution for the autocorrelation function brought by Equation 1-43 is a generalized stretched exponential, the Mittag Leffler (ML) function $E_\alpha[t]$

$$\phi(t) = E_\alpha\left[-\left(\frac{t}{\tau}\right)^\alpha\right], \tag{1-44}$$

where τ is the relaxation time

$$\tau = \frac{\tilde{\tau}^{1-\frac{1}{\alpha}}}{\eta}. \tag{1-45}$$

The ML function is defined by the series [69, 70, 71],

$$E_\alpha(z) = \sum_{k=0}^{\infty} \frac{z^k}{\Gamma(1+\alpha k)}, \tag{1-46}$$

with $z \in \mathbb{C}$ and $\alpha \in \mathbb{C}$.
It can be understood as a "generalization" of the exponential function for fractional calculus, such that $\exp(t)$ verifies $\frac{df(t)}{dt} = f(t)$ and $E_a(t^\alpha)$ verifies $\frac{df(t)}{dt} =_0 D_t^{1-\alpha} f(t)$ for an arbitrary function f, therefore explaining that it arises as the solution of the fractional Fokker-Planck equation. It interpolates between a stretched exponential at very low times and a power law function at very long times : $E_\alpha^\infty(t) = \frac{t^{-\alpha}}{\Gamma(1-\alpha)}$, $E_\alpha^0(t) = \exp(-\frac{t^\alpha}{\Gamma(1+\alpha)})$, see

Figure 1-5 [70].

In the limit $\alpha \to 1$, the Mittag-Leffler function is the solution to the OU process $\phi(t) = \exp(-\eta t)$.

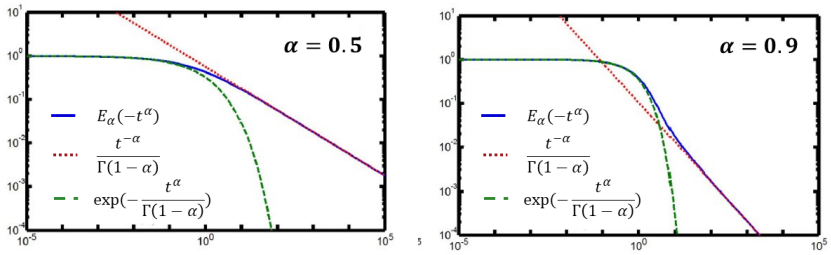

Figure 1-5: Interpolation of the Mittag Leffler fonction (blue full line) between a stretched exponential (green dotted line) and a power law (red dotted line) as a function of time, adapted from [70].

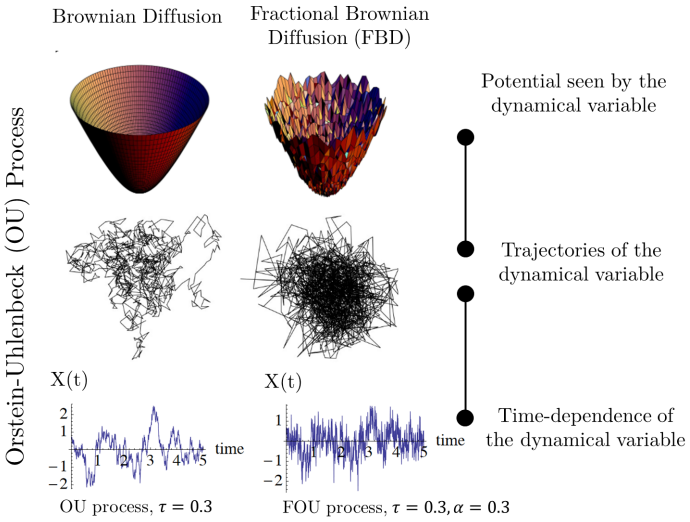

Figure 1-6: Figure adapted from [55], illustrating the behaviour of the dynamic variable in a quadratic potential, in the case of normal and fractional Brownian diffusion.

Mori-Zwanzig formalism and memory effects

The concept of "memory effect" is perfectly illustrated in the Mori-Zwanzig formalism, which is briefly described to enhance the difference between simple diffusion and fractional diffusion [72, 73].

The derivative of the dynamic variable $x(p, q)$ dependent on phase space variables is determined by the Liouville operator L, such that $\frac{dx}{dt} = Lx$. L is separated into its projection onto the dynamic variable space, and onto the orthogonal space of non-relevant variables.

It yields a generalized form of the Langevin equation [74] were "slow" and "fast" varying

functions do not have to be specified, avoiding strong hypothesis on the timescales of the Brownian particle velocity with respect to its environment. Indeed, projectors naturally express the derivative of the dynamic variable as the sum of a "friction term" $\int_0^t d\tau\kappa(t-\tau)x(\tau)$ and a "fluctuating force" $f^+(t)$. The latter is projected onto the orthogonal space and is uncorrelated to the dynamic variable x such that $\langle x, f^+(t)\rangle = 0$. For a classical system one gets :

$$\frac{\partial}{\partial t}x(t) + \int_0^t d\tau\kappa(t-\tau)x(\tau) = f^+(t). \tag{1-47}$$

From this, we get an expression for the derivative of the autocorrelation function $\phi(t)$ of x, for which the fluctuating term disappears, only the friction term remains.
Let us notice that the remaining term is the convolution of $\phi(t)$ with a "memory kernel" $\kappa(t)$, where $\kappa(t)$ is determined by the autocorrelation of the fluctuating force $f^+(t)$.

$$\frac{d}{dt}\phi(t) = -\int_0^t d\tau\kappa(t-\tau)\phi(\tau). \tag{1-48}$$

The memory kernel for Brownian dynamics For Brownian motion, i.e. free diffusion, the memory kernel is proportional to the Dirac distribution function for an exponential decay

$$\kappa(t)_{\mathrm{BD}} = \frac{1}{\tau}\delta(t). \tag{1-49}$$

Hence, no "memory" effects. It gives rise to the "Gaussian noise" of the fluctuating function introduced in the Langevin equation formalism, which models the weak interaction of the particle with its surrounding environment

The memory kernel for Fractional Brownian dynamics The memory kernel for fractional Brownian motion, which is a non-Markovian process, takes a more complex form. For the Mittag-Leffler function, for $t > 0$, it writes

$$\kappa(t)_{\mathrm{FBD}} = \frac{\alpha-1}{\Gamma(\alpha)\tau_\alpha^2}\left(\frac{t}{\tau_\alpha}\right)^{\alpha-2}, \tag{1-50}$$

and expresses, in a nutshell, how the fluctuating force determines the time-evolution of the auto-correlation function. It accounts for the large number of interacting particles, where the mass of particles in the bath are sensibly close to the diffusing particle.

1.4.2 Application to the intermediate neutron scattering function

The intermediate neutron scattering function

Now, why being interested in the autocorrelation function of a dynamic variable ? When it comes to neutron scattering, the quantity obtained with experiments is the dynamic structure factor,

$$S(\mathbf{Q},\omega) = \frac{1}{2\pi}\int_{-\infty}^{+\infty} dt\, F(\mathbf{Q},t)\exp(-i\omega t), \tag{1-51}$$

where $\mathbf{Q}$ and ω are, respectively, the momentum and energy transfer from the neutron to the scattering atoms in units of $\hbar$. It is the Fourier-transform of the intermediate scattering function F($\mathbf{Q}$,t)

$$\boxed{\begin{aligned} F(\mathbf{Q},t) &= \frac{1}{N}\sum_{j,k}\langle b_j^* b_k \exp\Big(-i\mathbf{Q}\hat{R}_j(0)\Big)\exp\Big(i\mathbf{Q}\hat{R}_k(t)\Big)\rangle \\ &= \frac{1}{N}\sum_{j}\sum_{k}\Gamma_{j,k}\langle\exp\Big(-i\mathbf{Q}\hat{R}_j(0)\Big)\exp\Big(i\mathbf{Q}\hat{R}_k(t)\Big)\rangle. \end{aligned}} \tag{1-52}$$

N is the number of atoms in the sample, $\langle\ldots\rangle$ denotes a quantum ensemble average, and $\hat{\mathbf{R}}_j(t)$ is the position operator of atom j in the Heisenberg picture. We write

$$\Gamma_{j,k} = \left(b_{coh,j}^* b_{coh,k} + \delta_{jk}|b_{inc,j}|^2\right), \tag{1-53}$$

where $b_{j,\mathrm{coh}}$ is the coherent and $b_{j,\mathrm{inc}}$ the incoherent scattering lengths of atom j.
Separate terms weighted by coherent and incoherent scattering lengths raises the incoherent and coherent intermediate scattering functions. They can only be separated with polarisation analysis. We recall that the coherent part reflects the structural dynamics of the atoms in the scattering system, and the incoherent part results from single-atom contributions. Separating the sum into "self" terms ($j = k$) and distinct terms ($j \neq k$) emphasises that incoherent scattering is only self scattering, while coherent scattering is composed of both a self and distinct parts.

Introduction of a dynamic variable

General case We need to introduce a dynamic variable $\hat{\chi}(\mathbf{Q},t)$ to account for both self and distinct scattering [37, 42]. It is a collective variable, expressed as the sum of all

nuclei

$$\boxed{\hat{\chi}(\mathbf{Q},t) = \sum_{j}^{N} w_j \delta\hat{\rho}_j(\mathbf{Q},t),} \tag{1-54}$$

where w_j are weights determined by scattering lengths ($w_j = b_j$ for total scattering and b_{coh} for coherent scattering), and

$$\delta\hat{\rho}_j(\mathbf{Q},t) = \exp\Big(i\mathbf{Q}\hat{R}_j(t)\Big) - \langle\exp\Big(i\mathbf{Q}\hat{R}_j(t)\Big)\rangle, \tag{1-55}$$

is the temporal fluctuation of the Fourier transform of the particle density,

$$\hat{\rho}_j(\mathbf{Q},t) = \int_{-\infty}^{\infty} d\mathbf{r}\exp(i\mathbf{Q}\mathbf{r})\delta(\mathbf{r} - \hat{R}_j), \tag{1-56}$$

from its equilibrium.
We introduce the Elastic Structure Factor (ESF)

$$\boxed{ESF(\mathbf{Q}) = \lim_{t\to\infty} F(\mathbf{Q},t) = \frac{1}{N}|\langle\hat{\chi}(\mathbf{Q})\rangle|^2}. \tag{1-57}$$

$F(\mathbf{Q},0)$ is the static structure factor $S(\mathbf{Q})$

$$\boxed{F(\mathbf{Q},0) = S(\mathbf{Q}) = \int_{-\infty}^{+\infty} d\omega\, S(\mathbf{Q},\omega)}, \tag{1-58}$$

such that the intermediate scattering function is a function of $\phi(t)$, the autocorrelation function of $\hat{\chi}(\mathbf{Q},t)$. $F(\mathbf{Q},t)$ relaxes from $S(\mathbf{Q})$ to the $ESF(\mathbf{Q})$ via $\phi(t)$,

$$\boxed{F(\mathbf{Q},t) = ESF(\mathbf{Q}) + (S(Q) - ESF(\mathbf{Q}))\underbrace{\frac{\langle\hat{\chi}(\mathbf{Q},0)^\dagger\hat{\chi}(\mathbf{Q},t)\rangle}{\langle\hat{\chi}(\mathbf{Q},0)^\dagger\hat{\chi}(\mathbf{Q},0)\rangle}}_{\phi(t)}.} \tag{1-59}$$

† indicates the Hermitian adjoint. The calculations are provided in the Appendix, Equation A-20.

Incoherent scattering We introduce, in the special case of incoherent scattering, the self dynamic variable $\hat{\chi}_{\text{self},j}(\mathbf{Q},t)$ of a single atom j

$$\boxed{\hat{\chi}_{\text{self},j}(\mathbf{Q},t) = w_j\delta\hat{\rho}_j(\mathbf{Q},t)}, \tag{1-60}$$

where $w_j = b_{j,\mathrm{inc}}$. Thus, the intermediate scattering function is instead the sum of autocorrelations of N individual variables.

$$\boxed{F_{\mathrm{self}}(\mathbf{Q},t) = EISF(\mathbf{Q}) + (1 - EISF(\mathbf{Q}))\underbrace{\frac{1}{N}\sum_{j=1}^{j=N}\frac{\langle\hat{\chi}_{\mathrm{self},j}(\mathbf{Q},0)^{\dagger}\hat{\chi}_{\mathrm{self},j}(\mathbf{Q},t)\rangle}{\langle\hat{\chi}_{\mathrm{self},j}(\mathbf{Q},0)^{\dagger}\hat{\chi}_{\mathrm{self},j}(\mathbf{Q},0)\rangle}}_{\phi(t)}}. \quad (1\text{-}61)$$

$F(\mathbf{Q},0) = 1$, and $F(\mathbf{Q},\infty)$ corresponds to the Elastic Incoherent Scattering Factor, $EISF(\mathbf{Q})$.

Hydrogen atoms are abundant and homogeneously distributed within a biomolecule. Combined to the large incoherent cross section of hydrogen nuclei, it usually entails to express $\phi(t)$ for a protonated protein in D_2O as a sum of individual self variables stemming from protonated hydrogens only, such that $j \in H$.

Introduction of a model for protein dynamics

We suppose, in the general case, that $\hat{\chi}(\mathbf{Q},t)$ is submitted to a FOU process. Hence, we model its autocorrelation with a Mittag-Leffler function

$$\boxed{\phi(t) = E_{\alpha}\left[-\left(\frac{t}{\tau}\right)^{\alpha}\right]}. \quad (1\text{-}62)$$

$\phi(t)$ takes its values in [0,1]. Hence, the autocorrelation function in Equation 1-61 in replaced with Equation 1-62.

Hence, we emphasize that it is the dynamics of the collective variable $\hat{\chi}(\mathbf{Q},t)$ (coherent scattering) or an average of all self variables $\hat{\chi}_{\mathbf{self},j}(\mathbf{Q},t)$ (incoherent scattering) that we analyse with the model all along the manuscript.

Therefore, to model the intermediate function $F(Q,t)$ in the general case without assuming self-diffusion, we introduced a 3 parameter model dependent on parameters τ, α and ESF which are Q-dependent parameters.

A few remarks

- Let us notice that the dynamic variable is a function of $\mathbf{Q}$, as opposed to usual models expressed in the Van-Hove formalism [18], where the dynamic variable is the particle density and depends on position $\mathbf{r}$.

- In practice, relaxation functions are defined such that $\phi(\mathbf{Q}, 0) = 1$ and $\phi(\mathbf{Q}, \infty) = 0$. They require to normalize Equation 1-59 such that :

$$\lim_{Q \to \infty} F(\mathbf{Q}, 0) = \frac{1}{N} \sum_j \Gamma_{jj} = 1. \text{ [75]} \tag{1-63}$$

1.4.3 Physical meaning of the FBD model applied to protein dynamics

Properties of the Mittag-Leffler function

Further than being the solution of fractional Brownian dynamics processes, appearing in complex energy landscapes [76, 66, 77], the Mittag-Leffler function has several mathematical properties making it a strong candidate to model slow processes in biomolecular systems.

1. The Mittag-Leffler function tends to a power law for long times : $E_\alpha(t) \underset{t \to \infty}{\sim} \frac{t^{-\alpha}}{\Gamma(1-\alpha)}$, which is typical for proteins and, more widely, complex systems [78, 79, 80, 81]. Therefore it is an asymptotically self-similar function, meaning form-invariant under the scale transformation $t \to \mu t$ for any $\mu > 0$.

2. Furthermore, in the frame of asymptotic analysis [82], Kneller et al essentially prove that any relaxation function that follows an asymptotic power-law decay and which memory kernel reaches almost instantaneously its asymptotic form (i.e. in a time τ^* negligible with respect to the relaxation time τ of the system) is expressed by a Mittag-Leffler function. It highlights the inherent requirement to use this particular function for systems following power-law relaxations when external force fluctuations are rapidly set.

3. In [83], Kneller et al extend the range of self-similarity by introducing a "weak" self similar asymptotic form for the Mittag-Leffler function at very long times and its derivatives at very short times. The asymptotic behaviour is approached by expressing the Mittag-Leffler function as the product of a self-similar power law function $f(t) = \frac{(t/\tau)^{-\alpha}}{\Gamma(1-\alpha)}$ and a slowly varying function $L(t)$ verifying $\frac{L(\lambda t)}{L(t)} \overset{t \to \infty}{\sim} 1$ and $\lim_{t \to \infty} L(t) = 1$. This form extends self-similarity on a larger timescale both ends of the spectrum. It indicates the Mittag-Leffler function as a good candidate for self-similar relaxation spanning on several decades, which is a property found in proteins

[1]. Nb : Both weak self-similarity and the requirement for a fast converging memory kernel increase when α (heterogeneity) decreases.

4. For $\alpha \to 1$, a single exponential decay is retrieved for the relaxation function : $\lim_{\alpha\to 1} E_\alpha(t) = \exp(-t)$ and the power law long time tail vanishes. This has been observed experimentally for bulk water [57].

By definition this model does not resolve single processes. It englobes all processes as a whole, considering that the complexity and heterogeneity of the system does not permit such a decomposition into elementary diffusive, rotational and vibrational motions as is often performed even in such complex systems as proteins. The model does not require that the conformational space be fractal to use fractional dynamics.

Interpretation of the 3-parameter model

The model is minimalist and enables to fit only 3 Q-dependent parameters

1. the form parameter $\alpha \equiv \alpha(\mathbf{Q})$,
2. the time scale parameter $\tau \equiv \tau(\mathbf{Q})$,
3. the elastic intensity $F(\mathbf{Q}, \infty)$.

Let us discuss briefly how those three parameters shall be interpreted :

- The order of the fractional derivative, the form parameter $0 \leq \alpha \leq 1$, models the heterogeneity of the system : it can be understood from the concept of memory kernel where it models the impact of the environment and its delay with the friction term. It can also illustrates the heterogeneity of internal processes in the protein, (modeled by exponential decays with a broad range of relaxation times) or the non-exponential decay of individual nuclei. It is because the spectral distribution of the Mittag Leffler function writes, with dimensionless rate λ

$$E_\alpha[-(t)^\alpha] = \int_0^\infty p(\lambda)\exp(-\lambda t)dt. \tag{1-64}$$

  where the relaxation spectrum $p_\alpha(\lambda)$ is equal and expressed as :

$$p_\alpha(\lambda) = \frac{1}{\pi\lambda}\frac{2\sin(\pi\alpha)}{(\lambda)^\alpha + (\lambda)^{-\alpha} + 2cos(\pi\alpha)}. \tag{1-65}$$

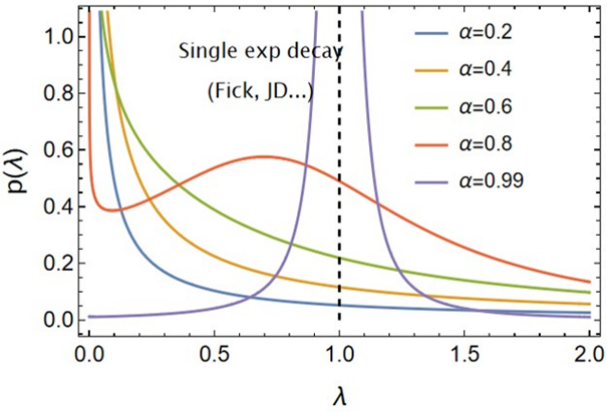

Figure 1-7: Relaxation spectrum $p_\alpha(\lambda)$ of the Mittag-Leffler function, Equation 1-65

- τ is a scale factor defined in Equation 1-45, describing the time scale at which dynamics occur. It is highly dependent on the instrumental resolution. Figure 1-7 illustrates how τ differs from the relaxation time of an exponential function. Noticing that the exact same expression holds for the rate and time spectra of the Mittag-Leffler function, one sees on Figure 1-7 that the distribution $p_\alpha(\lambda)$ broadens strongly around $\delta(x-1)$ (exponential case) already for $\alpha = 0.99$, and is distributed along a large range of values and diverging at $\lambda = 0$ when $\alpha \to 0$.

- The ESF is the asymptotic plateau value towards which $F(\mathbf{Q},t)$ decays. Normalisation by [Equation 1-63] yields $0 \leq ESF(\mathbf{Q}) \leq 1$ and $\lim_{Q\to 0} ESF(\mathbf{Q}) = 1$.

1.4.4 Review of usual models for incoherent neutron scattering in proteins.

Incoherent QENS in proteins consists in probing self diffusion of the hydrogen atoms, and most models are indeed expressed in the classical limit of the Van Hove formalism where operators $\hat{R}$ commute

$$G_{\text{inc,cl}}(\mathbf{r},t) = \frac{1}{N}\sum_i \int d\mathbf{r} \langle \exp\left(\mathbf{r} - (\mathbf{R}_i(t) - \mathbf{R}_i(0))\right)\rangle. \tag{1-66}$$

It is usually tackled by assuming that distinct processes are at stake in the sample and can be multiplied due to their dynamic independence [21]. Usually, distinction is performed between translational diffusion (L), rotational diffusion (R) and molecular vibration (V).

$$F_{\text{inc}}(\mathbf{Q},t) = F^{\text{L}}_{\text{inc}}(\mathbf{Q},t) F^{\text{R}}_{\text{inc}}(\mathbf{Q},t) F^{\text{V}}_{\text{inc}}(\mathbf{Q},t). \tag{1-67}$$

Diffusion While proteins in solution undergo translational and rotational diffusion of their center-of-mass, protein powders only display localised confined motions, hence a non-vanishing ESF(Q). The latter processes are usually expressed from Markovian models and analysed in ω-space from $S(\mathbf{Q},\omega)$:

$$\begin{aligned} S(\mathbf{Q},\omega) &= EISF(\mathbf{Q})\delta(\omega) + (1 - EISF(\mathbf{Q}))\,\frac{1}{\pi}\frac{\Gamma(\mathbf{Q})}{\Gamma(\mathbf{Q})^2 + \omega^2} \\ \Leftrightarrow F(\mathbf{Q},t) &= EISF(\mathbf{Q}) + (1 - EISF(\mathbf{Q}))\exp(\Gamma(\mathbf{Q})t), \end{aligned} \tag{1-68}$$

where $S(\mathbf{Q},\omega)$ and $F(\mathbf{Q},t)$ respectively take exponential and Lorentzian forms, $\Gamma(\mathbf{Q})$ is the HWHM of the Lorentzian function. Most models in ω-space can be expressed as a single Lorentzian (Fick diffusion) or an infinite sum of Lorentzian decays (Hall and Ross, diffusion inside a sphere, isotropic rotational diffusion models). For proteins, the first term of the sum is usually enough to describe the motion, since amplitudes of terms decay rapidly for $n > 1$ for Q sufficiently small, where n is the incrementation term of the sum of Lorentzians. Furthermore, considering the whole sum would significantly increase the number of parameters.

In a nutshell, those models provide explicit timescales of motion (diffusion coefficient, residence time..) with $\Gamma(\mathbf{Q})$, and information on confinement geometry with $ESF(\mathbf{Q})$. A few models are briefly introduced here [84], in the case of 1D diffusion, illustrated with Figure 1-8:

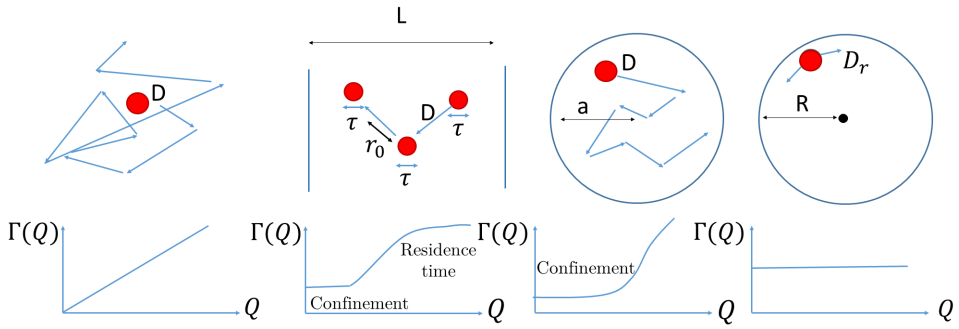

Figure 1-8: Illustrations for the Fick free-diffusion, confined Hall-Ross diffusion, diffusion inside a sphere and isotropic rotational diffusion from left to right. Sketch of the particle's motion and Γ behaviour as a function of Q^2.

- **Fick diffusion** (translational) : Accounts for the translational diffusion of a free particle (no external potential), with no boundary conditions. In the Fokker-Planck equation Equation 1-40 applied to the position $\mathbf{r}$ it consists in setting $a_1(x) = 0$, $a_2(x) = 2D$.

It yields a solution of the form of Equation 1-68 with $\Gamma(Q) = DQ^2$, $EISF(Q) = 0$.

- **Hall and Ross model** (translational) [22] : Defining 3 dynamical parameters, the model accounts for non-continuous diffusion within boundaries of width L due to uncorrelated jumps, which lengths are distributed according to a Gaussian distribution defined with $\langle r^2 \rangle = 3r_0^2$. During jumps, the particle diffuses with diffusion coefficient D. In between two jumps, the residence time τ of the particle is defined such that the number of jumps follows a Poisson law. This is a special case of jump-diffusion models, which are largely used to analyze global motions in solubilized proteins [6], hydration water [85], as well as protein localised motions [6].
  Dynamical parameters : For low Q ($\equiv$ large r, confinement) $\Gamma(Q) = \frac{\pi^2 D}{L^2}$, and for higher Q, $\Gamma(Q) = \frac{1}{\tau}\left(1 - \exp\left(-\frac{Q^2 r_0^2}{2}\right)\right)$, *Geometry* : $EISF(Q) = j_0(QL/2)$ (j_N are the spherical bessel functions of order N).

- **Diffusion in a sphere** [86] : Considering a free particle inside a sphere of radius R ($V(r) = 0$ when $r < R$) with boundaries set by an infinite radial potential outside the sphere ($V(r) = \infty$), Volino and Dianoux introduced a model for a particle free-diffusing inside a sphere based on spherical harmonic decomposition. Only the two first terms of the sum of Lorentzian functions are usually accounted for as explained in [87]. Eg : hydration water motions [87], protein localised motions in powders [88]
  Dynamical parameters : low Q (confinement) $\Gamma \approx 4.33\ D/R$, large Q (diffusive motions) $\Gamma \approx DQ^2$ *Geometry* : $EISF(Q) = (3j_1(QR)/QR)^2$.

- **Isotropic rotational diffusion** [89] : Random small-angle rotations with no specific preferred orientation on a sphere of radius R, leading to rotational diffusion with coefficient D_r. Many refined models account for preferred orientations in a finite number of sites. *Dynamical parameters* : $\Gamma = 2D_r$, no Q-dependence (no translational motion). *Geometry* : $A_0(Q) = j_0^2(QR)$. Eg : localised rotations of H atoms in fluorescent proteins [90, 91].

However, regarding the complexity of protein motions, our fractional model rather assumes coupled and indistinguishable motions, far from exponential behaviour. Some models also following the same paradigm :

- The complexity of protein motions is also often accounted for by the Kohlrausch–Williams–Watt

(KWW) function. It is applied in time-domain

$$F(Q,t) = \exp\left(-\left(\frac{t}{\tau}\right)^{\beta}\right). \tag{1-69}$$

It is a stretched exponential used to describe the final decay in the Mode-Coupling Theory (MCT) accounting for the dynamics of glass-forming materials [92] and applied to protein [88] and water [93] localised motions. It yields similar parameters to our model, β, which can also be understood as a motional heterogeneity ($\beta \to 1$ retrieves the exponential relaxation) and τ a timescale of motions, and is similar enough to provide comparison with our own results. However, it does not provide an analytical memory kernel.

- Some authors rather work with the dynamic susceptibility $\chi"(Q,\omega) = S(Q,\omega)/nb(T,E)$ with $nb(T,E)$ the temperature Bose factor. This formalism is derived from linear response theory. Using a Cole-Cole function raises a Mittag Leffler function in time-domain [94], and has also been used to model the GFP protein localised motions [91]. Hence, it also provides a baseline for comparison to our model.

Vibrations Usually, harmonic vibrations are accounted by a Debye-Waller factor

$$F^{\mathrm{V}}_{\mathrm{inc}}(\mathbf{Q},t) = \exp\big(-(\langle r_v^2\rangle + \langle r_L^2\rangle)\mathbf{Q}^2\big), \tag{1-70}$$

with $\langle r_v^2\rangle$ and $\langle r_L^2\rangle$ MSD corresponding to internal and lattice vibrations. However in proteins, it is often encountered (e.g. the Boson Peak) that collective vibrations spanning a large portion of the proteins present strong softening (close to the QENS region, $\approx$ 3 meV) and anharmonicity with an excess of vibrational density compared to what is expected from the Debye model, reminiscent of glassy dynamics. Those motions are usually modelled with log-normal functions [95, 96, 97].

1.5 An overview of coherent quasielastic scattering modeling in soft matter and proteins

We present here the current situation for the study of coherent quasielastic scattering in proteins and more generally soft matter. We focus on the work of Arbe et al. which greatly influenced us as reported in chapter 3 and chapter 4. It requires the knowledge

of the different neutron spectrometer types and characteristics, see subsection 2.1.3 and subsection 2.2.2.

1.5.1 Models for coherent scattering in soft matter

The collective information encoded in quasielastic coherent neutron scattering has been scarcely studied in proteins so far. Contrary to some liquids which can provide coherent data in the Q region where TOF and backscattering spectroscopy are performed [98], protonated biomolecules are inherently highly incoherent scatterers. Therefore, it requires per-deuteration [24, 25], scattering from a polarised neutron beam [33], or ideally both methods in order to study directly coherent dynamics : it is costly, and adapted instrumentation is rare.

Nevertheless, models for coherent scattering have been investigated and cover small ($Q > 0.01\text{Å}^{-1}$) and large ($Q > 1\text{Å}^{-1}$) Q ranges:

- At long timescales and for motions spanning large distances ($\gg$ nm) englobing subunits of the system, neutron spin echo (NSE), which is more adapted to protein solutions due to the fast decay of internal modes, gives access to coherent scattering ($F(Q,t) = F_{\text{coh}}(Q,t) - 1/3\ F_{\text{inc}}(Q,t)$ in the classical description). This is inherent to the technique, relying on the precession of the spin of the neutron. Models emerged to understand collective dynamics in proteins : coarse grain models for polymers (Rouse model, reptation dynamics... [99]) applied to intrinsically disordered protein [100], study of domain motions [101, 102] or global diffusion and internal motions [100, 3]. Analyses of internal motions can benefit from the investigation of the principal normal modes in the protein [100, 24]. However, it concerns much larger amplitudes than what TOF and even backscattering can probe.

- On the contrary, at local scales close to near-neighbour distances ($Q \approx 1.5 - 2\text{Å}^{-1}$), a few models account for collective dynamics directly from the knowledge of self-dynamics and the structure of the sample which is embedded by S(Q), Equation 1-58. Both incoherent and coherent timescales tend to merge at that scale, but the coherent one undergoes a "De-Gennes" rescaling [103] : an increase of the relaxation timescale at the main diffraction peak due to increased space correlations, predicted from the 2nd and 4th moments of the sum-rules of the intermediate scattering function. A first convolution approximation was proposed initially by Vineyard [104] for monoatomic liquids, proposing $S_{\text{coh}}(Q,\omega) \approx S_{\text{tot}}(Q) S_{\text{inc}}(Q,\omega)$.

Upon violation of the moment relation and liquid properties at very low Q, more adequate Ansätze were then proposed over the years by Sköld where $S_{\mathrm{coh}}(Q,\omega) \approx S_{\mathrm{tot}}(Q)S_{\mathrm{inc}}\left(Q/\sqrt{S(Q)},\omega\right)$ [98]or Swingi [105] for instance, and demonstrated correct adequation for Q large enough and even for complex systems [106].

However, there is a lack of available models at intermediate scales spanning intermediate Q ranges, as illustrated on Figure 1-9 ($Q \approx 0.01\text{Å}^{-1}$ to $Q \approx Q_{max} \approx 1.5\text{Å}$) for the cases of polymers or more generally glass-forming materials [107, 108]. Minimalist interpolating models for distinct coherent scattering were proposed for glass-forming liquids [109] and polymers [108]. It bridges the gap between the Q-independent mean relaxation time $\langle\tau\rangle$ for $Q \to 0$ and the diffusive τ perturbed by structural correlations ($Q \to Q_{\max}$). Still, those

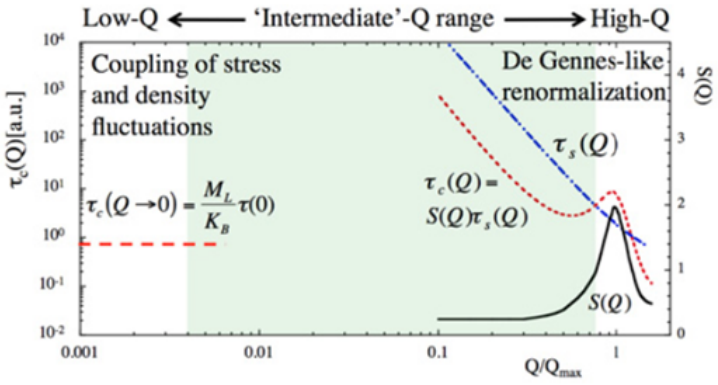

Figure 1-9: Graph proposed by Colmenero in [108] to illustrate the Q-range where coherent scattering lacks a unified model, grounded on physics arguments, in the case of glass-forming materials.

models are not casually used, and model-free approaches [31] or stretched exponentials [110] are also proposed to model $F(Q,t)$ this Q region. However, to our knowledge a formalism that applies to protein internal dynamics has never been put forward. Hence, for many reasons, coherent protein dynamics at the local scale remain experimentally unexplored and lack theoretical background.

1.5.2 A model introduced for the dynamics of liquids studied with polarized neutrons

Arbe et al have introduced a model, Equation 1-71, for incoherent and coherent neutron scattering in both D_2O and deuterated tetrahydrofuran (THF, used as a model for a simple Van-der-Waals liquid) [111, 112] applied to a similar Q range ($[0.4, 2.2]$ Å^{-1}) to

ours corresponding to "Intermediate Scales" (ILS) below hydrodynamic scales and above intermolecular distances. This is especially interesting for us regarding the importance of D_2O hydration water in our sample. Similarly, it was performed on polarised LET instrument with incoming energies 1.05, 1.81 and 3.84 meV at a temperature of $T = 300$ K[32].

The intermediate function accounts for vibrational processes with $F_v(Q,t)$ described as a damped resonance term with an amplitude $(1 - C(Q))$. Simulations have identified it with hydrodynamic-like modes [113]. The other term with amplitude $C(Q)$ corresponds to a pure relaxational process $I_r(Q,t)$. They argue that relaxation can be expressed as the product of two independent processes :

-One corresponds to a diffusional process with time-constant τ_d, which can be estimated from incoherent (self) scattering.

-One is a "local" Q-independent process that they identify with the forming and breaking of H-bonds during the relaxation of the H-bond network of D_2O [112]. Its relaxation time is $\tau_{c,0}$. It has a Q-dependent amplitude $(1 - A(Q))$.

Reformulating this model to factorize it by $A(Q)$ introduces two effective time constants : τ_d, a diffusive relaxation time, and $\tau_c = \left(\frac{1}{\tau_{c,0}} + \frac{1}{\tau_d}\right)^{-1}$, the Q-independent mode affected by the diffusional process. Hence, we emphasize that the model is based on a bi-exponential Markovian relaxation, making it not directly comparable to our results.

$$F_{\text{coh}}(Q,t) = S(Q)\left((1 - C(Q))F_v(Q,t) + C(Q)\underbrace{\left((1 - A(Q))e^{-\frac{t}{\tau_c}} + A(Q)e^{-\frac{t}{\tau_d}}\right)}_{F_r(Q,t)}\right). \tag{1-71}$$

At very low Q, the Q-independent mode is dominant and not affected by diffusion (see the ratios of amplitudes Figure 1-10 (a)) implying $\lim_{Q\to 0} F_r(Q,t) = e^{-\frac{t}{\tau_{c,0}}}$ with $\tau_{c,0,D_2O} = 1.7ps$ and $\tau_{c,0,\text{THF}} \approx 1.3ps$ at $T = 300K$.

Some important conclusions from their works are the following :

1. **Coherent neutron scattering** is the linear combination of a "distinct" (dist) and a "self" contribution. The first term corresponds to correlations of different nuclei only, while the latter corresponds to self-correlations. In D_2O, the amplitude of vibrational motions is almost constant over Q, while the Q-independent process is preponderant below $Q = 1.5\text{Å}^{-1}$ with a cross-over with dominating diffusion for

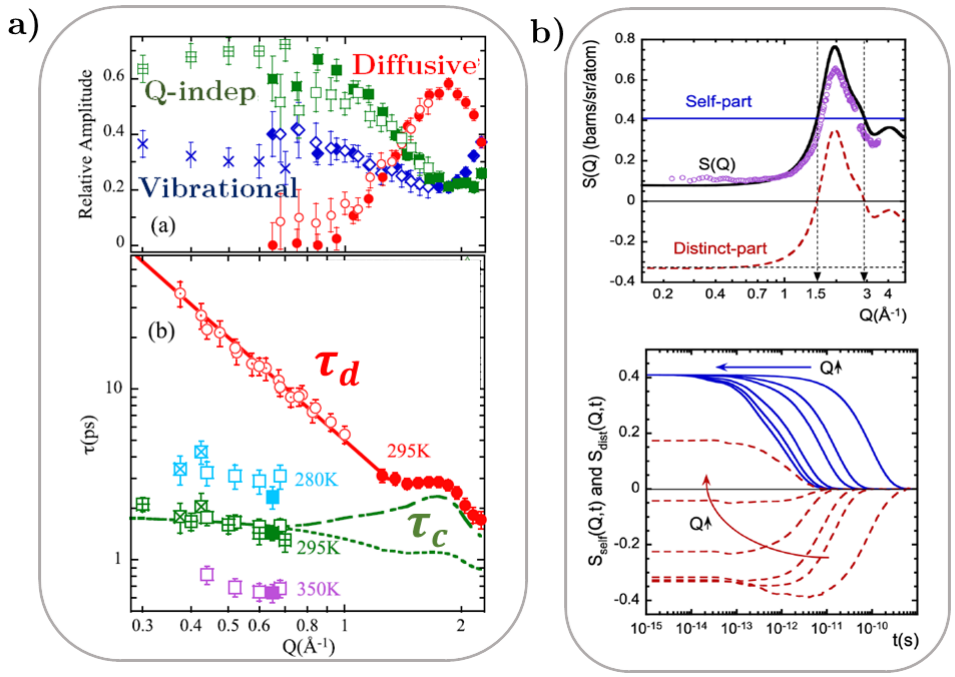

Figure 1-10: Figure adapted from results of Arbe et al, [114], [113], [32], from experiments performed on LET and molecular dynamics studies (MD). a) Dynamical results obtained from LET. Top : comparison of the relative amplitudes of vibration (blue), Q-independent (green), and diffusion processes (red) (top figures) for D_2O [32] as a function of momentum transfer Q. Bottom : time scales for self-diffusion (τ_d, in red) the Q-independent mode (τ_c, in green) for D_2O (295K, $E_i = 1.81$ meV and 3.84 meV).
b) Explanations obtained from MD simulations. Top : static structure factor of D_2O separated in its self and distinct parts [114], bottom : time and Q dependence of distinct (red) and self (blue) coherent dynamic structure factors calculated from simulations for D_2O. [114].

$Q \geq 1.5\text{Å}^{-1}$, see Figure 1-10 (a). This is explained with the **cancellation of diffusion in self and distinct scattering** below $Q = 0.7\text{Å}^{-1}$, where the amplitudes and timescales of diffusion are similar but of opposite signs in both contributions, as illustrated in Figure 1-10 (b) for the static and dynamics structure factors. At higher Q, there is intrusion of diffusion with the increase of $S_{\text{coh,dist}}(Q)$ around the main peak at $Q \approx 2\text{Å}^{-1}$, Figure 1-10 (b). Hence, it is important to understand how the two dynamic contributions of the coherent dynamic structure factor $S_{\text{coh}}(Q,\omega)$ scale with respect to one another, in this Q range where the amplitude of distinct correlations varies a lot. It can only be accessed with Molecular Dynamics (MD) simulations. However, as illustrated with Figure 1-10 (b) the Q-dependent contributions $S_{\text{coh,dist}}(Q)$ and $S_{\text{coh,self}}(Q)$ to the static structure factor are already a decent proxy to spot eventual cancellation of diffusion.

2. D_2O is qualitatively different from THF, a model for simple liquids. Their mean

relaxation times $\langle\tau\rangle$ at Q_{max} are respectively very close to the Q-independent time τ_c for D_2O and largely influenced by the diffusion time τ_d for THF. Therefore, D_2O is particularly impacted by the Q-independent mode, that follows an Arrhenius law with twice the energy activation found for THF, underlying how the restructuring of the H-bond network influences the characteristics of the local mode and its amplitude in the relaxation of density fluctuations, compared to simple liquids relying on repulsive forces.

3. A clear De Gennes narrowing (scaling of $\tau_{d,coh}$ with $S(Q)/Q^2$) is present in THF but not in D_2O, which is again a hint towards the specificity of the intermolecular bonding of the H-bond network.

We retain here the presence of a local Q-independent mode in coherent scattering of D_2O that relaxes at the ps-scale, emphasized by the peculiarity of the H-bond network in this liquid, and which dominance is driven below the structure factor peak by to the cancellation of distinct and self contributions. The amplitude of this Q-independent mode is higher than for simple liquids.

CHAPTER 2

Materials and Methods

2.1 Presentation of neutron scattering instrumentation

What does a neutron experiment probe ?

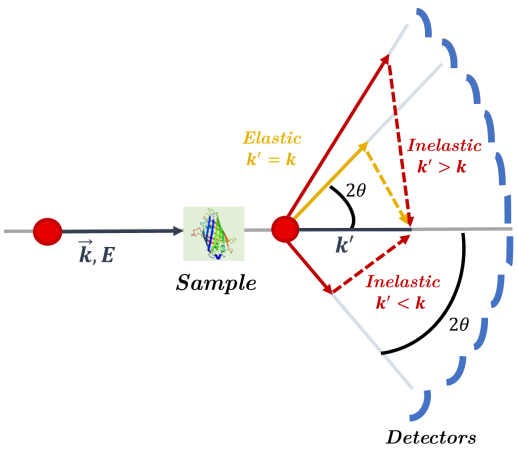

Figure 2-1: Schematics describing elastic and inelastic neutron scattering, resolved along θ.

During a neutron experiment, we measure the solid angle $\mathbf{\Omega}$ in which the neutron scatters, defined by spherical coordinates ϕ and θ, in order to retrieve the momentum transfer $\mathbf{Q} = \mathbf{k}^{'} - \mathbf{k}$. To study dynamics, the experimenter has to resolve the energy $E^{'}$ of scattered neutrons and relate it to their incoming energy E to get the energy

transfer $\hbar\omega = E^{'} - E$. Those two quantities are enough to obtain the double-differential cross section of the neutron's interaction with the sample, Equation 1-33. Figure 2-1 demonstrates this in two dimensions for elastic and inelastic scattering. Since we work with powders, scattering functions are only dependent on $Q = |\mathbf{Q}|$, the scalar norm of vector $\mathbf{Q}$.

Remark: The number N of scattered neutrons follows a Poisson law, such that $\delta N/N = 1/\sqrt{N}$. It means that to increase twice the quality of data, one has to measure experiments 4 times longer.

2.1.1 Neutron production

There are several pathways that can induce the production of neutrons. For a long time, nuclear fission in reactors was the main source of neutrons for research purposes (ILL was operational by 1971 and provided at that time the highest flux worldwide), however it has been replaced overtime by spallation sources due to their high-flux condition, such as the European Spallation Source currently under construction. Such sources produce neutrons for experiments that require a strong brilliance.

Nuclear reactors Fission in nuclear reactors is initiated from the collision of a thermal neutron and ^{235}U (contained in a highly compact 40×80 cm^2, 93% enriched fuel element at ILL). This collision yields an unstable $^{236}U^*$ that undergoes a fission process. It raises two product nuclei dependent on the fission pathway (one of the most probable events is displayed in Figure 2-3), an average of 2.5 neutrons per fission event, representing 192 MeV of energy. Product elements, with average 95 and 136 mass numbers, are unstable compounds that can undergo β and α decay, producing further neutrons. Neutrons released by fission can then interact again with ^{235}U in a cascade of fission events.

We typically refer to neutrons as "cold", "thermal" or "fast" considering the energy range they belong to, see Figure 2-2. Around 100 eV, the correspondence between the neutron's energy and the internal energies states of the nucleus raises resonant effects, implying an erratic behaviour of the absorbance cross sections. Fission events produce fast neutrons, thus to increase the total yield of neutrons, it is important that the neutrons belong to the thermal range of energy, in order to maximise the fission cross section over capture cross section ratio, as seen from Figure 2-2. This thermal neutron energy range can be reached by slowing down the neutron upon inelastic collision with an adapted component. D_2O heavy water is a good moderator considering both its high $\frac{\sigma_{scatt}}{\sigma_{abs}}$ ratio and its light

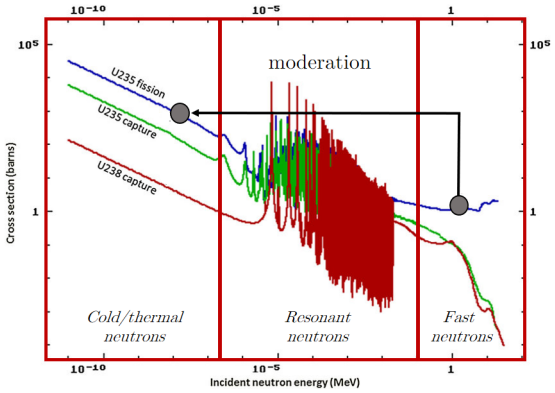

Figure 2-2: Description of thermal, resonant and fast neutron energy zones for the fission and capture cross sections of Uranium 235. Adapted from [115]

mass implying as small recoil energy for the neutron. D_2O serves as main moderator in the 2.5m diameter pool surrounding the nuclear core at ILL.

Furthermore, in order to keep a constant number of produced neutrons as a function of time and remain in the so-called "critical" regime, mobile control rods with a high capture cross section such as the Silver, Indium, Cadmium alloy at ILL reactor, are positioned around the core. Produced neutrons are collected at beam tubes and guided along neutron guides to the instruments. Their energy follow a Maxwell-Boltzmann distribution centred on thermal energies $\lambda \approx 2$Å. This is why cold and hot sources, made out of D_2 and graphite respectively, are positioned at the entry of beam tubes to modify the distribution of energy to produce either to cold neutrons (eg. quasielastic scattering) or fast neutrons (eg. high-energy vibrations), see Table 2-II.

Spallation sources In spallation sources, protons are confered a very high energy (hundreds of MeV) by acceleration in linacs or synchrotrons. They reach a target, which is a solid cylinder of tungstene in target station 2 -TS2- at ISIS. Upon collision, an intranuclear cascade occurs where a few high-energy particles are released in the direction of the initial proton. Protons with an energy of about 20 MeV will then initiate further collisions in the target material. The collision nucleus, after releasing those particles, reaches an excited state that relaxes in an isotropic evaporation of low energy ($\approx$ 1meV) particles, among which neutrons. Neutrons are emitted in white beam pulses centered on the thermal region (10Hz at ISIS TS2) in the shape of an asymetric peak as a function of time. Characteristics of both sources are compared in Table 2-I.

Figure 2-3: a) Fission reaction upon interaction of a neutron and a radioactive compound. b) Spallation induced on a target.

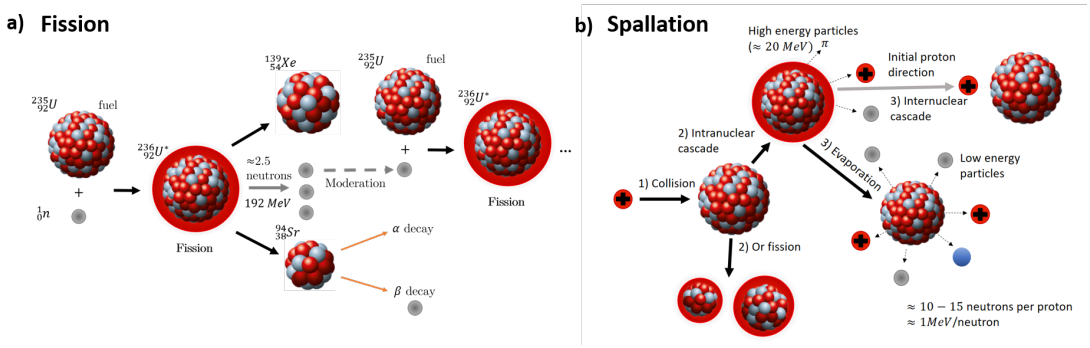

Table 2-I: Comparison of characteristics of a spallation source and a reactor source, to which ISIS and ILL facilities respectively belong.

Reactor	Spallation Source
1.5 free neutron/event	≈ 30 free neutrons/event
150 MeV/neutron	25 MeV/neutron: 10 times higher brightness/unit heat
Continuous source	Pulse source
Symetric resolution function	Asymetric resolution function
≈ 50 MW source (58 MeV at ILL)	≈ 5 MW source
ILL 1.5 10^{15}n/cm^2/s	ISIS 2 10^{16}n/cm^2/s [116]

2.1.2 Neutron optics

Neutrons enter the guides unpolarised and with a very low flux (Table 2-I), and optics teach us how to transport neutrons, select a wavelength, collimate the beam and detect where neutrons scatter. It is feasible because neutrons behave as waves and can be refracted or reflected at the interface of chosen materials and alloys. As for any optical system, the beam is defined by its wavelength range, energy and angular resolution, divergence, polarisation state... etc. In this section we want to specifically highlight that polarised neutrons require specific optical systems which are different from conventional systems.

Beam tubes and neutron guides In order to guide neutrons with a minimal loss of intensity, neutrons have to be transported in a similar way as optic cables for photons. It relies on neutron reflectivity. Incident neutrons can be represented as plane waves, $\phi(z) = \exp(ikz)$. Upon scattering on a nucleus of mean nuclear scattering length $\overline{b_n}$ (for simplicity, we consider a non magnetic material), the wave becomes spherical: $\phi'(z) = -\frac{\overline{b_n}}{r}\exp(ikr)$. The neutron refractive index can be shown to be independent of the structure of the

material (e.g. nickel) and equal to:

$$n = 1 - \frac{\rho\lambda^2}{2\pi}(\overline{b_n}), \tag{2-1}$$

ρ is the number of nuclei per unit volume and is of the order of $\rho = \frac{1}{\lambda^3}$ for thermal neutrons, yielding a value for n that scales very close to unity [46]. Mirrors or guides are characterised by the critical glancing angle

$$\theta_c = \lambda\sqrt{\frac{\rho}{\pi}(\overline{b_n})}, \tag{2-2}$$

defining the wavelengths that can be reflected, and reflectivity $R \in [0, 1]$ which defines the efficiency of the mirror. Properties are tuned by superposing layers or materials with a gradient of thickness.

Beam tubes are placed almost isotropically around the nuclear core to capture produced neutrons. They are made of aluminium to ensure mechanical resistance and are coated with nickel to enable reflection and transport. Guide tubes further transport neutrons to the instruments and are made of absorbing glass coated with nickel, and are tilted with alternative critical angles to increase security, flexibility and performance.

Monochromaters Whether instruments work in direct geometry (incoming selected beam, analysed multi-wavelengths beam) or indirect geometry (incoming multi-wavelengths beam, analysis of a unique wavelength), they require to produe or analyse a monochromated beam with optimised energy resolution.

We describe monochromaters of 2 categories: crystals and choppers. Each spectroscopy instrument favors a certain type of monochromater, such as crystals for backscattering spectrometers and triple-axis spectrometers (IN12), or choppers for time-of-flight spectrometers (IN5).

- A crystal is a solid with microscopic arrangements of atoms associated to a lattice parameter d. Crystal monochromaters rely on Bragg elastic scattering, following Equation 2-3:

  $$2d\sin(\theta) = n\lambda. \tag{2-3}$$

  Hence, chosing the angle of incidence θ along one plane of the crystal enables to get the required λ wavelength as an output, with orders $n \in \mathbb{N}$, see Figure 2-4 (a). The incoherent and absorption scattering lengths of the crystal shall be weak enough

to avoid background and loss of neutrons. Mosaïc crystals, which feature defects, improve intensity of the reflected beam as a trade-off with resolution, and curved assemblies of mosaïc crystals can be used to focus the beam on the sample instead of just tuning the wavelength.

- Chopper monochromaters are rotating disks of absorbing material with transparent slits, so that only neutrons that enter the slit are not absorbed, see Figure 2-4. A first chopper cuts the beam into pulses, while a phase-shifted second chopper with same pulsation selects the wavelength of the neutrons, which disperse from the first chopper to the second chopper according to their velocity. λ is therefore a function of the speed, phase and distance between the two choppers, with a resolution of $\approx 10\%$. Choppers are typically used in TOF experiments.

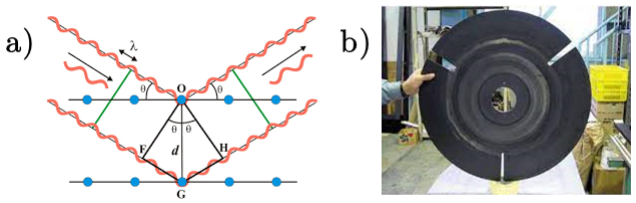

Figure 2-4: (a) Bragg-scattering on a perfect crystal (b) Disk-chopper.
Adapted from https://www.xtal.iqfr.csic.es/Cristalografia

Optics dedicated to polarization analysis We focus on uniaxial polarisation analysis, for which the spin is projected along one axis. As explained in subsection 1.3.4, Equation 1-28 and Equation 1-29, we need to polarize the beam ahead of the sample and analyze the spin projection after scattering to separate coherent from incoherent scattering, which requires adapted polarizers, detectors, and to chose a single spin projection with "flippers". This general picture of a polarized experiment, which is compatible with non-polarised instrument layouts, is presented on Figure 2-5.

Let us broadly introduce the three constitutive methods to polarise or analyse a neutron beam :

- Supermirrors are composed of a gradient of magnetic and non magnetic bilayers (eg: Fe/Si). They are characterised by an dimensionless ratio of glancing angles (Equation 2-2), $m = \theta_c/\theta_{nickel}$. When m increases, the range of wavelengths that reflects through the guide extends. This system polarises neutrons because its reflectivity is

spin-dependent : for a superposition of layers defined with nuclear scattering length $\overline{b}_1$ for the non-magnetic layer and nuclear and magnetic scattering lengths $\overline{b}_2$ and $\overline{p}$ for the magnetic layer, it can be shown that spin-up or spin-down reflectivity $R\pm$ is proportional to $\rho_1\overline{b}_1 - \rho_2(\overline{b}_2 \pm \overline{p})$. R can be maximised for one spin and cancelled for the other with the right choice of bilayer materials such that $\rho_1\overline{b}_1 = \rho_2(\overline{b}_2 \pm \overline{p})$ [117]. Therefore supermirrors transmit one spin and absorb the other, they are well adapted as upstream beam polarizers and polarizing guides (on LET, IN12 and D7 for the neutron's polarisation, and on D7 for the analysis of the neutron's spin).

- Spin filters transmit one neutron spin while absorbing the other. In $^3\mathrm{H}_e$ spin filters, gas $^3\mathrm{H}_e$ is optically pumped so that it is fully polarised ($\uparrow$). The absorption cross section gets close to a resonance and becomes highly spin-dependent. Hence, spin down of the neutron is fully absorbed while spin-up is transmitted. Filters are adapted for λ dependent analyzers (i.e. for TOF equiped with polarisation analysis, LET), although they have an exponential depolarisation time and require regular pumping.

- Polarizing crystals (eg: Heusler alloys, Cu_2MnAl) reflect only one neutron spin by cancelling the magnetic (M) and the nuclear (N) cross sections for Bragg-scattering, under a uniform magnetic field $\mathbf{B}$ of unitary direction $\mathbf{n}$. Writing $\mathbf{P}$ the polarisation of the neutron and $F_{N,M}$ the nuclear and magnetic structure factors, if $\mathbf{nP} = 1$ then $\frac{d\sigma}{d\mathbf{\Omega}} = (F_N(\mathbf{Q}) + F_M(\mathbf{Q}))^2$, otherwise if $\mathbf{nP} = -1$ then $\frac{d\sigma}{d\mathbf{\Omega}} = (F_N(\mathbf{Q}) - F_M(\mathbf{Q}))^2$. It yields that a crystal verifying $|F_N(\mathbf{Q})| = |F_M(\mathbf{Q})|$ is a perfect polarizer absorbing one spin and reflecting the other. Those polarizers are usually used on triple axis spectrometer where the final neutron energy is selected, contrary to TOF or diffractometers (a Heussler analyzer is used on IN12).

Remark : The beam undergoes fast depolarisation due to external fields: it requires a strong uniform magnetic field applied along the neutron guides.

Spin flippers The techniques described above are designed to polarize and analyse the beam along only one defined spin projection. It is not enough to investigate the 4 matrix elements presented inEquation 1-28, Equation 1-29 associated to all spin projections. It is therefore paramount to have a technique to flip the spin by 180°. In spin flippers, a rotational magnetic field $\mathbf{B}$ is applied with pulsation $\omega_\mathbf{B}$ on a short defined distance. If the Larmor frequency ω_L of the neutron caused by $\mathbf{B}$ is small compared to $\omega_\mathbf{B}$, $\omega_\mathbf{B} \gg \omega_L$,

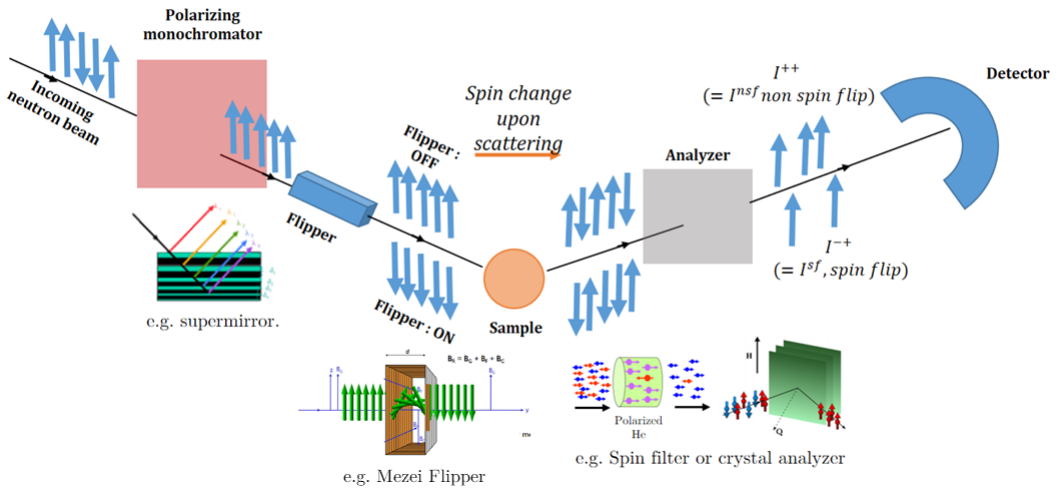

Figure 2-5: Schematics of the uniaxial polarisation analysis performed for neutron spectroscopy or diffraction. It consists in polarizing the beam ahead of the sample and analysing it downstream. Flipping the spin makes it possible to get the differential cross sections in the spin-flip and non spin-flip cases. Figures for optical systems are adapted from Refs. [118, 119].

it raises an adiabatic change of the spin to get a 180° rotation out of the flipper. More convenient because it does not require to modify the guide's magnetic field after the flipper, other flippers rely on sudden non-adiabatic magnetic field transition ($\omega_{\mathbf{B}} \ll \omega_L$). An example are Mezei flippers [120].

Detectors Eventually, neutron specific detectors count the number of neutrons per solid angle. For instance, highly absorbing particles such as ^3H_e or ^{10}B permit prompt detection by interaction with the incident neutron, expulsing ionized particles that are amplified and detected above a certain voltage threshold.

2.1.3 Determinant instrumental parameters in a neutron experiment

The range of phenomena probed during an experiment is intrinsically determined by the instrument's characteristics. We present here the three determinant quantities during a neutron spectroscopy experiment :

1. First and foremost, instruments are designed to function with a certain range of energy, see Table 2-II. Hence, neutrons are moderated at the source to arrive with an appropriate speed. The incoming energy E_i and the resolution $\hbar\omega_{res}$ (second bullet point) determine **the dynamical range** which is the range of energies avail-

able on the spectrum hence, the timescale probed. The largest incoming energy, the shortest relaxation times we observe.

Positive energy exchanges $\hbar\omega$ correspond to neutrons that have lost energy (e.g. slow neutrons) and this transfer is limited by the incoming energy E_i, while negative energy exchanges correspond to an energy gain for the neutron, and is theoretically limited by the internal energy of the nucleus ($E_{max} = k_B T$ for a set of harmonic oscillators). Detailed balance (Equation 1-37) favours energy gain over energy loss for the neutron.

Table 2-II: Approximate range of energies corresponding to cold, thermal and hot neutrons, and examples of phenomena or experiments that are favoured in this energy range.

Cold Neutrons	$E_i \leq 25$ meV	e.g. Elastic scattering, diffusional processes
Thermal Neutrons	$200meV \geq E_i \geq 25$ meV	e.g. Phonons, librations...
Hot Neutrons	$E_i \geq 200$ meV	e.g. Vibrations, deep inelastic scattering...

2. Another important quantity is **the energy resolution** $\hbar\omega_{res}$, which is experimentally determined from the spectrum of an incoherent crystal scatterer such as Vanadium. For biological sample, measuring the sample at very low temperature also provides a good resolution spectrum. In a TOF instrument, this resolution equals [121]

$$\hbar\omega_{res} = 2E_f \frac{\delta t}{t}, \tag{2-4}$$

where E_f is the neutron's final energy, t is the neutron's time-of-flight and $\delta t = \sum_i \delta t_i$ is a sum of uncertainties depending on the choppers' characteristics and relative distances, therefore energy resolution and incoming energy ($\equiv$ dynamical range) are not independent (Equation 2-12 relates the incoming energy to the chopper's characteristics). The energy resolution determines t_{res}, the maximum experimental observation time. Hence, $\hbar\omega_{res}$ determines which processes are too "slow" to be observed, which fall into the elastic peak for $\hbar\omega \leq \hbar\omega_{res}$:

$$t_{\text{res}} = \frac{2\pi\hbar}{\hbar\omega_{res}}. \tag{2-5}$$

$\hbar\omega_{res}$ is obtained from the resolution function $R_\sigma(\mathbf{Q}, \omega)$ of the instrument, which is

generally of Gaussian form on a TOF spectrometer.

$$R_\sigma(\mathbf{Q},\omega) = \frac{1}{\sigma\sqrt{2\pi}} \exp\left(-\frac{\hbar\omega^2}{2\sigma^2}\right), \tag{2-6}$$

$\hbar\omega_{res}$ is calculated as the Full-Width at Half-Maximum of the resolution :

$$\hbar\omega_{res} = 2\sqrt{2\ln(2)}\sigma. \tag{2-7}$$

We also name this quantity ΔE in the rest of the manuscript.

3. **The momentum transfer range** determines whether one probes large scale motions and structure (for instance, protein large-scale structure, domain motions...) at small Q values $\lessapprox 0.1$ Å^{-1}, or short scale motions (internal protein motions, translational diffusion of hydration water...) at larger Q values.
   The scalar momentum transfer writes [122]

$$Q^2 = (k_f - k_i)^2 = 2\left(\frac{2\pi}{\lambda_i}\right)^2 \left(1 - \frac{\hbar\omega}{2E_i} - \sqrt{1 - \frac{\hbar\omega}{E_i}}\cos(2\theta)\right), \tag{2-8}$$

   which is once again dependent on the incident energy. Figure 2-6 (a) shows how for an incident energy $E_i \approx 3.3$ meV, the energy transfer $\hbar\omega$ and Q are related in a TOF instrument in direct geometry.

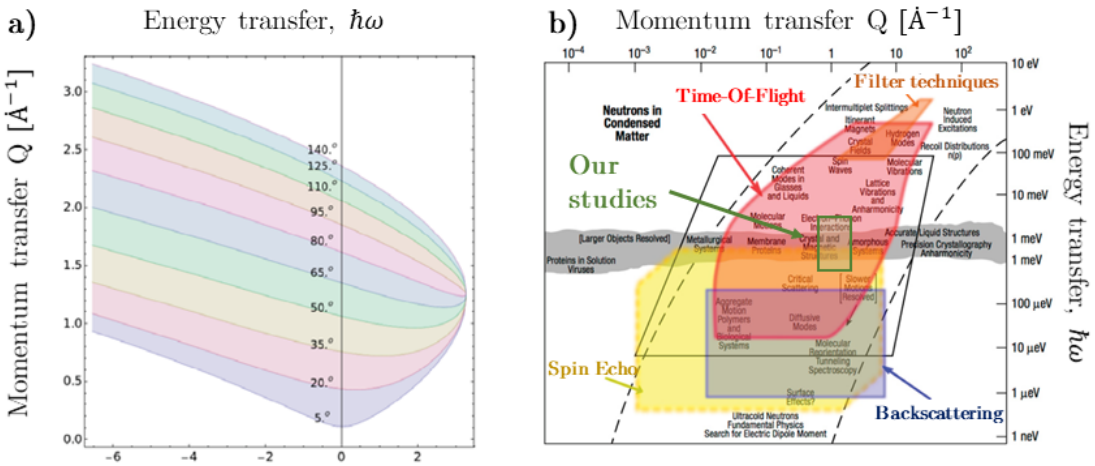

Figure 2-6: a) Kinematically allowed region for indirect geometry TOF instrument: energy transfer as a function of Q plotted for $E_i \approx 3.3$ meV (Equation 2-8), adapted from [121]. b) Energy and momentum transfer ranges associated to the 4 main categories of neutron scattering instruments and the phenomena they probe, our ranges used in the manuscript are framed in green, adapted from [121].

What will be a topic of discussion in chapter 3, is that the choice of the energy and momentum transfer ranges defines the relative significance of incoherent and coherent contributions. In proteins, very large Q ranges correspond to local dynamics with a majority of incoherent scattering, while coherent scattering can be preponderant at low Q where secondary, tertiary and inter-protein structures arise. Furthermore, in order to probe collective motions implying pairs of different nuclei, they have to relax in the right experimental time-window with an amplitude of displacements corresponding to the available Q range. Therefore, making the right choice of E and Q ranges is paramount when one considers performing polarisation analysis.

2.2 Experiments and data analysis

2.2.1 Principles of data reduction

Corrections for the instrument Instruments do not display perfect counting rates due to inherent variability in detectors' efficiency, the scattering from sample holders containing the sample, and general background that is not totally prevented with shielding. Sample holders are in aluminium for QENS studies due to their high transmission, low incoherent scattering and lack of spatial information except for a Bragg peak situated around $Q \approx 2.6$ Å^{-1}. The sample data is corrected for the empty sample holder counting rate N_{EC} and for the cadmium counting rate N_{Cd} which acts as a "black" sample which fully absorbs neutrons. The sample is normalised with the counting rate of a Vanadium sample, N_{Vana}, which is an incoherent and isotropic material with no inelastic contribution that corrects the energy and angular dependent efficiency and geometry of detectors.
We used Beer-Lambert law $T = \exp[-\sigma_s n_s t]$ to estimate the transmission of Vanadium (T_{Vana}) for a flat sample holder of thickness t in cm, $\sigma_s = \sigma_{\mathrm{abs}} + \sigma_{\mathrm{coh}} + \sigma_{\mathrm{inc}}$ the total macroscopic cross section in barn, and ns the number density in barn^{-1} cm^{-1}. We measured experimental transmission values for dGFP and pGFP (T_S) on D7. The number of neutrons N_s scattered is obtained from the measured counting rate N_m

$$N_s(Q,\omega) = \frac{(N_m(Q,\omega) - N_{\mathrm{Cd}}(Q,\omega) - T_S(N_{\mathrm{EC}}(Q,\omega) - N_{\mathrm{Cd}}(Q,\omega)))}{(N_{\mathrm{Vana}}(Q,\omega) - N_{\mathrm{Cd}}(Q,\omega) - T_{\mathrm{Vana}}(N_{\mathrm{EC}}(Q,\omega) - N_{\mathrm{Cd}}(Q,\omega)))}. \tag{2-9}$$

In case of polarisation analysis, the correction is applied to the coherent and incoherent parts of the scattering.

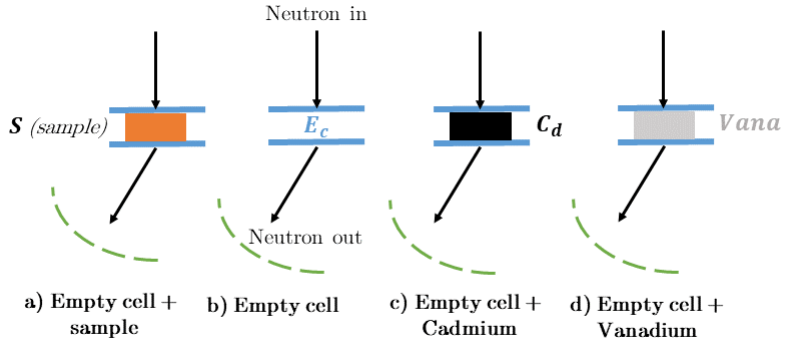

Figure 2-7: Sets of experiments required to study the sample (a) and correct for background (b and c) and detectors (d). Inspired from Practical Neutron Scattering Course, Oxford School on Neutron Scattering 2019, R. Stewart [123].

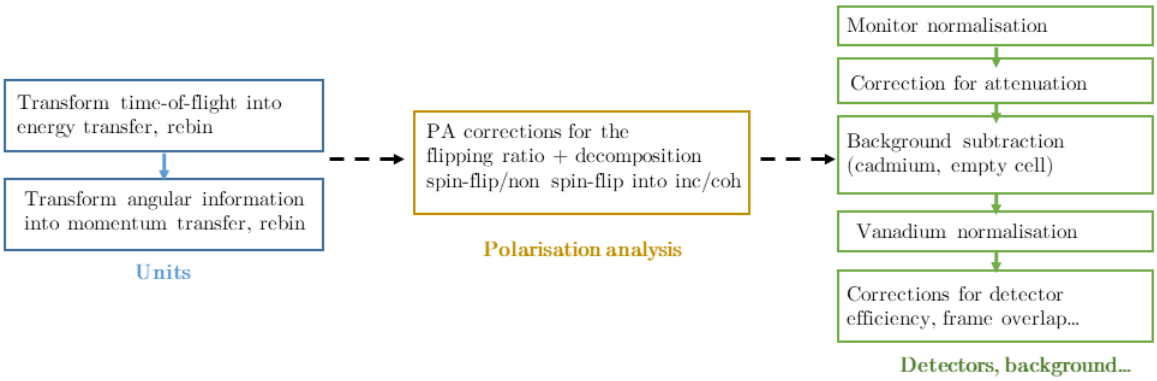

Figure 2-8: Workflow of data reduction (simplified) to correct for background and efficiency of the instrument and obtain scattering functions from double-differential cross sections.

Corrections for the sample: multiple scattering Multiple scattering occurs when a neutron scatters several times inside the sample before detection, which is an unwanted phenomenon that is not taken into account in the differential cross section, Equation 1-33. It occurs when the mean free path l of the neutron, calculated from the scattering and absorption cross sections of the sample per volum unit Σ_s and Σ_a, is short compared to the size of the sample [21]. Let us write:

$$l = \frac{1}{\Sigma_s + \Sigma_a} = \frac{mM}{\rho N_a \sum_i N_i(\sigma_{\text{inc},i} + \sigma_{\text{coh},i} + \sigma_{\text{abs},i})}. \tag{2-10}$$

Where m is the sample's mass, M its molar mass, ρ its density, σ the nuclear cross sections summed over the N_i nuclei of each type i and N_a Avogadro's number. For a flat sample-holder of thickness d, it is related to the measured transmission T of the sample: $l = -d/log(T)$. Choosing the right sample geometry and thickness d regarding the theoretical

mean free-path will decrease transmission while increasing multiple scattering: to the zeroth order, the probability of double diffusion is equal to $(1-T)^2$ [121]. Our measured transmission on D7 yield $T_{\mathrm{pGFP}} = 0.91$ and $T_{\mathrm{dGFP}} = 0.98$. It should be enough to ensure that less than 1% of neutrons undergo multiple scattering: we do not require to perform any correction.

However, we remain aware that multiple scattering has strong impact on polarisation analysis, where two consecutive spin flip events will end up being considered as non spin-flip. Thus, the main effect of multiple scattering is to increase artificially coherent scattering [124].

2.2.2 Presentation of instruments and experiments

IN5 and LET Time-Of-Flight

Description of the instruments LET and IN5 are direct geometry Time-Of-Flight instruments. TOF instruments are versatile instruments typically used for quasielastic and inelastic measurements, with incoming energies in the range $[1, 130]$ meV at ILL, and Q ranges $> 0.1\text{Å}^{-1}$. They bridge the gap in both energy and momentum transfer between very high resolution instruments (backscattering and spin-echo spectrometers) and lower energy resolution instruments (triple axis spectometers) [Figure 2-6 (b)]. The principle is to measure the time $t_{s\to d}$ taken by the neutron to travel from the sample to the detectors, and deduce the energy transfer $\hbar\omega = E_f - E_i$ from the knowledge of the travelling distance $l_{s\to d}$, such that the final neutron energy writes

$$E_f = m_n \frac{l_{s\to d}^2}{2t_{s\to d}^2}, \tag{2-11}$$

with m_n the neutron's mass.

On IN5, the continuous ILL beam requires to be pulsed into packets of ≈ 10 μ s with a first chopper, diminishing the continuuous flux in the same time by a factor of $\approx 10^2$ n/cm^2/s. Then, two choppers ahead of the sample rotating with the same speed act as a monochromater and select an incoming wavelength λ_i which is determined by their phase ϕ. In between them, a set of choppers are used to successively discard contaminating orders of higher harmonics (the aforementioned phase is defined modulo 2π) and avoid frame overlap such that very slow neutrons are not mistaken for the following neutron packet (the sample-detector distance is about 4 meters to improve resolution, however

it increases the spread of neutrons due to imperfect monochromatization). The incident wavelength is determined by the first chopper's frequency ν_c and the phase ϕ[122]

$$\lambda_i = \frac{h\phi}{m_n l_{s\to d} 2\pi\nu_c}. \tag{2-12}$$

IN5 instrument is presented in Figure 2-9 (a).

On the other hand, for LET the beam obtained from the spallation source is already pulsed. LET is is a multiplexer spectrometer, meaning that the multi-chopper system is designed to enable a few measurements at the same time, i.e. more than one incoming energy are available by using the whole 100ms time-frame. The chopper system is similar but also provides for pulse shaping and long-tail removal [125]. In both instruments, detection is operated with ^3H_e position sensitive detectors (PSD).

LET is also designed to perform uniaxial polarisation analysis (PA). Therefore, a few removable additional elements are added when performing PA: the beam is polarised upstream with a supermirror (m=5), guided and analysed downstream with ^3He spin filters ahead of the PSD. Flipping is performed with a current-ramped precession coil to correctly spin the neutron's flip for the different chopper-selected velocities .

Experiments

1. **LET, DOI: 10.5286/ISIS.E.RB2220225-1 [36]. 03/10/22 → 06/10/22**: We acquired the spin flip (sf) and non spin flip (nsf) intensities for dGFP, pGFP and the empty cell at $T = 310$K and $T = 2$K. We used annular cylinders sample holders of outer diameter 16mm, 1mm thickness and 40 mm height. Spectra were normalised to a Vanadium spectrum and corrected for the empty cell and Cadmium. We measured multiple incident energies at the same time: $E_i = 1.83$ meV, 3.27 meV and 7.44 meV. For our resolution of interest corresponding to $E_i = 3.27$ meV, we obtained a flux of approximately 4.5 10^4n/cm^2/s (that is about 35 % of the incoming unpolarised beam). We covered a Q range from about 0.6 Å^{-1} to 2.2 Å^{-1}.

2. **IN5, DOI: 10.5291/ILL-DATA.DIR-173 [20]. 04/10/19 → 07/10/23**: We carried out QENS measurements at $T = 2$ K, $T = 220$ K and $T = 310$ K for dGFP, pGFP and the empty cell (Vanadium was measured at $T = 180$ K). We used flat sample holders of thickness $t_{\mathrm{dGFP}} = 0.7$ mm and $t_{\mathrm{pGFP}} = 0.4$ mm. We corrected for the empty cell and normalised with Vanadium. We measured 3 incident

energies, $E_i \approx 36$ meV (unused because of a wrong set-up for Vanadium measurement), $E_i \approx 3.3$ meV and $E_i \approx 0.8$ meV with respective resolutions $\Delta E \approx 80$ μeV and $\Delta E \approx 13$ μeV, for a neutron flux of approximately 6.8 10^5n/cm^2/s. Each {temperature,resolution} configuration was measured for 30 minutes. Elastic scans were measured with $E_i \approx 3.3$meV during sample heating for $\approx$ 5min/temperature, raising 234 and 95 temperatures for dGFP and pGFP respectively (more measurements were performed in the region $T \approx 220K$ around the dynamical transition). We covered $Q \in [0.5, 2.3]$ Å^{-1} for the lowest resolution and $Q \in [0.27, 0.92]$ Å^{-1} for the highest resolution.

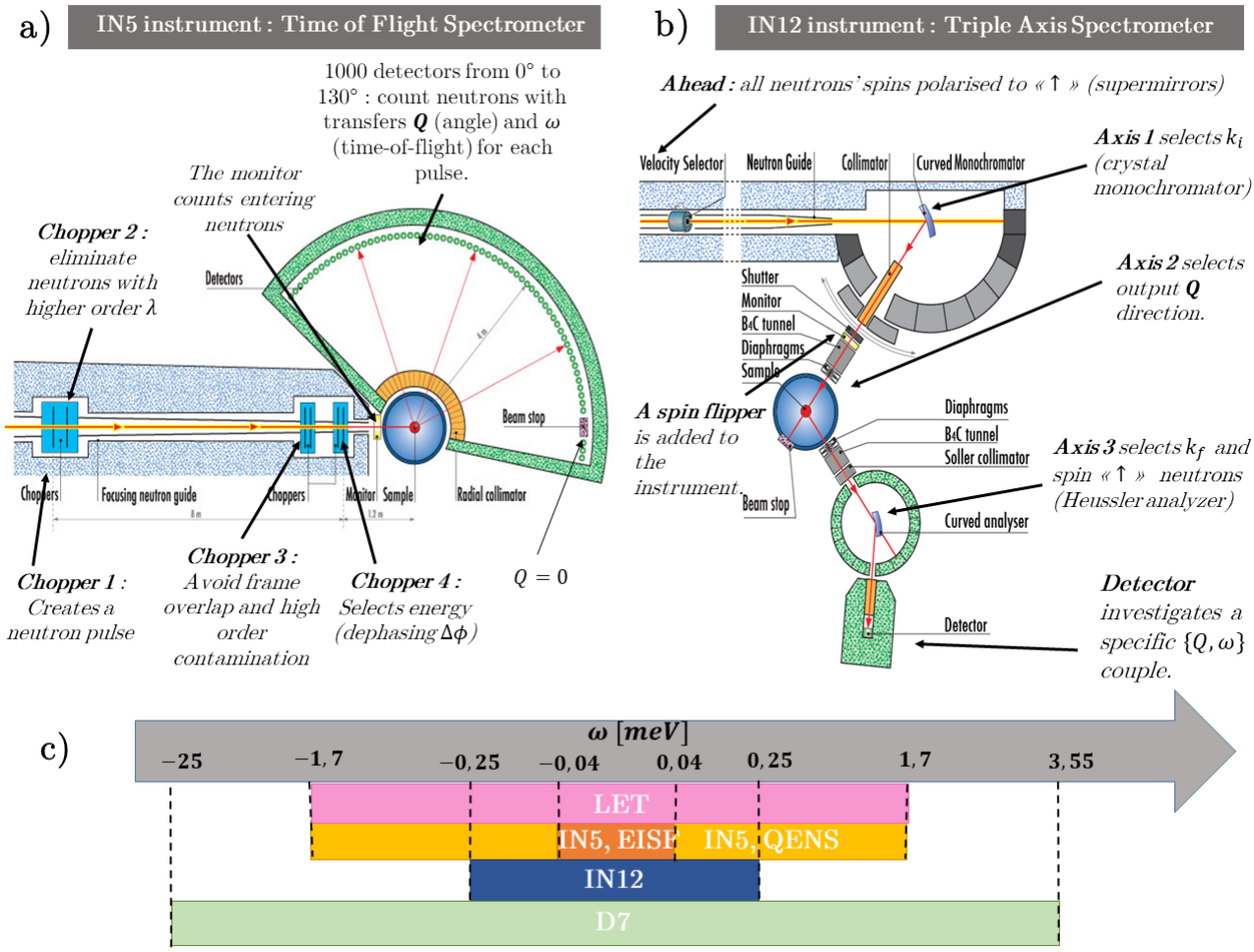

Figure 2-9: Detailed diagram for IN5 (a) and IN12 (b) instruments, adapted from https://www.ill.eu/users/instruments/instruments-list. Figure (c) proposes a visual representation of the dynamical ranges studied in the manuscript.

IN12 Triple-Axis Spectrometer

Description of the instrument Triple axis spectrometers are typically used for the observation of phonons and magnetic excitations. Measurements are performed for fixed transfers of energy E and momentum Q, owing to the two rotating axis with crystal monochromaters and analyzers. The main difference with TOF is that it is only measuring one energy and one momentum at a time, but it receives a high direct continuous flux from the source which is adapted to condensed matter studies and measurements of dispersion curves.

Here IN12 was equipped with an uniaxial polarisation analysis set-up and a vacuum box around the sample to reduce air scattering in the flight path of the neutrons in the vicinity of the sample and therefore drastically reduce the background at low Q [126]. The beam was polarised ahead of the monochromator with a polarizing cavity transmitting spin down neutrons (for $\lambda \in [2, 6]$ Å, spin up neutrons are reflected while spin downs are transmitted). A magnetic field applied to the guides and Helmholtz coils around the monochromator ensured that the neutrons do not depolarise until they reach the sample. The flipping of the beam is performed with a single high efficiency Mezei spin flipper [120] ahead of the sample, and then analysed with a vertically focusing Heusler(111) alloy.

Experiment. DOI: 10.5291/ILL-DATA.8-05-468 [34]. 11/06/21 → 15/06/21
We performed elastic neutron scattering centered on $E = 0$ meV with resolution $\Delta E = 500$ μeV. We have acquired the sf and nsf intensities of dGFP and pGFP with a 0.55mm thick flat sample holder, as well as the intensities of a 1.5mm thick Cadmium slab and a 1mm thick Vanadium slab. It was carried out at room temperature ($T \approx 300K$), with incoming energy $E_i = 9$ meV. The flux reached about 5 10^7 n/cm^2/s. Momentum transfer Q was probed from 0.05 Å^{-1} to 2.2 Å^{-1} (steps of 0.05Å^{-1}, 650ms acquisitions for each sf/nsf state). The overall efficiency is determined by the flipping ratio R=24 (Equation 2.2.4) obtained experimentally from a Quartz sample, corresponding to a 92% polarisation efficiency.

D7 Diffuse scattering spectrometer

Description of the instrument D7 is a neutron diffuse scattering spectrometer adapted to disordered materials [29], which was used in diffraction mode (no TOF analysis).
Contrary to spectrometers, diffractometers do not resolve energy and integrate over the

whole energy range $E \in [-k_BT, E_i]$, hence providing structural information as a function of momentum transfer Q. D7 data is analysed in the frame of the static approximation, Equation 3-7 [52].

The beam is polarised using a focusing bender-type suppermirror polarizer and the neutron spins are flipped with a Mezei-type flipper. The incoming energy is selected with a double-focusing monochromater. The scattered neutrons are analysed downstream by 66 bender-type supermirror analyzers, in front of 132 ^3He detectors.

Experiment. DOI: 10.5291/ILL-DATA.EASY-1064 [35]. 04/10/23 We calibrated the acquisition windows and the flipper magnetic field values. We acquired data for Quartz, Empty Cell, Cadmium and Vanadium, 30 minutes each and measured the transmission of each sample. Then we acquired 1h30 of neutron scattering intensity for each sample, dGFP and pGFP. Thicknesses of flat sample holders were $t = 0.55$mm for the GFP sample and $t = 1$mm for Vanadium and Cadmium. Data was normalised with Vanadium and corrected with the sample holder and Cadmium, the flipping ratio was measured with the Quartz sample.

Experiments were carried out at room temperature ($T \approx 300K$). For an incident energy of 3.55 meV, it yields a flux of around 2 10^6n/cm^2/s, for Q ranging between 0.1Å^{-1} and 2.5Å^{-1}. Sample preparation was common to IN12 experiment, Table 2-V.

2.2.3 Instruments characteristics

The characteristics of the instruments for which experiments have been performed is summed-up in Table 2-III. Q ranges used for static and dynamic studies are separated.

2.2.4 Data reduction and analysis: diffraction data

Separate incoherent and coherent scattering from spin-flip and non-spin flip data

In order to separate the incoherent and coherent intensities of the sample, $I_{coh}(\mathbf{Q})$ and $I_{inc}(\mathbf{Q})$, the spin-flip (sf) and non spin-flip (nsf) intensities of a polarised incoming beam have to be corrected for the polarizing efficiency of the instrument, which is carried out calculating the flipping ratio $R = \frac{I_{nsf}}{I_{sf}}$ of the instrument obtained from a coherent scatterer

Table 2-III: Energy and momentum-transfer characteristics of instruments used for diffraction and QENS experiments

	IN5 (ILL)	LET (ISIS)	D7 (ILL)	IN12 (ILL)
Date	10.19	10.22	06.21	10.21
Type of instrument	TOF Spectrometer	TOF Spectrometer	Diffractometer	Triple Axis Spectrometer
Polarisation analysis	No	Yes	Yes	Yes
Energy Range [meV], S(Q)	$E \in [-2.3, 2.2]$	$E \in [-2.2, 2.2]$	$E \in [-25, 3.55]$	$E \in [-0.5, 0.5]$
Energy Range [meV], QENS	$E \in [-1.7, 1.7]$	$E \in [-1.7, 1.7]$		
Resolution [μeV]	$\Delta E \approx 70$	$\Delta E \approx 95$		$\Delta E \approx 500$
Q range [Å^{-1}]	$Q \in [0.6, 2]$	$Q \in [0.6, 2.2]$ (QENS: $[0.8, 2]$)	$Q \in [0.1, 2.2]$	$Q \in [0.05, 2.2]$

(eg., Quartz).

$$\begin{aligned} I_{\text{coh}}(\mathbf{Q},\omega) =& \frac{RI^{\text{nsf}}(\mathbf{Q},\omega) - I^{\text{sf}}(\mathbf{Q},\omega)}{R-1} \\ &- \frac{1}{2}\frac{RI^{\text{sf}}(\mathbf{Q},\omega) - I^{\text{nsf}}(\mathbf{Q},\omega)}{R-1} \end{aligned} \tag{2-13}$$

$$I_{\text{inc}}(\mathbf{Q},\omega) = \frac{3}{2}\frac{RI^{\text{sf}}(\mathbf{Q},\omega) - I^{\text{nsf}}(\mathbf{Q},\omega)}{R-1}.$$

LET is a special case where R is a function of time. As explained in Ref. [32], the flipping ratio $R(t, \gamma, E_i, E_f) = \frac{I_{nsf}}{I_{sf}}$ holds the information of the polarizing efficiency and is a function of time t, the out-of-plane scattering angle γ, and the incident and final energies E_i and E_f, because of the time dependence of ^3He polarisation in the filters used ahead of the detectors (they require to be changed during experiments). After correction for the flipping ratio obtained from a coherent scatterer, the dynamical structure factor was also corrected for the transmission through ^{3}He filters.

Calculate the coherent static structure factor

Gabrys et al show that the incoherent Q-integrated intensity of polymers ($\sigma_{\text{inc}} = \int_0^{\pi} d\theta \left(\frac{d\sigma}{d\Omega}\right)_{\text{inc}} 2\pi \sin(\theta)$), which is always stated to be flat, is indeed decreasing with Q due to anisotropy. Furthermore they attribute it to inelasticity, comparing the decrease in Q for PMMA with different flexibilities. This drop in Q cannot be sim-

ply corrected with a Debye Waller factor [127]. This echoes Maconnachie's work, who demonstrates with polystyrene and polybutadene that the effective hydrogen cross section is dependent on the sample's dynamics, the incoming wavelength, and increases with temperature. The measured values are way above the expected ≈ 80 barns bound cross section of the hydrogen nucleus [128]. Therefore, we need to be careful and correct for this anisotropy.

The static structure factor $S(Q)$ is defined as the first moment of the scattering function $S(Q,\omega)$

$$\boxed{S(Q) = F(Q,0) = \int_{-\infty}^{\infty} d\omega S(Q,\omega) \approx \int_{\omega_{\min}}^{\omega_{\max}} d\omega S(Q,\omega)}. \tag{2-14}$$

with $[\omega_{\min}, \omega_{\max}]$ the experimentally accessible dynamical range. We shall use the following notations: $S_{\text{tot}}(Q)$ is the total structure factor as obtained with non-polarised experiments such that $S_{\text{tot}}(Q) = S_{\text{inc}}(Q) + S_{\text{coh}}(Q)$ expressed with the incoherent and coherent structure factors obtained from polarised intensities, with normalisation condition

$$\lim_{Q\to\infty} S_{\text{tot}}(Q) = 1. \tag{2-15}$$

Gabrys et al have proposed a method to correct for inelasticity effects, [129, 127]. Therefore, we introduce a differential cross section in barns normalised by instrumental effects and the Debye-Waller factor to retrieve a constant incoherent structure factor.

$$\frac{I_{\text{coh}}(Q)}{I_{\text{inc}}(Q)} = \frac{4\pi}{\sigma_{\text{inc}}} \left(\frac{\partial\sigma}{\partial\Omega}\right)_{\text{coh,barn}}. \tag{2-16}$$

It yields

$$\begin{aligned} S_{\text{tot}}(Q) &= \frac{\sigma_{\text{inc}}}{\sigma_{\text{tot}}} + \frac{4\pi}{\sigma_{\text{tot}}} \left(\frac{\partial\sigma}{\partial\Omega}\right)_{\text{coh,barn}} \\ &= \underbrace{\frac{\sigma_{\text{inc}}}{\sigma_{\text{tot}}}}_{S_{\text{inc}}(Q)} + \underbrace{\frac{\sigma_{\text{inc}}}{\sigma_{tot}} \frac{I_{\text{coh}}(Q)}{I_{\text{inc}}(Q)}}_{S_{\text{coh}}(Q)}. \end{aligned} \tag{2-17}$$

Where the cross sections σ were introduced in the first chapter, Equation 1-26, and is further expressed in Equation 3-1. This approach, consistent with further polarisation analysis diffraction studies on protein powders and solutions [33] yields the ratio of co-

herent over total scattering (Equation 2-16 and Equation 2-17) :

$$\boxed{\frac{S_{\text{coh}}(Q)}{S_{\text{tot}}(Q)} = \frac{I_{\text{coh}}(Q)}{I_{\text{tot}}(Q)}}. \tag{2-18}$$

that does not rely on prior estimation of the macroscopic cross sections. Also, following from Equation 2-17, we have :

$$\boxed{S_{\text{coh}}(Q) \propto \frac{I_{\text{coh}}(Q)}{I_{\text{inc}}(Q)}}. \tag{2-19}$$

Comments on data reduction and analysis

IN12 For IN12 data, background was subtracted with both Cadmium and the empty cell following Equation 2-9. However, we could not normalize it to Vanadium because of strong anistropy that seems to occur from the sample holder's flat geometry [occurence of a peak at $Q \approx 0.8$ Å^{-1}, Figure 2-10 (b)] when the beam gets close to 90° with respect to the sample holder. Further test measurements were performed [Figure 2-10 (a)], showing that the peak gets shifted with experiments due the strong sensitivity of the triple axis on the position of the sample holder. However, trying a correction by shifting the Vanadium spectrum to match the peak visible on Figure 2-10 (b) in pGFP increases normalisation artefacts. Therefore, a flat sample holder was not an adapted geometry to ensure good normalisation, but was required to avoid the loss of sample that would occur with cylindrical geometry.

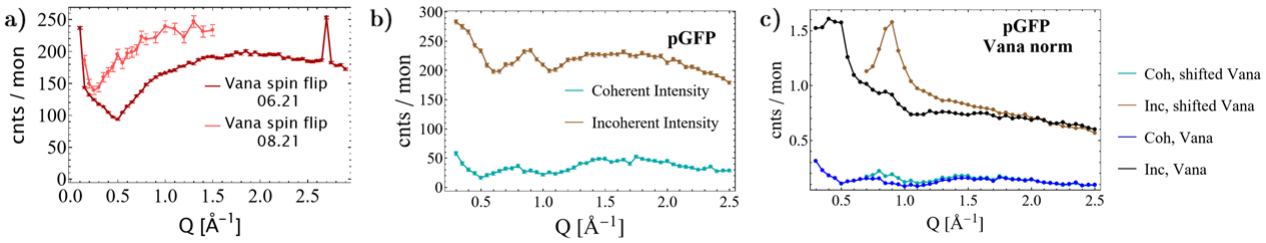

Figure 2-10: IN12, $\Delta E = 500$ meV, $E \approx 0$ meV. a) Vanadium acquisitions performed on IN12, during the experiment (dark red) and during the control (red). b) Non-normalised pGFP incoherent and coherent spectra. c) pGFP spectrum normalised to Vanadium or to shifted Vanadium.

LET LET data is normalised to Vanadium, corrected for the flipping ratio dependent on Helium depolarisation. For this, a Quartz sample was acquired, and corrections followed the workflow presented in [130].

D7 D7 data was normalised to Vanadium, corrected for the flipping ratio with acquisition of a Quartz sample and subtracted for background by the linear combination presented in Equation 2-9 using LAMP software. We cut the Q range around 2.2Å^{-1} because of a strong artificial decrease in intensity which is due to the neutron path that becomes parallel to the sample at high angles.

Remark:
All data sets are still in very good agreement with each others, highlighting that correction issues have minor effects on results.

2.2.5 Data reduction and analysis: quasielastic scattering data

Procedure for QENS analysis

The analysis was performed with Mathematica software [131]. The model was introduced earlier in subsection 1.4.2. Ref. [75] contains also a link to the corresponding deposited codes written by Kneller et al on zenodo platform, 10.5281/zenodo.7058345. We ensure that the quantum intermediate scattering function $F(\mathbf{Q},t)$, which fulfils the detailed balance, is adapted to our classical model for which the intermediate scattering function requires to be real and symmetric, subsection 1.3.5.
The dynamical structure factor is mirrored using the neutron gain side of the spectrum and symmetrised following Schoffield's prescription [46], such that after Fourier Transform, the intermediate scattering function $F(\mathbf{Q},t)$ has the form :

$$F^{+}(\mathbf{Q},t) = F(\mathbf{Q},t+\frac{1}{2}i\hbar\beta) \approx F(\mathbf{Q},t)^{cl}, \tag{2-20}$$

where $F^{+}(\mathbf{Q},t)$ is the fitted function. This has been described in Kneller's articles [40, 39, 41]. Experimentally, the dynamical structure factor $S_{\text{exp}}(\mathbf{Q},\omega)$ results of the convolution of $S(\mathbf{Q},\omega)$ and the resolution function $R(\mathbf{Q},\omega)$ of the instrument. Therefore, the convolution theorem implies that

$$F^{+}_{exp}(\mathbf{Q},t) = F^{+}(\mathbf{Q},t)\tilde{R}^{+}(\mathbf{Q},t), \tag{2-21}$$

with $\tilde{R}^{+}(\mathbf{Q},t)$ the symmetrized and Fourier-Transformed (denoted by $\tilde{}$) resolution function, obtained usually with a Vanadium or low temperature sample spectrum. It implies that the resolution function can be simply divided from the experimental function to yield

$F^+(\mathbf{Q},t)$.

$F^+(\mathbf{Q},t)$ is normalised by $F^+(\mathbf{Q},0)$

$$\frac{F^+(\mathbf{Q},t)}{F^+(\mathbf{Q},0)} = \frac{F^+(\mathbf{Q},\infty)}{F^+(\mathbf{Q},0)} + \left(1 - \frac{F^+(\mathbf{Q},\infty)}{F^+(\mathbf{Q},0)}\right)\phi(\mathbf{Q},t), \tag{2-22}$$

where $F^+(\mathbf{Q},\infty) = \lim_{t\to\infty} F^+(\mathbf{Q},t) = ESF(\mathbf{Q})$, and $\phi(\mathbf{Q},t)$ is the Mittag-Leffler function.

Handling of IN5 data IN5 data was reduced on LAMP software, [132]. The different choices made for analysis are summed-up in Table 2-IV and explained shortly, details are in the appendix. They concern good practice when working in the time domain.

Table 2-IV: Sum-up of choices made for reduction and analysis for IN5 data

	Reduction: Normalisation	Deconvolution	Q range	Choices for energy range
Elastic data	Low temperature spectrum	/	$Q \in [0.3, 2.1]\text{Å}^{-1}$	$E \in [-0.4, 0.4]$ meV
QENS data	Vanadium spectrum	Full low temperature spectrum	$Q \in [0.6, 2]\text{Å}^{-1}$	$E \in [-1.7, 0]$ meV, mirrored

- Normalisation of data in the reduction phase was performed with the low temperature spectrum for elastic data, which is used to correct for both detectors and the structure factor at low temperature (section 6.2). However, we normalised data to Vanadium for QENS in order to recover the correct structure factor, see comparison in Figure A-2.

- Deconvoluting with a Vanadium spectrum instead of a low temperature spectrum raises non-monotonous intermediate scattering functions denoting a wrong deconvolution process, Figure A-3 (c) and (d), and the two convolution processes yield strongly dissimilar parameters for pGFP (which exhibits narrower broadening with respect to dGFP), Figure A-3 (a) and (b). It is suggested in Ref.[133] that sample geometry and self-shielding characteristics are important for resolution deconvolution in time space, encouraging the use of a low-temperature sample instead of a vanadium spectrum. One can see that Vanadium, $\text{dGFP}_{2\text{K}}$ and $\text{pGFP}_{2\text{K}}$ bear very different behaviours as a function of Q and ω. Hence, the sensitivity to the choice made for deconvolution, see Figure A-3 (e).

- We decided to cut the spectrum to lower energies than the accessible range (1.7 meV instead of 2.5 meV). This is due to the presence of collective vibrations ascribed to the Boson peak, that are ubiquitous in glassy materials [97]. They arise around $E = 1.7$ meV at T=150K as observed on PANTHER hybrid TOF instrument, $E_i = 19$ meV [Figure A-4 (c)]. Although they seem to vanish at $T = 310K$, the impact is still non-negligeable, as probed with both the intermediate function [Figure A-4 (d)] and resulting parameters [Figure A-4 (a) and (b)] that become increasingly noisy and apparently slowed down when $E > 1.7$ meV. Below this threshold, cutting the range has no impact on fitted parameters. Let us notice that in literature (GFP, h=0.4), vibrations of pGFP/D_2O [134, 135] also appear more intense than for dGFP/D_2O [25].

- The time-dependent data is analysed for $t \leq t_{\text{res}}$, where t_{res} is the maximal time of observation defined by the instrument's resolution (Equation 2-5).

- We used the mirrored neutron energy-gain side of the spectrum rather than its energy-loss side for the study: the latter remains subject to the TOF-energy transformation where t^{-4} arises as a proportional factor between the double differential scattering function and $S(Q, \omega)$ [121], despite corrections.

- We emphasize that using the whole resolution function for deconvolution is paramount. On IN5, the resolution function is highly non-symmetrical (which is not an effect of the detailed balance factor, Equation 1-37) and cannot be fitted with conventional Gaussian or Voigt functions.

  We checked our assumptions by deconvoluting with three different functions :

  1. A Gaussian fit of the resolution.
  2. The central peak of the raw resolution function where wings defined by $E \notin [-2.58\sigma, 2.58\sigma]$ are padded to zero (where σ is the standard deviation of the Gaussian fit, such that 99% is contained in the interval).
  3. The whole resolution function.

  Corresponding figures for $T = 310K$ are available in the appendix, Figure A-5, and prove that a Gaussian fit of the resolution function is not adapted as a deconvolution function in time. The cropped resolution function raises similar results as the full resolution function, but the information held in the wings remains important in the

case of pGFP to correctly estimate parameters, since it does not broaden as much as dGFP.

Handling of LET data LET QENS analysis was performed similarly to IN5 data: Vanadium reduction, empty cell and vanadium corrections are the same. Choices for binning, dynamical range and deconvolution were also performed similarly, more information is available in Table 5-II.

The only difference lies in the choice of cutting the deconvoluted $F(Q,t)$ function at $t_{\max} = 0.7\ t_{\text{res}}$ instead of t_{res} (Equation 2-5). This choice was performed because of the high uncertainties and oscillations of the deconvoluted function for coherent scattering above that limit. This choice is justified by comparing the parameters obtained for $t_{\max} = t_{\text{res}}$ and $t_{\max} = 0.7\ t_{\text{res}}$ for total scattering, see appendix, Figure A-6. Parameters remain similar within error bars except for $Q = 0.8$ Å^{-1}. Furthermore, upon comparison to IN5 parameters, using $t_{\max} = 0.7\ t_{\text{res}}$ on LET raises better agreement for both instruments, see Table A-II.

2.3 Description of the sample

2.3.1 The Green Fluorescent Protein (GFP)

The GFP protein was purified from bioluminescent jellyfish Aequorea Victoria and studied extensively from 1962 on [136], leading to the Nobel Price of Chemistry in 2008 for Roger Y. Tsien, Osamu Shimomura, and Martin Chalfie due to its large pannel of applications in bio-imaging. GFP is used as a fluorescent tag in a wide range of applications, and was obviously one of the pillars of modern bio-physics. It can be fused to another protein's gene and expressed from the protein's terminal or with a peptide linker to follow the presence or dynamics of the protein of interest. It can be used as a gene expression reporter when added in a DNA sequence, and then be controlled by the promoter of interest. It can be employed for FRET studies or even used for photobleaching to follow diffusion of a protein in cells or interaction between proteins.

The advantages of GFP as a fluorescent tag for proteins are several: it does not alter the protein structure or the diffusion behaviour inside the cell thanks to a flexible hinge between the two proteins [137], it is not phototoxic and it is resistant to heat, pH, high pressure, photobleaching [138]... The Green fluorescent protein has a peculiar secondary structure, composed of 11-strand β barrel surrounding an inner chromophore held by α helices. The chromophore absorbs in ultra-violet at 398nm, and excites around 508 nm, hence its name, and displays a high quantum yield (number of emitted photons per absorbed neutrons) of 0.8. It has a cylindrical structure with a 24Å diameter and a 42Å height. It is therefore a particularly rigid compound, also due to the role of the barrel matrix to sustain the spectral characteristics of the chromophore by a large H-bond network of side chains and internal water molecules around the chromophore [138], to sustain planarity and to avoid quenching.

The chromophore 65Ser-Tyr-Gly67 is formed by autocatalytic post-translational cyclization (which is a rare event in protein formation) in the presence of oxygen, extending the maturating time of the protein to about 90 minutes [138]. The stability of its H-bond network also drives its stability characteristics: it is reversible upon denaturation with full recovery of its spectral properties.

Ever since, a large amount of mutants have been engineered in order to enhance or modify the natural emission wavelength of the protein, as well as reducing maturation time and providing an optimal folding at physiological temperatures. It results in a large family of

mutants, with currently 567 structures on the Protein Data Bank obtained from X-rays, electron-microscopy or neutron diffraction.

2.3.2 Sample production and preparation

Experiments were performed on a powder sample of Green-Fluorescent Protein and a powder sample of its per-deuterated counterpart, both hydrated in D_2O with hydration level close to $h = 0.4 g D_2O/g GFP$ which corresponds to about one layer of hydration water. About 100mg of protein powder were produced for both samples. The protein atomic formula is $H_{1505}D_{414}C_{1261}N_{342}O_{379}S_8$, considering a full $H \rightarrow D$ exchange of labile atoms of the protein estimated to 414 D atoms when hydrated in D_2O (see section Table 2.3.4).

GFP production Deuterated GFP (dGFP) was produced at the D-Lab of the Institut Laue Langevin (ILL) by Martine Moulin. It was over-expressed in *E.coli* strain BL21 (DE3) adapted to growth in deuterated minimal medium [139]. A 1.6 L (final volume) deuterated high cell-density fed-batch fermenter culture was carried out at $30°C$. Feeding with glycerol was started at an OD600 value of about 3.8. Expression of dGFP was induced at an OD600 of about 11 by addition of IPTG (1mM final concentration). Cells were harvested at an OD600 of 14 yielding 40g wet weight of perdeuterated cell paste.
Protonated GFP (pGFP) was produced at INSA Lyon by Pilippe Oger from the same GFP sequence. Hydrogenated GFP was over-expressed *E.coli* strain BL21 (DE3) pLys. A 10L (final volume) of LB medium fermenter culture was carried out at 37°C until it reached OD600 0.4. Expression of h-GFP was induced by addition of IPTG (1mM final concentration) for 16h at 37°C. Cells were harvested by centrifugation at 14000g for 20mn yielding 20g of cell paste.
Purification was carried-out identically for both deuterated and protonated proteins. GFP was purified essentially as described in Bernaudat and Bülow [140]. In brief, 30 g of cell paste were resuspended in 200 ml of Lysis buffer (20 mM Na phosphate pH7.2, 500 mM Nacl), and sonicated 8 times 25 s 50% power with a pause of 25 s in between. The sonicated mixture was centrifuged at 45000g for 30 min at 4°C. The supernatant containing the soluble GFP was transfered to a clean tube and heated 15 minutes at 70°C to remove *E.coli* proteins. Denatured proteins were removed by centrifugation at 45000 g for 30 minutes. The cleared supernatant was further purified with a Ni-NTA resin pre-equilibrated in lysis buffer. The resin was combined with the supernatant and incubated 1 hour at 4°C under gentle agitation prior to loading on an empty chromatography column.

The resin was washed with 25 volumes of wash buffer (lysis buffer+ 12m M imidazole). The protein was eluted with 10 column volume elution buffer (Lysis buffer + 250 mM imidazole). The protein was further purified by Size Exclusion Chromatography on an AKTA® FPLC system, using an XK50-60 column packed with 1 L of Superdex® 75 Prep-Grade resin, calibrated with the GE Healthcare® Low Molecular Weight kit. Fractions containing the protein were then pooled, concentrated by ultrafiltration (Amicon® Ultra-30 centrifugal filter units, Millipore, Burlington, MA, USA) and lyophilised. The purity of the proteins was assessed by SDS-PAGE, and was greater than 99%.

GFP preparation Neutron scattering is sensitive to isotope exchange which is used to highlight specific parts of the sample, for instance to enhance the protein self-dynamics compared to the surrounding water. This is known as H/D contrast matching [139]. Sample preparation was carried-out following the usual protocol performed in the group [141]. Hydration was carried-out with D_2O adsorption of the lyophilised powder in a D_2O saturated desiccator until total weight of the protein/water system was reached. We estimate the amount of fast exchanged labile atoms equal to 268, and fast + slow amide protons equal to 414 [142], see Table 2-V. The hydrated powder was sealed with Indium in a flat 0.5 mm thick aluminium flat sample holder (D7, IN12) or wrapped in an aluminium foil in an annular cylinder sample holder of 4 cm long, 1mm diameter (LET). It implies a few seconds of exposure to the air during weighing before sealing the sample holder, never exceeding 30 s (the longest time was for LET experiment, the powder was deposited on an aluminium foil wrapped in the cylinder, see Figure 2-11). No dehydration of the sample was noticed during experiments (less than 3% of hydration was lost between the weight of the sample and the end of experiments on LET).

IN5 experiment was performed right after the sample production. For D7 and IN12 experiments, the protein was lyophilised and hydrated again in the D_2O saturated dessicator.

Table 2-V: Sample preparation of dGFP and pGFP hydrated samples in D_2O for D7/IN12 and LET experiments..

	IN5		D7/IN12		LET	
Sample	dGFP	pGFP	dGFP	pGFP	dGFP	pGFP
Mass dry protein ±0.2 mg	108 mg	103 mg	95.6 mg	126 mg	84.7 mg	132.8 mg
% initial hydration	$46 \pm 4\%$	$29 \pm 3\%$	$43 \pm 4\%$	$37 \pm 4\%$	47 ± 4 %	$27 \pm 3\%$
% final hydration	$46 \pm 5\%$	$24 \pm 3\%$	/	/	$45 \pm 5\%$	$25 \pm 3\%$
Exposure time to the air	< 15 s		< 15 s		< 45 s	

Figure 2-11: Sample preparation for LET, hydrated powder deposited on an aluminium foil wrapped around the inner cylinder of an aluminium hollow cylinder sample holder.

For LET experiments, upon suspicions of exchange, the sample was checked for aggregation with gel electrophoresis and deuteration of non-labile atoms with mass-spectrometry, see subsection 2.3.5 and then solubilised three times against D_2O, lyophilised and hydrated in the dessicator.

2.3.3 Comparison with 6l26.pdb, a GFP mutant used for calculation purposes

In section 3.3, we perform calculations of the static-structure factor $S(Q)$ from an existing structure of a GFP protein. Among the available structures on the Protein Data Bank (PDB), the X-ray structure 1GFL.pdb is the closest in term of amino acid sequence. However, since we study the effect of hydrogen-deuterium isotopic exchange on the structure factor of the hydrated protein, an X-ray structure deprived of explicit hydrogen atoms does not guarantee at all that we reach a reasonable Q-dependence of $S(Q)$.
This is why we used 6l26.pdb (2020, [143, 144]), the only GFP structure resolved with neutron-scattering available on the PDB, obtained from a mutant enhanced green-fluorescent protein. Its atomic formula is $D_{1765}C_{1151}O_{306}N_{348}S_6$; It differs by 8 amino-acids from the wild-type protein as displayed in Figure 2-12. The histidine tag MEFYHHHHHH in the wild-type protein was used to enhance production of deuterated GFP and might not have been cleaved, hence its presence in the sequence.
Neutron diffraction data were collected by Shibazaki et al at T= 100 K on BioDiff diffractometer (Garching) with a 1.45 Å resolution, enough to discrimate hydrogens in water molecules. The protein is a protonated protein crystallised in presence of D_2O. 377 heavy water molecules are present in the PDB file.

This structure holds several advantages :

Red : hydrophobic aliphatic
Orange : hydrophobic aromatic
Blue : Polar neutral
Dark Green : Basic

```
                                10        20        30        40        50        60
Wild-type GFP  →MEFYHHHHHH MSKGEELFTG VVPILVELDG DVNGHKFSVS GEGEGDATYG KLTLKFICTT
Enhanced GFP, 6l26.pdb →      M   GEELFTG VVPILVELDG DVNGHKFSVS GEGEGDATYG KLTLKFISTT
                               70        80        90       100       110       120
Wild-type  → GKLPVPWPTL VTTFSYGVQC FSRYPDHMKR HDFFKSAMPE GYVQERTISF  KDDGNYKTRA
6l26.pdb   → GKLPVPWPTL VTTLTYGVQC FSRYPDHMKR HDFFKSAMPE GYVQERTIFF KDDGNYKTRA
                     130       140       150       160       170       180
Wild-type  → EVKFEGDTLV NRIELKGIDF KEDGNILGHK LEYNYNSHNV YITADKQKNG  IKANFKIRHN
6l26.pdb   → EVKFEGDTLV NRIELKGIDF KEDGNILGHK LEYNYNSHNV YIMADKQKQG IKVNFKTRHN
                     190       200       210       220       230       240
Wild-type  → IEDGSVQLAD HYQQNTPIGD GPVLLPDNHY LSTQSALSKD PNEKRDHMVL LEFVTAAGIT
6l26.pdb   → IEDGSVQLAD HYQQNTPIGD GPVLLPDNHY LSTQSALSKD PNEKRDHMVL LEFVTAAGIT (H)
```

Figure 2-12: Amino-acid sequence for the produced wild-type GFP, compared to the structure of a enhanced green fluorescent protein available in 6l26.pdb. Mutations are coloured according to the type of amino-acid involved.

1. The presence of D nuclei in the structure yields direct information on the position and proportion of labile atoms in the protein, see subsection 2.3.4. This is precious information for a good derivation of the diffraction profile of the protein.

2. Explicit hydrogens in the PDB file avoids to resort to simulations to elucidate hydrogen atoms;

3. The presence of a layer of 251 water molecules ($\approx$ 0.17 $gD_2O/gGFP$) included with fully explicit D and O coordinates that can be compared to the simulated 0.4 $gD_2O/gGFP$ layer.

2.3.4 Labile hydrogen atoms in the GFP

Categories of labile atoms

A protonated protein exposed to a D_2O solvent, or a deuterated protein exposed to H_2O, will undergo fast exchange of their labile protons. Labile protons are hydrogens covalently bound to oxygen (O), sulfur (S) and nitrogen (N) atoms of polar amino-acids. The exchange is acid or based catalyzed, and therefore depends on the pH of the solvent. Labile atoms are also situated on H-bond acceptor and donnor positions depending on the functional group, reducing the exchange rater of labile atoms in protein compared to simple peptides [142, 145].

Exchange rates occurring from H to D in deuterated solvents are well-documented due to

their relevance in the field of Mass-Spectometry based H/D exchange methods, and are usually separated into three groups according to their kinetics of exchange :

1. Side chains labile atoms involved in hydroxyl, carboxyl, amine or sulfhydryl fonctional group, exchange at faster rate than what most experiments can probe (the kinetic rate constant approaches $k \approx s^{-1}$ [146]), and are supposed to be instantaneously exchanged.

2. Amide backbone hydrogen atoms exchange more slowly. Their exchange time has been measured to extend from 10 to 1000 ms in random coils. However, it has also been calculated in lysozyme at physiological temperature and pH to extend over 6 orders of magnitude, from milliseconds to years: $k \in [10^{-2}, 10^{-9}]s^{-1}$ [147]. These labile protons are used as probes of the protein's accessibility in solvent, or to probe ligand-protein interactions [148] because the exchange rate depends on the opening and closing rates of the local protein state. Amide backbone labile protons exchange rate presents a V-shaped curve as a function of pH with a minimum around 2.3 (this pH value is used to quench the system), therefore high temperature and neutral pH physiological conditions favour exchanges [149]. Neighbouring side-chains also exert a steric effect that modifies the rate [150], explaining also the slower rates within a protein compared to random coils.

3. Hydrogens involved in carbon bounds of aliphatic chains or aromatic groups do not exchange at the scale of experiments if it is not favoured by a catalyst or high temperature conditions: it cannot exchange without a ionization process [151].
   Indeed, it is not an easy process to exchange all labile atoms: successive incubations of a hydrated protein in a deuterated solvent are not sufficient to yield more than 80% of exchange among amide backbone hydrogen[152]. In the Appendix, Table A-I gives the list of common amino acids and their respective labile hydrogen atoms, sorted into side-chains or backbone. Let us notice that we define a Pk_x for most charged and polar amino acids, which is the pH required to balance acidic and basic side-chain functional groups of one type. It implies that for those side-chains we need $Pk_x \gg 7$ to observe exchange of labile atoms.

Characterisation of labile atoms in 6l26.pdb

6l26.pdb structure displays two configurations A and B. In **configuration A**, all explicit D atoms (labile atoms) have an **occupancy level equal to 1**, while **configuration B**

features additional labile atoms **with occupancy levels** < 1.

We verified that labile atoms in configuration A correspond to labile atoms of types 1 and 2 described above (fast+amide) which are not involved in the secondary structure H-bonds [153], while configuration B corresponds to all labile atoms of types 1 and 2.

For this purpose, we computed internal backbone H-bonds with Pymol software (see appendix, Figure A-1) implied in secondary structures. Subsequently, we estimated the number of labile atoms of types 1 and 2 from the FASTA sequence of "6l26.pdb" and "1GFL.pdb", which is the closest sequence to our produced wild-type GFP , using Table A-I. This is stored in subtable 2 of Table 2-VI.

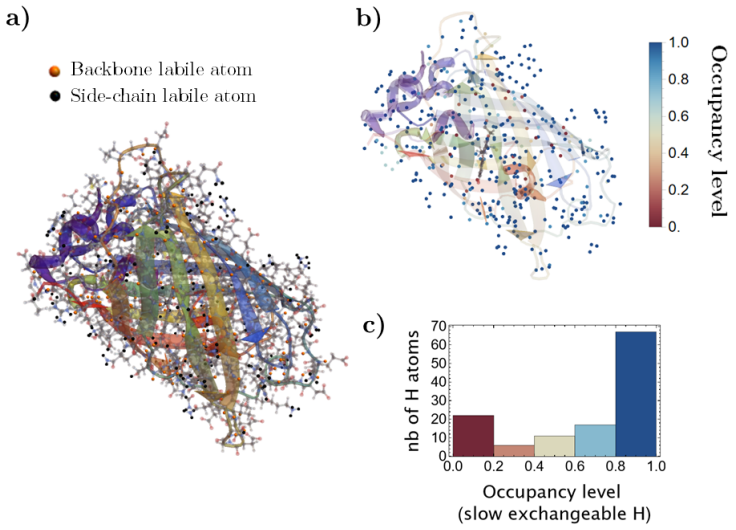

Figure 2-13: a) Labile atoms present in 6l26.pdb sorted into backbone and side-chains atoms. b) Labile atoms in 6l26.pdb sorted by occupancy levels. c) Occupancy levels of slow exchanging labile atoms (Occupancy levels < 1).

We compare to the labile atoms of configuration A (occupancy level =1) and B (occupancy level < 1), obtained directly from "6l26.pdb" structure. They are sketched in Figure 2-13 (a) and (b) and stored in sub-table 1 of Table 2-VI.

Successful comparison of explicit and calculated labile atoms for 6l26.pdb implies that

- For $S(Q)$ calculations, it is reliable to use explicit D atoms in 6l26.pdb file for labile atoms.
- **In configuration A, only fast labile atoms** which are not engaged in secondary-structure H-bonds **have exchanged**, and in **configuration B all fast and slower hydrogens from amide functional groups labile atoms have exchanged**. Hence, our calculations with 6l26.pdb can feature both situations.

- We can use the number of labile atoms corresponding to the wild type 1GFL.pdb, highlighted in yellow in Table 2-VI, to estimate the number of labile atoms in our protein (268 for configuration A and 414 for configuration B).

Furthermore, occupancy levels < 1 display an average of ≈ 0.67 and are distributed close to 1, Figure 2-13 (c). Hence it is highly probable that both slow and fast labile atoms (configuration B) have exchanged in our sample. **Hence, we can consider that ≈ 414 labile atoms have exchanged in our sample.**

Table 2-VI: Estimation of labile atoms, obtained from explicit deuterium atoms and from calculations of labile atoms using the FASTA sequence of in 6l26.pdb and 1GFL.pdb.

Explicit labile atoms in the PDB structure			
	Side Chains	**Backbone**	**Total**
6l26.PDB, config A	185	90	275
6l26.PDB, config B	186	202	388
Calculated labile atoms			
	Side Chains	**Backbone**	**Total**
6l26.PDB, fast labile atoms ($\equiv$ config A)	175	76	251
6l26.PDB, slow labile atoms ($\equiv$ config B)	175	215	390
Wild-type GFP, fast labile atoms ($\equiv$ config A)	185	83	268
Wild-type GFP, slow labile atoms ($\equiv$ config B)	185	229	414

2.3.5 Isotopic state of the protein

In order to verify that former experiments (IN5, D7, IN12) had not compromised the isotopic state of the protein, we performed gel electrophoresis and mass spectroscopy before pursuing the project with polarised QENS experiments on LET.

Sample aggregation state pGFP and dGFP were excluded by size with gel electrophoresis. It consists in applying a voltage to trigger the migration of biomolecules through the viscosity of the gel matrix, and the distance from the origin is a function of the fragment's size. The presence of oligomers in the sample appears as multiples of the expected mass of the monomeric form of the protein (27kDa).

Deuteration of non-labile atoms assessed with mass-spectrometry We quantified the percentage of deuteration of non-labile protons in the protein sample before performing LET experiment.

A MALDI mass spectrometry (MALDI TOF/TOF MS, Autoflex maX, Bruker Daltonics) experiment was carried on at Institut de Biologie Structurale (IBS, Grenoble) with the

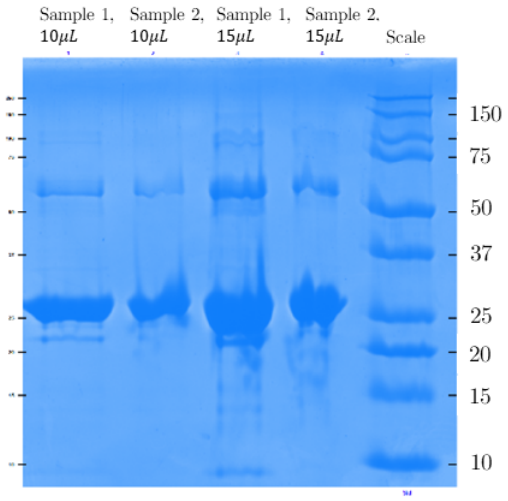

Figure 2-14: Gel electrophoresis of a deuterated GFP control sample dating back to production (sample 1, column 1: $10\mu L$ and column 3: $15\mu L$) and a sample used on IN5, D7 and IN12 (sample 2, column 2: $10\mu L$ and column 4: $15\mu L$)

help of Elisabetta Boeri on a H_2O diluted dGFP sample to check the deuteration percentage of non-labile atoms. The first sample dates back to GFP preparation 2019 and was stored at $2C$, while the second sample was used for three neutron experiments and stored in different conditions, then three times solubilised and lyophilized in D_2O before being checked with mass-spectrometry in view of LET experiment. Sample 1 corresponds to the state of the sample used on the first experiment on IN5 (never used under a neutron beam), and sample 2 to the state of the sample used on LET (sample prepared and then used several times). The output of a mass spectrometry experiment is the mass-to-charge ratio of the ionized protein fragments, leading directly to the mass of the protein.

Figure 2-16 displays the peaks associated to Sample 1 (a) and Sample 2 (b) as a functions of their mass-to-charge ratio m/z. The charge of the cation is denoted as z^+ next to the associated peak, and the mass-to-charge ratio is displayed above the peak.

The mass for a fully deuterated sample is estimated from the amino-acid sequence by doubling the mass of hydrogen atoms except labile atoms. It is then compared to the mass of the fully protonated sample to extract the deuteration ratio from the experimental mass M. We analysed the most intense peaks, such that $M = \left(\frac{m}{z}\right) z$. Results are exposed in table Table 2-VII, showing that non-labile atom exchanges are negligible in the GFP protein whether the sample has been used under a neutron beam or not.

Therefore, any difference between experiments and expectations cannot be explained by the deuteration state of the protein.

Method : The sample is dissolved into an acidic solvent exchanging all labile atomes,

Figure 2-15: Table of resulting deuteration ratios for sample 1 (unused 2019) and sample 2 (2022) obtained from mass-spectrometry experiments, MALDI-TOF, IBS.

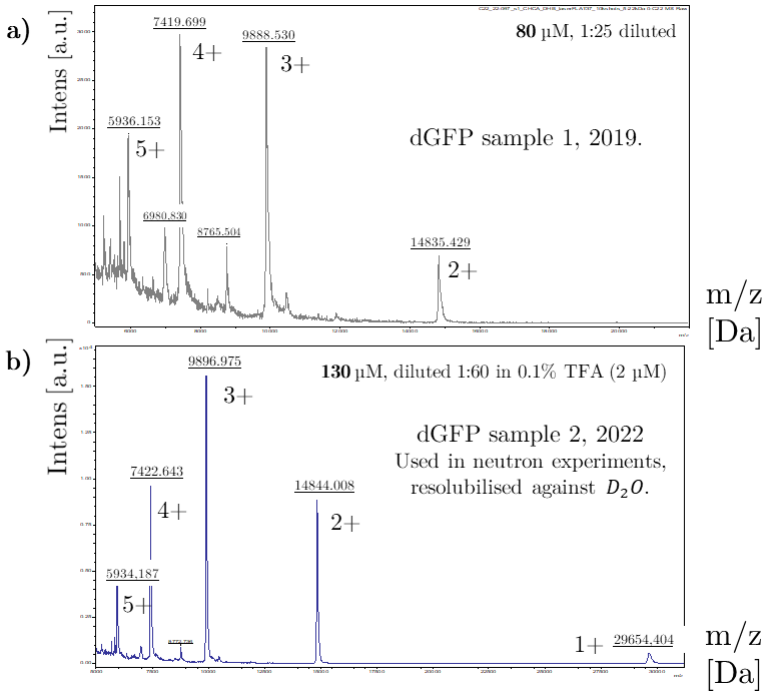

Figure 2-16: Mass-spectrometry intensity over mass-to-charge ratio, dGFP in D_2O. Sample 1: unused sample from initial batch, sample 2: sample used for IN12 and D7 experiments, resolubilised against D_2O. Performed at IBS mass-spectrometry platform.

Table 2-VII: Table of deuteration ratios obtained for sample 1 (unused, 2019) and sample 2 (used, 2022) obtained from mass-spectrometry experiments, MALDI-TOF, IBS.

	Sample 1	Sample 2
Expected mass, protonated sample H_2O [Da]	28187	
Expected mass, deuterated sample in H_2O [Da]	29673	
Experimental average mass [Da]	29668	29688
Deuteration ratio of non-labile protons (%)	99.7	101.1

containing an organic crystal "matrix". The solvent is vaporized, leaving a co-crystallized matrix with the embedded protein on a plate. This system is then excited in vacuum with a laser: the matrix containing the protein is desorbed, vaporized and ionized, which successively ionizes the protein. The application of a voltage induces a drift on the protein, and the time required to reach the detector is measured by time-of-flight and yields the mass-to-charge ratio. The presence of the matrix reduces the cleavage of covalent-bounds to study whole bio-molecules.

CHAPTER 3

Polarised diffraction at intermediate Q-scale in protein powders: infer a timescale of exchanges at the interface of water surface

Study of both the dynamics of a per-deuterated and a protonated protein requires to figure out what can be compared in such samples, regarding their very different expected coherent over total scattering ratios (83 % versus 16 %). Only quasielastic scattering can provide a clear assessment of the contamination of incoherent scattering with collective motions at the timescale of interest. However, diffraction already gives a paramount insight into the Q-dependence of coherent scattering, to decide the relevance of performing polarised QENS. Diffraction also corresponds to an experimental set-up that is already available and used in soft matter [154, 33], in comparison with polarised TOF that underwent a recent development for higher resolution studies and just opens to the dynamic study of non-magnetic samples. In this chapter we investigate the Q-dependence of coherent scattering in both a deuterated and a protonated protein powder samples hydrated in D_2O. Upon a surprisingly low percentage of coherent scattering in the deuterated sample, we perform calculations of $S(Q)$ to evaluate whether it stems from a strong amplitude collective term or from an exchange of both labile atoms and hydration water in the sample.

3.1 Introduction

Diffraction of protein powders is usually performed in the $Q < 0.1\text{Å}^{-1}$ range dedicated to Small Angle Scattering Studies (SANS) to study structure, organisation, interaction or polydispersity in a large panel of bio-molecular samples. It is feasible because coherent scattering is preponderant in this range corresponding to large distances (>nm). This is also why Neutron Spin Echo is performed to study collective dynamics in this range despite the presence of incoherent scattering with a factor $-1/3$.
On the other hand, incoherent quasielastic neutron scattering is usually performed for $Q > 0.1\text{Å}^{-1}$. Gaspar et al carried-out polarised diffraction on that Q-range using a protonated Myoglobin powder in D_2O and a deuterated C-Phycocyanin powder in H_2O [33], $h \approx 0.35$. They show that for $Q < 0.4\text{Å}^{-1}$ (0.6Å^{-1} in the deuterated C-phycocyanin), coherent scattering represents up to 80% of scattering, defining a criterion for the cross-over towards the predominance of incoherent scattering. Above that range, coherent scattering remains non negligible with a baseline of about 15% in D_2O hydrated protonated protein powders, which increases at the typical peaks of proteins around $Q = 0.7\text{Å}^{-1}$ and $Q = 1.7\text{Å}^{-1}$. Although Gaspar et al suggested the importance of carrying-out investigations with polarised quasielastic scattering to go beyond this "static" interpretation of the impact of both contribution of scattering, highlighting that ratios of coherent scattering should be dependent on the relaxation processes involved, it had not been performed so-far. Furthermore, there exists no information concerning the proportion of coherent scattering in a deuterated protein hydrated in D_2O, which further motivates our study.

Coherent scattering is the sum of a distinct and a self term, corresponding respectively to sums of correlations of pairs of different nuclei and of correlations from single nuclei. Therefore, estimating the coherent static structure factor $S_{\text{coh}}(Q) = S_{\text{coh,dist}}(Q) + S_{\text{coh,self}}(Q)$ implies to know of all inter-nuclei distances, which is not straightforward. Hence, for the sake of simplicity, often the Q-independent self coherent $\sigma_{\text{coh,self}}$ and incoherent macroscopic σ_{inc} cross sections are rather evaluated in literature [24, 25, 33] in order to raise an estimation of $S_{\text{coh}}(Q)/S_{\text{inc}}(Q)$.

$$\begin{aligned}\sigma_{\text{coh,self}} &= \frac{1}{4\pi}\sum_{i=1}^{i=n} b_{\text{coh},i}^2 N_i, \\ \sigma_{\text{inc}} &= \frac{1}{4\pi}\sum_{i=1}^{i=n} b_{\text{inc},i}^2 N_i,\end{aligned} \tag{3-1}$$

with $b_{coh,i}$ and $b_{inc,i}$ the coherent and incoherent scattering lengths of atom of type i and N_i the number of atoms of type i, such that n types of nuclei are present in the sample. However this is valid only in the large Q limit and in the frame of the static approximation, where

$$\lim_{Q\to\infty} \frac{S_{\text{coh}}(Q)}{S_{\text{inc}}(Q)} = \frac{\sigma_{\text{coh,self}}}{\sigma_{\text{inc,self}}}. \tag{3-2}$$

This approach is often used to justify that only the protein self-motions are visible in the case of a protonated protein hydrated with a single layer of D_2O. However, it is expected to be unrepresentative for $t \neq 0$ due to both the lack of consideration of pair-terms and the sample's inelasticity.

Figure 3-1 displays the expected contributions of scattering using Equation 3-1, for a polarised experiment on the dGFP sample, that is, for incoherent and coherent scattering disentangled. Figure 3-1 a) displays contributions from the different nuclei types while Figure 3-1 b) clarifies the contributions from either the protein or the hydration layer. In each figure, the case of no exchange in the sample (ideal case) is compared to the case of full labile atoms exchange + 40% of hydration water exchange.
This discussion will serve as a guideline along the manuscript to prove that those "static" considerations, usually held as a convincing argument that only self-dynamics of hydrogens are probed when contrast is made with deuterated hydration water, provide a wrong picture, and are not a good argument to interpret which nuclei are emphasized at a certain resolution and on a certain Q-range.

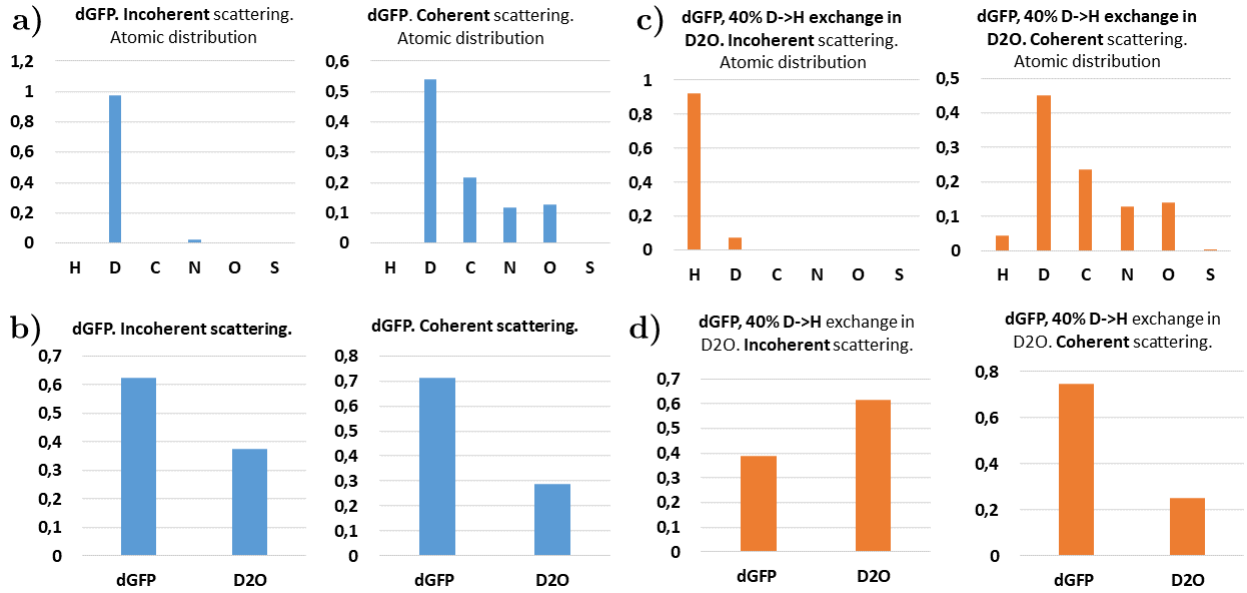

Figure 3-1: Expected contributions from Equation 3-1 for dGFP, in the ideal case without exchange [(a) and (b)] or in the case of $D \rightarrow H$ full exchange of labile atoms and 40% hydration water exchange [(c) and (d)]. (a) and (c) correspond to the contributions expected for each nucleus type, while (b) and (d) correspond to the respective contributions from protein and hydration water.

3.2 Polarised neutron diffraction experiments performed on pGFP and dGFP powders in D_2O

3.2.1 Evaluation of the coherent ratio of scattering in the static-structure factor

We performed diffraction with polarised neutrons on pGFP and dGFP, both hydrated with a single layer of D_2O, $h = 0.4$. Characteristics of the three instruments used for polarised diffraction are presented in Materials and Methods, Table 2-III, where the reader is referred. We will only highlight again the differences in set-up and dynamical range, noticing that the latter stretches from $E_{min} \approx 26$ meV on D7 (largely out of the QENS region and Boson peak region) to $E_{min} = 0.25$ meV on IN12 (in the QENS region).

Figure 3-2 shows the experimental ratios obtained on IN12 (blue dot), D7 (yellow dots) and LET (green curve). Table 3-I gives the average $S_{\mathrm{coh}}(Q)/S_{\mathrm{tot}}(Q)$ ratios obtained on the three instruments for dGFP and pGFP, Equation 2-18. $S_{\mathrm{coh}}(Q)$ is the static structure factor obtained from the coherent intensity, while $S_{\mathrm{tot}}(Q)$ is the static structure factor obtained from the merged incoherent and coherent intensities.

For dGFP the same ratio is obtained for all instruments within error bars.

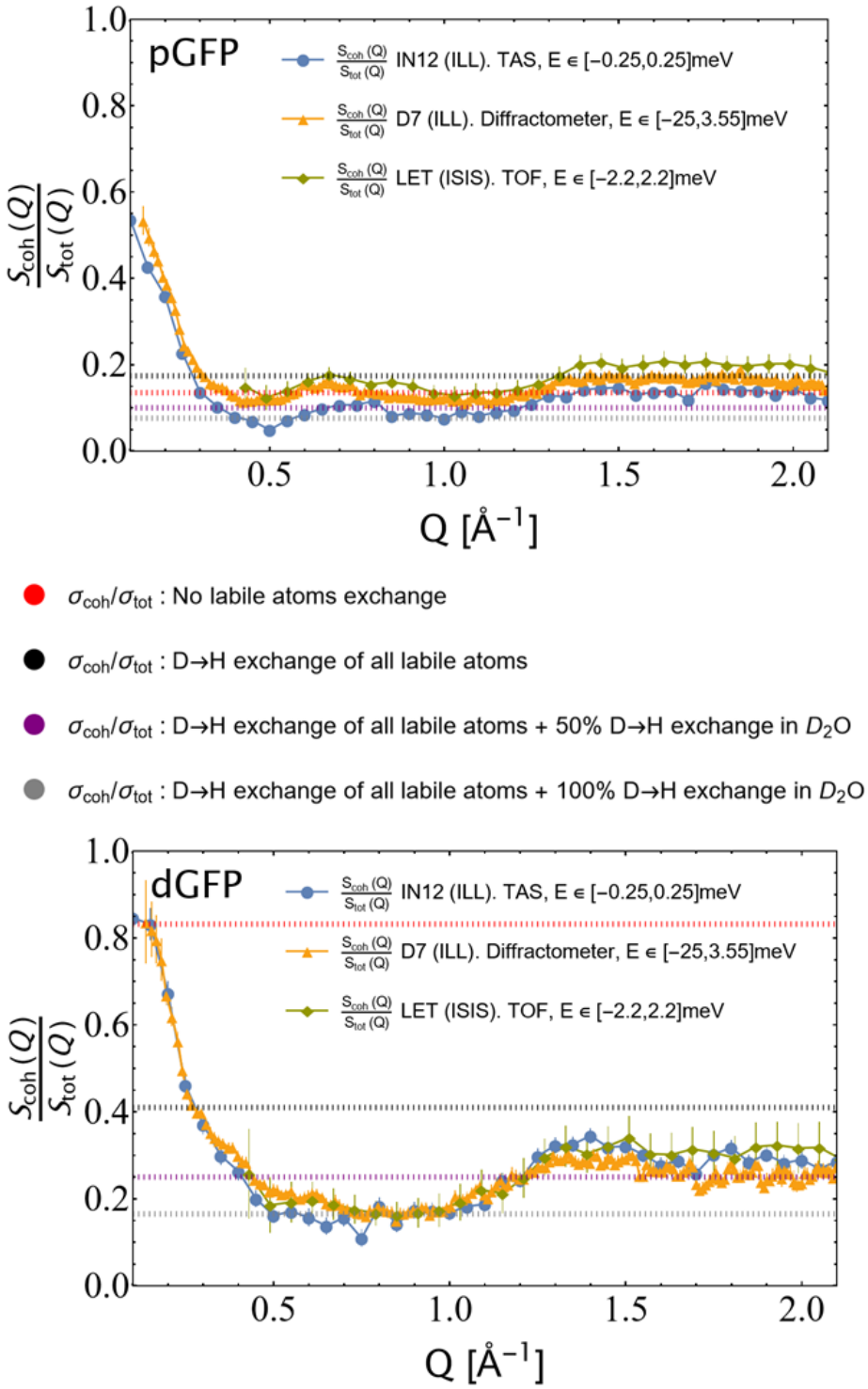

Figure 3-2: Experimental ratio $S_{\text{coh}}(Q)/S_{\text{tot}}(Q)$ obtained from polarised neutron diffraction on IN12 (Triple Axis Spectrometer-TAS), D7 (diffuse diffractometer) and LET (Time-Of-Flight Spectometer-TOF), their dynamical ranges are featured in the legends. Comparison is made with the expected ratios $\sigma_{\text{coh}}/\sigma_{\text{tot}}$ in the case of integration over $E \in [-\infty, \infty]$ and $Q \to \infty$, Equation 3-2, for different labile atoms and D_2O exchange situations.

However, discrepancies are larger for pGFP. We emphasize both the hazards in sample preparation (pGFP adsorbed water very slowly at each preparation, affinity with water

molecules was way more restricted than for dGFP) and the strong effect of the flat sample holder on IN12 around $Q \approx 0.8\text{Å}^{-1}$, see section 2.2.4. Furthermore, the substantial higher coherent scattering contribution on LET for both samples could be due to the cylindrical geometry of the sample holder reducing multiple scattering (with $T_{\text{pGFP}} < T_{\text{dGFP}}$) rather than a difference in sample preparation, see subsection 2.2.1.

As shown on figure Figure 3-3, the ratio of coherent over total scattering is barely a

Table 3-I: Average of experimental $S_{\text{coh}}(Q)/S_{\text{tot}}(Q)$ over $Q \in [0.4, 2.2]\text{Å}^{-1}$ for pGFP and dGFP. Uncertainties are below 10^{-3} except for pGFP, LET (± 0.04)

Sample	$S_{\text{coh}}(Q)/S_{\text{tot}}(Q)$		
	LET	D7	IN12
pGFP	0.172	0.148	0.113
dGFP	0.260	0.250	0.256

function of temperature for pGFP, and is the same within error bars (± 0.04) for $T = 2K$ and $T = 310K$ for dGFP. It was already found in polymers that the ratio calculated with polarisation analysis is not a function of temperature [127]. It further corroborates the robustness of results despite differences in instrument type, dynamical range and temperature. However, what directly strikes is the very low coherent ratio for dGFP

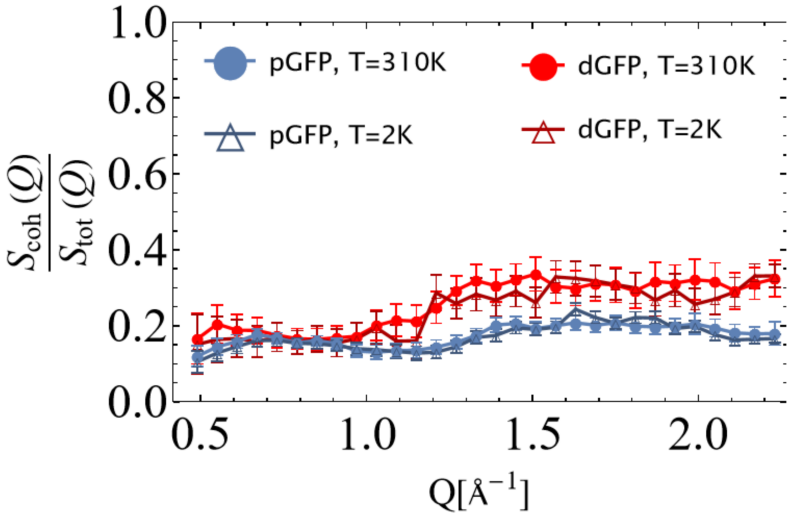

Figure 3-3: Structure factor ratio $\frac{S_{coh}(Q)}{S_{tot}(Q)}$ obtained for pGFP (blue) and dGFP (red) for temperatures $T = 310K$ (full markers) and $T = 2K$ (open markers) measured on LET spectrometer.

reported in Table 3-I. Although pGFP coherent ratio corroborates results of Gaspar et al for similarly hydrated protonated Myoglobin in D_2O [33], a dubious $\approx$ 25% ratio is obtained for a per-deuterated dGFP in D_2O where coherent scattering is supposed to prevail.

3.2.2 Discussion: deviations from asymptotic expectations

Results are at odds with the large Q limit, Equation 3-2, and it cannot be attributed to a inelastic effect regarding the agreement among instruments. For dGFP we asymptotically expect a ratio of coherent scattering of 83 % (red dotted line, Figure 3-2). It drops to 41 % in the situation where all labile atoms have exchanged with hydrogen (black dotted line). However, the highest peak around $Q = 1.4$ Å^{-1} exhibits a ratio of only ≈ 30 %. In literature of protein powder diffraction [155], this peak is reported to reach above the large Q limit, implying that experimental results are still at odds with Equation 3-2 even with the exchange of all labile atoms. Deuteration of non labile atoms has been shown to approximate 100% and cannot be held responsible for results, see subsection 2.3.5.

Exchange in deuterated hydration water at atmospheric pressure is not casually reported in literature but is rather discussed in the lab: a consensus with respect to the extent and the kinetics of this exchange does not exist among scientists. However, it is clear that upon weighing the hydrated sample under ambient atmosphere, mass changes at experimental timescale up to a few milligrams, which is usually attributed to evaporation (hence, a loss of water molecules). However, evaporation would concern at large a few percent of hydration and it does not affect the coherent over total scattering ratio ($< 1\%$ of decrease for $h = 0.4 \rightarrow h = 0.35$).
In order to explain our results, we raise two hypotheses :

1. D→H exchange occurs in the hydration layer, explaining both the very high incoherent intensity in the dGFP ($I_{\text{inc,pGFP}}/I_{\text{inc,dGFP}} \approx 3$ while $\sigma_{\text{inc,H}} = 80.3$ barns and $\sigma_{\text{inc,D}} = 2.05$ barns [23], see section 3.4) and the decrease in coherent scattering. Two scenarios are proposed, calculated with Equation 3-2, to illustrate this hypothesis on Figure 3-2: a 50% exchange that fits very correctly experimental results (purple dotted line), and a 100% exchange which raises a very low ratio (gray dotted line).

2. Although quite unlikely regarding existing powder-form protein and peptides diffraction patterns [155], the distinct part of the coherent structure factor could be highly negative and almost constant in this Q range, as has been observed in bulk water (see subsection 1.5.2, [156, 113]), and explain that the asymptotic limit is not reached at all in this Q region, resulting in a seemingly low coherent ratio.

Those hypotheses are briefly resumed graphically in Figure 3-4. Verifying such hypothesis

requires formal calculation of the static structure factor $S(Q)$ for a hydrated protein powder with the required hydration.

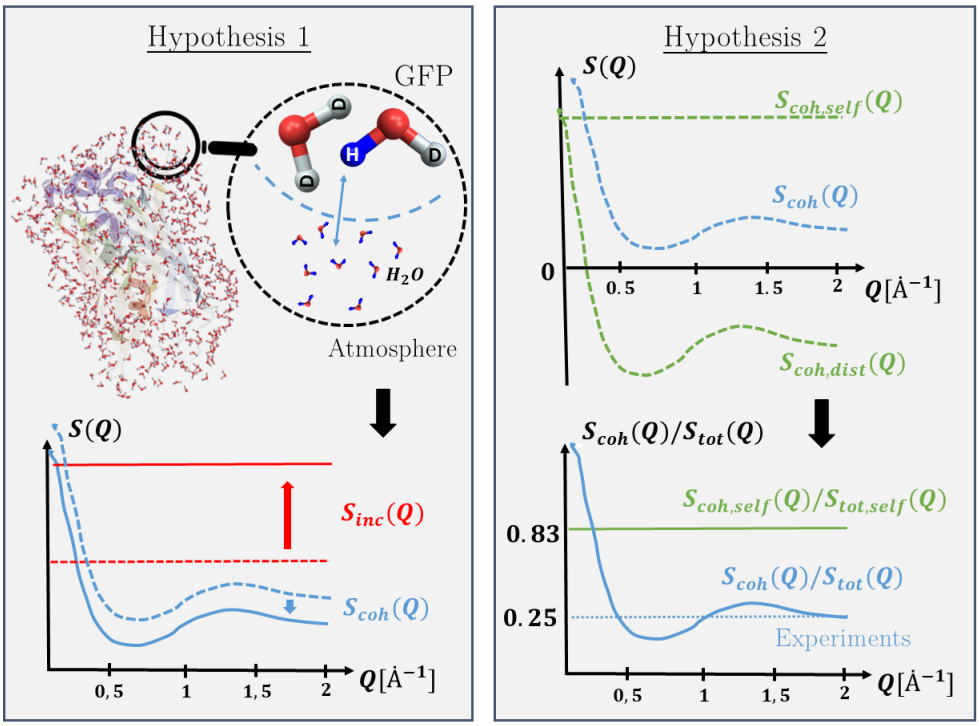

Figure 3-4: Schematics representing hypothesis 1 and 2, raised to explained the experimental $\frac{S_{\mathrm{coh}}(Q)}{S_{\mathrm{tot}}(Q)}$ ratio. Hypothesis 1 involves D→H exchange in the atmosphere. Hypothesis 2 involves a steady and negative distinct coherent structure factor $S_{\mathrm{coh,dist}}(Q)$.

Due to experimental variation in pGFP and its lower affinity to exchange and the Figure 3-2 and the lesser quantitative distinction between scenarios, dGFP will be used as the model to answer that question.

3.3 Calculation of the static structure factor of a powder sample from its PDB structure

3.3.1 Method

We want to provide a simple estimation of $S(Q)$ and avoid the resort to molecular dynamics simulations to check our hypothesis.

Hence, we propose a general expression for the static structure factor $S(Q)$, Equation 2-14, and suppose that atoms are highly localised at time t=0, therefore dropping the thermal average $\langle ... \rangle$ in Equation 1-52. We write

$$S(\mathbf{Q}) = \underbrace{\frac{1}{N}\sum_{i,j} b_{i,\mathrm{coh}} b_{j,\mathrm{coh}} \exp\left(i\mathbf{Q} \underbrace{(\mathbf{R}_j - \mathbf{R}_i)}_{\mathbf{r}_{ij}} \right)}_{S_{\mathrm{coh}(\mathbf{Q})}} + \underbrace{\frac{1}{N}\sum_{i} N_i b_{i,\mathrm{inc}}^2}_{S_{\mathrm{inc}}(\mathbf{Q})}, \tag{3-3}$$

with $b_{i,\mathrm{coh}}$ and $b_{i,\mathrm{inc}}$ the coherent and incoherent scattering lengths corresponding to nucleus i, and $\mathbf{r}_{ij}$ the vectorial distance between nuclei i and j introduced as the difference of space operators $\mathbf{R}_j$ and $\mathbf{R}_i$ at time t=0, where they commute.

In powder state, the static structure factor is averaged over θ and ϕ in spherical coordinates due to the isotropy of the sample. It yields a simple formula for $S(Q)$ detailed in the appendix, Equation A-22

$$S(Q) = \underbrace{\frac{1}{N}\sum_{i,j} b_{i,\mathrm{coh}} b_{j,\mathrm{coh}} \frac{\sin(Qr_{ij})}{Qr_{ij}}}_{S_{\mathrm{coh}(Q)}} + \underbrace{\frac{1}{N}\sum_{i} N_i b_{i,\mathrm{inc}}^2}_{S_{\mathrm{inc}(Q)}}. \tag{3-4}$$

$S_{\mathrm{coh}}(Q)$ contains itself two terms, namely: $S_{\mathrm{coh,self}}$ and $S_{\mathrm{coh,dist}}$ corresponding to self correlations ($i = j$) and distinct correlations ($i \neq j$). Let us highlight again that "distinct" means distinct pairs of nuclei, not distinct types of nuclei. In the distinct term, each different couple of nuclei counts twice in the sum.

Therefore, knowledge of respective distances of all nuclei in the {GFP+hydration water} system is enough to yield an approximate $S(Q)$ for the protein. This is valid above $Q \approx 0.5$ Å^{-1}: the largest distances in the protein (height $h \approx 40$Å) correspond to

$Q = 2\pi/h \approx 0.2\text{Å}^{-1}$ hence, small Q values below 0.5Å^{-1} lack the protein-protein and protein-water interdistances information which is present in the real system. Indeed, we only calculate distances within the protein and its hydration water, so inter-protein distances are not feature: a box with more than one protein, equilibrated with MD simulations, would be required to refine the low Q range.

6l26.pdb, a model for nuclei inter-distances in the protein

The only way to get distances between all nuclei in the protein is to perform diffraction on a crystallised sample. Since we are interested in estimating D/H exchange, it is paramount to have access to explicit positions of all hydrogens, which are not resolved with X-rays: we require neutron diffraction data with high resolution, which is furnished by the sole available neutron diffraction PDB file for a mutant GFP (described in subsection 2.3.3 [143, 144]), see Figure 3-5. Besides the information of inter-nuclei distances, 6l26.pdb also provides explicit D_2O hydration molecules and labile atoms, this is reported in Table 3-II. Hence, the amount of labile atoms is sufficiently close to account for our own protein sample, but the hydration layer is not dense enough and needs to be simulated and compared to the crystallised water of 6l26.PDB.

Table 3-II: Comparison of hydration and labile atoms of wild type GFP used for experiments, to the features available from 6l26.PDB.

	Hydration	Nb of water molecules	Nb of labile atoms (fast exch)	Nb of labile atoms (fast+slow exch)	Temperature [K]
Wild type GFP, experiments	$h = 0.4$	≈ 600	268	414	$\approx$ 300 K
Enhanced GFP, 6l26.PDB	$h = 0.25$	377	251	388	100 K

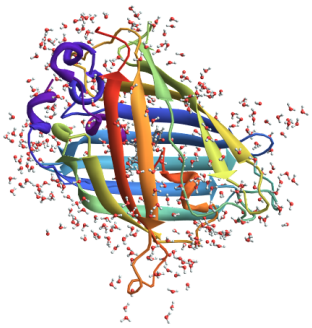

Figure 3-5: Hydrated enhanced green fluorescent protein, 6l26.pdb. Water molecules correspond to crystallised water in the first hydration layer.

Create a hydration water layer with exchanged water in the layer

We generate a PDB file with explicit hydrogen and oxygen atoms calculated for a hydration layer using Solvate software written by H. Grubmüller [157] yielding a layer optimised for sterical constraints. The simulated layers correspond to 2376 water molecules, that is $h \approx 1.7$. In order to reduce hydration to $h = 0.4$, we kept only D_2O molecules with the minimal distance to the envelope of the protein (≈ 600 molecules, dependent on the protonation state of the protein).

Comparison of the static structure factor of the generated water with crystallised water is performed by reducing the simulated hydration layer to $h = 0.25$, see Figure 3-6 (b). $S_{\mathrm{coh,dist}}$ differs mainly by the position of the main peak at 2 $\mathrm{Å}^{-1}$ in the simulated water towards 1.7 $\mathrm{Å}^{-1}$ in the crystallised water, see Figure 3-6 (a). In the following figures, lines are only used as a guide for the reader to join the calculated data points.

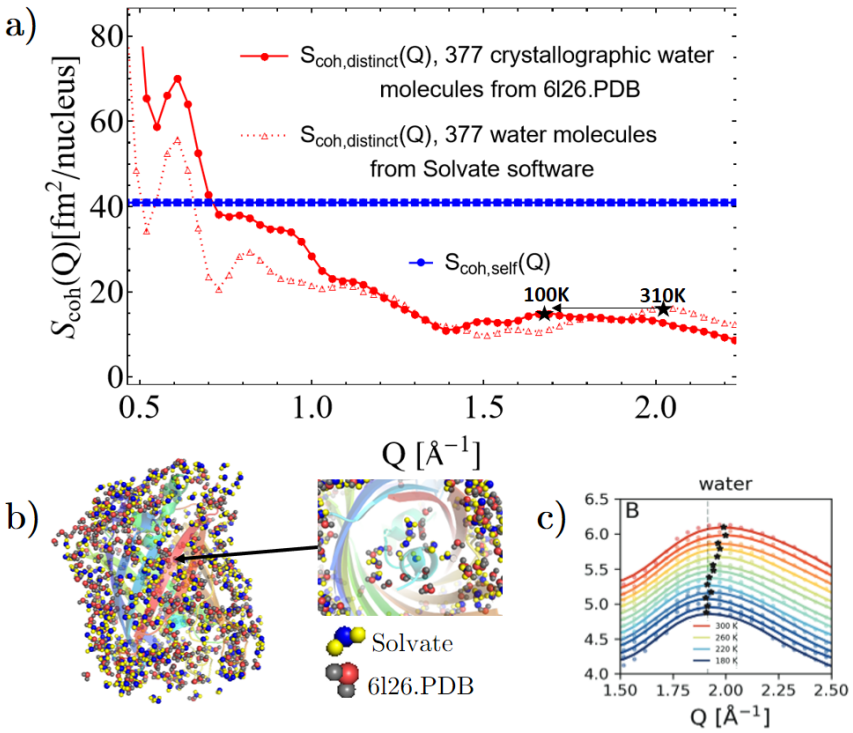

Figure 3-6: a) Comparison of the coherent structure factor distinct and self contributions (fm^2/nucleus) using the crystallographic water collected at 100K from 6l26.PDB [143] representing an amount of 377 water molecules, and the water layer simulated with Solvate software. b) Comparison of the two water layers, featuring a zoom on the internal cavities. c) $S(Q)$ (X-ray diffraction, O-O correlations) obtained from MD simulations on hydrated lysozyme ($h = 0.23$) at different temperatures (red: $T = 300$ K, blue: $T = 180$ K), adapted from Ref. [158], displaying a peak-shift upon temperature.

This shift arises mainly from D-O correlations, Figure 3-7 (a), and might be explained by the lack of energetic consideration in Solvate or by a temperature effect implying greater

order of the crystallographic water at $T = 100K$ [158], Figure 3-6 (c) hence a shift of the peak towards lower Q. However, it is not expected to play a major role in the total structure factor calculation. This generated hydration layer is therefore a correct model in the frame of our study.

D→H exchanges in hydration water were carried-out uniformly at the surface of the protein, to a given percentage of the initial D_2O content, see Figure 3-6 (b). We did not chose to specifically exchange whole molecules or to simulate an equilibrium with HDO molecules following the known equilibration curve [159], regarding our lack of knowledge of the exact involved phenomenon.

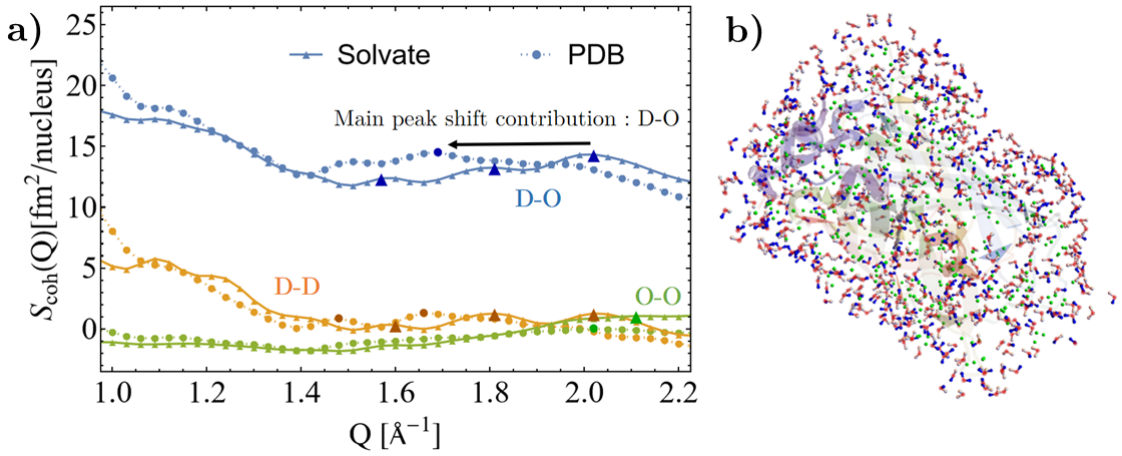

Figure 3-7: a) Comparison of D-D (orange curve),D-O (blue curve) and O-O (green curve) contributions to the distinct coherent structure factor of water for either crystallographic water (PDB) or Solvate simulated water (Solvate). The main shift between distinct structure factors arises from D-O correlations ($Q \approx 1.69$ Å^{-1} PDB $\rightarrow$ $Q \approx 2.02$ Å^{-1} Solvate)
b) Picture of the dGFP cartoon with hydrogen labile atoms in green and D_2O water molecules surrounding the protein and simulated with Solvate, such that deuteriums are in white and hydrogens are in blue.

Assess the dry protein structure factors

Dry protein structure factors have already been experimentally reported by Gaspar et al in [33] with polarised neutron diffraction for $Q \in [0.1, 2.3]$ Å^{-1}, offering a good basis to check our simulated dry protein factors (dGFP to deuterated C-phycocyanin in H_2O, pGFP to protonated Myoglobin in D_2O), Figure 3-8 (c) and (d).

Interestingly, as observed on Figure 3-8 (a) and (b), isotope exchange does not alter much the distinct correlation peak arising around $Q = 1.5$ Å^{-1}, because it implies heavy atoms and is rather a signature of the backbone structure. It is retrieved for GFP (β barrel

structure) as well as myoglobin or C-Phycocyanin α rich proteins [Figure 3-8 (c) and (d)]. However it does impact low Q values where isotope-specific partial structure factors have higher amplitudes and stronger variations.

Strong intensity below $Q = 0.6$ $\AA^{-1}$ is present in our dry proteins while it is absent in Gaspar's et al work (they report that it appears upon hydration and those correlations are assigned to water-protein correlations), somehow explaining the variations between experiments and simulations at low Q values.

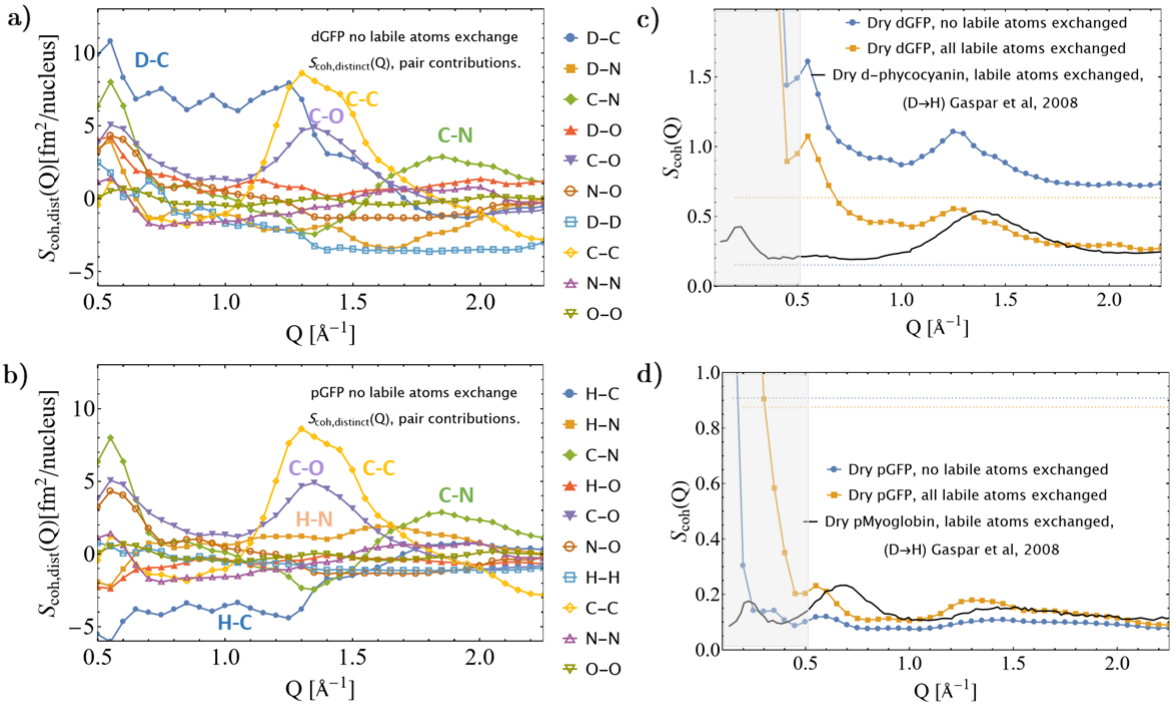

Figure 3-8: a) and b): Partial contributions to the distinct coherent static structure factor, strong contributions are labelled. a) corresponds to dGFP (dry, no labile atoms exchange) and b) corresponds to pGFP (dry, no labile atoms exchange). c) and d) Coherent structure factor $S_{\text{coh}}(Q)$ for dry dGFP (c) and dry pGFP (d), in the case of no labile exchange (blue curve) and full labile atom exchange (orange curve). It is normalised to verify $\lim_{Q\to\infty} S_{\text{coh}}(Q) = S_{\text{coh,self}}/(S_{\text{coh,self}} + S_{\text{inc,self}})$. The latter curve is compared to Gaspar et al [33] coherent structure factors for deuterated C-Phycocyanin with D→H exchange and protonated Myoglobin with H→D exchange. The gray curtain corresponds to lower Q values where our model fails to reproduce data.

3.3.2 Compare the calculated static structure factor to experiments

The static structure factor $S(Q)$ was calculated for dGFP and pGFP for H→D exchanges taking values in $\{10, 20, 30, 40, 50, 60\}\%$. It was calculated for $Q \in [0.1, 2.5]$ Å^{-1} with a step of $\Delta Q = 0.03$ Å^{-1}. It was calculated in fm^2/nucleus using the scattering length available on the NIST base, and then normalised using $S_{\text{inc}}(Q) + S_{\text{coh,self}}(Q) = 1$ to retrieve the asymptotic condition in Equation 3-2 and

$$\lim_{Q \to \infty} S_{\text{tot}}(Q) = 1. \tag{3-5}$$

Root-Mean-Square Deviations measure the difference between calculations and experiments for $Q \geq 1$ Å^{-1}. It raise the most probable hydration exchange for each experiment as featured in Table 3-III. We discard low Q values for RMSD calculations because we only consider a single protein instead of a powder, hence, all distances above ≈ 50Å lack in the model.

Table 3-III: Exchange ratios for hydration water, obtained from minimising RMSD between the computed and experimental structure factor ratio $\frac{S_{\text{coh}}(Q)}{S_{\text{tot}}(Q)}$ (Equation 3-4). Full labile atom exchange is supposed for dGFP while full recover of labile atoms (H→D) is supposed for pGFP.

Sample/Instrument	LET	D7	IN12
pGFP, exchange ratio	0%	30%	40%
dGFP, exchange ratio	40%	50%	30%

Results for the dGFP sample

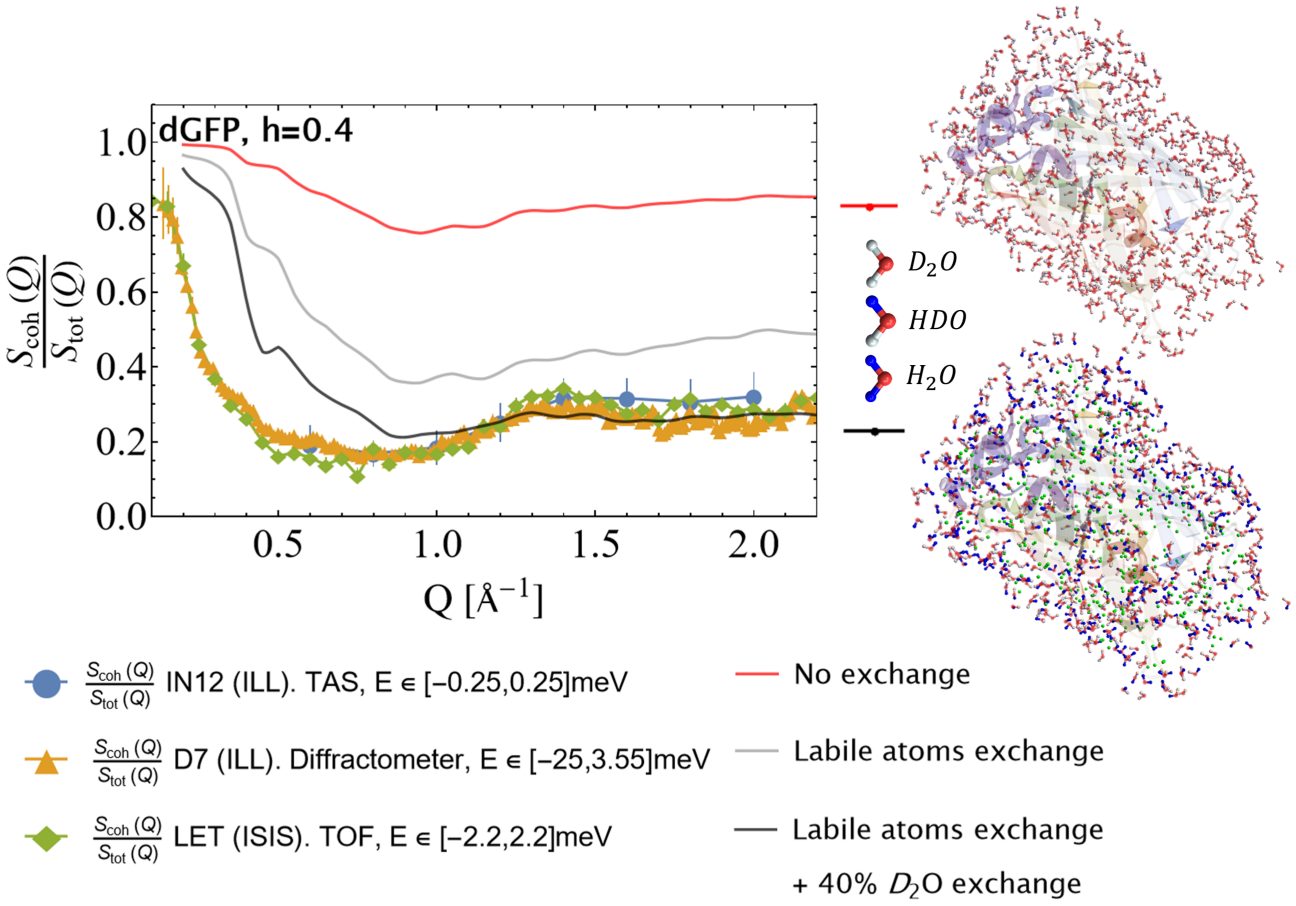

Figure 3-9: dGFP sample, $h = 0.4$ at T= 310 K. Experimental ratio of the coherent static structure factor over the total static structure factor $S_{\text{coh}}(Q)/S_{\text{tot}}(Q)$ has been measured on D7 diffuse diffractometer (orange △), IN12 triple-axis spectrometer, ILL (blue ∘) and LET TOF, ISIS (green ♢) with different resolutions and dynamical ranges, Table 2-III. As a comparison, calculation of the static structure factor raises the ratio in case of no exchange occurring in the sample (red line), the ratio in case of labile atoms exchange in the protein (414 hydrogens in total, gray line), and the ratio in case of labile atoms exchange in the protein + 40% D→H exchange in its hydration water (black line). Figures on the right side show the sketch of the protein surrounded by hydration water (top figure, deuterium in white) and a sketch of the protein where labile atoms and exchanged water are explicitly displayed (labile atoms in green, hydrogen in blue).

It appears that exchange of all labile atoms (gray curve) is not enough to obtain correspondence between experiments and calculations for dGFP. Hence, D→H exchange in hydration water is be required to explain the low $S_{\text{coh}}(Q)/S_{\text{tot}}(Q)$ ratio in dGFP. **About** 40% **of exchange is necessary to explain deviations with theoretical expectations**.

Results for the pGFP sample

Figure 3-10 shows the structure factor obtained for pGFP at different percentages of hydration exchange. It appears that experimental uncertainty makes it ambiguous to distinguish exactly which proportion of D_2O has exchanged in the range [0%,50%] and depends on our arbitrary $Q = 1$ Å^{-1} cutoff used for RMSD. It seems that pGFP undergoes less exchange with respect to dGFP. It might arise from the strength between the protein and its hydration water, since D-bonds are stiffer with respect to H-bonds [152]. It plays a role in both affinity to hydration water and its propensity to exchange with hydrogen. Let us remark in that sense that experimental time to hydrate pGFP to $h = 0.4$ was much longer (> 2 days) than to hydrate dGFP < 8hours. pGFP also difficultly exceeded $h = 0.35$.

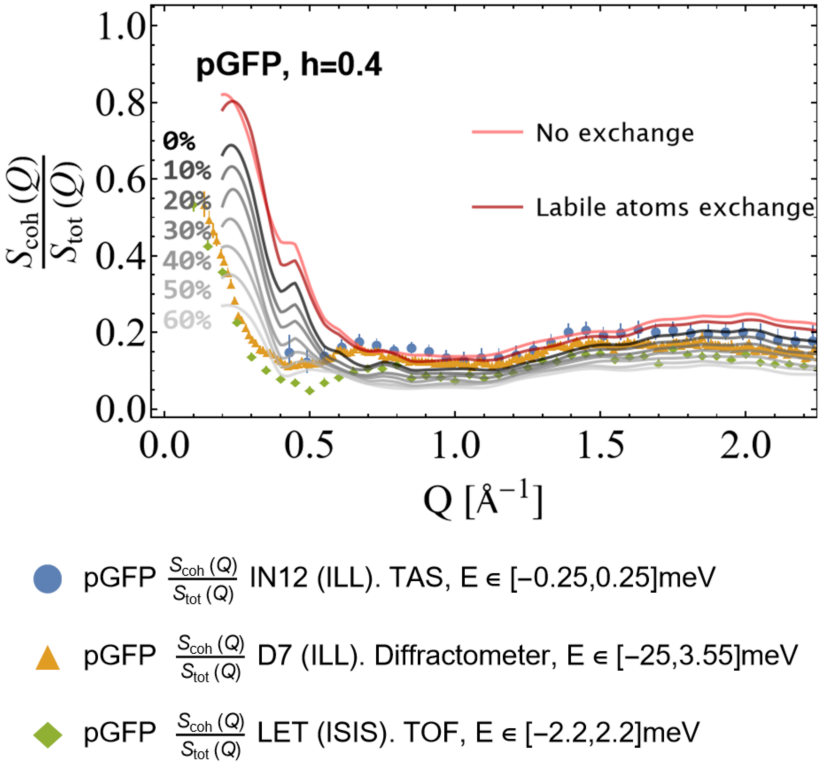

Figure 3-10: Comparison of experimental against computed $\frac{S_{coh}(Q)}{S_{tot}(Q)}$ ratio, for different $D \rightarrow H$ hydration exchange conditions in gray from 0% to 60% (0% in black, no labile atoms exchange in light red, labile atoms exchange in dark red)

3.4 Validate the exchange of hydration water: comparison of incoherent intensities

Comparing the ω-integrated incoherent intensities obtained from both dGFP and pGFP samples from the same experiment with polarisation analysis is a good indicator of the presence of D→H exchanges in the sample.

We calculate $\frac{I_{\text{inc,pGFP}}}{I_{\text{inc,dGFP}}}$ as a function of $r_{\text{exch}} \in [0\%, 100\%]$, the percentage of D→H exchange in hydration water, and compare it to the ratio obtained from polarised incoherent diffraction on D7, IN12 or LET in order to get an estimation of the percentage of exchanged hydration water in the sample.

Instrumental conditions are the same for pGFP and dGFP in each experiment (sample holder thickness, homogeneity of the powder sample, incoming beam, detector efficiency and resolution). Hence, Equation 3-6 holds for the ratio of raw incoherent intensities for both samples, normalised with vanadium [123].

$$\begin{aligned}\frac{I_{\text{inc,pGFP}}(\theta)}{I_{\text{inc,dGFP}}(\theta)} &= \frac{\phi_{\text{p}} E(\lambda)_{\text{p}} \Delta\Omega n_{\text{s,p}} T_{\text{p}} \left(\frac{\partial\sigma}{\partial\Omega}\right)_{\text{inc,p}} / (\phi_{\text{p}} E(\lambda)_{\text{p}} \Delta\Omega cst)}{\phi_{\text{d}} E(\lambda)_{\text{d}} \Delta\Omega n_{\text{s,d}} T_{\text{d}} \left(\frac{\partial\sigma}{\partial\Omega}\right)_{\text{inc,d}} / (\phi_{\text{d}} E(\lambda)_{\text{d}} \Delta\Omega cst)} \\ &= \frac{\left(\frac{m_{\text{p}} T_{\text{p}} \left(\frac{\partial\sigma}{\partial\Omega}\right)_{\text{inc,p}}}{M_{\text{p}}}\right)}{\left(\frac{m_{\text{d}} T_{\text{d}} \left(\frac{\partial\sigma}{\partial\Omega}\right)_{\text{inc,d}}}{M_{\text{d}}}\right)},\end{aligned} \tag{3-6}$$

p and d subscripts stand for protonated and deuterated. With I_{GFP} the raw intensity of the GFP sample, ϕ the incoming flux of neutrons, $E(\lambda)$ the detector efficiency, n_{s} the sample's number density, T_{GFP} the sample's transmission, $\Delta\Omega$ the solid angle of the detector, m_{GFP} the sample's mass and M_{GFP} the sample's atomic mass. Transmissions are obtained from D7 measurements such that $T_{\text{dGFP}} = 0.976$ and $T_{\text{pGFP}} = 0.910$.

Since we experimentally verify $I_{\text{inc}}(Q) \approx$ cst for all instruments when $Q < 2.2$ Å^{-1} and that we place ourselves in the limits of the static approximation [46], such that:

$$\int d\Omega \left(\frac{\partial\sigma}{\partial\Omega}\right)_{\text{inc}} = \sigma_{\text{inc}}. \tag{3-7}$$

One gets :

$$\langle \frac{I_{\text{inc,pGFP}}}{I_{\text{inc,dGFP}}} \rangle \approx \frac{\left(\frac{m_{\text{p}} T_{\text{p}} \sigma_{\text{inc,p}}}{M_{\text{p}}}\right)}{\left(\frac{m_{\text{d}} T_{\text{d}} \sigma_{\text{inc,d}}}{M_{\text{d}}}\right)}, \tag{3-8}$$

with $\langle ... \rangle$ the mean over accessible θ or Q values. $\sigma_{\text{inc,GFP}}$ is the total incoherent scattering cross section expressed in Equation 3-1. m_{GFP} and M_{GFP} are functions of hydration h and exchange ratio r_{exch}.

Labile atoms are supposed to have exchanged completely (414 labile atoms). The rest of the protein is not subject to exchanges (99% deuteration). $r_{\text{exch}} = 0\%$ corresponds to a 100% deuterated hydration water, $r_{\text{exch}} = 100\%$ corresponds to a 100% protonated hydration water.

The curves for $\frac{I_{\text{inc,p}}(r_{\text{exch}})}{I_{\text{inc,d}}(r_{\text{exch}})}$ are displayed in Figure 3-11 for both sample preparations in black and gray. Experimental ratios are displayed as colored lines and calculated from the average of $\langle \frac{I_{\text{inc,p}}}{I_{\text{inc,d}}} \rangle_{\text{exp}}$ over the accessible Q range for $Q \geq 0.2\text{Å}^{-1}$. The percentage of hydration exchange is obtained from the adequacy of the calculated and experimental ratios of incoherent intensities.

It raises an exchange ratio r_{exch} of $\approx 40/50\%$, Table 3-IV. It is in agreement with the

Table 3-IV: Most probable D→ H exchange percentage of hydration water obtained from the ω-integrated incoherent intensities $\langle \frac{I_{\text{inc,p}}}{I_{\text{inc,d}}} \rangle_{\text{exp}}$ on D7, LET and IN12, for $T = 310$ K. All 414 labile atoms have exchanged. Uncertainties for $\langle \frac{I_{\text{inc,p}}}{I_{\text{inc,d}}} \rangle_{\text{exp}}$ do not exceed ± 0.05. Considering only "fast" labile atoms exchange raises r_{exch} 54%, 62% and 63% for IN12, D7 and LET respectively.

	$\frac{I_{\text{inc,p}}(r_{\text{exch}})}{I_{\text{inc,d}}(r_{\text{exch}})} = 0$	$\langle \frac{I_{\text{inc,p}}}{I_{\text{inc,d}}} \rangle_{\text{exp}}$	$D \rightarrow H$ exchange, obtained from $\langle \frac{I_{\text{inc,p}}}{I_{\text{inc,d}}} \rangle_{\text{exp}}$	$D \rightarrow H$ exchange, obtained with $S(Q)$ Table 3-III
IN12	7.39	3.30	39%	$\approx 30\%$
D7	8.7	2.90	46%	$\approx 50\%$
LET	7.39	3.01 (3.04 for T=2K)	59%	$\approx 40\%$
Average	/	2.950 ± 0.021	48%	$\approx 40\%$

estimation raised in Table 3-III, and reinforces the insight that the low $S_{\text{coh}}(Q)/S_{\text{tot}}(Q)$ stems from an increase of incoherent scattering intensity upon D→H exchange rather than a strong decrease in coherent scattering due to cross-correlation terms in the distinct term of coherent scattering. However, this estimation is prone to large variation compared to previous methods, due to the theoretical curve convex shape, the sensitivity on sample preparation, and the probably larger exchange for dGFP than for pGFP (Table 3-III) .

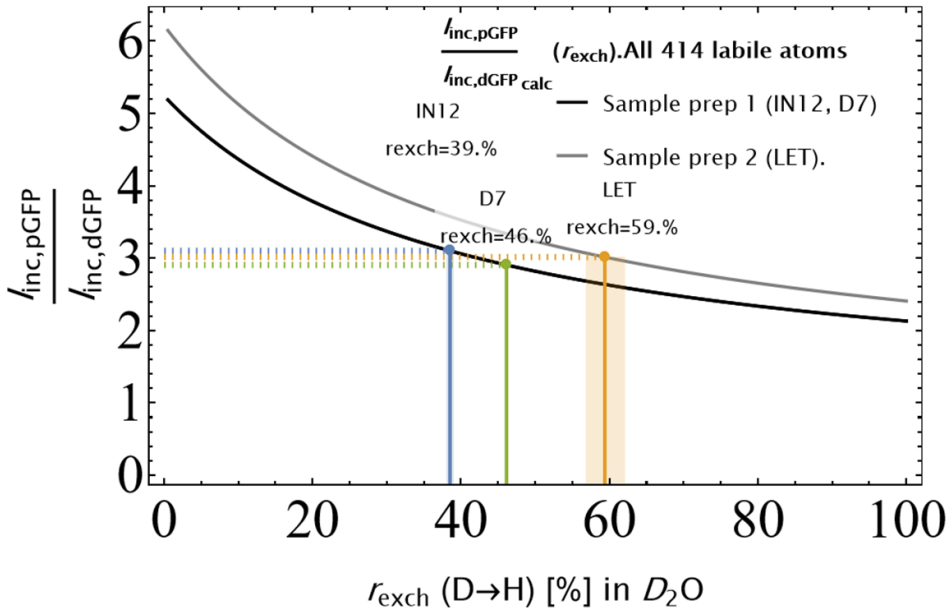

Figure 3-11: Ratio of ω-integrated and Q-averaged incoherent intensities $\langle \frac{I_{\mathrm{inc},p}(Q)}{I_{\mathrm{inc},d}(Q)} \rangle$ of the protonated over the deuterated protein, corresponding to data obtained on LET (orange dotted line), D7 (green dotted line) and IN12 (blue dotted line), see Table 2-III. Correspondence is made with the calculated curve of $\frac{I(Q)_{\mathrm{pGFP}}}{I(Q)_{\mathrm{dGFP}}}$ as a function of $r_{\mathrm{exch}} \in [0, 100]\%$ (dependent on the mass of the preparated sample) which corresponds to the percentage of $D \rightarrow H$ exchanged hydration water. Labile atoms have all exchanged.

3.5 Discussion

3.5.1 Hydration water exchange in protein powders

We mentioned two hypothesis in the frame of this chapter to explain polarised diffraction data obtained with dGFP: The low experimental coherent over total scattering ratio stems either from **1) exchange in hydration water**, or **2)** from **a negative distinct coherent structure factor** explaining deviation from the asymptotic ratio expected for $Q \rightarrow \infty$. Eventually, D→H exchange is responsible for most of the deviation. It is illustrated with Figure 3-12, where we observe that with or without exchange in the hydration layer, $S_{\mathrm{coh,dist}}(Q)$ oscillate closely to 0 implying that $S_{\mathrm{coh}}(Q) \approx S_{\mathrm{coh,self}}$, discarding hypothesis 2 as an explanation for experimental results. Calculations of $S_{\mathrm{coh}}(Q)/S_{\mathrm{tot}}(Q)$ for different hydration ratios in dGFP shown in Figure 3-9 and the comparison of incoherent intensities in pGFP and dGFP illustrated Figure 3-11 further validate hypothesis 1. Variations in sample preparation and in accessible dynamical ranges in this versatile study do not substantially modify resulting exchange ratios: it points-out a robust exchange phenomenon.

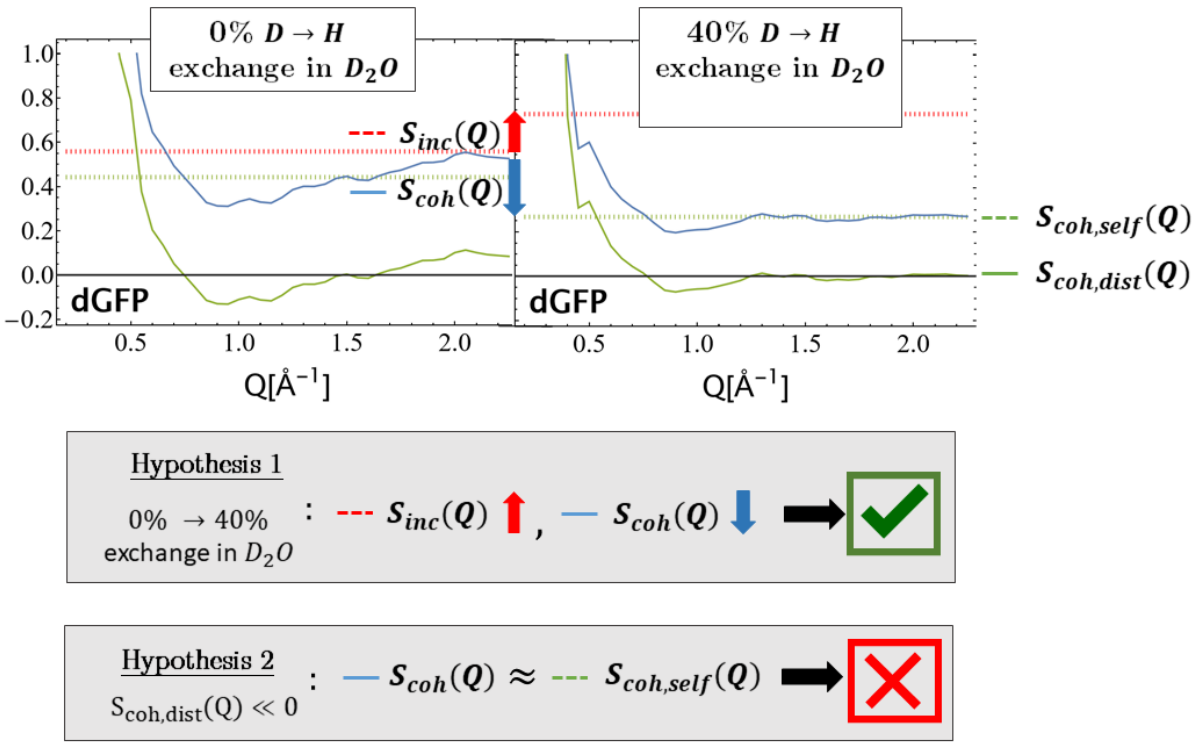

Figure 3-12: Illustration of the resolution of hypothesis raised for the low experimental $S_{\mathrm{coh}}(Q)/S_{\mathrm{tot}}(Q)$ represented in Figure 3-4. Structure factors are normalised to $S_{\mathrm{coh,self}} + S_{\mathrm{inc}}$. All labile atoms are supposed to have exchanged.

Hence, it appears that for hydrated dGFP, sole labile atoms exchange cannot explain our results: D→H exchange has occurred to an extent of 40% during sample preparation, before sealing the sample while weighting it. Most importantly, since the distinct term of coherent scattering is negligible in our case ($S_{\mathrm{coh}}(Q) \approx S_{\mathrm{coh,self}}$), Equation 3-1 and Equation 3-2 which were previously introduced to estimate the coherent fraction of scattering with atomic cross-sections only, are enough to approximate the exchange occuring in the sample, raising $r_{\mathrm{exch}} \approx 37 \pm 3\%$. Hence we do not require the full calculations of $S(Q)$: self-terms are enough to raise correct estimations in this Q-range.

Polarisation analysis is paramount to observe this exchange phenomenon. It might be challenging to trace this effect in standard studies with protonated proteins, due the negligible impact of increasing water exchange on the coherent to total scattering ratio. Furthermore, hydration water exchange appears less favorable in the case of pGFP compared to dGFP.

3.5.2 Proposition for the implicated phenomenon

We propose that a hygroscopic effect leads to isotopic exchange at the liquid-gaz interface between deuterated hydration water and the H2O-satured atmosphere. The hygroscopic effect occurs following the chemical reaction H_2O+$D_2O \longleftrightarrow$ 2 HDO [160].

Considering that the atmosphere is an infinite reservoir of H_2O molecules dependent on the ambient humidity rate, exchange between D and H nuclei can occur between the surface of the initial D_2O liquid phase and the atmospheric gaseous phase. It has been reported with Vibrational Sum-Frequency Spectroscopy [161] that although D-bonds are isotropic in the bulk phase, at the surface free D donors orientate perpendicular to the surface while the hydrogen-bond network remains liquid-like. The intermolecular D-bonds strength is also almost recovered from the first layer [162].

Therefore, isotopic exchange is rather a surface phenomenon, as testified by the estimation of a $\tau = 8s$ exchange-time of D to H in bulk D_2O measured from change in the maximum-density temperature of water D_2O:H_2O mixtures (initially 100%D_2O) in a 10 cm diameter petri-dish [163], compared to the $\tau = 1.7$ ms exchange time in a 20μ L droplet as probed with Surface Plasmon Resonance [159] or the $\tau = 50$ ms exchange time reported in [164]. The order of the reaction is also reported to change from bulk (0th order) to surface (2nd order). When equilibrium is reached, water remains a mixture of D_2O, H_2O and HOD [159].

Both experiments were performed at ambient humidity, pressure and temperature, where it is important to notice that there is a competition between exchange and evaporation that cannot be easily quantified. Therefore, a single hydration layer that displays transient jump-like and rotational dynamics due to the protein's surface topology and electrostatic interactions is very likely to present such isotopic-exchange effects, where the final exchange hydration ratio must depend on surface properties (hence, differences between protonated and deuterated proteins).

Such an explanation makes sense regarding the amount of exchanged water: it seems to reach an equilibrium within the experimental preparation time of a few seconds, with negligible variation in the final exchange percentage ($\approx 40\%$) despite hazards in sample preparations and in ambient humidity rate.

Further propositions to explain exchange are :

- Residues of H_2O hydration water in the lyophilised protein before D_2O adsorption in the dessicator. However, we tried to avoid such a phenomenon with multiple

lyophilisation and solubilisation against D_2O before LET experiment, which we did not perform for D7 and IN12, Table 2-V. It did not prevent from any exchange in the sample.

- The fast exchange between labile hydrogen atoms of the protein and isotopes in the hydration layer, which is reported to scale around the millisecond with NMR relaxometry ($\tau_{\text{exch}} = 0.13$ms in bovine serum albumin, $\tau_{\text{exch}} = 0.10$ms in lysozyme [165]). However, once the sample is sealed, the total amount of deuterated nuclei in the isolated {labile atoms + hydration water} system cannot change. Hence, this phenomenon can increase the speed and total amount of exchange in the layer, but still require hydration water exchange to explain that not only the amount of labile atoms N_{labile} has exchanged.

3.6 Conclusion

Both the kinetics and the extent of hydration water D$\rightarrow$ H exchange in protein powders at room temperature and at atmospheric pressure are almost always underestimated during sample preparation. It implies that the ratio of coherent intensity is only about 25% instead of 83% in deuterated GFP hydrated in D_2O, $h = 0.4$, due to D$\rightarrow$H exchange of all labile atoms and $\approx$ 40% of hydration water. We point out very fast ($<$ s) D/H exchange upon exposition to the atmosphere. Hence, we reckon that D_2O adsorption should be performed systematically under controlled hydrogen-free atmosphere to avoid contamination from hydrogen nuclei in the hydration layer of the powder-state protein. This issue seems to concern mostly hydration water since exchange is mainly an interface phenomenon, and should be negligible in bulk solutions.

CHAPTER 4

Polarised QENS experiments, impact of coherent scattering on protonated and deuterated protein samples

4.1 Introduction

Incoherent Quasielastic Neutron Scattering is a technique used to investigate the self-dynamics of hydrogen-rich samples from the picosecond to the nanosecond timescale, such as biological molecules, which contain a majority of equally spread H atoms (typically around 50%).

The situation is more complex for a deuterated protein, since several atoms contribute more or less equally to the total coherent scattering cross section. Deuteration is usually used for H/D contrast matching [139], or the investigation of hydration water dynamics at the protein surface when using a perdeuterated protein hydrated in H_2O [166, 87, 134]. Furthermore, deuteration has also been proposed to investigate internal collective motions of proteins in D_2O [24, 25, 26].

Neutron scattering is sensitive to isotope exchange and is used when to highlight specific parts of the sample, for instance to enhance the protein self-dynamics compared to the surrounding water. This is known as H/D contrast matching [139]. A typical interest is the investigation of hydration water dynamics at the protein surface when using a perdeuterated protein hydrated in H_2O [166, 87, 134]. Moreover, perdeuteration has also been proposed as a possibility to investigate internal collective motions of proteins in D_2O

[24, 25, 26].

However, scarce are the studies demonstrating the effectiveness of such a deuteration procedure to hide or separate contributions in QENS. This is now made possible with the advent of high-flux time-of-flight instruments equipped with polarisation analysis set-ups [167] to separate exactly incoherent and coherent contributions [168] from the analysis of the neutron's spin state at the detectors, with good energy resolution. This had long remained a challenge due to strong flux reduction and technical impediments [29]. LET is currently the instrument that provides data with enough resolution to apply to biomolecular sample, although several projects of polarised QENS instruments have recently developed (e.g. backscattering SHERPA [169]). Moreover, TOF probes large ranges of momentum transfers Q that can span from very low values corresponding to few intra and inter-molecular distances ($Q \approx 0.1$ Å^{-1}) where coherent scattering usually dominates [33], towards higher Q values ($Q \approx 2$ Å^{-1}) where incoherent scattering dominates, but structural information remains non-negligible. This makes an unambivalent separation of contributions impossible without polarisation analysis.

Up to now, the few studies that have explored coherent QENS on samples in solution with a polarised beam have highlighted the non-triviality of structural relaxation as a function of momentum transfer and time in D_2O and Van-der-Waals liquids [32, 156, 112], subsection 1.5.2, or reported systematic underestimation of incoherent diffusion coefficients in the case for ionic liquids in non-polarised experiments [31, 106].

Upon separation of incoherent and coherent dynamics in a protonated and a deuterated GFP powders hydrated in D_2O, we extract dynamical parameters with the FBD model presented in section 1.4, and interpret them in the light of analysis of coherent scattering in other materials. Therefore, we question in this chapter what happens when a perdeuterated protein is measured in D_2O, where sample and hydration water equally contribute to coherent scattering. We also challenge the assumption that a protonated protein should dominate the signal when surrounded by heavy hydration water. Generally speaking, we dispute the use of the "static picture" offered by the comparison of atomic cross sections in the sample to deduce which parts of the sample are invisible or emphasized. This is especially true in dynamical studies of biomolecules, where relaxation timescales are broad and heterogeneous.

4.2 Elements of bibliography: dynamics of a protein powder and its hydration water

4.2.1 Internal protein dynamics in a hydrated protein powder

Proteins are functional bio-molecules, composed of amino acids assembled by condensation and linked by peptide bonds -(C=O)NH- formed by a carboxylic acid group and an amine group. The backbone (the peptide bond structure) essentially undergoes slow restructuration, rotating along the dehydral angles ϕ and ψ. Those angles are defined from the N and C atoms of the functional groups to the C_α atom linking the residue to the backbone. They usually take values in regions "allowed" by the Ramachandran plot to form the secondary structures: it raises flexible α helices and more rigid β barrels, see figure Figure 4-1.

Side-chains are the residues of amino-acids. They present a wide range of polarities and hydrophobicities. Most hydrophobic amino-acids are buried in globular proteins while polar amino-acids interact with the solvent. Side-chains promote the tertiairy 3D structure of the protein by forming intra-molecular non-covalent bounds. The strength of the latter scales as units of the thermal energy k_BT, which is at the base of resilience, flexibility and function of proteins [170]. Side-chains are more flexible than the backbone, and undergo a large scale of vibration and relaxation motions.

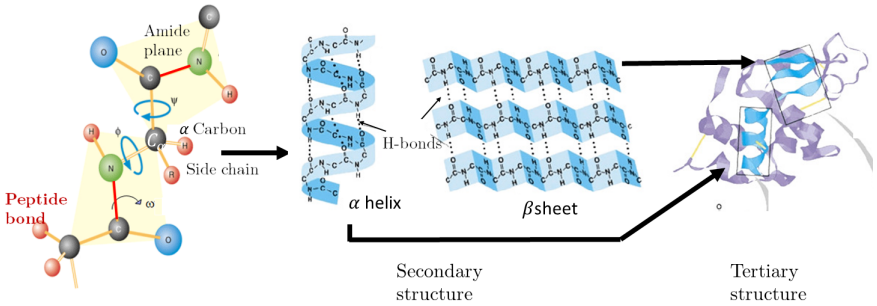

Figure 4-1: Schematics of the primary, secondary and tertiary structures of a protein. Adapted from [171] and https://www.chemistrylearner.com

Proteins have dynamics spanning approximately from the femtosecond to the second timescale, hence requiring many different spectroscopy techniques to span and analyse motions. Neutron spectroscopy focuses on the fs-μs timescale. Protein dynamics are now commonly described as hierarchised into "tiers" of motions since Frauenfelder conception of the energy landscape of proteins [172, 173], that is a succession of hierarchised sets of

energy minima in the configurational space. Large gaps in energy barriers exist between those "tiers", hence defining different classes of motions. We introduce here Khodadadi and Sokolov description in Ref. [67] :

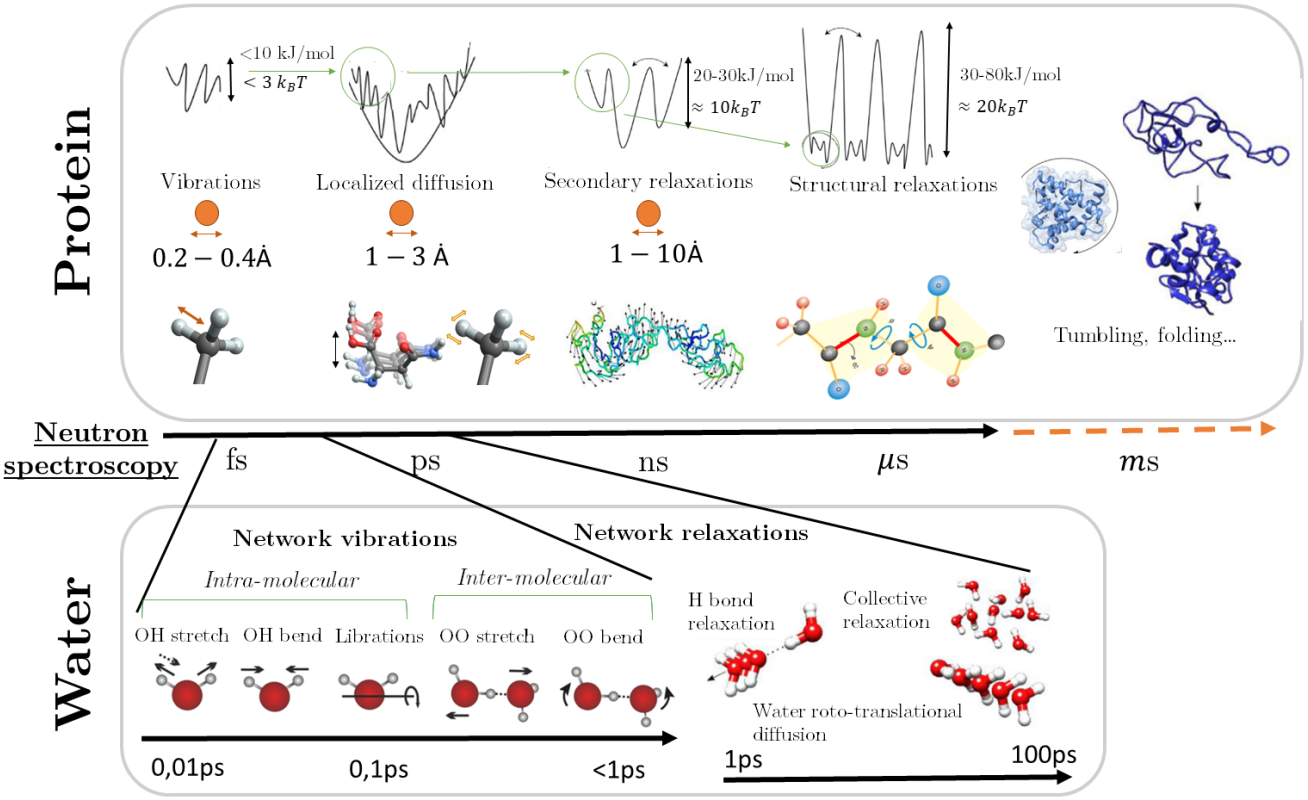

Figure 4-2: Representation of the protein energy landscape and hierarchical ranges of motions probed by neutron spectroscopy, with their respective energy barriers, on the range probed with neutron spectroscopy. Water motions on the same ranges are compared on the lower pannel. Adapted from [67, 174, 175, 56].

1. Fast $\leq$ ps motions, implying subÅ displacement (bond vibrations, Boson peak...).

2. Motions appearing from about 10 to 100 ps time scale. This category of motions includes the "localised diffusion" coupled with hydration water and corresponds to $\approx$ $1-3$ Å displacements [91]. This category includes as well the highly heterogeneous methyl group rotations, which are strongly correlated with the protein function. Authors point out that those small-amplitude motions correspond to diffusion in a rugged harmonic potential, rather then jumps between conformational states, which is in line with our own model. The GFP backbone is still rigid on this timescale [176]

3. At $\approx$ ns, motions implying crossing larger energy-barriers and spanning larger amplitudes ($\leq$ 10Å) arise. Khodadadi and Sokolov name them "secondary relaxations"

in the sense that they do not lead to major structural changes, and are driven by faster motions described earlier.

4. With neutrons, the slowest motions observable occur at the $\approx$ μs scale, where backbone restructuration becomes dominant.

Those motions are presented in the upper panel of Figure 4-2. Above that scale, long-range slow dynamics occurs such as tumbling (ns), structural transitions (μs) or folding (ms-s) [175]. Let us notice that in protein powders at $h = 0.4$, side chain motions are just activated [177], and their dynamics increase with h [178] and are fully activated in solution [179].
In this manuscript we focus on the first two types of local motions accessible with TOF spectroscopy, and we mainly use the term "localised motions" to differentiate internal dynamics from centre-of-mass motions.

4.2.2 Impact of isotope exchange on protein stability, structure and dynamics

The effect of deuterating the hydration water on the protein itself is well recognised: it has a stabilising effect in intra-protein H-bonds with decreased flexibility [180, 181] due to stiffer D-bonds [182], and decreased hydrophobic effect (burial of non-polar residues [180]). It also impacts the secondary structure [183]. Strong kinetic isotope effect is even found in azurin for electron transfer upon D/H exchange in the solvent [184].
However, the effect of protein per-deuteration is not yet clear. Structure is left almost identical [185] although changes in protonation states have been reported in GFP upon deuteration [186]. It is clear from DSC experiments that thermal stability is reduced in deuterated proteins with respect to protonated proteins [185, 187, 188, 189] , and hydrophobicity is reduced as well [190, 185, 189]. However, the impact on dynamics is clearly non-trivial, and has not sparked many studies on the subject yet. A few studies have demonstrated the dependence on the choice of the protein and the probed timescale. A reduced enzymatic activity was probed in deuterated lysozyme [185], while FTIR ligand rebinding shows non significant change in local and global dynamics of the P450cam-CO complex [188]. However, long-time correlations in the backbone (with a timescale of ≈ 150 s^{-1} for $^{13}C_\alpha - ^{13}C_\beta$ cross-correlated chemical shift modulations) of a perdeuterated GB3 protein probed by NMR are slowed down in comparison to the protonated one,

Ref. [190]. However, the same authors [187] highlight non-trivial effects: per-deuteration increases the global flexibility of HP36 while decreasing this of GP3.
Subsequently, there exists no quantitative nor qualitative knowledge of the impact of protein deuteration on dynamics. It would rather point-out towards negligible effects, and if, a slow-down of dynamics. Basically, the main effect from isotope deuteration is the change of mass, implying also modified zero-point fluctuations and an isotopic shift in vibrations.

4.2.3 Hydration water of a protein powder

Water is a unique liquid, with anomalous properties [191, 192] due to the fact that intermolecular bonding relies on H-bonds. Pictures underlying the microscopic behaviour of water are several: it stretches from the initial picture of a continuous process of cooperative interactions, to a picture of jump-like motions with for instance decoupled rotational translational motions at low temperature [193] or transitions between solid-like and short-lived continuous liquid-like dynamics [194]. Models constantly evolve, including markovian continuous-random walk models [195], relaxing cage models inspired from α relaxation in glasses [196], non-Markovian fractional Brownian dynamics [197] etc. But the global picture tends towards a strong heterogeneity and cooperativity at the ps-scale, which are inherent to the H-bond network restructuration that occurs through the consequent breaking of H-bonds driven by <ps librations and slow vibrational modes in water [198, 199]. Those motions are presented in the bottom panel of Figure 4-2 and compared to protein motions.

Hydration water of proteins is confined water in close contact with the protein's surface, undergoing subdiffusion [200]. It is indeed a dynamically and structurally perturbed layer of water, stretching up to 2 to 5 Å [201, 202] (5.5 Å [203] for GFP) and still continuously perturbed until reaching bulk water dynamics around 10 Å from the protein's surface [204]. Regular exchanges of molecules occur from the first layer to the bulk phase. Perturbation arises upon interaction of water with patches of hydrophobic and hydrophilic amino acids [205, 206] the latter increasing strongly the lifetime of H-bonds [204], but also the topology of the surface [207, 165, 208], and electrostatic interactions with amino-acids charges [209]. Both entropic (modification of conformational possibilities) and enthalpic (difference of H-bond energies at the surface) contributions are implied in the slowing

down of the first hydration layer [56].

Its structure is clearly different from bulk water: it is more dense (at least 6% density excess) [210] and displays a more tetrahedral network of H-bonds in the vicinity of the interface [201, 198, 211] compared to bulk water, while being topologically closer to supercooled water [211].

It dynamics are reported to resemble bulk water under pressure. It has a spectral distribution (> meV) corresponding to the superposition of Low and High Density Amorphous (LDA-HDA) water states [208] driven by hydrophobic and hydrophilic sites of the protein respectively [206], and its collective dynamics (sound velocity and damping coefficients) are that of 2kbar bulk water [198]. Furthermore, its dynamics are said to be "analogous to that of bulk water at temperatures typically 20 degrees lower" [199].

Hydration water is paramount due to its impact on protein's activity. Dewetting zones correlate with interaction sites of the protein [205], desolvation cost is highly implicated in ligand binding [212]. Water-protein decoupling of motions and reducing water cavities is also key to adaptation to pressure [213].

4.2.4 Dynamics of hydration water and its coupling with proteins

Water is essential to permit the onset of motions and the function of the protein. Motions essentially take place on the fs-ns scale. The femtosecond timescale consists essentially of librations (hindered rotations, 70 meV-60 fs), intra (OH bending mode 220 meV-19 fs, OH stretching 420 meV-10fs) and inter (HB collective stretching mode 25 meV-166 fs, HB collective bending mode 6 meV-700 fs) molecular bonds vibrations [214, 215, 216] and are essential to permit H-bonds breakage, such that the network locally restructures through large amplitude reorientations on the picosecond-timescale, when water changes H-bond acceptor (Laage et al, [217]). Modes in brackets correspond to modes observed with neutron inelastic scattering. The H-bond lifetime is evaluated to $\approx$ 2 ps in bulk water, while for hydration water it centres around 4 ps with a long-time tail for hydration water according to Ref.[218], although Ref.[212] gives $10 - 100$ ps. Large timescales of hydration water motions are specific to macromolecule solutes, such as the motions of water inside clefts ($\approx$ ns) or cavities ($\approx$ ms) [56].

Hence, it raises a retardation of hydration water with respect to bulk water ($\xi = \tau_{\text{hydration}}/\tau_{\text{bulk}}$)

on the ps timescale, with a large range of proposed values in different techniques ($\xi \approx 2-3$ in NMR, $\xi < 20$ in femtosecond fluorescence spectroscopy, $\xi \approx 6-7$ in optical Kerr-effect spectroscopy [56]). Concerning neutron scattering, Perticaroli et al [204] report a Q-dependent retardation of H_2O for dGFP (h=0.4) scaling from about 4 at $Q = 2$ Å^{-1} to 10 at $Q = 0.5$ Å^{-1}. Hence they explain that a local probe (NMR) versus large scale probe (THz spectroscopy) report different scales of perturbation due to this Q-dependence.
Concerning timescales of the H-bond network relaxation, femtosecond fluorescence Stokes shift spectroscopy applied to single tryptophan (Trp) reports a bi-modal exponential decay with a first fast decay assigned to vibrations and diffusive rotation ([219] 800 fs, [220] 5 ps) and a slow decay assigned as coupled to side-chains ([219] 38 ps, [220] 87 ps). Especially, Zhong et al [221] recently studied the cooperation of collective motions simultaneously in hydration water and side chains in DNA polymerase IV with single Trp mutations situated at regions of interest. They reported a double exponential decay at the ps scale for hydration water and, two corresponding decays at similar time scales in side chains. They observe local collective reorientational relaxation of water's H-bond network with $\tau_1 \in [3, 6]$ ps, that drives the structural relaxation of the network that occurs at larger timescales with $\tau_2 \in [50, 120]$ ps. They are correlated to the timescales of side-chain motions, the latter always being slower, by a factor from 1 to 3 from τ_1 and up to 10 for τ_2 corresponding to a higher solvent-protein cooperation.
Generally speaking, hydration water tends to be classified into two or three classes: slow, embedded water and almost bulk-like fast transient water [207, 165, 215, 218] picturing the cooperativity between protein surface side-chains and water. It has also been proposed that water molecules closer to the surface mainly undergo rotational motions, transitioning to translational motion when reaching the bulk area [222] or in cavities [218]. Both experiments and simulations propose that $\approx 30\%$ of hydration water is simply retarded while the rest is strongly coupled to side chain motions [219, 81].

Hence, ps relaxation concerns both the protein and its hydration water, and separating both contributions is not an easy task, even enhancing contrast with deuterated water. The concomitant role of water and protein side chains has sparked discussions for decades, concerning whether water or protein enslaves one another. Neutron scattering provides many insights to answer that question, we mention here that water translations are required for the onset of the dynamical transition [222] and water arrest "rigidifies" the protein below 220K compared to the dry form of the protein [134]. Hence, hydration water

was long thought as "slaving" the protein fast motions [173]. However, the fact that both water and protein necessary couple to induce slower processes is now established [220, 67].

In a nutshell, despite differences in techniques and motions probed (self diffusion is probed in neutron scattering, NMR while collective diffusion in fs spectroscopy, optical Kerr effect), one picture remains: hydration water has a large spectrum of relaxation timescales. Especially, two average relaxation times around $\tau = 5$ps and $\tau = 80$ ps seem to emerge, the latter corresponding to strong protein-water coupling. Although protein and water motions are usually both non-separable in neutron scattering, it seems that protein side-chain dynamics coupled to water relax on longer time scales compared to water dynamics.

4.3 Experimental separation of coherent and incoherent scattering

We performed quasielastic neutron scattering with polarisation analysis on LET. In this chapter we analyse data obtained with incoming beam $E_i = 3.27$ meV, such that $\Delta E = 95$ μeV, at $T = 310$ K. Due to the isotropy of the sample, $F(Q,t)$ is a function of the norm of $\mathbf{Q}$.

LET $S(Q,\omega)$ data and its fitted model are compared for both proteins for $Q = 1.4$ Å^{-1} on Figure 4-3, (e) and (f). The quality of the fit is assessed for $F(Q,t)$ for $t \in [1,16]$ ps at all Q values for dGFP, see Figure 4-3, (a) and (b). It appears that both incoherent and coherent scattering functions $S(Q,\omega)$ present a clear broadening with increasing Q [Figure 4-3 (g) and (h)]. However, while pGFP and dGFP incoherent dynamic structure factor are clearly distinct [Figure 4-3 (f)], their coherent dynamic structure factors are almost superimposed at fixed Q [Figure 4-3 (e)], reflecting strong similarity of coherent dynamics in both samples.

Intermediate scattering functions display interesting features: $F_{\mathrm{coh}}(Q,t)$ reflects that the asymptotic regime is quickly reached (a plateau is already visible around 10ps for most Q values), hence fast dynamics and high Elastic Scattering Factor (ESF) compared to $F_{\mathrm{inc}}(Q,t)$ (although long decays are typical for slow power-law relaxations and require more than visual inspection). As will be confirmed with the analysis of parameters, strong variation of the coherent ESF ($ECSF$) with Q entails that $F_{\mathrm{coh}}(Q,t)$ do not nicely superimposed with decreasing Q, compared to what is usually probed, see the self

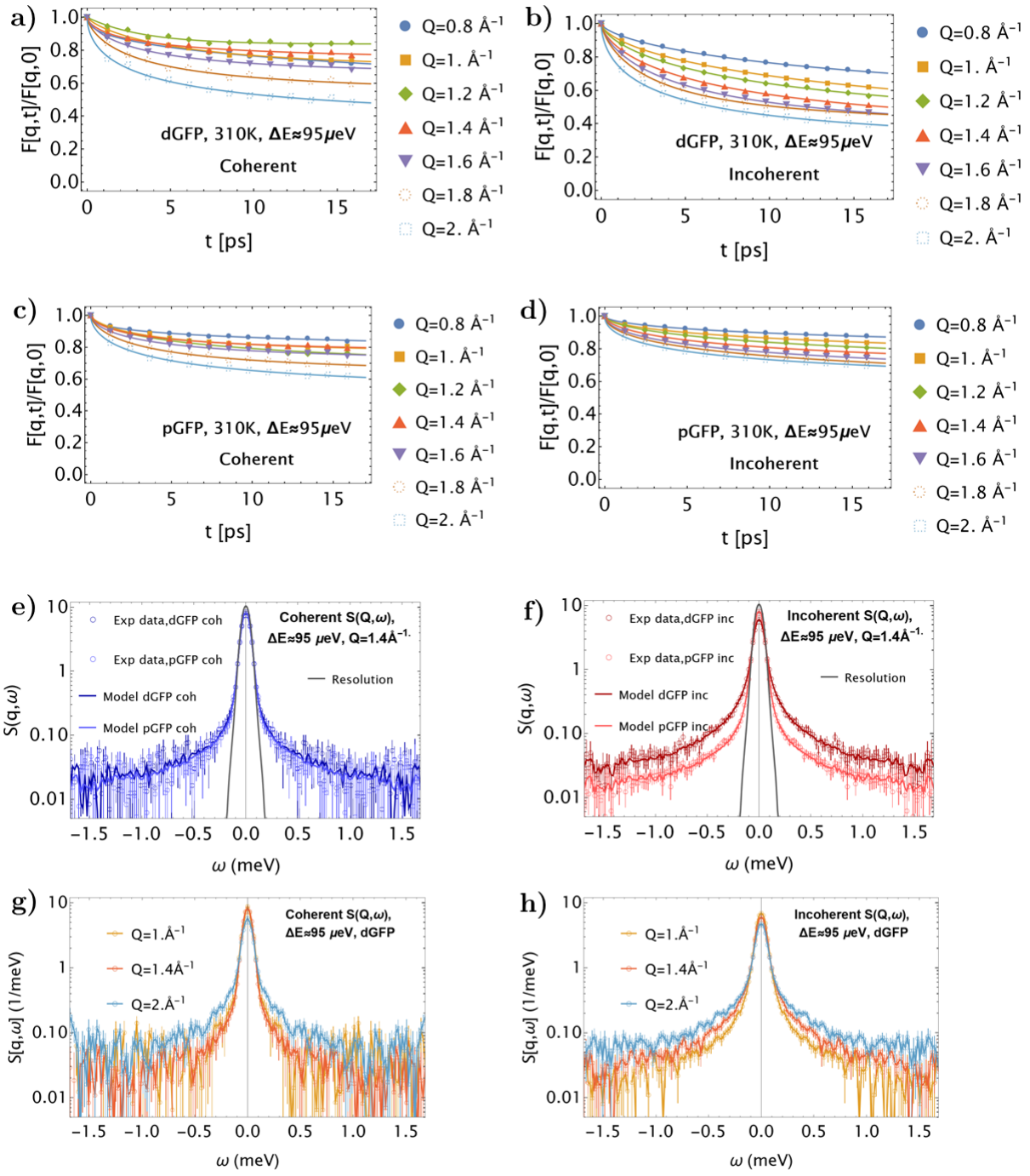

Figure 4-3: Scattering functions obtained on polarised LET, $\Delta E \approx 95\ \mu eV$ and $T = 310\ K$. (a) and (b) Experimental intermediate scattering function F(Q,t) for dGFP sample (markers) compared to the fitted model expressed in Equation 1-62 and Equation 1-59 (lines) for $Q \in [1, 2]$ Å^{-1}, for coherent and incoherent contributions respectively.
(c) and (d) Experimental (open dots) and modeled (lines) dynamical structure factors compared for dGFP (dark labels) and pGFP (light labels) in the case of coherent scattering [(c), blue] and incoherent scattering [(d), red] for $Q = 1.4$ Å^{-1}.

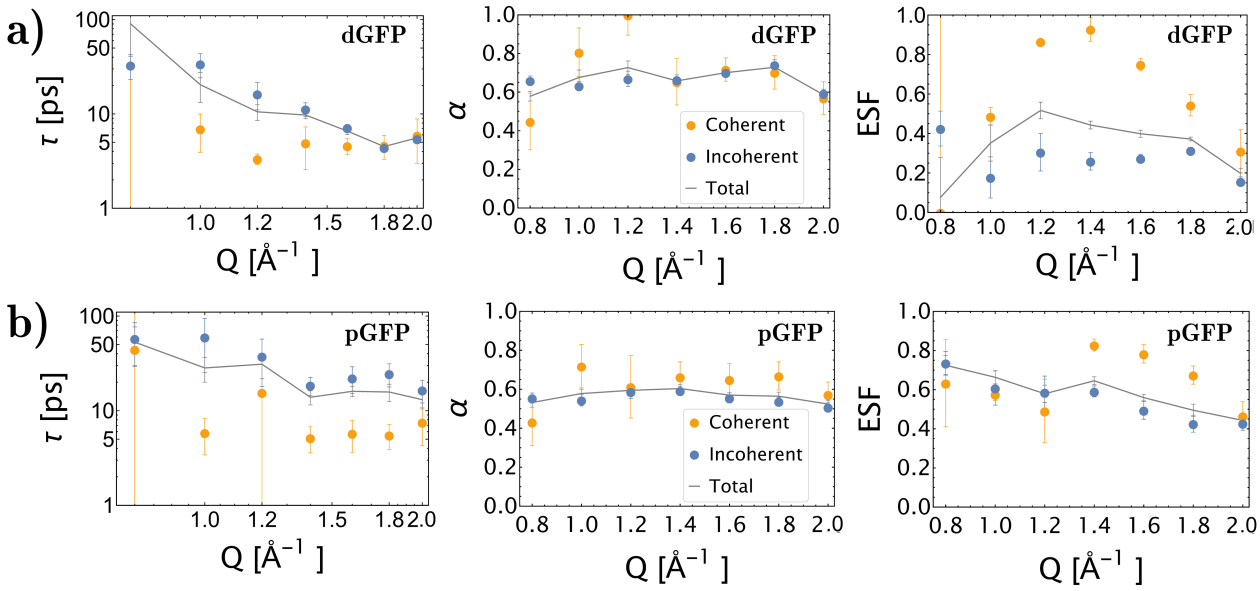

Figure 4-4: τ, α and ESF parameters for incoherent (blue dots), coherent (orange dots) and merged (gray lines) contributions on polarised LET at $T = 310$ K. (a) Parameters obtained for pGFP, (b) parameters obtained for dGFP.

intermediate function $F_{\text{inc}}(Q,t)$.

The same Fractional Brownian Dynamics model is used for the analysis of both incoherent and coherent scattering, described in section 1.4. Our relaxing dynamic variable is a function of both momentum transfer Q and the position operator $\hat{R}$, which is a self variable previously introduced for incoherent scattering Equation 1-60, and a collective variable for coherent or total scattering Equation 1-54.

Results from the model applied to LET data are presented in Figure 4-4 (a) and (b). It displays dynamic parameters for the separated and total (inc+coh) contributions. A few remarks beforehand are the very fast and more homogeneous dynamics of the coherent variable in comparison to the incoherent one, such that total scattering interpolates between both contributions as expected.

Finally, in order to check the validity of our results, we also verified that we experimentally obtained the following linear combination for ESF(Q) from EISF(Q) and ECSF(Q)

$$ESF(Q)_{\text{norm,exp,LET}} \approx \frac{S_{\text{coh}}(Q)}{S_{\text{tot}}(Q)} ECSF(Q)_{\text{norm,exp,LET}} + \frac{S_{\text{inc}}(Q)}{S_{\text{tot}}(Q)} EISF(Q)_{\text{norm,exp,LET}}, \tag{4-1}$$

This relationship is correct because we normalise the intermediate function $F(Q,t)$ before applying the model for all three contributions, $F_{\text{norm}}(Q,t) = F(Q,t)/S_{\text{tot}}(Q)$. Even replacing $S_{\text{coh}}(Q)/S_{\text{tot}}(Q)$ with $\sigma_{\text{coh}}/\sigma_{\text{tot}}$, is a good estimation, see Figure 4-5.

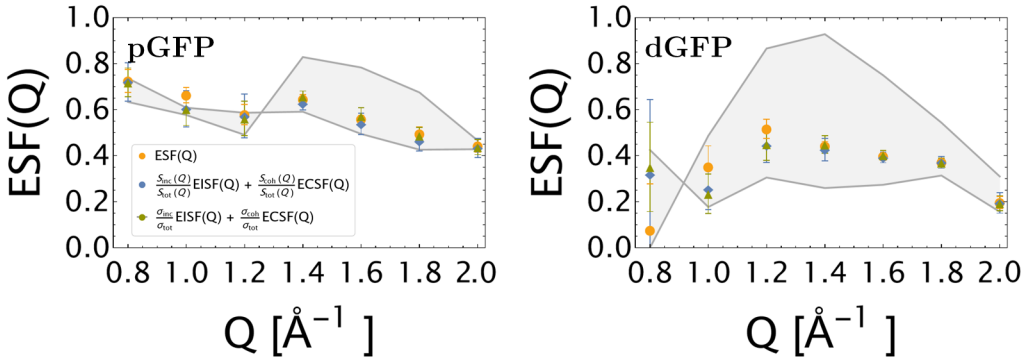

Figure 4-5: ESF parameters obtained for non polarised scattering on LET, merging incoherent and coherent data before fitting the model, are displayed in orange dots. The estimation of ESF from incoherent and coherent scattering follows Equation 4-1, using either the structureless ratio that can be estimated from scattering lengths ($\sigma_{\text{inc}}/\sigma_{\text{tot}}$, blue $\diamond$) or the exact Q-dependent ratio requiring polarised diffraction data ($S_{\text{inc}}(Q)/S_{\text{tot}}(Q)$, green $\triangle$). The gray enveloppe is a guide corresponding to values taken by incoherent and coherent parameters.

4.4 Incoherent quasielastic scattering of protonated and deuterated protein powders

Considering results presented in the last chapter, namely that 40% of hydration water has exchanged from D to H in both pGFP and dGFP, it is expected that incoherent quasielastic scattering for the deuterated protein is fairly impacted by hydration water's self-dynamics ($\sigma_{\text{inc,H}} = 80.3$ barns, $\sigma_{\text{inc,D}} = 2.05$ barns [23]) while it should be negligible for the protonated protein sample ($\sigma_{\text{inc,GFP}}/(\sigma_{\text{inc,D}_2\text{O}} + \sigma_{\text{inc,GFP}}) = 80$ %).

Incoherent dynamical parameters are directly compared on Figure 4-6. We first discuss the insights obtained from the relaxation timescale τ, indicating much faster relaxation for dGFP compared to pGFP. Locally at $Q = 2\text{Å}^{-1}$, we get $\tau_{\text{inc,dGFP}} = 5.5 \pm 0.6$ ps and $\tau_{\text{inc,pGFP}} = 17 \pm 4$ ps. On the one hand, H-bond network relaxation in hydration water is dependent on the H-bond lifetime that scales very close to $\tau_{\text{inc,dGFP}}(\approx 4\text{ps})$ for high Q/local motions, such that water molecules re-orientate at the pico-second time scale with

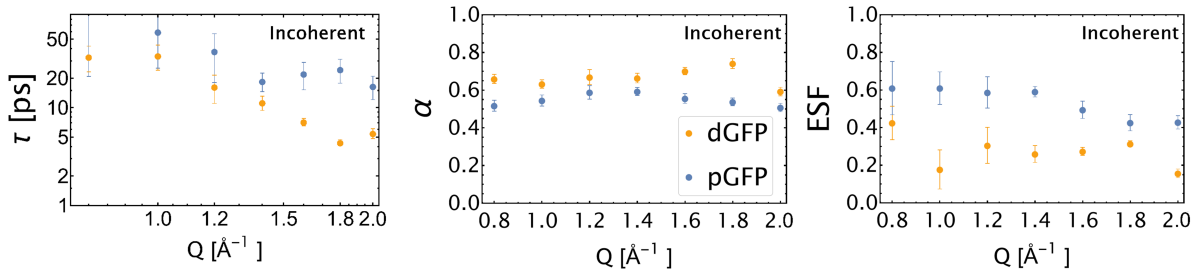

Figure 4-6: Dynamical parameters α , τ and ESF (Elastic Structure Factor) as a function of Q, obtained for the incoherent contribution of scattering for both dGFP (full orange circles) and pGFP (full blue circles) hydrated powders

large amplitude rotations after H-bond breaking. Regarding the time-window defined by our dynamical range ($t_{\max}$ = 16 ps) we shall mainly probe the fast and weakly coupled relaxations, for which Zhong et al [221, 223] report a 1 to 3 ratio for the protein dynamics relaxation time with respect to hydration water.[224, 56]. This is in agreement with the timescale obtained for pGFP if we hypothesize that mainly internal protein dynamics are probed in the protonated sample: on average we have $\tau_{\text{pGFP}}/\tau_{\text{dGFP}} \approx 3$. It rationalises both timescales obtained obtained for dGFP and pGFP, assigned to self-motions of hydrogen atoms in hydration water and the protein respectively. Although, we cannot rule-out minor presence of water dynamics in pGFP and especially the 414 exchanged hydrogens in dGFP.

Concerning parameter α, we expect internal powder-state GFP dynamics to reflect highly local motions of hydrogen nuclei in the residues as probed by Nickels et al [91] due to the rigidity of the protein brought by β-barrels [135], hence a very low heterogeneity parameter. We observe here that α almost does not depend on Q, such that $\alpha_{\text{inc,dGFP}} \approx \alpha_{\text{inc,pGFP}} + 0.12$, with $\alpha_{\text{inc,pGFP}} = 0.55 \pm 0.01$ and $\alpha_{\text{inc,dGFP}} = 0.67 \pm 0.01$. This is a non-negligible change in α parameter: for instance, inhibition of acetylcholynesterase has been reported to decrease α only by 0.05 on average [39]. Therefore, it supports the hypothesis of two very different contributions in dGFP and pGFP. Concerning the high heterogeneity factor of water, MD suggest a power-law tail distribution of reorientation times for the slowest molecules [81, 218] which entails strong retardation with respect to bulk-water [204], explaining discrepancy with incoherent scattering of bulk H_2O for which α is reported to decrease from 1 at large Q values down to 0.9 at $Q = 1$ Å^{-1} [197]. The difference in α parameters suggests that the quadratic potential in which the self-dynamic variable corresponding to H atoms diffuses is more rugged for the protein than for hydration water. This analyses is further developped in chapter 5.

Even the EISF is particularly low in dGFP compared to pGFP, such that dGFP self-variable is strongly decorrelated at $t \to \infty$, indicating large motional amplitude in the hydration shell. The low EISF is also the signature that H atoms in water overtake the signal, hence a reduced weight for slow deuterium dynamics of the protein. It explains that on average, $\text{EISF}_{\text{dGFP}} \approx 0.27 \pm 0.02$ while $\text{EISF}_{\text{pGFP}} = 0.55 \pm 0.02$: motional amplitude is reduced inside GFP because all H atoms are still not mobile at this timescale inside the protein.

To avoid any counter-argument, the slow and heterogeneous dynamics in pGFP compared to dGFP cannot likely be attributed to an "isotope effect" taking place in the protein internal dynamics. As mentioned earlier, effect of the protein perdeuteration on its dynamics is still under study and is highly dependent on the timescale and the protein under-consideration [187]. Indeed, even in a light system such as water, isotopic exchange only induces a $D_{\text{D}_2\text{O}}/D_{\text{H}_2\text{O}} \approx 1.2$ ratio for the translational diffusion coefficient D at 310 K [225, 226, 227], and this isotope effect remains below 1.15 in many liquids for both rotational and translational diffusion [228].

It is thus reasonable to admit that ps-scale local self-dynamics of a deuterated protein are highly sensitive to exchanges occuring in the hydration layer, while a protonated protein is almost not affected and still is a probe for protein internal motions.

Validation of our results with literature Table 4-I compares incoherent dynamical parameters obtained in literature from protein powders ($h \approx 0.4$) studied with models accounting for the stretching of the relaxation function (embedded by parameter β) with timescale τ(Q) at $T \approx 300$ K. It gathers parameters assigned to H_2O relaxation ($\beta_{\text{H}_2\text{O}}$ and $\tau_{\text{H}_2\text{O}}$) and to the slow process usually assigned to protein relaxation coupled to water motions (β_{protein} and τ_{protein}). Methyl group rotations are calculated separately in dry proteins in Ref. [229, 134] and provide a typical timescale of motions τ centered on $60 - 80$ ps.

Parameters do not all corroborate, however they all point towards a lower heterogeneity for hydration water $\beta_{\text{H}_2\text{O}} \approx 0.6$ compared to the protein itself $\beta_{\text{protein}} \approx 0.3$. On the other hand, timescales are highly dependent on the FWHM of the resolution function, but provide the insight that for $\Delta E \approx 100$ μeV, hydration water relaxes faster, $\tau_{\text{H}_2\text{O}} \approx 10$ ps, than protein side chains and backbone $\tau_{\text{protein}} \approx 30$ps.

It is in correspondence with our own results presented in the gray column, where $H_2O \equiv$dGFP and protein$\equiv$pGFP. Weaker stretching for the protein sample in literature might arise from non-negligible signature of water in the incoherent scattering of pGFP (increasing our α parameter), or simply from the ML model.

Table 4-I: Comparison of incoherent dynamical parameters obtained for dGFP (hydration water) and pGFP (hydrated protein) on LET, gray column, with data from litterature. Extracted parameters have been chosen considering similar hydration and temeprature, and for the use of similar models adapted to anomalous diffusion. We report here the corresponding stretching parameter β and the dynamical timescale τ.

Protein type[1]		GFP [204, 134, 91]	hAChE [88]	Mgb [178]	LYS,[229]	hAChE [230]	LYS [231, 232]	LYS [233]	LYS [234]	Snase [235]	GFP, LET
Hydration (g protein/g D_2O)		$h = 0.4$	$h = 0.4$	$h = 0.5$	$h = 0.4$	$h = 0.4$	$h = 0.4$	$h = 0.3$	$h = 0.3$	$h = 0.4$	$h = 0.4$
FWHM (μeV)			90	17.5	1	90	34	140	0.8	106	90
Temperature (K)			300	310	295	300	295	300	270	300	310
Model[2]		C-D (≡KWW)	KWW	KWW (2)	KWW	ML	C-C (≡ML)	KWW	RCM	KWW	ML
Hydration water [3]	β_{H_2O}	0.6	0.44	0.8					0.9	0.44	0.67 ± 0.01
	τ_{H_2O}	$\tau_{Q=1Å^{-1}} =$ 40−50 ps, $\tau_{Q=2Å^{-1}} =$ 10 ps	12.1 ps	$\tau_{Q=1Å^{-1}} =$ 14 ps, $\tau_{Q=2Å^{-1}} =$ 8 ps					50 ps	12.1 ps	$\tau_{Q=1Å^{-1}} =$ 34 ± 10 ps, $\tau_{Q=2Å^{-1}} =$ 5.5 ± 0.6 ps
Hydrated protein powder: localised dynamics (water-coupled)	$\beta_{protein}$	$0.2 - 0.4$	0.3	0.38	0.2	$0.5 - 0.6$	0.3	$0.2 - 0.3$			0.55 ± 0.01
	$\tau_{protein}$	15−50 ps	300 ps	3.7 ns	50 ps	$\tau_{Q=1Å^{-1}} =$ 12ps, $\tau_{Q=1.6Å^{-1}} =$ 4 ps	25 ps				$\tau_{Q=1Å^{-1}} =$ 60 ± 35ps, $\tau_{Q=2Å^{-1}} =$ 17 ± 4 ps

[1] hAChE stands for acetylcholinesterase, Mg for myoglobin, LYZ stand for lysozyme, Snase for Staphylococcal nuclease

[2] CC stands for Cole-Cole, C-D for Cole-Davidson, KWW for Kolrausch-William-Watts, ML for Mittag Leffler

[3] As a mean of comparison, bulk water stretching factor is reported $\approx 0.7 - 0.9$, while $\tau_{Q=1Å^{-1}} < 8$ps, $\tau_{Q=1Å^{-1}} \approx 1$ ps [204, 235, 197].

Hence, the relaxation observed in pGFP seems to correspond to the slow and localised [91] water-coupled side chain motions previously observed in proteins, while dGFP undergoes similar dynamics as H_2O hydration water. This insight is pushed forward noticing that Ref. [229, 233] mention a Q-independent τ for protein internal motions, as we also observe within error-bars for $Q > 1.2$ Å^{-1} in pGFP, see Figure 4-6. Furthermore, in Ref. [204], GFP H_2O hydration water τ follows a power law $\tau(Q) \propto Q^{-2.5}$. We also find a power law, $\tau_{H_2O}(Q) \propto Q^{-3.3}$ for $Q \geq 1$ Å^{-1} with dGFP.

4.5 Coherent dynamics in proteins at the picosecond timescale are overtaken by hydration water dynamics

4.5.1 Coherent scattering of a protein powder at the ps-scale

While incoherent scattering favours the visibility of hydrogens and to a lower extent deuteriums, all nuclei are weighted similarly in coherent scattering [23]. Therefore, reasoning from a "static" point of view, a large contribution from the protein itself is expected in the coherent channel, as exposed in the previous chapter, Figure 3-1. This figure also shows that the nucleus-specific contributions in coherent scattering is supposedly minor upon D→H.

However, τ coherent parameter unravels much faster dynamics than was observed for incoherent scattering, see Figure 4-4 (c) ($Q = 1.2$ Å^{-1} is an outlier that could not be fitted correctly in both pGFP and dGFP). Furthermore, parameters are almost identical within error bars for pGFP and dGFP with $\tau_{coh} \approx 5$ ps and $\alpha_{coh} \approx 0.65$, see Figure 4-7. The timescale is much faster than self-dynamics of hydrogen atoms ($\tau_{inc} \approx 30$ ps) in sidechains of the protein, as seen from incoherent scattering in pGFP. Furthermore, we expect slower dynamics from heavier atoms -C,O,N,S- in the backbone as reviewed in Ref.[236]: it is clear that the impact of internal protein motions arising from heavy atoms in the coherent signal is negligible. Instead, τ_{coh} corresponds to the timescales found for local collective re-orientations of the H-bond network in hydration water by Zhang et al [221, 223], favouring the hypothesis of a strongly visible hydration water. Therefore, the dynamics probed by neutrons stems from structural relaxation in hydration water, involving both oxygen and hydrogen isotopes. One important conclusion is that it seems unfeasible to probe

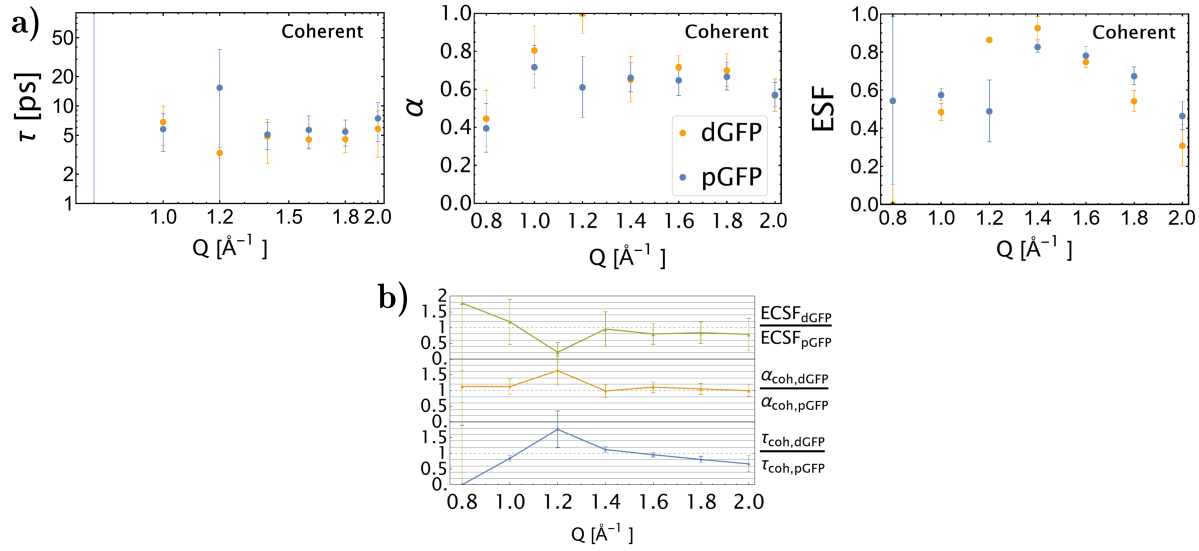

Figure 4-7: (a) Dynamical parameters α, τ and ESF (Elastic Structure Factor) as a function of Q, obtained for the coherent contribution of scattering for both dGFP (full orange circles) and pGFP (full blue circles) hydrated powders. b) Ratios of dynamical parameters for the coherent contribution, obtained for dGFP and pGFP.

the protein collective dynamics on this timescale due to the presence of fast water nuclei, even stemming from deuterium inside the protein. Concerning heavier nuclei in the protein, these contributions appear static, as observed from the high ECSF: a large amount (1/3 of all nuclei) of immobile heavy atoms are invisible to incoherent scattering due to their low cross-sections, but are visible to coherent scattering. However their motions are too slow with respect to the resolution of the instrument, hence the signal remains in the elastic region. Therefore, it explains the strong discrepancy in both incoherent and coherent ESF(Q). Hence, considering ranges of motions of the protein with respect to its hydration water as featured in Figure 4-2, it is paramount to work with a higher energy resolution verifying $t \gg 100ps$ to avoid any contributions from water dynamics.

Furthermore, we also observe the merge of incoherent and coherent timescales of motions in dGFP [32], [Figure 4-8, (c)] at short distances in the range of nearest-neighbours distances when $Q \geq 1.4$ Å^{-1}, comforting the interpretation that both contributions arise from hydration water. This merge is also observed by Arbe et al in bulk D_2O. Hence, we can characterize the confinement effect of hydration water with respect to bulk water, with a collective retardation factor $\xi_{D_2O,\,coh}$ for D_2O.

$$\xi_{D_2O,\,coh} = \frac{\tau_{D_2O,hydr,coh}}{\tau_{D_2O,bulk,coh}} \approx 2.5, \tag{4-2}$$

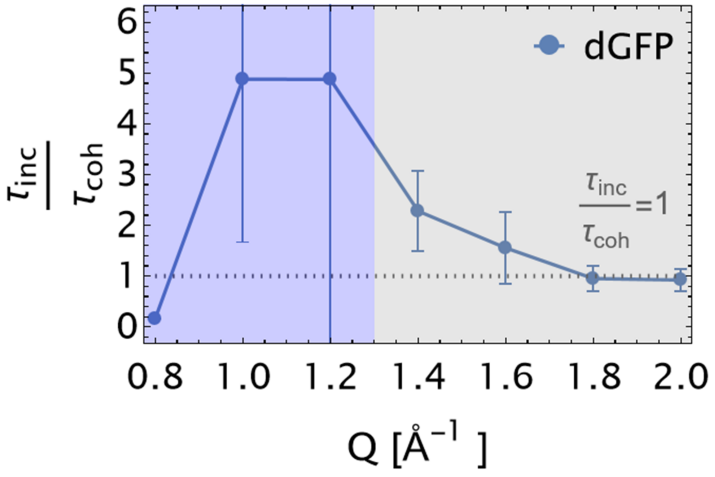

Figure 4-8: $\frac{\tau_{inc}(Q)}{\tau_{coh}(Q)}$ ratio, dGFP. The gray area indicates the region where both timescales merge. Lines are only displayed to join data points.

which is scale-free, contrary to the Q-dependent incoherent retardation factor $\xi_{H_2O,\,inc}$ obtained for H_2O in GFP [203] which strongly decreases with Q. $\tau_{D_2O,bulk,coh}$ is extracted from [32] and $\tau_{D_2O,hydr,coh}$ corresponds either to pGFP or dGFP τ_{coh} parameter. The same magnitude $\xi \approx 2.5$ for self ($\xi_{H_2O,\,inc}$)[203] and collective ($\xi_{D_2O,\,coh}$) retardation factors is recovered at higher Q values. However, our comparison of bulk and hydrated water dynamics has limits, due to our model corresponding to a wide-spread distribution of exponential relaxations, in comparison to the bi-exponential relaxation proposed by Arbe et al.

4.5.2 Explanations for the Q-independent mode

Then, how can we explain the Q-independence of the timescale of motions, which seems to be a feature of collective motions ? Indeed, it has not been observed with our model for incoherent scattering either in protein powders [39], protein solutions [39, 42] or confined water in clays [237] where τ decreases with Q.

First and foremost, as introduced in section 1.5, this Q-independent mode has been evidenced in bulk D_2O by Arbe and collaborators with polarised neutrons scattering experiments and molecular dynamics simulations of coherent neutron scattering [113, 32] and further with Van der Waals liquids [112]. It has been assigned to a mode that they identify with the local H-bond network relaxation due to forming and breaking of H-bonds [32], which is visible in coherent scattering at intermediate length scales. In section 1.5 we mentioned that they rationalize this behaviour showing that in D_2O, the diffusive term

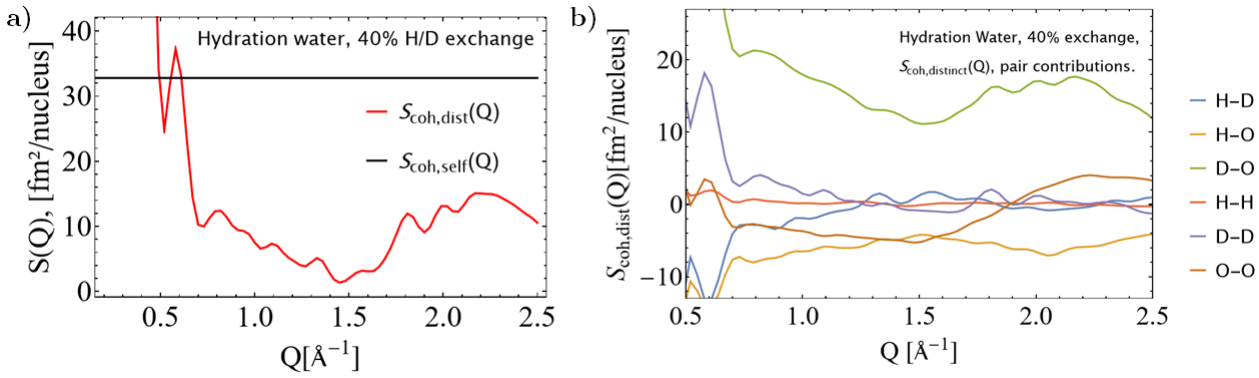

Figure 4-9: a) Coherent static structure factor calculated for hydration water (40% D→H exchange) expressed in fm^2/nucleus, separated into its distinct part (red) and self part (black). b) Separations of the distinct structure factor into contributions from pairs of atoms, into HD (blue), HO (orange), DO (green), HH (red), DO (purple) and OO (brown).

contained in both the self and distinct partial dynamical structure factors bear opposite signs until $Q \approx 1.5$Å^{-1} (nearest neighbours distances), explaining the Q-independence of the coherent relaxation time. Above this threshold, strong correlations arise in the dynamic structure factors, such that diffusive terms do not vanish anymore.

In order to perform a similar study, MD simulations are required to yield the self and distinct coherent dynamic structure factors of the system. However, in Arbe et al work, the distinct and self coherent static structure factors, bearing opposite signs, also display a signature of this cancellation. We have performed this separation in our calculations of the hydration water of GFP in the case of 40% of D→H exchange, yet we do not observe such a cancellation of the self and distinct terms of our coherent static structure factor, see Figure 4-9 (a), that could point towards a similar explanation. However, Figure 4-9 (a) shows that the distinct coherent static structure factor is non-negligible, especially for the D-O pair of nuclei [Figure 4-9 (b)]. It explains that we do have strong discrepancy between dynamical parameters for self (incoherent) aFfor nd distinct scattering of water, hence a signature of "purely" collective motions in water in the sample.

Otherwise, this Q-independent timescale of motions has been observed in colloidal and polymeric systems at sufficiently small Q values, in the form of relaxation functions $\langle\hat{\chi}(Q,0)^{\dagger}\hat{\chi}(Q,t)\rangle/\langle\hat{\chi}(Q,0)^{\dagger}\hat{\chi}(Q,0)\rangle$ superposed over Q ($\hat{\chi}(Q,t)$ is the collective dynamic variable defined in Equation 1-54). Handle et al evidenced with MD simulations that it is a general feature of slowly-relaxing systems with a Q-independent memory function [238]. Although $Q = 1.2$ Å^{-1} remains an outlier, we almost observe a superposition of coherent relaxation functions for pGFP and dGFP, see Figure 4-10 (b) and (d), as opposed to incoherent relaxation functions which are typical of diffusive motions. For $Q = 2$ Å^{-1}

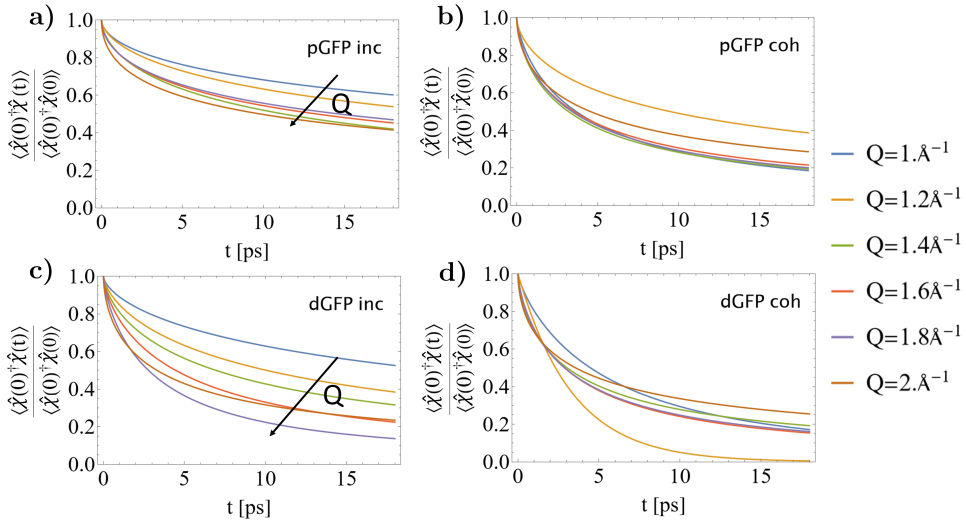

Figure 4-10: Relaxation function $\phi(t) = \langle\hat{\chi}(Q,0)^\dagger\hat{\chi}(Q,t)\rangle/\langle\hat{\chi}(Q,0)^\dagger\hat{\chi}(Q,0)\rangle$ displayed for incoherent scattering [pGFP (a), dGFP (c)] and coherent scattering [pGFP (b), dGFP (d)] obtained on LET, $\Delta E = 95\mu$eV, $T = 300$K.

where diffusive and collective timescales merge in dGFP Figure 4-8, the superposition does not hold anymore. It is paramount to notice that their studies highlight that this mode occurs for t large enough ($> 1 - 10$ ps) but they only study $Q \leq 0.3$ Å^{-1}. For bulk water the Q independent mode sustains until $Q = 1.5$ Å^{-1} as observed by Alvarez et al [32], and seems to be preserved for larger Q values ($Q < 2$ Å^{-1}) in our case for hydration water, probably due to confinement.

We are still left with open questions concerning an explanation for this Q-dependent mode. Let us just mention a nice microscopic approach proposed by Nava et al [239], showing that beads in a 1D network submitted to harmonic potential applied by its direct neighbours will present a Q-independent relaxation if the stiffness k reversibly changes from a value k_1 to k_2 verifying $k_1 < k_2$, with a characteristic time Γ^{-1}. It models a topological relaxation of the network with elastic fluctuations. The Q independent mode with timescale τ_0 arises from k fluctuations. Furthermore, in the presence of viscous flow, a cross-over from the Q-independent to a Q-dependent mode occurs when the slow viscoelastic time $\tau_e \propto Q^{-2}$ [both dependent on viscosity and the average of elastic moduli $(k_1 + k_2)/2$] approaches Γ^{-1} for Q large enough. In that case it raises $\tau_0 = \Gamma^{-1}$, which is reminiscent of our Q-independent mode having a relaxation time close to the H-bond lifetime which governs the local stiffness. Basically, it means that elastic relaxation arises without mass transport for Q small enough.

Presence of a De Gennes narrowing ? Eventually, we do not observe any scaling of τ with $S(Q)$ that could be assigned to a De Gennes narrowing [103]. This principle based on sum-rules formulates the increase of the relaxation timescale due to increased space correlations around the main diffraction peak. It has been observed for complex systems with heterogeneous dynamics (glass-forming liquids [240, 241, 112], inter-domain motions in proteins. [4]), however not in D_2O [32]. Nevertheless, let us notice that the heterogeneity parameter α and more convincingly the Elastic Coherent Structure Factor (ECSF) follow the trend of S(Q) where structural correlations are maximal around $Q = 1.4$ Å^{-1}. This has been observed in glass-forming liquids, see Ref.[242], and this is a direct expression of the impact of structure in collective processes.

In conclusion, coherent scattering of a protein powder at the ps time scale is strongly overtaken by confined heavy-water fast collective dynamics, which display a Q-independent relaxation time as already observed in bulk D_2O with polarisation analysis.

4.6 The significance of using a polarised beam for the study of proteins

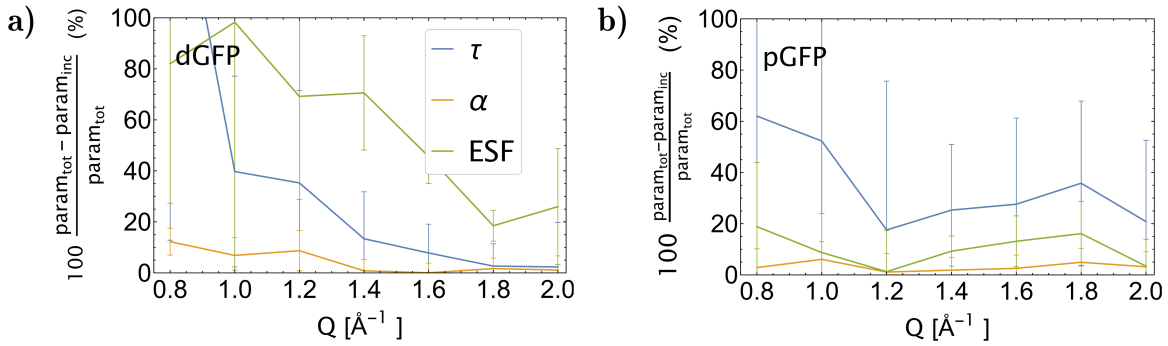

Figure 4-11: Relative gaps for dynamical parameters τ (blue), α (orange line) and ESF (green line) as a function of Q, corresponding to the error made using a non-polarised beam (inc+coh) compared to polarised incoherent scattering.

Figure 4-11 (a) expresses the error made not using a polarised beam when assessing self-diffusion.

- The gap for the protonated protein is due to the fast pico-second fluctuations of the collective motions of the hydrogen-bond network of water entering the scattering signal from the coherent contribution. It artificially decreases the relaxation

timescale for the slow and heterogeneous self-dynamics of proteins. It therefore mainly impacts τ (in blue) by about 30%, but it leaves α (in orange) and the ESF (in green) almost identical ($\leq 5\%$ and $\leq 10\%$).

- The impact of collective dynamics on total scattering is more important for the deuterated protein. The ESF is poorly estimated on the whole Q range, whereas τ is almost retrieved at higher Q. α is subject to an error below 10%. The question still remains for the error made on a deuterated protein in D_20 if no D→H exchange occurs: incoherent scattering would certainly be negligible and lead to strong errors.

Therefore, for both samples it implies a systematic underestimation of the timescale of motions and overestimation of the heterogeneity in the sample, while the impact on the asymptotic regime is less measurable. For pGFP, the error performed on the ESF is close to 10% as already observed in protonated or partially deuterated polymers [243, 28], while it is the parameter that depends the most on polarisation analysis for dGFP due to the presence of heavy scatterers in coherent scattering.
At $Q = 0.8$ Å^{-1} the trend seems to exchange suddenly in both samples, with a strong increase of coherent time scales and decrease of heterogeneity. However, statistics are not good enough to infer if it is due to the entrance of protein motions at larger scales.

With respect to literature, the impact of coherent scattering on non polarised scattering had already been estimated experimentally with pyridinium-based ionic liquid [BuPy][Tf2N], and with MD simulations on lysozyme protein [244]. Both coherent and incoherent MD simulations were performed by Matsuo [244] on lysozyme, analyzing internal localised motions with a jump-diffusion model (similar conditions: $\Delta t = 77\ \mu eV, t_{\max} = 50$ ps, 4 free parameters + background). Analyzing the protein motions only (hydration water is dismissed for model fitting) raises a maximum 6% of discrepancy in incoherent and total dynamical parameters. Therefore, it seems that hydration water plays a strong role in widening the gap between incoherent and total scattering in experiments although the protein itself plays a role.
Polarisation analysis on ionic liquids by Burankova et al [106] (D7 TOF, $\Delta E = 140\mu$eV) succesfully observed an underestimation of the global and localised incoherent diffusion coefficient (hence, an over-estimation of motions timescales) without polarisation, but unchanged ESF. This is in opposition to our findings in proteins and hydration water, and highlights that there is no common and systematic effects in hydrogen-rich samples.

4.7 Conclusion

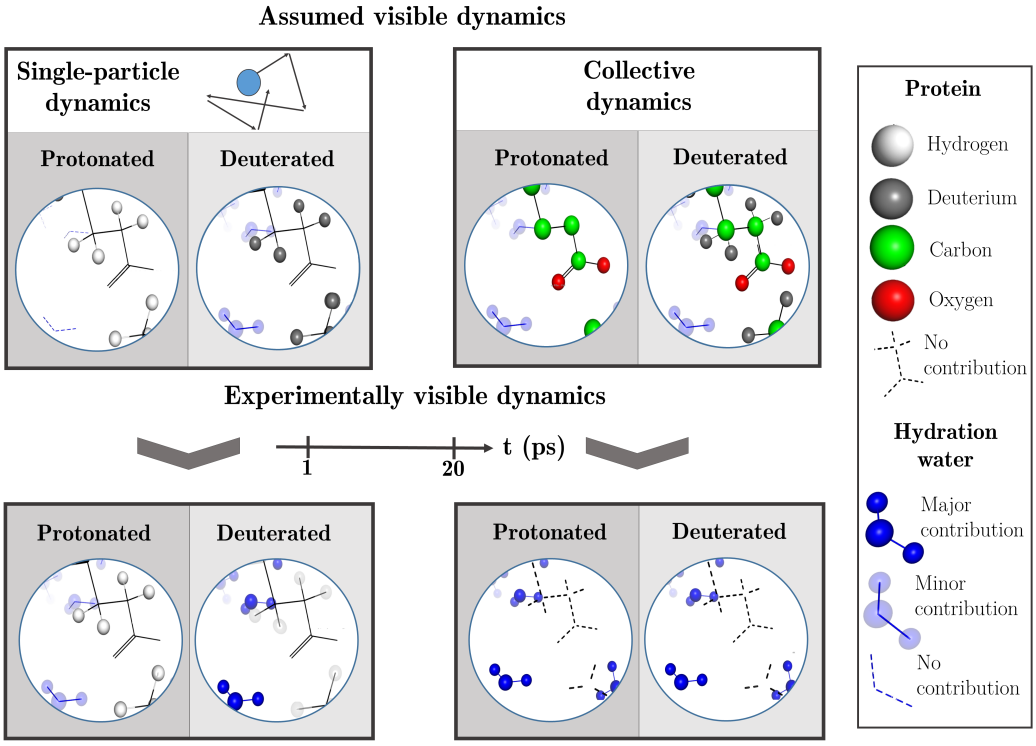

Figure 4-12: a) and b) Relative gaps for dynamic parameters τ (blue), α (orange line) and ESF (green line) as a function of Q, corresponding to the error made using a non-polarized beam (inc+coh) compared to polarized incoherent scattering, for pGFP (a) and dGFP (b).
c) Dynamics expected to prevail in the sample using usual self cross section arguments (Equation 3-1 and Equation 3-2) are displayed in the upper panel and divided into incoherent (self) dynamics and coherent (collective) dynamics. Opacity identifies which species or atoms provide major contributions, while transparency and dashes express minor and non existent contributions respectively, see the chart on the right. Colours designate different atomic types. The lower panel maps the effective dynamics that prevail in the sample, as analyzed from polarized neutron scattering for $t \in [1, 16]$ ps and $Q \geq 1\text{Å}^{-1}$. The figure is produced with Pymol software [245] with a 4 Å diameter focus on GLU34.

We show in this study how critical D→H exchange is for incoherent scattering in a deuterated protein, almost deleting any signature from the protein itself in favour of water molecules. It contrasts with the little impact it has on a protonated protein. This is illustrated on the left pannel of Figure 4-12.

On the other hand, we demonstrated that dynamics in a hydrated protein powder, both protonated and deuterated and probed at the picosecond timescale, is highly contaminated by the fast collective motions of the heavy-water D-bond network, to the point that the protein seems invisible, see the right pannel of Figure 4-12. This is all the more unexpected, since dGFP hydration water represents only 26% of coherent scattering if we

estimate its contribution from scattering lengths with the formula introduced in chapter 1, Equation 3-1.

Although the intensity of coherent scattering is low compared to incoherent scattering, it implies a non-negligible discrepancy with scattering from an unpolarised beam due to the difference in timescales of water and protein dynamics. Hence, eventhough deuteration of the hydration layer is used in principle for the purpose of enhancing the protein's dynamics against its solvent for incoherent scattering, its impact unexpectedly arises from coherent scattering.

It puts into perspective the momentum and energy scale relevance of deuteration as a contrast tool for neutron scattering. Water dynamics should mainly be present in the time scale below 100ps where water motions are non-negligible. It also questions using sole ratios of coherent and incoherent atomic cross sections, which is an argument that holds for "static" studies such as diffraction, to deduce which parts of the sample will be highlighted in case of energy-dependent neutron scattering experiments. Hence, spanning towards slower relaxation times with increasing resolution should modify the relative impact of the solvent on the dynamics.

Our insights might be extended to the impact of collective water dynamics in a protein solution as well, for which the Q-dependent retarded first hydration layer cannot be subtracted from a bulk-water spectrum. Moreover, the impact of coherent scattering on the total signal shall increase at lower Q-scales where the coherent fraction of scattering is preponderant due to water-protein and protein-protein correlations [33], raising the question of the choice of the Q range to avoid prominent contamination from coherent scattering, espacially on backscattering instruments reaching lower than $Q = 0.4$ Å^{-1}.

We want to point out that our results may vary with secondary structure: the latter has a global impact on the elastic modulus of the protein, such that α helices and loops provide a smaller global Young Modulus ($\approx$ 7 GPa for myoglobin) than rigid beta sheets and especially barrels ($\approx$ 12 GPa for GFP, closer to the values confered to solid-state materials) as probed by Brillouin scattering and QENS [135].

CHAPTER 5

Understand conventional QENS studies in the light of polarised QENS

5.1 Introduction

Polarisation analysis is currently available on very few Time-Of-Flight spectrometers (LET at ISIS, D7 at ILL, HYSPEC at SNS, MACS at NIST...), and do not permit casual polarised QENS experiments. Furthermore, accessible Q ranges are narrow due to instrumental limitations, and the flux is strongly reduced with the polarisation analysis set-up, which makes it tricky to analyse high resolution data. It is therefore paramount to make sure that the model raises similar results on standard instruments to infer general properties from systematic polarised QENS experiments. For this purpose we compare the dynamics of dGFP and pGFP obtained on IN5 spectrometer, $\Delta E = 80$ and on to LET polarised neutrons spectrometer, $\Delta E = 90$, on similar dynamical ranges.

5.2 Comparison of unpolarised and polarised QENS

5.2.1 Estimate D→H exchange in a non-polarised sample from polarised diffraction data

A prerequisite to our study is to verify whether exchange has occurred similarly during unpolarised neutron scattering experiments on IN5 in the water layer of dGFP . As exposed in previous chapters, the ratio $S_{\text{inc}}(Q)/S_{\text{tot}}(Q)$ is an estimator of hydration exchange. However this information is not directly available on IN5, but can be approximated using diffraction data from D7, IN12 and LET. For this purpose, we express IN5 normalised static structure factor $S^{\text{IN5}}_{\text{tot,norm}}(Q)$ as a linear combination of a flat normalised incoherent structure factor $S^{\text{IN5}}_{\text{inc,norm}}(Q) = 1$ and a normalised coherent structure factor obtained with polarisation analysis (pol), $S^{\text{pol}}_{\text{coh,norm}}(Q) = S^{D7/IN12/LET}_{\text{coh,norm}}(Q)$. The three structure factors are normalised to verify :

$$\lim_{Q\to\infty} S(Q) \approx \overline{S(Q)} \approx 1. \tag{5-1}$$

Where the overline stands for Q average over $[0.6, 2.1]\text{Å}^{-1}$, since our Q range does not extend far enough to extrapolate a limit for $Q \to \infty$. We estimate the experimental coherent structure factor with $S^{\text{pol}}_{\text{coh}}(Q) = \left(I^{\text{pol}}_{\text{coh}}(Q)/I^{\text{pol}}_{\text{inc}}(Q)\right)$, Materials and Methods Equation 2-18 The model for the total structure factor of IN5 is expressed in Equation 5-2.

$$\begin{aligned} \left(\frac{\partial\sigma_{\text{tot}}}{\partial\Omega}\right) &= \left(\frac{\partial\sigma_{\text{inc}}}{\partial\Omega}\right) + \left(\frac{\partial\sigma_{\text{coh}}}{\partial\Omega}\right) \\ \implies S^{\text{IN5}}_{\text{tot,norm}}(Q) &= \left(\frac{\sigma_{\text{inc}}}{\sigma_{\text{tot}}}\right)^{\text{IN5,fit}} + \left(\frac{\sigma_{\text{coh}}}{\sigma_{tot}}\right)^{\text{IN5,fit}} S^{\text{pol}}_{\text{coh,norm}}(Q), \end{aligned} \tag{5-2}$$

where $\left(\frac{\sigma_{\text{inc}}}{\sigma_{tot}}\right)^{\text{IN5,fit}}$ is a free parameter verifying $\left(\frac{\sigma_{\text{inc}}}{\sigma_{tot}}\right)^{\text{IN5,fit}} + \left(\frac{\sigma_{\text{coh}}}{\sigma_{\text{tot}}}\right)^{\text{IN5,fit}} = 1$. Equation 5-1 implies

$$\left(\frac{\sigma_{\text{inc}}}{\sigma_{tot}}\right)^{\text{IN5,fit}} \approx \lim_{Q\to\infty} \frac{S_{inc}(Q)}{S_{tot}(Q)}^{\text{IN5}}. \tag{5-3}$$

The ratios obtained from this method are presented for each instrument in Table 5-I, and the quality of the fits can be assessed from Figure 5-1. The ratio obtained with IN5 is similar to the ones obtained for LET, D7 and IN12 ($\lim_{Q\to\infty} \frac{S_{\text{inc}}(Q)}{S_{\text{tot}}(Q)} \approx 0.7$). As a comparison, the expectation based on cross sections when no exchange occurs is $\lim_{Q\to\infty} \frac{S_{\text{inc}}(Q)}{S_{\text{tot}}(Q)} = 0.46$. The Chi-squared goodness of fit compares IN5 data with the model such that

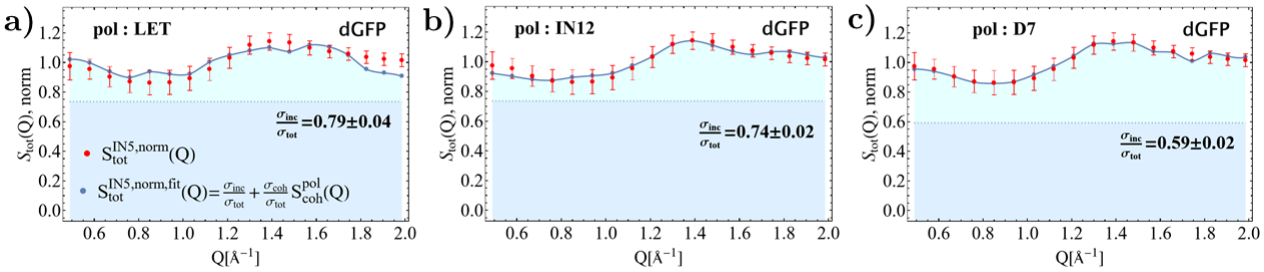

Figure 5-1: Comparison of IN5 normalised total structure factor $S_{\text{tot}}^{\text{IN5,norm}}(Q)$ (red dots) to the model expressed in Equation 5-2 (blue line), performed with coherent structure factors obtained on LET, IN12 and D7. The filled dark blue area illustrates the ratio of incoherent over coherent scattering cross sections obtained with the model.

Table 5-I: Comparison of ratios of incoherent over total structure factors obtained on IN5 and for polarised neutrons experiments.

$\lim_{Q\to\infty} \frac{S_{inc}(Q)}{S_{tot}(Q)}^{\text{IN5}}$ [1]	LET fit	D7 fit	IN12 fit
	0.79	0.59	0.74
$\lim_{Q\to\infty} \frac{S_{inc}(Q)}{S_{tot}(Q)}^{\text{pol}}$ [2]	LET	D7	IN12
	0.74	0.76	0.76

[1] IN5 ratio of incoherent over total S(Q). Expressed from Equation 5-2 and Equation 5-3.

[2] Ratio of incoherent over total S(Q) obtained in polarised experiments.

$$\chi^2 = \sum_{i\in Q} \frac{(S(Q_i)_{\text{IN5}} - S(Q_i)_{\text{IN5,fit}})}{\sigma(Q_i)^2_{\text{IN5}}}, \tag{5-4}$$

where the uncertainty on IN5 data, $\sigma(Q)_{\text{IN5}}$, should compare to the residues such that $\chi^2 \leq N$ where $N = 18$ is the number of Q points, which is the case for all instruments. We get $\chi^2_{\text{LET}} = 20.6$, $\chi^2_{\text{D7}} = 2.86$ and $\chi^2_{\text{IN12}} = 3.5$

Therefore, although IN5 experiment was performed right after sample production, it underwent the same exchange phenomenon. D7 data is most accurate to minimize the sum of squared residues, indicating that at least 30% of water has exchanged.

5.2.2 Comparison of unpolarised and polarised QENS from similar TOF instruments. $\Delta E_{\mathbf{IN5}} = 70\ \mu\mathbf{eV}$, $\Delta E_{\mathbf{LET}} = 95\ \mu\mathbf{eV}$

In this section, we compare the scattering functions and fitted parameters acquired with two TOF spectrometers with similar characteristics, summed-up in Table 5-II. For that, incoherent and coherent contributions have been summed for LET.

We chose similar binnings along the energy range, in order to have a dozen data points in the resolution function. We cut the Fourier-transformed spectrum at $t = t_{\text{res}} = 2\pi/\omega_{res}$ for IN5, and $t = 0.7\ t_{\text{res}}$ for LET.

Table 5-II: Characteristics of instruments and data reduction performed on both IN5 and LET instrument, ensuring good comparison between the two data-sets.

	IN5	LET
Energy resolution (μeV)	70	95
Energy Binning (meV)	0.02	0.02
t_{max} (ps)	16	28.5
Δt (=t_{min}) (ps)	1.2	1.2
Q [Å^{-1}]	[0.8,2]	[0.6,2.2]
Q binning [Å^{-1}]	0.1	0.2

At first sight, strong discrepancies are observable in $S(Q,\omega)$ [Figure 5-2 (a)] and $F(Q,t)$ [Figure 5-2 (b)] between both instruments. It is the case for both samples, on the whole energy range.

The corresponding fitting parameters are exposed in Figure 5-3. For the sake of comparison, IN5 data Q range was cropped for $Q < 0.6\ \mathring{A}^{-1}$, smaller Q values are available on Figure 6-6. dGFP parameters corroborate on both instruments and pGFP parameters are completely at odds, which is unexpected from raw scattering functions. Discussion is carried out for the two samples separately.

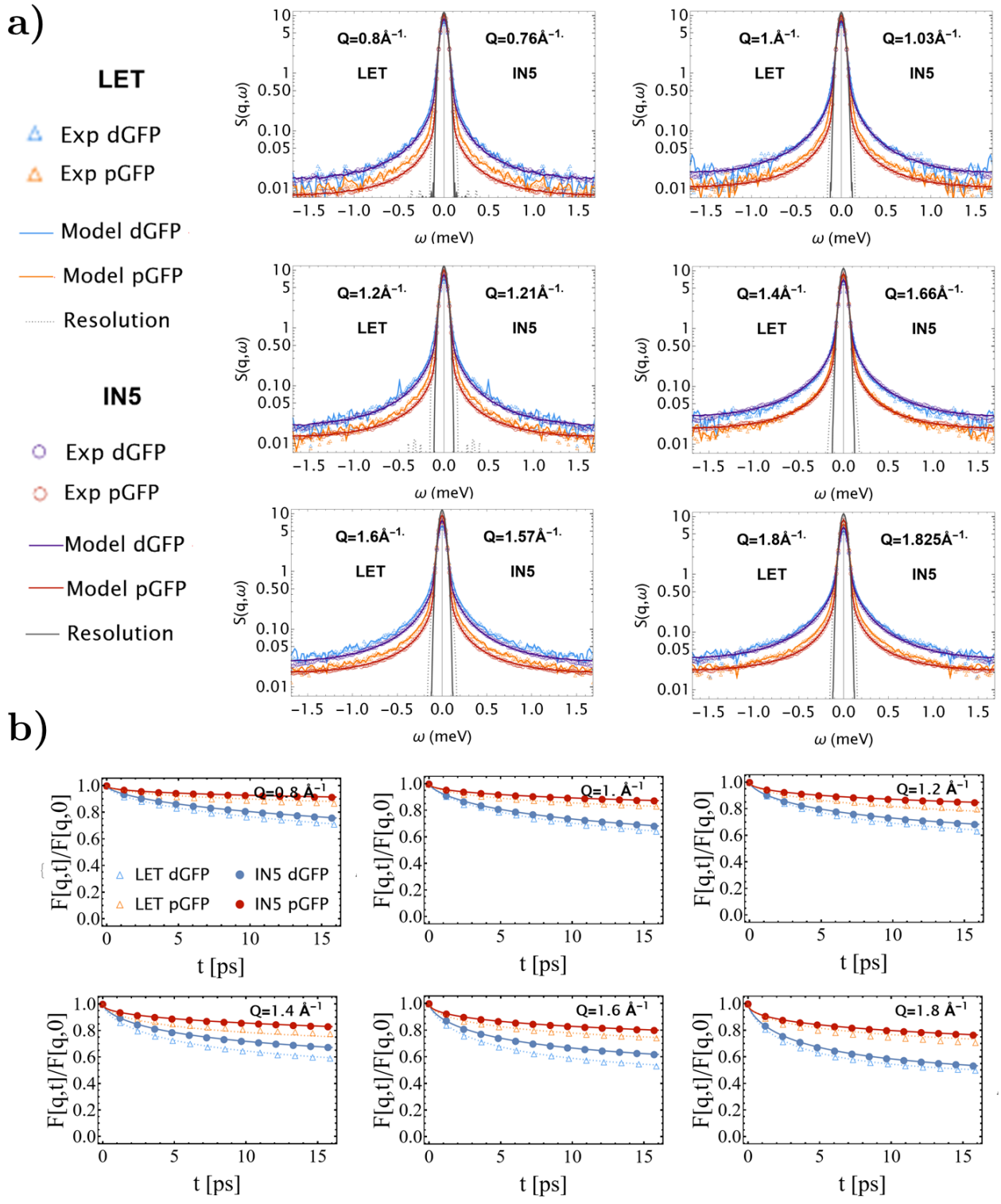

Figure 5-2: a) $S(Q,\omega)$ at $T = 310$ K compared for IN5 (unpolarised, light labels) and LET (polarised, dark labels), dGFP in blue and pGFP in red, resolution is represented as a dotted line for LET and full line for IN5.
b) $F(Q,t)$ at $T = 310$ K experimental data for dGFP (blue: LET, light blue: IN5) with pGFP (IN5) in red as a comparison.

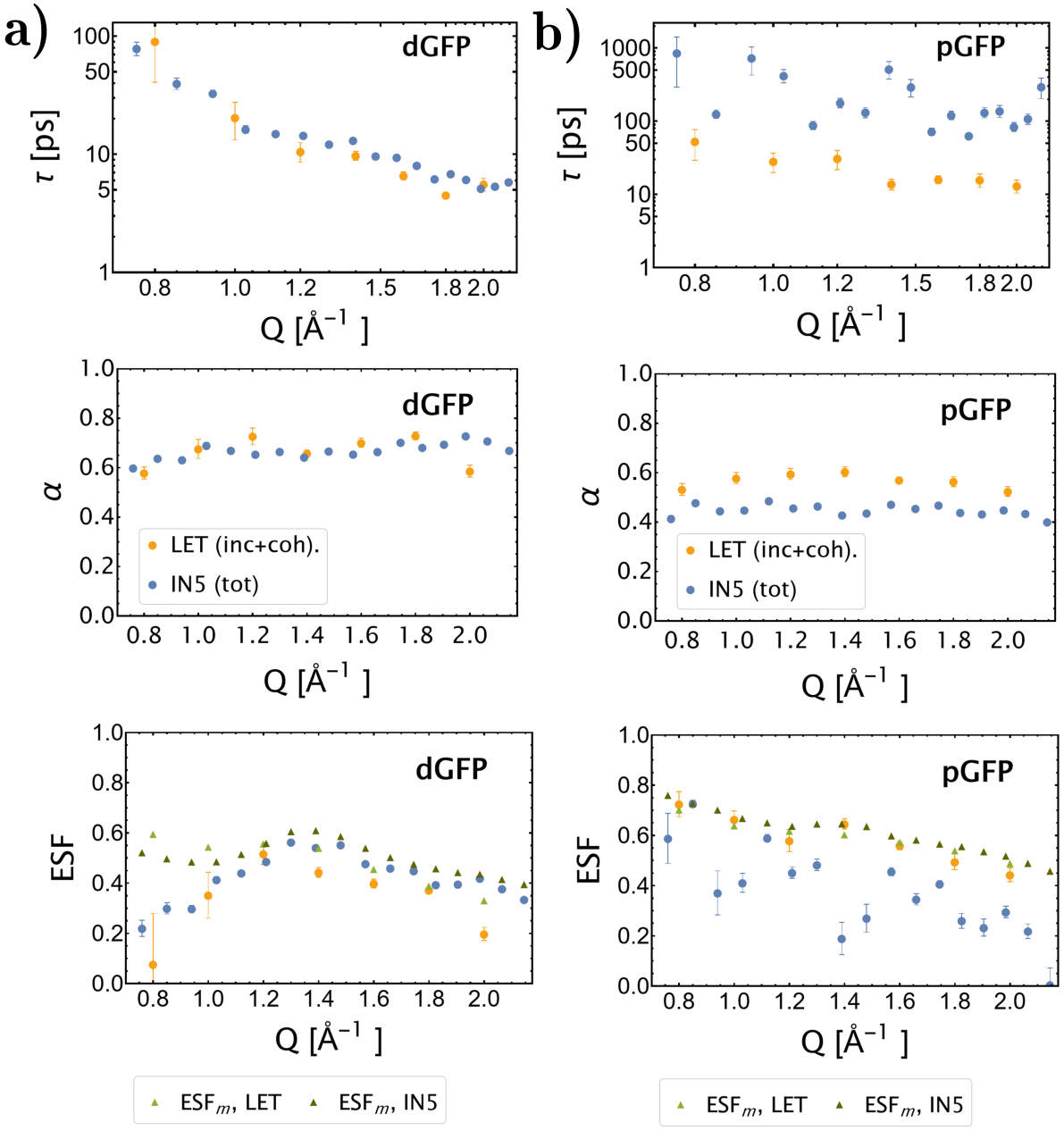

Figure 5-3: τ, α and ESF parameters obtained as a function of Q on polarised LET (blue $\circ$), $\Delta E = 95\ \mu eV$, compared to unpolarised IN5 (orange $\circ$), $\Delta E = 70\ \mu eV$.(a) corresponds to dGFP, (b) to pGFP. $\triangle$ corresponds to the measured ESF following Equation 6-5 for $\epsilon_m = \text{FWHM}/2$.

dGFP sample: similar dynamics, different asymptotic relaxation.

A stricking point of the comparison of scattering functions (Figure 5-2) and parameters [Figure 5-3, (a)] for both instruments is how for dGFP, $F(Q,t)$ and $S(Q,\omega)$ appear to differ strongly between both instruments. However, parameters inform that dynamics embedded by τ and α remains almost the same (there is a slight decrease of the timescale of relaxation for LET compared to IN5), and only the static information held by ESF(Q) is modified, with $ESF(Q)_{\text{LET}} \approx ESF(Q)_{\text{IN5}} - 0.1$ for $Q > 1\text{Å}^{-1}$. An interpretation is probably that from a sample preparation to another, an increase of D→H exchange or h value can modify the amount of relaxing deuteriums in hydration water: hence changing the proportion of relaxing nuclei and the ESF(Q) without modifying their dynamics. This might not an artefact from the model: measuring ESF from the elastic peak with Equation 6-5 raises a similar 0.1 gap between instruments, see Figure 5-3 (ESF_m, green triangles). Of course, resolution effects hiding slower dynamics in LET ($\Delta E_{\text{IN5}} < \Delta E_{\text{LET}}$) could also be at stake, which explains that τ is slower for IN5.

pGFP sample: observation of hydration-induced dynamics.

For pGFP, the clear difference between the two instruments is visible from the broadening of $S(Q,\omega)$ on the whole energy range, which is essentially an effect of the slower dynamics on IN5. Parameters clearly indicates a strong discrepancy that is not due to a resolution effect.

Several hints show that dehydration of the sample on IN5 is responsible for this :

- Measuring the pGFP sample holder before and after experiments on IN5 pointed out a leak in the indium sealing, permitting the sample to dehydrate from $h = 0.4$ to $h = 0.2$ during the experiment. It was not the case during LET experiment. Dehydration implies that side chains motions are reduced: methyl group rotations occur in dry proteins for $T \geq 150$ K, while hydration-induced side chains dynamics occur for hydrated proteins only for $h \geq 0.2$ and increase until $h \approx 0.5$. Methyl group motions are highly heterogeneous, centered on $\tau = 75ps$ and stretching from about 20 to 200ps [229] compared to the localised side-chains diffusion implying $\tau \approx 15 - 50$ ps for h=0.4 [229, 91]. Both timescales correspond respectively to our results on IN5 and LET, implying that only methyl group motions allowed in dry-state are activated on IN5.

- We measured non-polarised intensity on LET in the elastic peak during sample

heating, providing measurements for Mean Square Displacements (MSD) for $T \geq 250$ K (methods presented in chapter 6), and compared to MSD measured on IN5. This is exposed in Figure 5-4, and MSD for $T = 295$ K are reported in Table 5-III. For dGFP, MSD are almost identical, but differ by 0.1 $Å^2$ for pGFP. This is because dry proteins display no dynamical transition (although it has been observed for backbone dynamics in deuterated dry GFP and CYP, for $\Delta t \approx 1$ ns [3]): pGFP only displays a very soft transition at $T \approx 260$ K. Above $h = 0.2$, the MSD suddenly increase due to the entrance of side chain motions [246, 247, 248, 249], which is here observable for LET but not IN5.

Table 5-III: MSD [$Å^2$] obtained for $T = 295$ K on LET and IN5 for dGFP and pGFP.

MSD/Instrument	LET	IN5
dGFP [$Å^2$]	0.493	0.475
pGFP [$Å^2$]	0.386	0.296

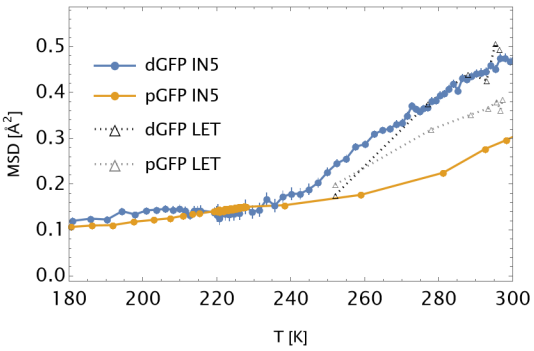

Figure 5-4: Comparison of the MSD obtained with LET for $T \geq 250$ K, $\Delta E \approx 0.097$ meV (scan performed during sample heating) and the MSD obtained with IN5 for $310K \geq T \geq 10$ K, $\Delta E \approx 0.080$ meV (5 minutes elastic window scans).

- pGFP structure factor measured with IN5 strongly differs from the one measured with polarised instruments, see Figure 5-5, indicating strong structural and dynamical discrepancies in IN5 sample.

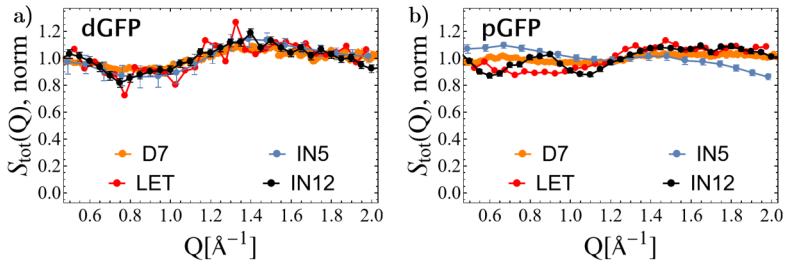

Figure 5-5: Unpolarised structure factors obtained on LET, D7, IN12 and IN5, for (a) dGFP, (b) pGFP. The peak at $Q \approx 0.9$ Å^{-1} in IN12 data (pGFP) is an artefact from the flat sample holder geometry.

Therefore, we have shown that at the pico-second scale, it is feasible to compare parameters analysed in the frame of Brownian dynamics for two similar instruments where one is equipped with polarisation analysis. However, discrepancies arising from sample preparation (or resolution) are unavoidable and are indeed the limiting parameter for comparison. The dGFP sample bears almost the same dynamical information in both instruments, while for pGFP the model catches the strong difference in heterogeneity and timescales occuring from the onset of side-chain motions in LET, which is prevented in IN5 due to hydration close to $h = 0.2$ where the onset takes place. Hence, all the insights obtained from LET shall steer us towards better understanding of unpolarised data for similar instrumental characteristics. However, it is useless to perform quantitative comparison: the error made using a non-polarised beam due to coherent scattering, previously introduced in chapter 4, Figure 4-11, is even less significant than the gap between the two instruments. It is shown for dGFP sample in Figure 5-6, respectively with full and dotted lines.

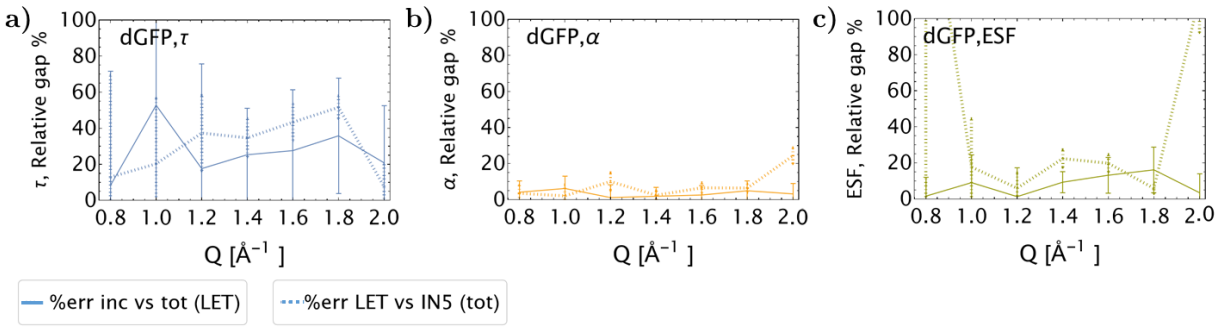

Figure 5-6: Comparison of the error made using a non polarised beam due to coherent scattering (full lines) compared to the error made comparing similar instruments (dotted line). $\tau(Q)$ parameter is in blue (a), $\alpha(Q)$ in orange (b) and ESF(Q) in green (c).

5.3 Interpretation of dynamics as arising from diffusion in a rugged harmonic potential

5.3.1 Theory

The FBD model provides an interesting insight into the sample's heterogeneity, through the expression of the Mittag Leffler function as a relaxation of exponential decays for which we can extract the spectral density.

We follow the procedure introduced in [230], where further information is available. While a Ornstein Uhlenbeck (OU) process describes the dynamic variable diffusing in a harmonic potential, a Fractional OU process (FOU) corresponds to a rugged potential which consists of a set of local minima spread along the quadratic potential with barriers ΔE that scale close to the thermal energy k_BT and in which the variable is temporarily trapped, see Figure 5-7 (b). It echoes the energy landscape image for the protein conformational states fluctuations on the ps-scale. Under the assumption of a heterogeneity of internal processes in the protein, the relaxation function writes as a superposition of exponential decays with dimensionless rate λ ;

$$E_\alpha[-(t)^\alpha] = \int_0^\infty p_\alpha(\lambda)\exp(-\lambda t)d\lambda, \tag{5-5}$$

with relaxation spectrum $p(\lambda)$ expressed as

$$p_\alpha(\lambda) = \frac{1}{\pi\lambda}\frac{2\sin(\pi\alpha)}{(\lambda)^\alpha + (\lambda)^{-\alpha} + 2\cos(\pi\alpha)}, \tag{5-6}$$

and verifying $\int_{-\infty}^{\infty} p(\lambda)d\lambda = 1$. Figure 5-7 is illustrated for dGFP and pGFP and compared for the two experiments on Figure 5-7.

From this expression we want to derive a useful semi-quantitative tool to understand how the protein nuclei see their environment. Therefore, we write the dimensionless relaxation constant $\lambda = \frac{\eta}{\eta_0}$ as the ratio of the inverse relaxation times of FOU (η) and OU (η_0) models respectively, modelling the retardation of diffusion in the rugged potential. Considering a scale-independent Gaussian distribution of energy barriers, adapted from Zwanzig's [65] qualitative approach, we introduce an effective diffusion constant in the rugged potential expressed from the quadratic potential diffusion constant, that writes

$$D = D_0 \exp\left(-(\Delta E/k_BT)^2\right), \tag{5-7}$$

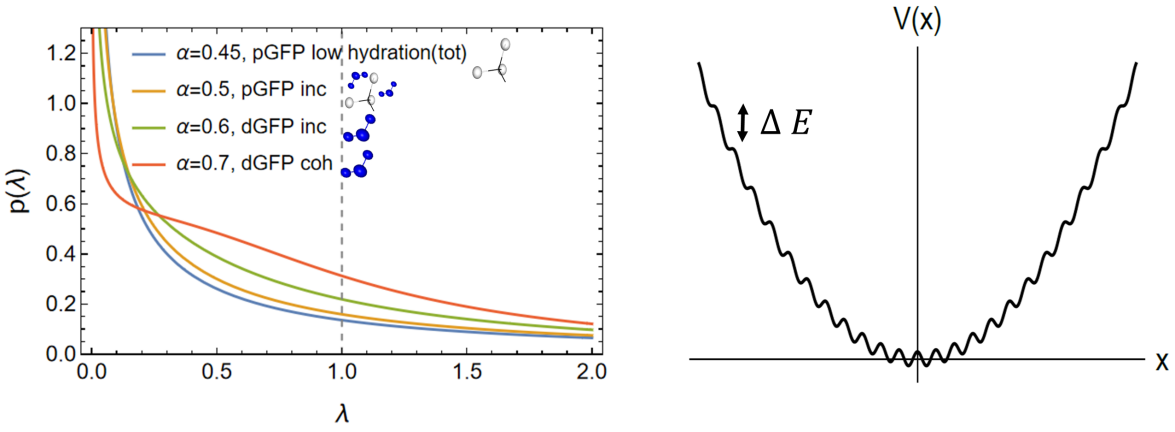

Figure 5-7: a) Distribution $p_\alpha(\lambda)$ defined by for α values corresponding to water coherent (dGFP coh, red) and incoherent (dGFP inc, green) motions at $T = 310$ K, hydrated protein (pGFP inc, orange) and dehydrated protein (pGFP tot IN5, blue) motions, see Table 5-IV. b) Sketch of a rugged potential for the FOU process with energy barrier ΔE.

with D_0 the diffusion constant of the OU model. Therefore

$$\lambda = \frac{\eta}{\eta_0} = \exp(-\epsilon) \ , \tag{5-8}$$

with

$$\epsilon = (\Delta E / k_B T)^2 \ , \tag{5-9}$$

where ϵ is a dimensionless energy barrier and is dependent on the scale of observation since lower Q values englobe larger fluctuations and a higher number of modes.

Thus the normalised distribution of dimensionless energy barriers ϵ writes as :

$$p_\alpha(\epsilon) = \frac{1}{\pi} \frac{2\epsilon \sin(\pi\alpha)}{(\exp(-\epsilon^2))^\alpha + (\exp(-\epsilon^2))^{-\alpha} + 2\cos(\pi\alpha)}. \tag{5-10}$$

Since moments of order n of $p_\alpha(\epsilon)$ are not defined for $n \geq 1$, we introduce the median value of the relaxation spectrum $\epsilon_{1/2}$ defined as :

$$\int_0^{\epsilon_{1/2}} p_\alpha(\epsilon) d\epsilon = \frac{1}{2}, \tag{5-11}$$

in order to evaluate the amplitude of energy barriers.

To conclude, we recall that the stiffness k of the potential writes $\frac{k}{k_B T} = \langle \hat{\chi}^2 \rangle_{eq}$ with $\hat{\chi}(Q)$ the self dynamic variable expressed in Equation 1-60. $\langle \hat{\chi}^2 \rangle_{eq}$ are the MSD provided by Elastic Neutron Scattering and therefore indicate the stiffness of the global potential experienced by $\hat{\chi}$. Therefore $\hat{\chi}$ sees a potential $V(\hat{\chi}) = k\hat{\chi}^2 + V_1(\hat{\chi})$ with V_1 an oscillating

potential distributed following a Gaussian distribution of standard deviation ϵ.

5.3.2 Application to IN5 QENS data for T=220K and T=310K.

We show the relaxation spectrum $\rho(\epsilon)$ for IN5 data in Figure 5-8, expressed from Equation 5-10 as a function of $\epsilon = \frac{\Delta E}{k_B T}$. Let us notice that ϵ expresses the ratio of ΔE, the height of distributed the energy barriers, to $k_B T$, the energy that is already brought by to the system by the thermal contribution. Therefore it expresses the capacity of the system to overcome transient energy barriers in given temperature conditions.
It appears that while internal dynamics of the pGFP protein undergo a slight shift towards lower energy barriers upon increasing temperature from 220K to 310K, this shift is much stronger for dGFP and indicates a radical change of the local landscape experienced by $\hat{\chi}$. Especially, the distribution width shrinks at high temperature for dGFP while remaining similar for pGFP. The bottom panel of Figure 5-8 displays the dimensionless potential $\frac{V(\hat{\chi})}{k_B T}$ experienced by the dynamic variable, for the energy barrier distribution parameterised by $\epsilon_{1/2}$.
We express an effective activation energy E_a featured in Table 5-IV for each temperature

$$E_a = N_a \epsilon_{1/2} k_B T, \tag{5-12}$$

with N_a Avogadro's number and k_B Boltzman's constant. It is important to notice that the energy barrier is not "per particle" per se, because it is experienced by the cross section weighted dynamic variable, hence we name it an "effective" energy.

Those energy barriers are displayed in Figure 5-9, and do not scale with activation energies of fundamental processes that take place at the ps timescale. To get a general idea, inside the protein, the activation energy of methyl groups rotations (present at both 220 K and 310 K) scale around 3.96 ± 0.5 kcal/mol[177, 251, 91] and H-bonds breaking scales from about 5 to 1.5 kcal/mol from dry to hydrated conditions in β-sheets at physiological temperature in peptides [252]. In bulk water, diffusion has an activation energy of around 4.4 kcal/mol and O-H reorientational time has an activation energy of around 4.1 kcal/mol [253]. Therefore, energy barriers are rather the picture of how heterogeneity impacts the local relaxation of the density of particles and the diffusion coefficient of the process, if it were to be a single exponential decay (Equation 5-7). Those small additional energy barriers are crossed only with a fraction of the activation

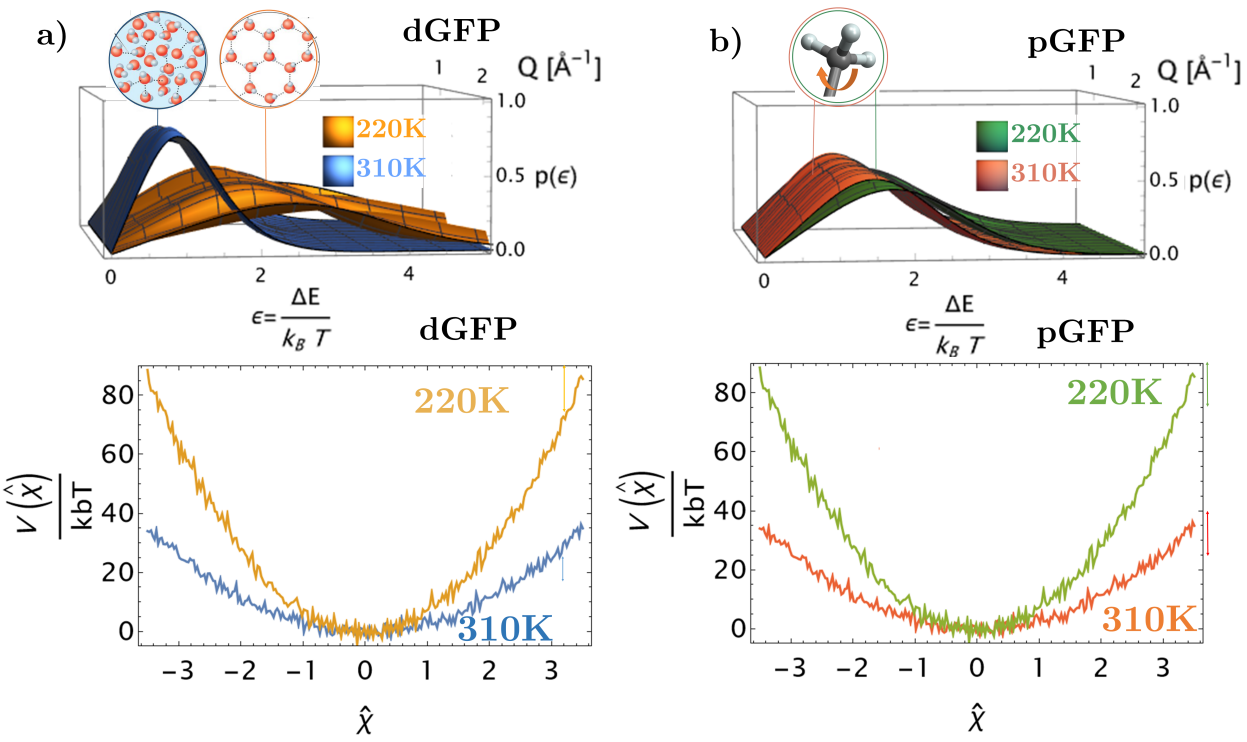

Figure 5-8: Study of energy barriers performed with IN5 data. Top panel: distribution of dimensionless energy barriers $p_\alpha(\epsilon)$ [Equation 5-10] with $\epsilon = \frac{\Delta E}{k_B T}$ as a function of Q, compared for both protein powder samples: dGFP (a), pGFP (b) at 220K (dGFP: orange, pGFP: green) and 310K (dGFP: blue, pGFP: red). Low Density Liquid (LDL) and High Density Liquid (HDL) water pictures are adapted from [250]. Bottom panel: corresponding potentials $V(\hat{\chi}) = k\hat{\chi}^2 + V_1(\hat{\chi})$ seen by the dynamic variable and normalised by $k_B T$. The color-code is the same as for energy barriers, $Q = 1.2\text{Å}^{-1}$.

energy for the main process, and are inherent to the "fractional" Brownian motion. The Q dependence of activation energies shows that the more local, the softer the potential.

Table 5-IV: $\Delta E_{1/2}$ calculated from Equation 5-11 for $Q = 1.2$ Å^{-1}.

Sample	α_{220K}	α_{310K}	$\Delta E_{1/2,220K}$ [kcal/mol]	$\Delta E_{1/2,310K}$ [kcal/mol]
pGFP	0.34	0.45	0.73	0.88
dGFP	0.21	0.65	0.87	0.64

Interpretation In Ref. [233], authors model the hydrated lysozyme powder ($h = 0.3$) relaxation function following a KWW law with stretching exponent β. β decreases with temperature in such that $\beta_{T=220K} \approx 0.8$ and $\beta_{T=310K} \approx 0.25$, with a linear trend and offset at $T \approx 220$ K. In dehydrated powders they see almost no change with temperature ($\beta \approx 1$ between $T = 200$ K and $T = 300$ K). However, in Ref. [234] the opposite trend is found for lysozyme hydration water: $\beta \approx 0.2$ is almost constant for $T \in [160, 210]$ K, suddenly increases to $\beta \approx 0.7$ until $T = 235$ K and finally slightly increases to reach $\beta = 0.9$ at

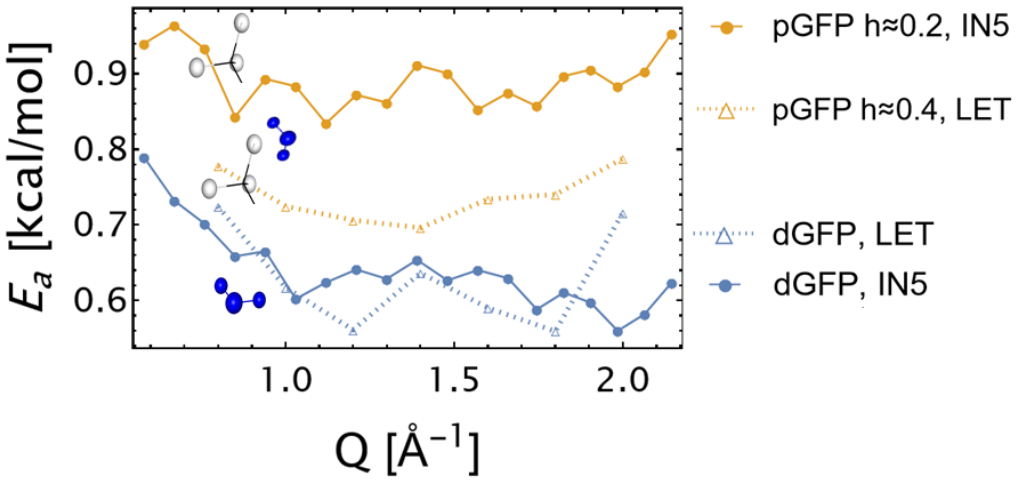

Figure 5-9: a) Distribution of activation energies E_a, Equation 5-12, for total scattering (inc+coh). pGFP at low hydration (IN5, orange full line) where mostly methyl groups are mobile, pGFP at $h \approx 0.4$ (LET, orange dotted line) where side chains are hydrated and mobile, and dGFP at $h \approx 0.4$ (IN5 and LET, blue lines) at $T = 310$ K corresponding to hydration water's motions.

$T = 280$ K. $T = 220$ K is analysed as a crossover temperature for β corresponding to the transition from a fragile ($\tau(T)$ follows a Vogel-Fulcher-Tammann law) to strong behaviour (Arrhenius law, $E_a = 3.13$kcal/mol) in hydration water, sign of a LDL to HDL transition [254]. The onset of rotational and translational motions in hydrations water (respectively occuring at $T = 200 - 250$ K and $T \approx 240$ K[222]) softens hydration water potential (β increases strongly, sigmoïd trend) but increases the heterogeneity of motions in the protein (β decreases strongly, linear trend).

It is in line with our results for dGFP ($\alpha_{\mathrm{T=220K}} = 0.21$, $\alpha_{\mathrm{T=310K}} = 0.65$) strongly softening with temperature like hydration water, and pGFP displaying almost no change ($\alpha_{\mathrm{T=220K}} = 0.34$, $\alpha_{\mathrm{T=220K}} = 0.45$) similar to a dehydrated protein powder, although α is small.

Hence we propose the two following interpretations :

- dGFP: We interpret the sudden change of dynamical environment of the deuterated sample in the frame of the liquid-liquid transition in supercooled hydration water around 220 K at ambient pressure from a low density liquid (LDL) to a high density liquid (HDL). In the case of bulk water it is assumed to imply a transition of the connective properties of the H bonds network from an almost crystalline tetrahedral network (LDL) to disordered interconnecting networks with a high degree of intersticial sites (HDL), typical of water under pressure [255]. In the case of interfacial water this transition occurs with the creation of patches of HDL water in

the preexisting LDL phase and is combined with a strong increase of mobile water molecules [256]. This has also been held by some authors as the explanation for the dynamical transition of hydrated proteins. Therefore, in deuterated GFP, at T= 220 K the dynamic variable is trapped in local minima requiring a few thermal energy unities to escape due to the ordered D-bond network, while at T= 310 K the potential drastically softens and thermal energy is enough to overcome most of energy barriers for pGFP ($\epsilon < 1$).

- For protonated GFP, we interpret the minimal change in dynamical landscape as arising from sample dehydration meaning that only methyl groups undergo relaxation (the onset is at 150 K) at 220 K and 310 K. Hence, the almost same distribution of ϵ for low and high temperatures for pGFP.

  Furthermore, energy barriers for pGFP at $h \approx 0.4$ obtained on LET are higher than for hydration water (dGFP), but lower than for the protein at low hydration level (pGFP, IN5), see Figure 5-9, which is the sign that the onset of side chain motions coupled with hydration water has been enabled on LET. It rationalizes the strong difference between parameters on IN5 and LET for pGFP, especially τ parameter Figure 5-3.

This interpretation is illustrated on the top pannel of Figure 5-8.

5.4 Conclusion

We performed comparison of polarised and unpolarised neutron spectroscopy at the ps-resolution, highlighting that results are highly comparable between similar instruments, in the limiting case of reproducible sample preparation and similar energy-resolution. Indeed, the error made using two different instruments is larger than the error due to the presence of coherent scattering.

CHAPTER 6

A discussion on elastic scattering in a protonated and a deuterated protein powders

6.1 Introduction

This chapter focuses on elastic scattering in biomolecules. An elastic scan performed on a large range of temperatures from T≈ 2K to T=310K is analysed and discussed in the light of a new quasi-analytical model proposed recently by Hassani et al [75] which illustrates the contamination of quasielastic scattering in elastic scans. This article also proposes a reduction of parameters for the FDB model, that we apply to IN5 data. We end-up with a new proposition to explain the dynamical transition, which yields approximate but encouraging results, although this is a "toy" model that requires refinement.

6.2 Elastic scattering in complex systems

6.2.1 Separation of elastic and quasielastic scattering in biomolecules

As introduced in Equation 1-59, in the framework of the proposed model, the intermediate scattering function $F(\mathbf{Q},t)$ is halved in a time-dependent and an asymptotic part where ESF(Q) is the elastic scattering factor of the protein and $\phi_{\alpha,\tau}(\mathbf{Q},t)$ the Mittag-Leffler

relaxation function dependent on α and τ.

$$F(\mathbf{Q},t) = ESF(\mathbf{Q}) + (1 - ESF(\mathbf{Q}))\phi_{\alpha,\tau}(\mathbf{Q},t). \tag{6-1}$$

Which raises upon Fourier transform, the following form for the dynamic structure factor

$$S(\mathbf{Q},\omega) = ESF(\mathbf{Q})\delta(\omega) + (1 - ESF(\mathbf{Q}))\tilde{\phi}_{\alpha,\tau}(\mathbf{Q},\omega), \tag{6-2}$$

where $\tilde{\phi}_{\alpha,\tau}$ is the Fourier Transform of the relaxation function. This quantity is convoluted in experiments resolution function of the instrument $R_\sigma(\mathbf{Q},\omega)$ of standard deviation σ, which defines the resolution energy ω_{res} in units of $\hbar$. In the case of a Gaussian resolution function,

$$\omega_{\text{res}} = \text{FWHM}\left(R_\sigma(\mathbf{Q},\omega)\right) = \sqrt{2\ln(2)}\sigma. \tag{6-3}$$

Hence, the elastic peak $\omega \approx 0$ broadens to $\omega \in [-\omega_{\text{res}}/2, \omega_{\text{res}}/2]$. This interval is called the elastic peak, or elastic window. Integration over the elastic peak writes

$$S_{\text{elastic}}(\mathbf{Q},\omega) = ESF(\mathbf{Q}) \int_{-\omega_{\text{res}}/2}^{\omega_{\text{res}}/2} d\omega R_\sigma(\mathbf{Q},\omega) + (1 - ESF(\mathbf{Q})) \int_{-\omega_{res}/2}^{\omega_{\text{res}}/2} d\omega R_\sigma(\mathbf{Q},\omega) * \tilde{\phi}_{\alpha,\tau}(\mathbf{Q},\omega). \tag{6-4}$$

Therefore, the elastic peak contains all dynamics occuring at time scales $t > t_{\text{res}}$ where $t_{\text{res}} = 2\pi/\omega_{res}$ As far as the nuclei in the sample do not undergo spatial dynamical disorder (such as Fickian diffusion for instance), they are confined in space which implies that the Elastic Structure Factor does not vanish.

Hence, ideally, the elastic peak is perfectly distinguished from quasielastic scattering, this is what motivates elastic scans, which consist in measuring the signal in the elastic peak under the assumption of a perfect separation of elastic scattering and QENS :

$$ESF_m(\mathbf{Q}) \approx \frac{\int_{-\omega_{res}/2}^{\omega_{\text{res}}/2} d\omega R_\sigma(\mathbf{Q},\omega) S(\mathbf{Q},\omega)}{\int_{-\omega_{\text{min}}}^{-\omega_{max}} d\omega R_\sigma(\mathbf{Q},\omega) S(\mathbf{Q},\omega)}, \tag{6-5}$$

where $[\omega_{\text{min}}, \omega_{\text{max}}]$ in units of $\hbar$ defines the dynamical range of the instrument. During an elastic scan, normalisation on the total energy range is indirectly performed from a low-temperature sample, see Equation 6-11

In reality, quasielastic and elastic peaks merge. A first reason is the convolution with the resolution function, which broadens the elastic peak. But this is not the only reason:

it is also due to the shape of the relaxation function of biomolecules. Indeed, it has been shown by Kneller et al [17] that while an exponentially decaying relaxation function can still permit the separation when the resolution is high enough compared to the timescale of the process, power-law relaxation functions such as encountered in proteins do not permit this separation even at very high resolution due to the intrinsic self-similarity of protein dynamics and the wide range of timescale captured in a single process. For a Mittag-Leffler relaxation function, it worsens when the heterogeneity parameter α decreases (which is rarely assessed above $\alpha = 0.7$ in proteins).

This is what motivates us to calculate the ESF directly within the model used for QENS and to further estimate the corrections that should be introduced to our elastic scans to ensure a good estimation of the MSD knowing the fitting parameters.

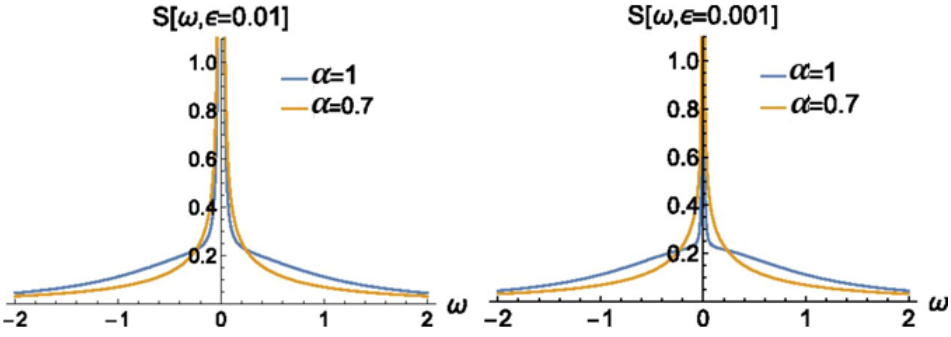

Figure 6-1: Scheme extracted from [17], showing the impact of the form factor α of the Mittag Leffler function, a self-similar relaxation function, on the distinction between elastic and quasielastic. $\alpha = 1$ corresponds to a single exponential decay and raises better disctinction. It is shown for two different effective resolutions $\epsilon = 0.01$ (left) and $\epsilon = 0.001$ (right).

6.2.2 Incoherent elastic scattering: models for the elastic scan

For the rest of that section, we suppose that incoherent scattering is the main contribution, although chapter 5 earlier evidenced the impact of coherent scattering in the ESF of dGFP. In the EISF, information on motional amplitude arises from the cumulant expansion of the incoherent intermediate scattering function [257]. Considering that all N nuclei in the sample are equivalent and remaining in the classical limit :

$$F_{\text{inc}}(\mathbf{Q}, t) = \langle \exp\left(-i\mathbf{Q}(\mathbf{R}(t) - \mathbf{R}(0)\right)\rangle = \exp\left((-1)^k Q^{2k} \gamma_{2k}\right), \tag{6-6}$$

where even cumulants γ_{2k} are expressed in terms of the velocity autocorrelation function and take the following values for the two first terms :

$$\begin{aligned}\gamma_2 &= \frac{1}{2!}\langle \mathbf{n_Q}(\mathbf{R}(t)-\mathbf{R}(0))^2\rangle \\ \gamma_4 &= \frac{1}{4!}\left(\langle \mathbf{n_Q}(\mathbf{R}(t)-\mathbf{R}(0))^4\rangle - 3\langle \mathbf{n_Q}(\mathbf{R}(t)-\mathbf{R}(0))^2\rangle^2\right),\end{aligned} \tag{6-7}$$

where $\mathbf{n_Q}$ is the unitary vector parallel to $\mathbf{Q}$.

The Gaussian approximation consists in keeping only the first harmonic term corresponding to the first cumulant. We assume isotropy of motions such that EISF(Q) depends only on the magnitude of $\mathbf{Q}$, and

$$\langle \mathbf{n_Q}(\mathbf{R}(t)-\mathbf{R}(0))^2\rangle = \frac{1}{3}\langle r(t)^2\rangle, \tag{6-8}$$

where $\langle r(t)^2\rangle$ is our notation for the time-dependent MSD. For motions confined in space, the plateau value reached by the MSD is such that $\lim_{t\to\infty}\langle r(t)^2\rangle = 2\langle r^2\rangle$ where $\langle r^2\rangle$ is our notation for static MSD.

Using Equation 6-7 and Equation 6-8 in Equation 6-6 raises the Gaussian Approximation (GA), holding for $Q^2\langle r^2\rangle \ll 1$

$$EISF(Q) = F_{\mathrm{inc}}(Q,\infty) = \exp\left(-\frac{Q^2\langle r^2\rangle}{3}\right). \tag{6-9}$$

This equation holds when hydrogen isotopes perform harmonic oscillations around their resting positions on the whole temperature range, provided that motions are not too anharmonic or anisotropic [258].

One of many models accounting either anharmonic motions or for distributions of individual mean square deviations was proposed by Kneller et al [259, 260]. Since single hydrogens undergo motions in an effective harmonic potential and verify the GA, deviations from the GA can be explained by a motional heterogeneity of MSDs among nuclei. EISF(Q) follows a Gamma distribution $p(\lambda,\beta_h)$ of Gaussian approximations of individual atoms, where a parameter β_h accounts for heterogeneity (GA is retrieved for $\beta_h \to \infty$) and a parameter λ scales single MSD,

$$EISF(Q) = \int_0^\infty d\lambda p(\lambda,\beta_h)\exp\left(-\lambda Q^2\right) = \frac{1}{\left(1+\frac{Q^2\langle r^2\rangle/\sqrt{\lambda}}{\beta_h}\right)^{\beta_h}}. \tag{6-10}$$

6.2.3 Elastic scans of dGFP and pGFP samples, IN5 ($\omega_{\mathbf{res}} \approx 0.08$ meV)

An elastic scan consists in a short time exposure of the sample to neutrons on a wide range of temperatures upon heating, estimating the ESF from the elastic peak. 5 minutes elastic scans have been measured with an increasing temperature ramp for $T \in [2, 310]K$ for both pGFP ($T_{\min}$) and dGFP ($T_{\max}$) and integrated over the elastic peak such that $\omega_{\text{res}} \approx 0.04$ meV. Considering that coherent scattering is negligible, normalisation is performed following

$$EISF(Q) \approx \frac{S(Q, \omega_{res}, T)}{S(Q \approx 0, \omega_{res}, T \approx 0)}. \tag{6-11}$$

We deviate from the standard normalisation process which uses $S(Q, \omega_{res}, T \approx 0)$, because it artificially eliminates zero-point fluctuations. We suppose that the absence of motions at minimal temperature for $Q \to 0$ (very large distances probed by a single nucleus) provides a perfect flat-line for $S(Q \approx 0, \omega_{\text{res}}, T \approx 0)$.

Applying the model accounting for heterogeneity featured in Equation 6-10 on both pGFP and dGFP yields very high values of β_h (> 1000) with no defined tendency as a function of temperature when the parameter is unconstrained, implying a high homogeneity of mean-squared deviations on this Q-range. Hence, all nuclei have similar motional amplitudes within the sample despite heterogeneous dynamics embedded by a strong α parameter in the FBD model in our QENS analysis. Therefore, the Gaussian approximation is good enough a model for the present data on our Q-range, although MD simulations tend to point out that MSD follow non Gaussian distributions in both hydration water [261] and proteins [259]. Figure 6-2 shows the MSD as a function of temperature, where the fit has been optimized using recommendations of Zeller et al [258].

Analysis of MSD in the high temperature range

As presented in Figure 6-3, MSD_{dGFP} are larger then pGFP on the whole temperature range, except for the dynamical transition where suddenly the motions slightly lose amplitude compared to pGFP around the liquid-liquid transition temperature of water at $T = 220$ K. The low hydration of pGFP is visible from the almost nonexistent slope after the dynamical transition T_{d} at $T_{\text{d}} = 260$ K, while dGFP's dynamical transition arises at $T_{\text{d}} \approx 260$ K.

At high temperature, MSD increase much faster for dGFP than for pGFP, indicating a

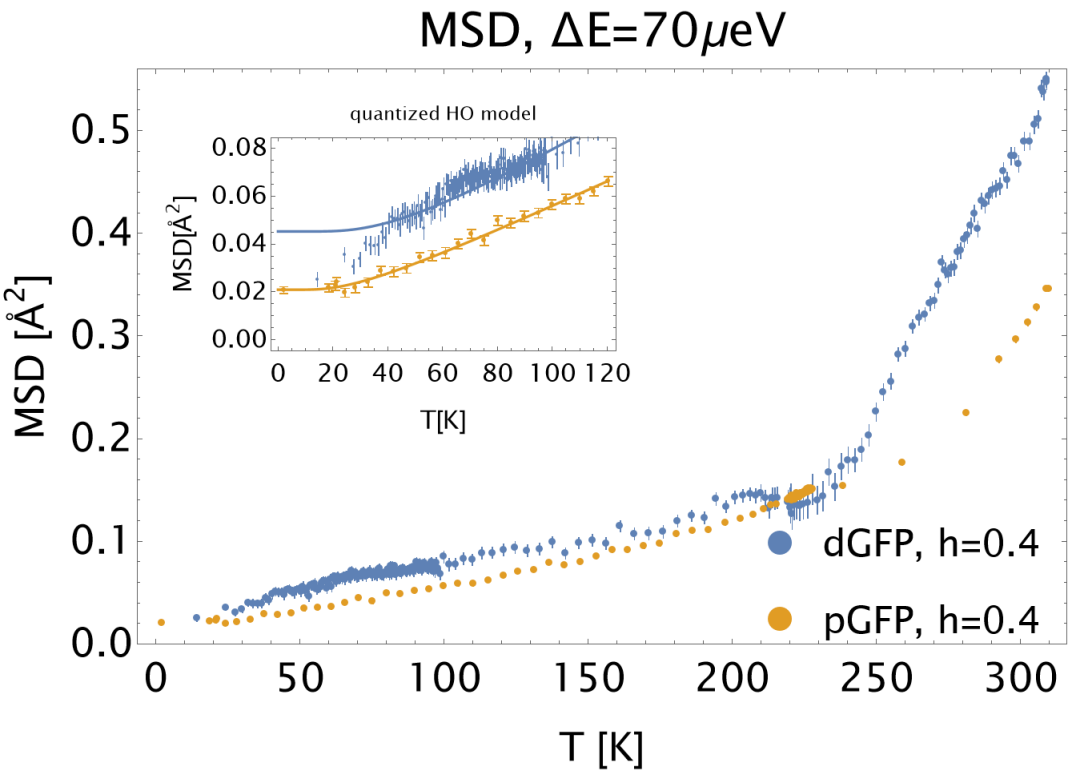

Figure 6-2: Mean-Square displacements $\langle x^2 \rangle$ (MSD) evaluated with IN5 elastic scan, $\Delta E = 70\mu$eV from equation Equation 6-9, and extrapolated at low temperature with expression Equation 6-12 for both the deuterated protein (dGFP) and the protonated protein (pGFP) hydrated in D_2O with $h = 0.4$.

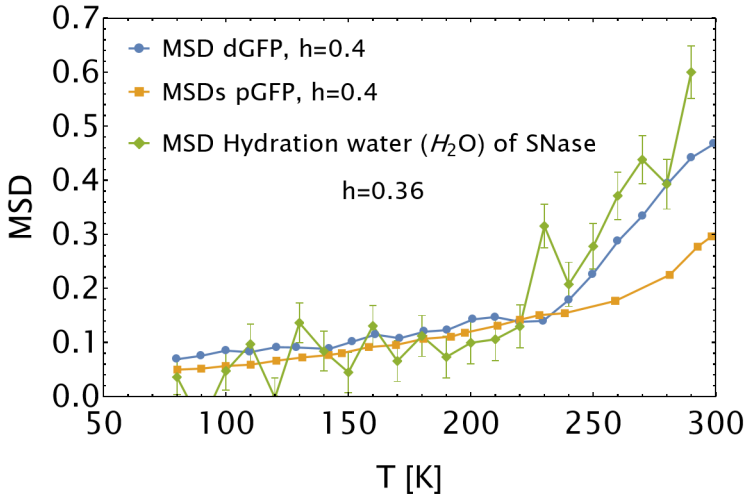

Figure 6-3: MSD of hydration water from staphylococcal nuclease (SNase) compared to hydrated pGFP and dGFP MSD at similar resolution and hydration conditions. Hydration water data was furnished by the authors of Ref. [96].

"softer" system in term of resilience [262]. In this region, the MSD obtained for dGFP tend to scale closely to H_2O hydration water of staphylococcal nuclease at similar resolution ($\Delta E = 106$ μeV), Q range ($Q \in [0.4, 2]$ Å^{-1}) and hydration ($h = 0.36$), see Figure 6-3. Data was provided by Nagakawa et al, see Ref. [96].

Zero-point fluctuations in dGFP and pGFP

Very low temperature MSDs are extrapolated with an analytical expression that holds for a single trapped hydrogen nucleus in a quantum harmonic oscillator potential [263]. In order to extract $\langle 0|r^2|0\rangle$, low temperature MSDs below T= 120 K were fitted considering that energy levels are populated according to Boltzmann's law. It yields Equation 6-12 [264].

$$\langle \mathbf{r}^2 \rangle = \frac{\hbar\langle\nu\rangle}{2\langle k\rangle} \coth\left(\frac{k_B T \hbar\langle\nu\rangle}{2}\right), \tag{6-12}$$

where parameters are averaged (brackets) on all hydrogens present in the sample. In the limiting case of zero-point fluctuations (zpf) which are the amplitude of motions associated to the ground state, MSD write

$$\mathrm{MSD}_{\mathrm{T=0K}} = \langle 0|r^2|0\rangle = \frac{\hbar}{2m\langle\nu\rangle} \underbrace{=}_{m=\frac{\langle k\rangle}{\langle\nu\rangle^2}} \frac{\hbar}{2\sqrt{\langle k\rangle m}}, \tag{6-13}$$

with $\langle\nu\rangle$ the mean pulsation of the potential well, $\langle k\rangle$ the mean stiffness of the harmonic potential. Therefore, for a given neighbouring environment defined by $\langle k\rangle$, $\mathrm{MSD}_{\mathrm{T=0K}} \propto 1/\sqrt{m}$.

Data for $T < 120$ K is fitted with Equation 6-12 with free parameters $\langle k\rangle$ and ω, reported in Table 6-I. For pGFP the harmonic oscillator model is extremely adapted until very low temperature, as can be seen on the insert in Figure 6-2. However, a sudden drop of the MSD below $T = 40$ K for dGFP makes it possible to fit zero-point fluctuations assuming that the tendency is drawn by upper values, but reveals a decrease of motional amplitudes at very low temperatures.

Table 6-I: Fit parameters extracted from Equation 6-12 applied to MSD evaluated from IN5 elastic scans with resolution $\Delta E = 70$ μeV on Q range $[0.3, 2.1]$ Å^{-1} from both pGFP and dGFP proteins hydrated in D_2O.

	$\langle k\rangle$ [Nm^{-1}]	$\langle\nu\rangle$ [cm^{-1}]	zero-point fluctuations [Å^2]	m_{eff} [u.]
pGFP	2.69	54.1	0.021	14.8 ± 0.1
dGFP	1.97	89.7	0.045	4.15 ± 0.01

Using relation $m = \dfrac{\langle k\rangle}{\langle\nu\rangle^2}$ with parameters in Table 6-I to calculate an effective mass diffusing in the potential, it appears that although zero-point fluctuations should scale with $\frac{1}{\sqrt{m}}$, see Equation 6-13, it yields masses corresponding to about 14 hydrogen nuclei in the case of pGFP and 2 deuterium nuclei in the case of dGFP, see Table 6-I. Basically, it

means that the amplitudes of motions correspond to a rigid unit of mass m_{eff}. Therefore the effective mass in pGFP corresponds to about the average mass of all hydrogens in a side chain (≈ 11 u. for the produced wild GFP sequence) in accordance with the picture that movements of the whole side-chain describes as well motions in MD simulations as motions of single nuclei. On the other hand, for dGFP it corresponds to the average mass of hydrogens in a D_2O molecule.

It would be a nice picture if the elastic scan was less dependent on the definition used for the elastic peak or on the impact of QENS, even at low temperature. We report below the parameters that we obtain when using only the central channel available on IN5 ($\Delta E = 8$ μeV) as our definition for the "elastic peak", instead of the whole elastic range defined by the FWHM of the resolution:

- **For dGFP**: $\langle k \rangle_{\text{dGFP}} = 1.76$ nm^{-1}, $\langle \nu \rangle_{\text{dGFP}} = 130$ cm^{-1} and $\text{MSD}_{\text{T=0K,dGFP}} = 0.073$ Å^{-2}, raising $m_{\text{eff,dGFP}} = 1.76$ u.
- **For pGFP**: $\langle k \rangle_{\text{pGFP}} = 2.01$ nm^{-1}, $\langle \nu \rangle_{\text{pGFP}} = 54$ cm^{-1}, and $\text{MSD}_{\text{T=0K,pGFP}} = 0.039$ Å^{-2}, raising $m_{\text{eff,pGFP}} = 3.01$ u.

It implies that despite restricting the definition of the elastic peak, hydrogens in dGFP still have larger amplitudes of motions and diffuse in a softer potential than hydrogens in pGFP. However, MSD at $T = 0$ K are larger and are associated to a lower effective mass which is closer to the expected $m_{\text{eff}} = 2$ u. value. It underlies that the impact of QENS vanishes, even for $T < 120$ K, for a more restrictive definition of the elastic window. Lower χ^2 also testify that the Gaussian approximation holds better in that case. For comparison, a study on horse myoglobin reports $\langle \nu \rangle = 210$ cm^{-1} and $\langle k \rangle = 1.29$ nm^{-1} [263], and a study on DMPA+MBP ($\Delta E = 8\mu$eV) raises $\langle \nu \rangle = 133$ cm^{-1}, $\langle k \rangle = 0.62$ nm^{-1}, [265]. It corresponds to much lower masses, respectively $m_{\text{eff}} = 0.49$ u. and $m_{\text{eff}} = 0.81$ u. But those studies relied on a small collection of lwo temperature values (6 and 2 values for T in $10 - 120$ K).

6.2.4 Limitations of the elastic scan: the pseudo-elastic correction

As exposed in section 6.2, elastic and quasielastic scattering cannot be separated unambiguously in an elastic window scan for complex system undergoing powerlaw relaxation.

In order to quantify the over-estimation of MSD due to the presence of relaxation in the energy window probed by the elastic scan, we refer to an article by Kneller et al [75] where a quasi-analytical correction for the MSD is introduced as a function of α and τ parameters of the Mittag-Leffler relaxation function $\phi_{\alpha,\tau}(Q,t)$. We briefly introduce here their correction method. As introduced previously, in the hypothesis of an isotropic sample where scattering functions depend only on the norm of the momentum transfer, $ESF_m(Q)$ measured with the elastic writes

$$ESF_m(Q) = \int_{-\omega_{\text{res}}/2}^{\omega_{\text{res}}/2} d\omega R_\sigma(Q,\omega) * S(Q,\omega). \tag{6-14}$$

However, the measured ESF contains by definition a non-elastic term due to the part of the relaxation function contained within $[-\omega_{\text{res}}/2, \omega_{\text{res}}/2]$:

$$\xi_{\tau,\alpha,\sigma}(Q) = \int_{-\omega_{\text{res}}/2}^{\omega_{\text{res}}/2} d\omega R_\sigma(Q,\omega) * \tilde{\phi}_{\alpha,\tau}(Q,\omega), \tag{6-15}$$

In [75], Kneller et al describe the implementation for the calculation of Equation 6-15. This pseudo-elastic factor is represented for our data on Figure 6-4 (a). Figure 6-4 (b) shows the two positions where $\xi_{\tau,\alpha,\sigma}(Q)$ has been measured as gray vertical lines. For dGFP, the pseudo-elastic factor is higher at $Q = 0.67$ Å^{-1} than at $Q = 1.48$ Å^{-1} where the measured $ESF_m(Q)$ (blue markers) significantly differs from the calculated $ESF(Q)$ (orange markers) from which the pseudo-elastic contribution $\xi_{\tau,\alpha,\sigma}(Q)$ has been removed. Directly from Equation 6-4, we get

$$\implies ESF(Q) = \frac{ESF_m(Q) - \xi_{\tau,\alpha,\sigma}(Q)S(Q)}{\int_{-\omega_{\text{res}}/2}^{\omega_{\text{res}}/2} d\omega R_\sigma(Q,\omega) - \xi_{\tau,\alpha,\sigma}(Q)}, \tag{6-16}$$

where $ESF(Q) \leq S(Q)$ and $ESF_m(Q) \leq ESF(Q)$, and $\int_{-\sqrt{2\ln(2)}\sigma/2}^{\sqrt{2\ln(2)}\sigma/2} d\omega R_\sigma(Q,\omega) = 0.758$. The limiting case $\xi_{\tau,\alpha,\sigma}(Q) = 0$ basically means that the resolution function and the quasi-elastic signal do not overlap in $[-\omega_{\text{res}}/2, \omega_{\text{res}}/2]$ interval and that therefore it is absolutely correct to use an elastic window scan. It is the case when $\alpha = 1$ (for a single exponential decay) or when the observation time defined by resolution is greater than the relaxation time.

A rule of thumb is that when τ is below 0.3 t_{res} (the relaxation is achieved within the

time of observation defined by resolution, and leads the a measurable asymptotic regime), then the correction to the measured ESF is low enough. Therefore, a very long relaxation time compared to resolution leads to large errors in the ESF. An increasing heterogeneity embedded by α parameter also increases the pseudo-elastic correction if $\tau \ll t_{\text{res}}$.

Can we use this information to correct elastic scans on a large temperature range such as presented on Figure 6-3, deducing $ESF(Q)$ from both the measured $ESF_m(Q)$ at temperature T and the pseudo-elastic factor $\xi_{\tau,\alpha,\sigma}(Q)$ fitted with QENS at the closest temperature to T ? Unfortunately, we do not get satisfying results because the $ESF(Q)$ calculated with the model is strongly non-Gaussian, and $\xi_{\tau,\alpha,\sigma}(Q)$ is strongly temperature dependent (seemingly strong around T=220 K). Otherwise, a first order correction for the Gaussian approximation at low Q values presented in Equation 6-17 was proposed by Kneller et al,

$$\langle r^2 \rangle \underset{Q\to 0}{\approx} \frac{\langle r^2 \rangle_m}{1 - \xi_{\tau,\alpha,\sigma}(Q)}, \tag{6-17}$$

where $\langle r^2 \rangle$ are the corrected MSD, and $\langle r^2 \rangle_m$ the MSD measured with the elastic scan. However, this correction assumes an elastic window of width $[-3\sigma, 3\sigma]$ with σ the standard deviation of the resolution: this is unreasonably large since experimenters usually define the elastic peak as the FWHM of the Gaussian resolution. Furthermore, this correction hold if $\xi_{\tau,\alpha,\sigma}(Q)$ takes values $\ll 1$ which is usually not the case since slow processes in proteins imply that τ is not negligible compared to t_{res}.

Therefore, we just settle for a discussion of the pseudo-elastic contribution in our samples. In both samples, α is almost constant and plays a minor role in determining the evolution of $\xi_{\tau,\alpha,\sigma}(Q)$ with Q. It appears with IN5 data, see Figure 6-4 (c), that diffusion of water in dGFP implies a decrease of $\xi_{\text{pGFP,tot}}(Q)$ from 0.6 to 0.3 over Q until $\tau \approx t_{\text{res}}/3$. It means that the correction is lower at higher Q where the relaxation timescale is shorter. For pGFP, the almost constant τ parameter verifying $\tau \gg t_{\text{res}}$ implies that the pseudo-elastic constant $\xi_{\text{pGFP,tot}}(Q) = 0.6$ is constant and high on the whole Q range, as featured on Figure 6-4 (c). It means that most of the elastic scan data has contribution from QENS. On LET, since τ and α parameters are almost constant for coherent scattering, the pseudo-elastic contribution is low and steady for the fast collective motions of water: $\xi_{\text{GFP,coh}} \approx 0.25$.

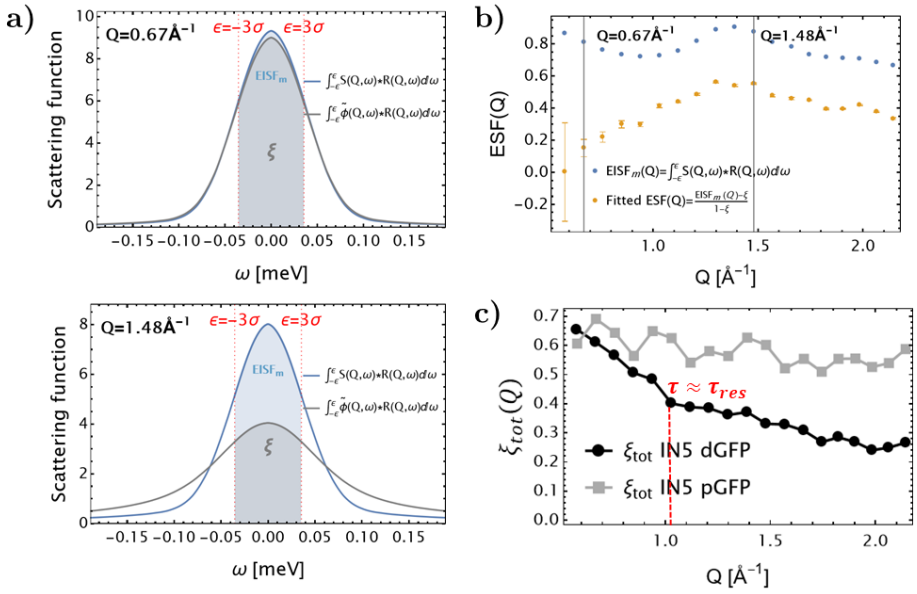

Figure 6-4: a) dGFP: Comparison of the quasielastic contribution $\xi_{\tau,\alpha,\sigma}(Q)$ [Equation 6-15] to the measured $ESF_m(Q)$ [Equation 6-14], $Q = 0.67$ Å^{-1} and $Q = 1.48$ Å^{-1}. b) Comparison of $ESF(Q)$ to $ESF_m(Q)$, Equation 6-14, the vertical lines correspond to the projections used for (a). c) Pseudo elastic contributions of pGFP and dGFP measured on IN5, as a function of Q. The red line shows where $\tau(Q) \approx t_{\text{res}}$.

As a conclusion, for heterogeneous dynamics slower than or equivalent to the resolution function, the pseudo-elastic contribution represent a non-negligible percentage of what is usually called "elastic scattering" within the resolution function. Since studies have until now reported α values that do not evolve much as a function of Q in proteins [230],[40], the determinant of the fraction of quasielastic in the elastic peak is mainly how the timescale of dynamics compares to the time-resolution of the instrument. As reported in [75], very fast dynamics compared to t_{res} are required to ensure that an elastic scan is correct.

Remark Diffusive dynamics implies a strong decay of τ with Q (see dGFP decay on Figure 6-5 (a), green markers) and, as a consequence, a decay of the pseudo-elastic contribution. The latter becomes steady when τ crosses the resolution time $\tau \approx t_{\text{res}}$, in our case at local Q scales for $Q \approx 1.3$ Å,

It might explain that fitting a bimodal $EISF(Q)$ for Q values below and above a determined threshold [266, 258] raises different MSD that are said to correspond to "localised" and "global" motions, see Figure 6-5 (b). We observe that in the frame of Equation 6-17, low Q values where $\tau \ll t_{\text{res}}/3$ yield high pseudo-elastic factors. It implies that corrections required to get the "real" MSD from the measured MSD of an elastic scan are higher for low Q values than for high Q values, due to the strong impact of quasielastic scattering

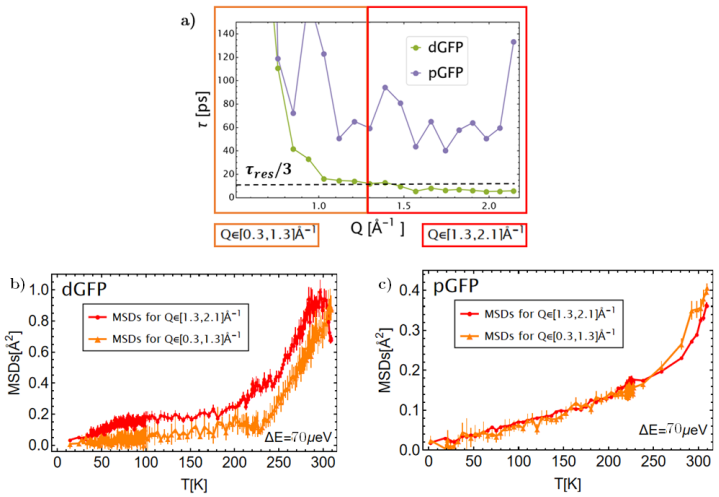

Figure 6-5: (a) dGFP and pGFP dynamical timescales compared to the resolution time t_{res} defined as $t_{\text{res}} = 2\pi/\omega_{res}$. (b) and (c) MSD obtained from fitting the elastic structure factor obtained from elastic scan (IN5) on Q ranges corresponding to before ($Q \in [0.3, 1.3]$ Å^{-1}) and after ($Q \in [1.3, 2.1]$ Å^{-1}) the time scale-factor τ of dGFP cross the third of the resolution time $t_{\text{res}} = 40$ ps. Lines are a guide to the reader.

within the window. It explains visibly "lower" amplitudes of motions at low Q. This effect is absent from pGFP where the timescale of motions is Q-independent [Figure 6-5 (c)], which also explains that MSD for pGFP are not impacted by the range used for the fitting procedure.

6.3 A 2-parameter fit model applied to protein dynamics

The estimation of the pseudo-elastic contribution $\xi_{\tau,\alpha,\sigma}(Q)$ was used in [75] to raise a pseudo-analytical expression $ESF_{\alpha,\tau}(Q)$ from α and τ parameters only.

Ref. [75] gives a detailed explanation of the approach. In a nutshell, Equation 6-16 gives an expression for $ESF(Q)$ where $\xi_{\tau,\alpha,\sigma}(Q)$ is expressed in ω-space as the convolution on a restricted interval (the elastic peak) of two model functions for dynamics of the sample and of the resolution. In our case we choose a Mittag-Leffler function $\phi_{\alpha,\tau}(Q,t)$ and a Gaussian resolution function $R_\sigma(Q,\omega)$ of standard deviation σ. The important condition is that both functions admit Laplace transforms and are even in time. It makes it possible to write a quasi-analytical expression of $\xi_{\tau,\alpha,\sigma}(Q)$ based on Padé approximants of both the resolution function and the boxcar function defining the limits of the elastic peak. Hence, using Equation 6-16, $ESF(Q)$ becomes a function of parameters α and τ (σ is

estimated from the resolution function and is not a fitting parameter), reducing the fitting parameters of F(Q,t) (Equation 6-1) to α and τ only. Hence, the 2 parameters model relies on the existence of a quasi-elastic contribution to the elastic window that can be expressed quasi-analytically.

Figure 6-6 (a) and (b) show its application on our data. For dGFP and $Q > 1\text{Å}^{-1}$, dynamics are fast enough and scale close to the resolution time t_{res}, therefore the nested 2-parameter model raises parameters that are highly comparable to the 3-parameter model, especially at higher Q values when the resolution window catches most of the relaxation decay.

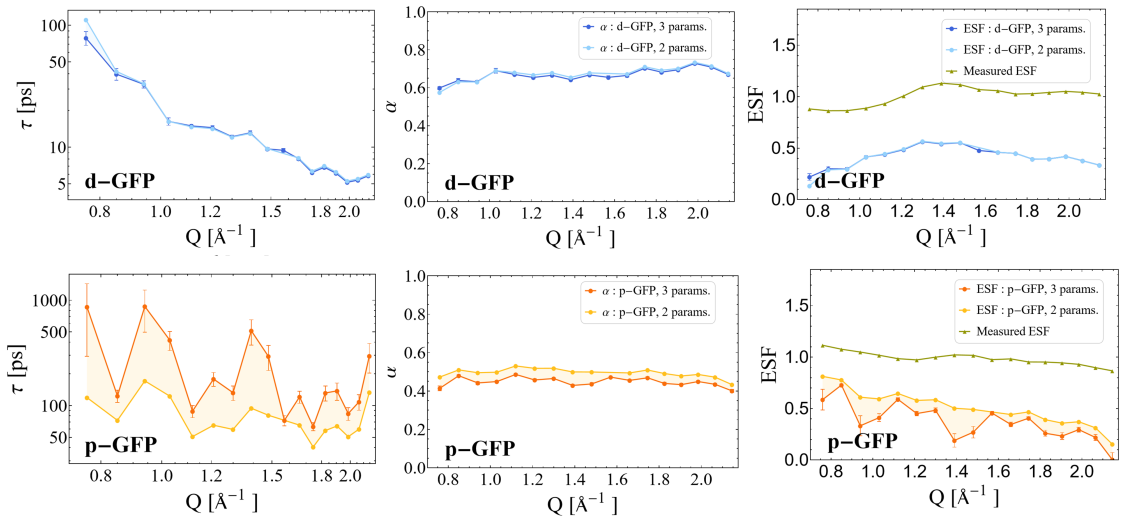

Figure 6-6: Parameters obtained for both dGFP (a) and pGFP (b) with IN5, $\Delta E = 70$ μeV, using the 3 parameters model (dark blue and orange respectively) or the 2 parameters model (light blue and orange respectively).

For pGFP, which displays strong heterogeneity and slow relaxation times, the 2 parameter-model enables to catch better τ and ESF(Q) parameters than the 3 parameter-model. Scrutiny of fitting quality show that differences in both fits arise only at large energy-exchanges $\hbar\omega$ (lower timescales), Figure 6-7 (a). A small bias is observable in residues and favors the 3-parameter model, see Figure 6-7, and a partial Fisher test with risk value of 0.05 performed to compare both models is not conclusive to accept the hypothesis that the 2-parameter model sensitively increases the fitting quality. However, from a physical point-of-view it is clear that the 2-parameter model discards the intrinsic correlation of $\tau(Q)$ and ESF(Q) parameters. We remark that an outlier for the ESF generally correspond to a τ outlier: a badly estimated "longer" relaxation time automatically implies a badly estimated "lower" asymptotic value when the timescale of dynamics are out of the

resolution window. Indeed, non-diagonal elements corresponding to τ/ESF in the covariance matrix of the 3 parameter non-linear regression are larger than other correlations. As a consequence, parameters as a function of Q are smoother with the 2-parameter model and enable to draw clearer behaviour of parameters as a function of Q.

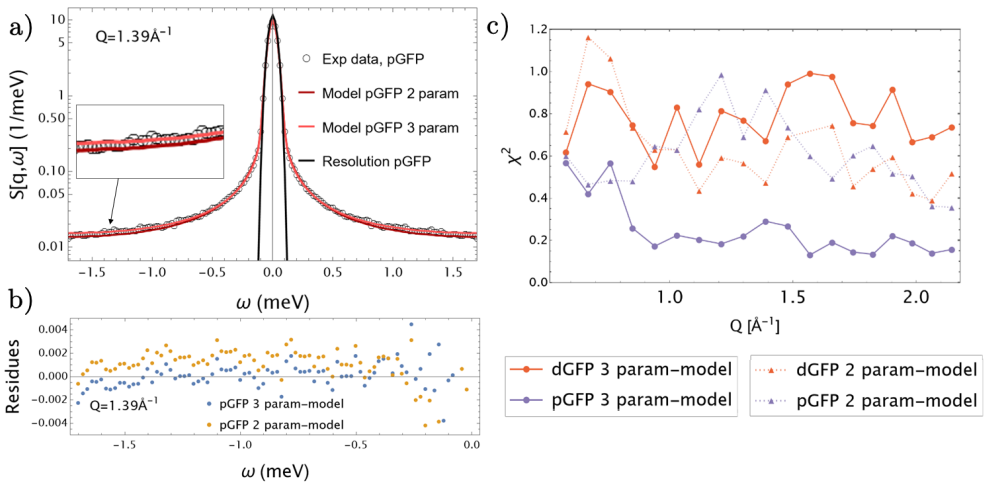

Figure 6-7: a) Non-linear regression of the pGFP data set on IN5 for $\Delta E = 70\ \mu eV$ and $Q = 1.39$ Å^{-1}, comparison of the 2 parameter-model (full light red line) and the 3-parameter model (full dark red line). b) Residues obtained for pGFP, $Q = 1.39$ Å^{-1}, compared for both models at large energy-exchanges. c) χ^2 values compared for both samples and models as a function of Q (legend at the bottom of the figure).

6.4 Can the dynamical transition arise from diffusion in an asymmetric potential with a single minimum ?

6.4.1 The dynamical transition in proteins and other systems

In 1989, Doster et al [267] reported a sudden rise in the MSD of proteins around T= 220 K as a function of temperature called the "Protein Dynamical Transition". Numerous explications have been proposed for this phenomenon. This transition occurs at higher temperatures than the hydration-independent transition attributed to methyl groups for $T \approx 120$ K.

It is clear that the solvent plays a major role in this transition [268], since hydration water motions are enhanced at similar temperature. Increasing hydration shifts the transition

temperature towards lower values [269]. Mainly hydrophilic residues undergo this transition [270], that arises concomitantly with hydration water dynamical transition and with the decrease of protein/water H-bond relaxation time [270, 271]. Hence, the water environment is key to understand the transition. However, the reason is unclear and among other explanations it has been proposed that:

- The transition is dependent on the instrumental resolution: the "frequency window" scenario implies that MSDs increase when relaxation processes suddenly enter the instrument's resolution time window [272].
- Considering that the hydrated protein displays the dynamics of a glass-forming material, β_h "statistically independent" fast inter-basin equilibrium fluctuations originating from hydration water are responsible for the dynamical transition [268].
- The transition is due to quasi-harmonic and multi-minima modes arising from T= 210 K and involving global motions of the protein [273].
- The nucleus sees a double-well harmonic potential with a strong stiffness and a softer stiffness, representing the local cages of the nucleus. Both are separated by an energy barrier defined by $E_a > k_B T$ [274].

However, it became obvious that the transition is not directly linked to to the onset of biological functions [275], and especially, the secondary and tertiary structures peculiar to proteins are not needed to observe this transition [276] which requires a minimum $h = 0.2$ for the onset of the dynamical transition [96]. Especially, the last few years have seen dynamical transitions reported in other systems: it does not appear as a "protein" feature anymore. It has been observed in PNIPAM ($\approx$ 225 K) [277, 278], trehalose ($\approx$ 250 K) [279] or even protein detergent NP40 ($\approx$ 250 K) [280], SI. In PNIPAM, the transition temperature is barely resolution dependent and is strongly affected by its environment, with strong a shift towards higher T upon dehydration ($T > 350$ K for $h = 0$) or in presence of glycerol and glucose [281]. Hence, the dynamical transition seems to be a "universal" feature of flexible macromolecules interacting with its aqueous environment. Hence, we propose here a general model that does not focus on protein characteristics.

6.4.2 Can a transition arise from the diffusion of a light particle in quantum formalism ?

In this section, we propose that the dynamical transition could arise from the temperature-driven excitations of energy-levels in an asymmetric potential. In this purpose, we choose a Morse potential in quantum formalism. It does not require to suppose diffusion in a multi-minima potential anymore, and would explain the university of the dynamical transition in macromolecules where the interactions exerted by the solvent seem to drive the dynamical transition T_{d}.

Introduction: a transition at very low temperature with an harmonic oscillator

This idea arises from the discussing differences between the classic and the quantum description of MSD as a function of temperature for a nucleus trapped in a harmonic potential ("HO") described by stiffness k, with potential

$$V_{\mathrm{HO}}(x) = \frac{1}{2}kx^2. \tag{6-18}$$

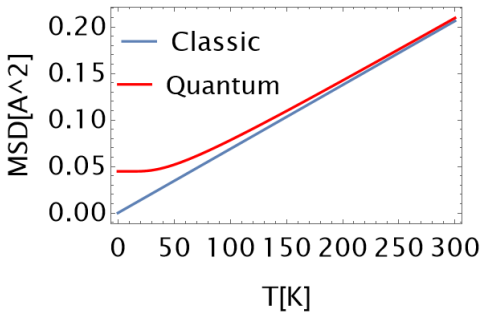

Figure 6-8: MSD(T) calculated for the classical case with Equation 6-19 and in the quantum case with Equation 6-20. k and m correspond to the values obtained with the low temperature elastic scan reported in Table 6-I for dGFP.

In the classical case, the MSDs are defined if the nucleus is subject to random forces, implying a statistical description of its dynamics. MSDs are calculated as a function of T considering that the particle is submitted to an Ornstein Uhlenbeck process (diffusion in a harmonic potential, viscosity $\eta = 0$), [38],

$$\langle (x - x(0))^2 \rangle_{\mathrm{HO,\ classic}} = \frac{k_B T}{k}, \tag{6-19}$$

with $x(0)$ the equilibrium position of the nucleus. One gets the same result using energy conservation (thermal energy with 1 degree of freedom $1/2k_BT = 1/2kx^2$ for the elastic energy). Diffusion in a quantum harmonic oscillator, assuming a Boltzmann distribution for energy levels at equilibrium,yields:

$$\langle(\hat{x} - \hat{x}(0))^2\rangle_{\text{HO, quantum}} = \frac{\hbar}{2\sqrt{km}} \coth\left(\frac{\beta\hbar\sqrt{k}}{2\sqrt{m}}\right), \tag{6-20}$$

where $\beta = \frac{1}{k_BT}$. Equation 6-19 is retrieved for $\hbar \to 0$.

The quantum and classic MSD converge at high temperature. The convergence depends on the values of m and k (or equivalently, $\omega = \sqrt{k/m}$), around $T = 150$ K in Figure 6-8. Classical and quantum MSD follow different trends: classical MSDs are simply proportional to temperature, while quantum MSD undergo a transition at low temperature ($T \approx 50$ K using the parameters obtained for GFP with the elastic scan, see Table 6-I) and gives rise to zero-point fluctuations.

Now, the question that we raise is whether a quantum description of a nucleus diffusing in a non-symmetric potential, as for example Morse potential, with a non uniform separation of energy levels ($E_{n+1} - E_n \neq \hbar\omega$) would yield a systematic transition at higher temperatures in contrast to a harmonic oscillator. The temperature-driven population of energy states would increase sharply the MSD, due to the strong increase of the distance between turning-points with higher energy levels.

Figure 6-9 compares the Morse potential with its approximate harmonic potential for low oscillations, obtained from second-order Taylor development around $x(0)$.

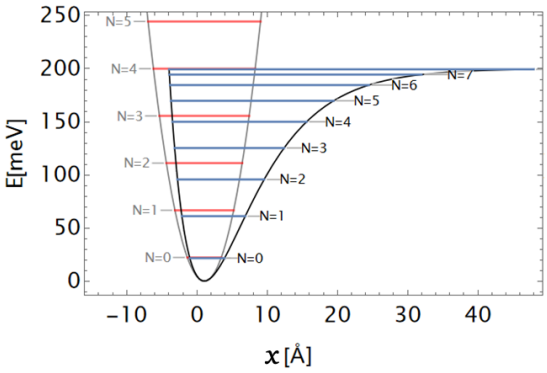

Figure 6-9: Comparison of a Morse potential ($De = 200$ meV, $m = m_{\text{hydrogen}}$, $x(0) = 1.05$ Å, $k = 8.6$ meV) with a harmonic oscillator obtained by linearisation, writing $\omega = \alpha\sqrt{\frac{2De}{m}}$ (see Equation 6-21).

Diffusion in the Morse potential

Morse potential was introduced by Philip Morse in 1929 to describe the potential of a diatomic molecule [282]. Its specificity is a finite number of energy levels determined by the potential depth De, and a potential width α. It describes how the bonding of the molecule loosens until dissociation

$$V_{\text{Morse}}(x) = De\left[\exp\left(-2\alpha(x-x_0)\right) - 2\exp\left(-\alpha(x-x_0)\right)\right]. \tag{6-21}$$

Resolving the Schrödinger equation is performed with an adapted variable change to recover a second-order differential equation. The stationary solution defines the following energy eigenvalues E_n

$$E_n = \hbar\omega(n+\frac{1}{2}) - \frac{(\hbar\omega(n+\frac{1}{2}))^2}{4De}, \tag{6-22}$$

where

$$\omega = \alpha\sqrt{\frac{2De}{m}}, \tag{6-23}$$

such that

$$E_{n+1} - E_n = \hbar\omega - (n+1)\frac{(\hbar\omega)^2}{2De}. \tag{6-24}$$

Inherent to the finite size of the well, there is a maximum energy level of index N defined by the first n value verifying $E_{n+1} - E_n \leq 0$ using Equation 6-24.

$$N = \left\lfloor \frac{2De}{\hbar\omega} - 1 \right\rfloor, \tag{6-25}$$

We are interested in the mean-squared displacements of the quantum Morse oscillator, which are defined as :

$$\langle(\hat{x} - \hat{x}(0))^2\rangle = \text{Tr}\left((\hat{x} - \hat{x}(0))^2\,\hat{\rho}\right) = \frac{1}{Z}\sum_{n=1}^{n=N}\exp\left(-\frac{E_n}{k_bT}\right)\langle n|\,(\hat{x} - \hat{x}(0))^2\,|n\rangle\,, \tag{6-26}$$

where $\hat{\rho} = \frac{\exp\left(-\beta\hat{H}\right)}{Z}$ and $Z = \text{Tr}\left(\exp\left(-\beta\hat{H}\right)\right)$.
Hence, we require the analytical expression for the diagonal matrix elements $\langle n|\,(\hat{x} - \hat{x}(0))^2\,|n\rangle$ for $n \in [0, N]$ to calculate the MSD. We do not report here the calculation, but we used the expression proposed in Ref. [283] eq.15 expressed from hypergeometric functions. We then study the emergence of a dynamical transition as a function of the parameters of the problem.

6.4.3 Numerical implementation

Method The Morse potential depends on 3 parameters α, De and m, where we always use $m = m_{\text{hydrogen}} = 1$ u. The matrix elements $\langle n| \left(\hat{x} - \hat{x}(0)\right)^2 |n\rangle$ [283] are numerically evaluated, and then averaged on energy states following Equation 6-26. We make an estimation of T_d, the dynamical transition temperature, with two methods

1. Minimizing the curvature radius

$$T_d = \min \rho(\text{MSD}(T)) = \min \left| \frac{\left(1 + \left(\frac{dMSD}{dT}\right)^2\right)^{\frac{3}{2}}}{\left(\frac{d^2MSD}{dT^2}\right)^2} \right|, \tag{6-27}$$

   of MSD as a function of T.

2. Fitting MSD with a piecewise function defined by

$$\text{MSD}(T) = \begin{cases} a_1 + k_1 T & T_{\min} \leq T \leq T_d \\ a_2 + k_2 T & T_d \leq T \leq T_{\max}, \end{cases} \tag{6-28}$$

   with a_1, a_2, k_1, k_2 and T_d free parameters, and $T_{\min} = 2$ K and $T_{\max} = 300$ K are the boundaries, in order to compare to our experimental data. Hence, T_d defines the transition between two "linear" regimes, which is not true experimentally (experiments also display a "soft" transition), but it coincides with how experimenters define it.

The curvature radius method yields more satisfying and robust results to estimate T_d, however tends to over-estimate the transition temperature.

Definition of dimensionless quantities We introduce a dimensionless energy gap ω_0:

$$\omega_0(\alpha, De, m) = \frac{\hbar\omega}{De}. \tag{6-29}$$

Which measures how the gap between energy levels ($\hbar\omega = E_1 - E_0$, see Equation 6-24) compares to the total size of the well De. as a function of ω_0. It implies from Equation 6-25 that

$$N = \lfloor \frac{2}{\omega_0} - 1 \rfloor, \tag{6-30}$$

so ω_0 also defines the maximal number of accessible energy levels.

Parametric studies In this study, we performed two parametric studies before applying the model directly to our data.

1. De varies with fixed ω_0 (thus, a fixed number of energy levels). Hence, what matters is the depth of energy of levels and the associated amplitude of matrix elements $\langle n| \left(\hat{x} - \hat{x(0)}\right)^2 |n\rangle$.

2. ω_0 varies with fixed potential depth De. It analyses the impact of the scaling of energy levels with respect to k_BT.

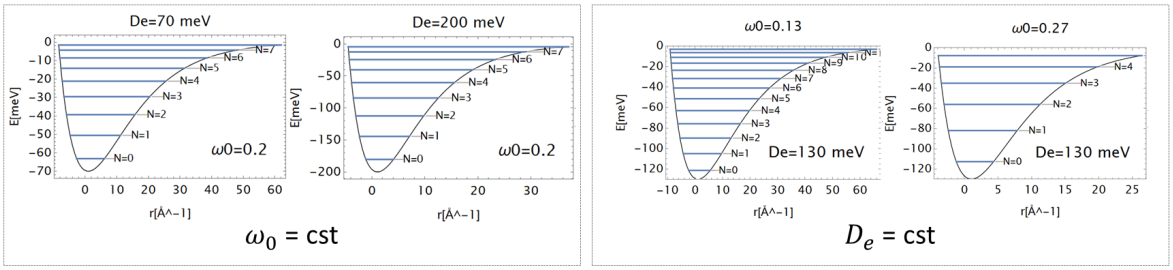

Figure 6-10: Picture of the parametric study on De and ω_0.

Although this is a coarse picture, the first study is about the impact of the thermal average (how energy levels populate and how distant they are) and the second one about the specific impact of the asymmetry and amplitude of energy levels.

Remark 1: Let us notice that De does not compare with spectroscopic values reported by Morse et al [282] where $De \approx 2eV$ corresponds to the energy dissociation for a diatomic molecule composed of two hydrogen nuclei. Indeed, we rather associate dissociation with a change of the local environment of the probe which cannot be simply reached with thermal fluctuations k_BT. Hence, we introduce for De a value that permits energy levels to weakly scale with k_BT ($k_BT = 0.17, 12.9$ and 26 meV for $T = 2$ K, $150K$ and 310 K respectively), hence, D_e is in the range of $70 - 150$ meV.

Remark 2: We are actually limited to $N \approx 18$ energy levels due to a large overflow during matrix elements calculations, since diagonal terms are successively negative and positive with increasingly large values.

6.4.4 Existence of a transition

A first observation is made with fixed $\omega_0 = 0.2$, $N = 8$, $m = m_H$, $De = 60$ meV. Matrix elements $\langle n| \left(\hat{x} - \hat{x(0)}\right)^2 |n\rangle$ increase almost exponentially with n, Figure 6-11 (b). With

this configuration, energy states are already all populated at $T = 150$ K and still increase with higher temperature, see Figure 6-11 (c). It raises a dynamical transition around $T = 100$ K.

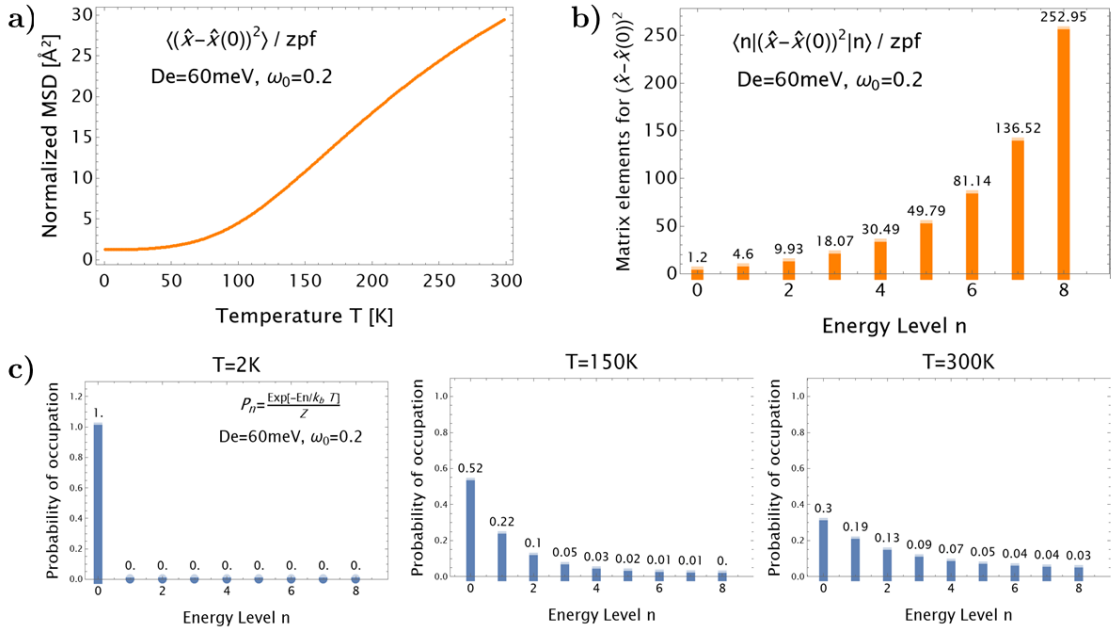

Figure 6-11: Calculations of MSD for $m = m_H$, $De = 60$ meV and $\omega_0 = 0.2$. a) Normalised MSD defined by $\text{MSD}_{\text{norm}} = \langle(\hat{x} - \hat{x}(0))^2\rangle/\text{zpf}$ where $\text{zpf} = \hbar/(2m\omega)$ are the zero-point fluctuations for the approximated HO potential. b) Normalised matrix elements $\langle n|\,(\hat{x} - \hat{x}(0))^2\,|n\rangle\,/\text{zpf}$ calculated from Matsumoto et al [283] as a function of n. c) Probability P_n for the nucleus to occupy energy level n, defined by $P_n = \exp\left(-\frac{E_n}{k_B T}\right)$.

6.4.5 Comparison of Morse matrix elements with the HO potential

The strong difference of the Morse potential with the harmonic oscilator comes from the expression of matrix elements, which for the HO are simply linear with n,

$$\langle n|\,(\hat{x} - \hat{x}(0))^2\,|n\rangle = \frac{\hbar}{2m\omega}(2n + 1). \tag{6-31}$$

Figure 6-12 shows how Morse-potential matrix elements evolve almost exponentially with n for $De = 117$ meV and $\omega_0 = 0.2$,where the HO matrix elements almost seem constant in comparison.

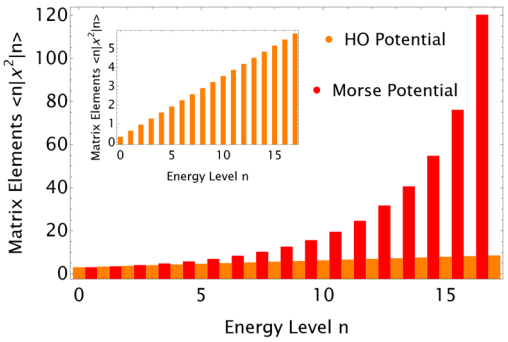

Figure 6-12: Morse potential (red) and harmonic oscillator (orange) matrix elements $\langle n|\,(\hat{x}-\hat{x}(0))^2\,|n\rangle$, compared for the case $De = 117$ meV and $\omega_0 = 0.11$

6.4.6 Parametric studies

Fixed ω_0

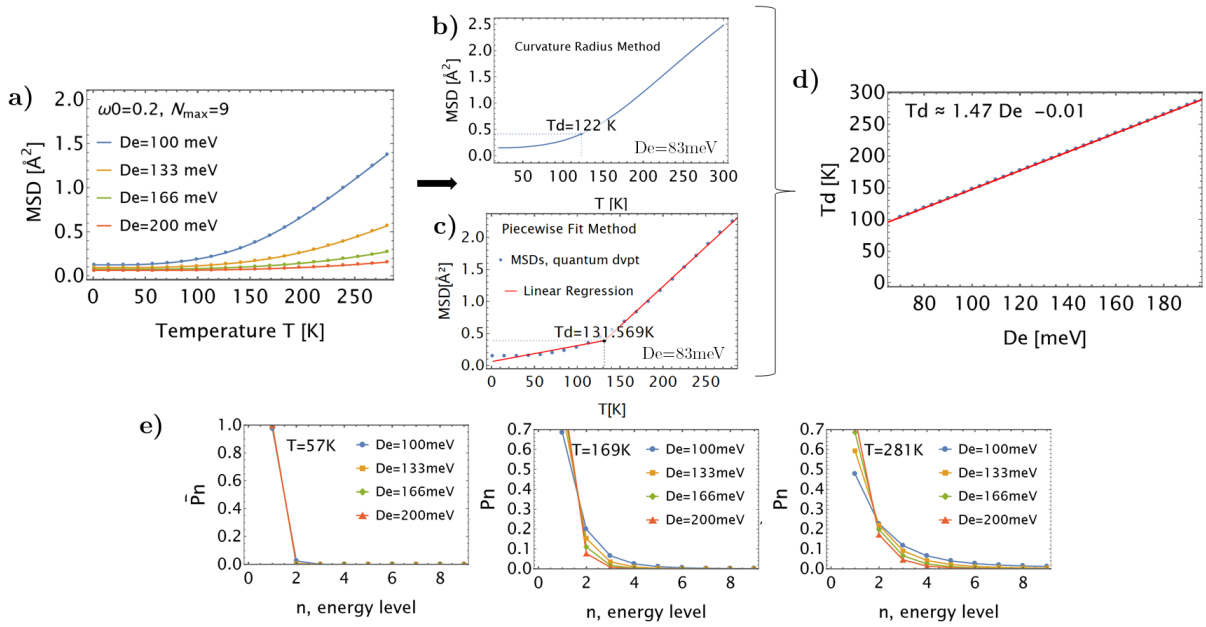

Figure 6-13: Parametric study for $De \in [70, 200]$ meV with fixed $m = m_H$ and $\omega_0 = 0.2$. a) D_e parametric study of the MSD as a function of T. b) and c) Dynamical transition temperature calculated with the curvature radius (b) and the piecewise fit (c) respectively. d) Fit of the dynamical transition as a function of De calculated with the curvature radius. e) Probability of occupation of the energy levels as a function of n, for three temperatures in the investigated range, and plotted for different the De values presented in (a).

We conduct a parametric study with $\omega_0 = 0.2$ ($N = 9$) and with De taking its values in $[70, 200]$ meV, to study the emergence of a transition with T.

As exposed on Figure 6-13 (a) to (d), increasing De for a fixed number of energy levels implies an increase of the transition temperature T_d. The trend is almost linear with T, see Figure 6-13 (d). It goes with an increasing probability of occupation for higher energy

levels with T, as shown on Figure 6-13 (e).

Hence, for a fixed number of energy levels, increasing the depth De (hence, the amplitude of energy levels) shifts the transition temperature T_d towards higher temperatures.

Fixed D_e

First, we have fixed the number of energy levels and modified the depth of the well, which appeared to tune T_d. Now, on the contrary, we modify the number of energy levels with ω_0 and keep De constant. To get a physical insight, we introduce an "effective" temperature T_{eff}, which is also fixed by ω_0. It represents the temperature required to reach the first energy level from the ground state.

$$T_{\text{eff}} = \frac{E_1 - E_0}{k_B}. \tag{6-32}$$

Results are summed up in Figure 6-14: for a fixed potential depth De, modifying the

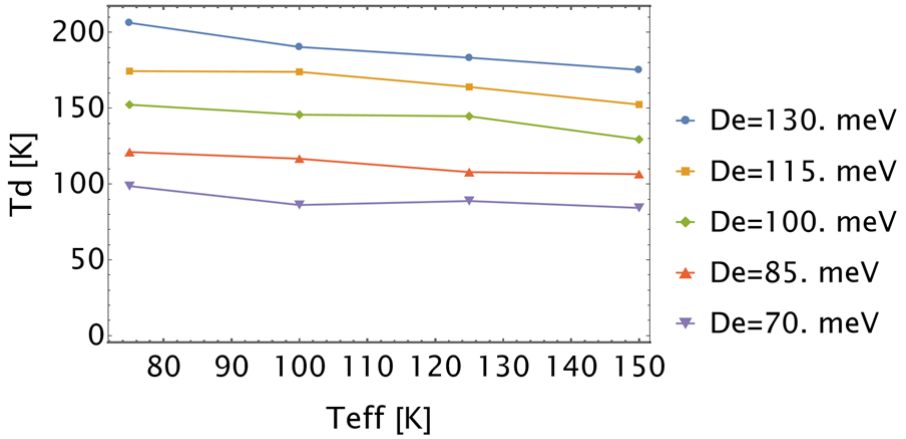

Figure 6-14: Dynamical transition T_d as a function of T_{eff}, for $De \in [70, 130]$ meV.

access to energy levels by increasing T_{eff} barely changes the transition temperature, although the number of energy levels drastically decreases with increasing T_{eff} (ex: for $De = 130$meV, N goes from 18 to 8 for T_{eff} going from 75K to 150K). Hence, this is not a determinant criterium to shift the transition, contrary to the depth of the well.

Discussion A dynamical transition, which position in T is highly dependent on the parameters of the potential, arises almost systematically. It is still unclear how it behaves as a function of ω_0 and De, but the potential well depth, in our simulations, is more of a determinant parameter in the location of the transition than the scaling of energy levels with k_BT. Hence, it means that the behaviour of $\langle n| (\hat{x} - \hat{x}(0))^2 |n\rangle$ as a function of n, determined by the potential shape, is paramount to raise this transition.

6.4.7 Application to dGFP data

In this section, we replace m and ω with the values fitted from experiments for dGFP, introduced in Table 6-I. De takes values in $[20, 110]$ meV (110 meV corresponds to $N = 18$, the maximum number of energy levels we can calculate without overflow).
We calculate MSD for both the harmonic oscillator (HO) and Morse potentials, see Figure 6-15.

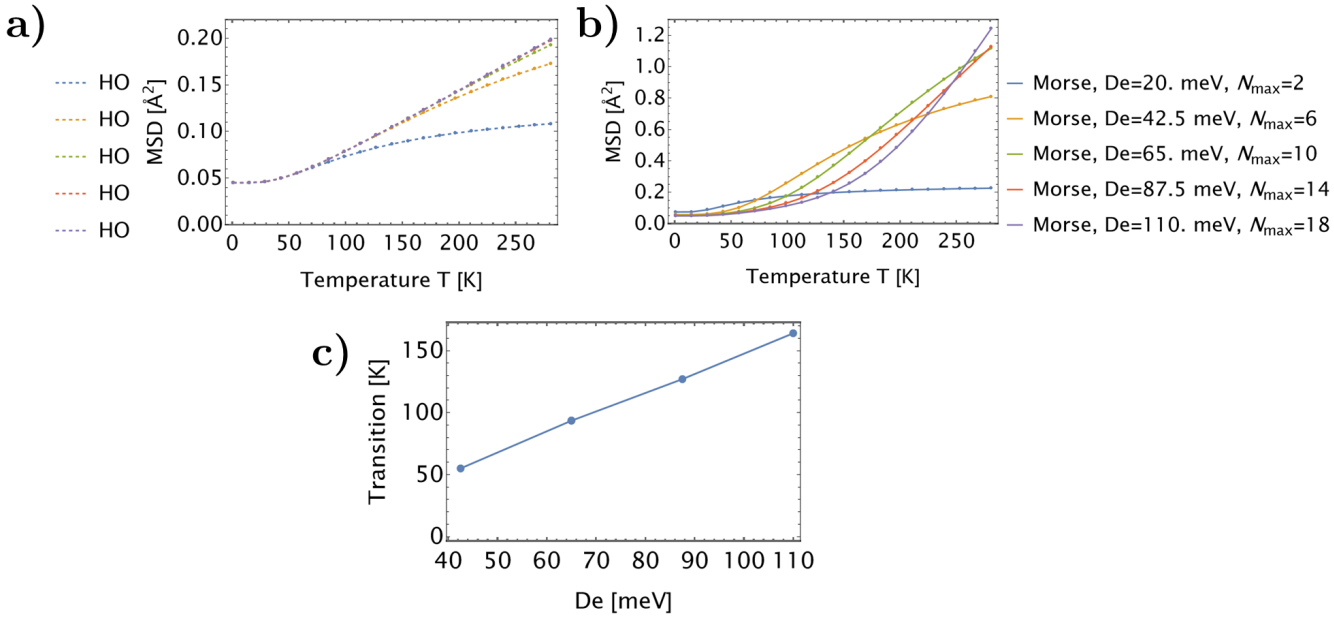

Figure 6-15: dGFP ω and m parameters fixed with values obtained by the low temperature fit of our experimental elastic scan with a quantum HO potential, Table 6-I. a) Normalised MSD(T) as a function of ω for the HO potential. b) Normalised MSD(T) as a function of ω for the Morse potential. c) Dynamical transition temperature calculated for $De = 42.5$ meV, $De = 65$ meV, $De = 87.5$ meV and $De = 110$ meV.
Rq: each colour of the legends of (a) (harmonic oscillator) and (b) (Morse potential) corresponds to the values of D_e and $N_{\max}$ specified in the legend of (b).

Harmonic potential Interestingly, the asymptotic form for the MSD of a quantum harmonic oscillator for $N \to \infty$ (Equation 6-20) is already reached for $De = 65$ meV, see

Figure 6-15 (a). The depth De defining the number of energy levels has no effect on the position of the effective transition around $T = 50$K.

Morse potential Increasing the depth De has a direct effect on the transition shift, as exposed for short time on Figure 6-15 (c) with an almost linear increase of T_d with De, with slope 1.6 KmeV^{-1} (same as Figure 6-13), $\mathrm{R}^2 > 0.99$. It is then a direct effect of the Morse potential, regarding its absence for the harmonic potential.

To compare experimental and simulated data, we calculate the pseudo force constants $k_{1,\mathrm{calc}}$ and $k_{2,\mathrm{calc}}$ with our parameters for $De = 110$ meV, deduced from the slopes of the MSD for temperatures below and above T_d. We compare them to the pseudo-force constants $k_{1,\mathrm{exp}}$ and $k_{2,\mathrm{exp}}$ obtained similarly with our elastic scan on IN5, and finally compare it to the force constants k_1 and k_2 introduced by Bicout and Zaccai in [274] . k_1 and k_2 correspond respectively to the low temperature and high temperature stiffnesses separated by $\mathrm{T_d}$.

$$\mathrm{MSD}(T) = k_B T / k_{1/2}. \tag{6-33}$$

We get $k_{1,\mathrm{exp}} = 2.76$ Nm^{-1} and $k_{1,\mathrm{calc}} = 0.98$ Nm^{-1}, while $k_{2,\mathrm{exp}} = 0.26$ Nm^{-1} and $k_{2,calc} = 0.16$ Nm^{-1} ($T_{\mathrm{d,exp}} = 234$ K, $T_{\mathrm{d,calc}} = 150$ K). For the sake of comparison, in Myoglobin [274], $k_1 = 2.76$ Nm^{-1} and $k_2 = 0.28$ Nm^{-1}.

Hence, diffusion in a single Morse potential is enough to raise a transition, although the obtained force constants are not strictly in the range of literature or experiments, or that the transition temperature obtained is here at maximum $T = 150$ K instead of $T = 220$ K due to computing limitations.

6.5 Conclusion

In this chapter we discussed different topics :

- First, the methods usually employed to study elastic scattering in proteins are highly dependent on how the timescale of motions ranges in comparison to the instrument's resolution time. It implies that a correction would be required to raise the correct MSD from elastic scans, but this correction is both non-straightforward and requires to perform QENS at different temperatures, which is not suitable. However, the estimation of this "error" made on MSD enables to improve the FBD model into a 2-parameter model that catches much better slow dynamics than the three-parameter

model.

- We propose an alternative explanation for the dynamical transition that takes roots in quantum formulation of MSD in an anharmonic Morse potential. A transition similar to the experimental one occurs as far as the scaling of $E_1 - E_0$ with $k_B T$ is reasonable, ensuring a decent number of energy levels in the well. The conditions to shift the temperature of the transition are non-trivial, and depends on all parameters. However, the transition temperature seems to shift towards higher T values with increasing potential depth for a fixed number of energy levels.
  This analysis yields reasonable results with our own experimental data: a transition around $T_\mathrm{d} = 220$ K with reasonable force constants for high temperature might arise from considering a nucleus diffusing in a local single-minimum asymmetric potential with sufficiently high depth De of the order of ≈ 100 meV exerted by neighbouring atoms. However, the stiffness $k_{1,\mathrm{calc}}$ at low T is clearly out of experimental expectation. This study is only a toy-model that requires refinement, but is a proof-of-concept for future works. In biomolecules we rather encounters a quasi-continuum of energy levels, but in this study we only computed the first energy terms due to overflow issues coming from the diagonal terms of $(\hat{x} - \hat{x}(0))^2$ matrix. We also need to compare our results to the classical equivalent like for the harmonic potential on Figure 6-8, in order to justify that this effect could not arise from classical approaches. It requires to solve the Fokker Planck equation for the Ornstein-Uhlenbeck process, where the harmonic potential is replaced with Morse potential. Another way would be to reach an analytical formula for Equation 6-26 and use $\hbar \to 0$ to reach the classical equivalent, but it seems unfeasible.

Outlook and conclusion

Outlook

Further data analyses on our dGFP and pGFP samples The present work was focused on the separation of the coherent and incoherent parts of protein dynamics and on the impact of quantum effects. To go beyond these results, other neutron data which were collected on the same samples could be further exploited:

- QENS data on LET and IN5 were also obtained for higher resolutions, $\Delta E = 10$ μeV and $\Delta E = 30$ μeV respectively, with dynamical range $E \in [-0.95, 0.95]$ meV. It corresponds to different Q ranges: on IN5, $Q \in [0.27, 0.92]$ Å^{-1} and on LET, $Q \in [0.6, 1.6]$ Å^{-1} . Although resolutions are different, we plot on a single graph the parameters that we obtained with the FBD model, see Figure 6-1.

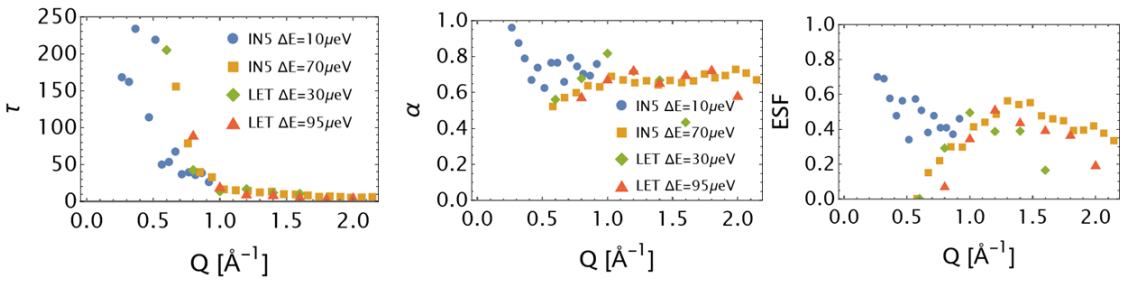

Figure 6-1: Parameters τ, α and ESF for total scattering on IN5 and LET, merged for different resolutions $\Delta E \in [10, 95]$ μeV. Uncertainties on parameters are not displayed.

For $Q > 0.8$ Å^{-1}, data corroborates the same trend for all resolutions: it is unlikely that more information is contained in high resolution data (LET, $\Delta E = 95$ μeV)

compared to low resolution data (LET, $\Delta E = 30$ μeV). Furthermore, coherent data obtained on LET at $\Delta E = 30$ μeV is too noisy to be interpreted. On the contrary, IN5 high resolution data shows interesting features: it probes lower Q values, where a sudden change of dynamics occurs: it could permit further analyses.

- We acquired inelastic neutron scattering data on the thermal neutron direct-geometry hybrid time-of-flight spectrometer Panther, ILL (incident energies $E_i = 19$ μeV, $E_i = 76$ μeV and $E_i = 171$ μeV) at $T = 2$ K, $T = 220$ K and $T = 300$ K. We also measured on Lagrange indirect-geometry TOF spectrometer, $E_f \in [20, 400]$ meV, at $T = 2$ K such that $\hbar\omega \gg k_B T$. The idea was to see if any strong isotopic effect could be explained by the presence of stronger zero-point fluctuations in pGFP with respect to the dGFP, or by quantum tunnelling, in the spirit of Ref. [284].

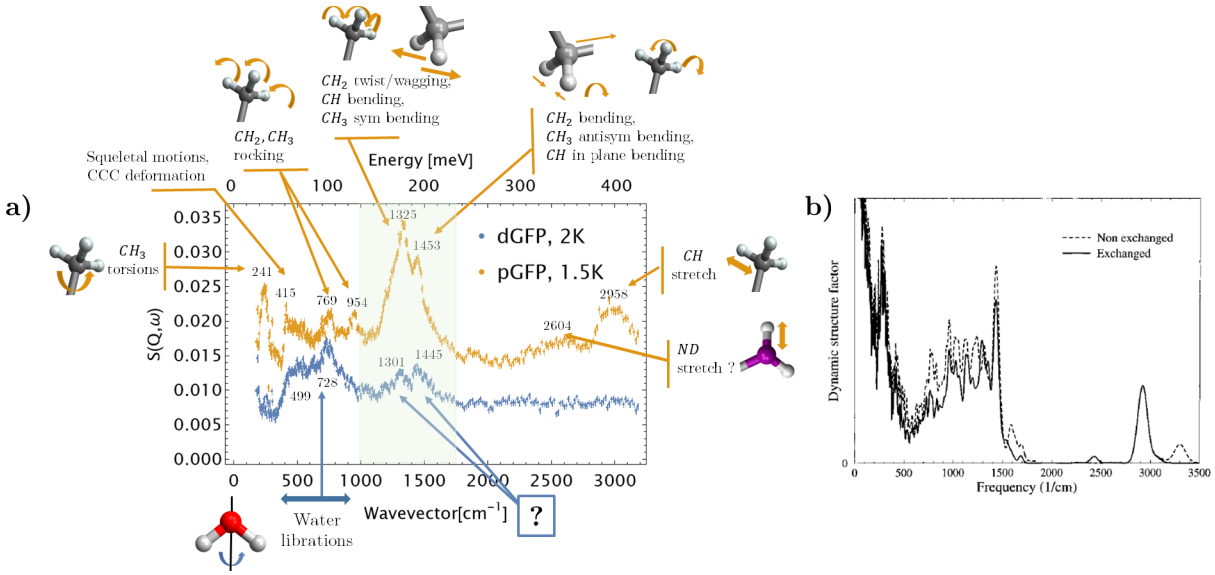

Figure 6-2: a) $S(Q, \omega)$ acquired on IN1 Lagrange for $T \approx 2$ K where the main peaks are assigned considering the simulation analysis results provided in Ref. [2, 285]. b) Isotope effects of deuterating the dry SNase (labelled "exchanged", dotted lines) obtained from simulations, adapted from Ref. [2].

We performed a first attribution of vibrational peaks using normal mode analysis and experiments on dry SNase performed by J.C. Smith et al [2, 285] and using results from experiments carried out on hydration water [286]. This attribution that can be visualised on Figure 6-2 (a) points-out that exchanged hydrogens in the D_2O layer of dGFP (dGFP: blue markers, pGFP: orange markers) hide incoherent protein contributions. It instead enhances hydration water vibrational contributions, as probed from the large impact of water librations for $E \approx 50 - 100$ meV in Figure 6-2 (a).

Figure 6-2 (a) shows the preliminary understanding of $S(Q,\omega)$ spectrum obtained on IN1. Ref. [2] already investigated the impact of perdeuteration with simulations, see Figure 6-2 (b), which entails rather small shifts ($\Delta k < 100$ cm^{-1}) for wave vectors in the $500-2000$ cm^{-1} window, but large shifts for wave vectors which are out of the spectrum (e.g. NH stretch shifts from 3300 cm^{-1} to 2430 cm^{-1}). The region where we might probe isotope effects is in light green, but it is obvious that normal mode analysis would be required for any detailed study.

Improvement of the protocol of protein powders preparation It is paramount to estimate the kinetics of H/D exchange in hydration water and to deduce whether an equilibrium is reached (as suggested from our experiments on dGFP). Especially, we did not manage to conclude on the extent of exchange occuring in a protonated protein, and if per-deuteration plays a role in the amount of exchanged water. Upon discussion with scientists, several ideas came up to assess the H/D exchange kinetics. They require a feasibility study, and are exposed below :

1. Prepare D_2O hydrated protein powders samples which are exposed to air for different periods of time, and perform polarised diffraction to monitor the percentage of exchange (no exchange case: $S_{\mathrm{coh}}(Q)/S_{\mathrm{tot}}(Q) \approx 0.8$). We could eventually derive a rate of exchange, if the time scale of exchange is slow enough to scale to the time of exposure. We could also discriminate at which stage H/D exchange occurs in the sample preparation: perhaps another explanation can be that residual H_2O was adsorbed after lyophilisation and remained despite D_2O adsorption. We also discussed using a humidity chamber developed at ILL [287] which permits to monitor the rate of humidity and its D_2O/H_2O ratio, but the relationship between ambient humidity rate and adsorption properties of the protein are non-trivial.

2. A convenient method could be ATR FTIR performed under nitrogen atmosphere, which is adapted to powder studies. Typical absorption lines of D_2O and HDO would also enable to discriminate if exchange implies single atoms or whole water molecules. It would also permit comparison of exchange between protonated and per-deuterated proteins.

3. Maithani et al [159] used surface plasmon resonance to monitor the kinetics of H/D exchange of a water droplet, but adaptation to the protein+water system and calibration with deuterium content is tricky.

Protein preparation should be performed under nitrogen atmosphere in a glove box. Under the advice of Jean Marc Zanotti (ILL) we propose the following protocol to avoid both labile atoms and hydration water exchange:

- Prepare a D_2O buffer where salts have been lyophilised in order to avoid that hydrogen remains in the buffer due to hygroscopic effects.
- Dialyse the protein against the buffer with regularly exchanged small volumes of the buffer, for about 2 weeks. The protein has to be placed in a tube with a cutoff smaller than the gyration radius of the protein.
- After lyophilisation of the protein, hydrate the protein powder in a D_2O saturated atmosphere before weighing and sealing the sample.

Buffer preparation, dialysis, hydration, weighting and sealing have to be performed under nitrogen atmosphere.
To finish with, flat sample holders are usually not adapted to the geometry of instruments used for condensed matter, as we observed on IN12 and D7 with strong variation of neutron counts when the path of the neutron is parallel to the slab. Furthermore, we lost a great amount of protein powder on LET because the annular cylinder shape requires to hydrate sticky protein powder on a thin aluminium foil. Hence, we should consider how to minimise both the impact of geometry and the loss of material during experiments on protein powders, when instruments are not optimised to flat sample holders.
Furthermore, performing polarised diffraction ahead of any polarised QENS experiment would ensure the sample's quality: especially, once the calibration is done, each measurement does not require more than an hour of acquisition. This would avoid wasting long measurements ($>$ 10h) for QENS if the sample is not correctly prepared.

Pursue the work on collective dynamics in proteins It is paramount to continue this work in a systematic way. We have only measured GFP, a rigid β-barrel protein. However, due to the prominent impact of secondary structure on protein dynamics and rigidity [135, 97] we suggest that a study on three proteins with a majority of α helices (e.g. lysozyme), a majority of β sheets (e.g. anti-freeze protein III β) or a mixed secondary structure (e.g. YFH1, yeast frataxin) could be the basis of a complete set of study. A set of 3/4 temperatures would enable to study the temperature dependence of relaxation times, which we could not do in our work.

On the other hand, to validate our work and strictly define the relaxation scales of collective dynamics, we need to study hydration water only. Ideally it implies to study a deuterated protein hydrated in H_2O at $h = 0.4$ (single hydration layer) and $h > 1$ (more than a single hydration layer) for $T = 220$K and $T = 310$K.

Of course, it is important to study higher resolution up to the ns-scale to probe side-chain fluctuations in the protein. To our knowledge the current best resolution available is $\approx 20\mu$eV on LET (ISIS) and MACS (NIST): hence, we cannot probe $t > 100$ps with polarisation analysis. Furthermore, a mass $m \approx 100$mg is not enough to assess high resolution with just a few hours of neutron exposure on LET, although this is already a huge work to produce this amount of protein. Hence, we could examine the feasibility of performing neutron spin-echo experiments on WASP (ILL) with $\lambda_i = 10$Å to reach sub-ns timescales and complete the Q range available on LET for $Q < 0.4$Å^{-1}, where coherent scattering is dominant.

Of course, we encourage strongly to perform polarised scattering with protein solutions to investigate the impact of D_2O and benefit from fully activated side-chains motions, with the same aforementioned proteins and temperatures.

We also think that we could benefit from discussions with other communities: coherent scattering has been studied in liquids, glass forming materials or polymers, for which theoretical frameworks have been proposed [109, 108], while no theoretical framework exists yet to explain coherent scattering in proteins.

Molecular dynamics simulations We recently started a collaboration with Jeremy C. Smith, Alan Hicks and Tasneem Kausar: they are currently performing molecular dynamics simulations and trajectory analysis on a hydrated GFP powder. We aim to analyse separately incoherent and coherent scattering, and analyse which motions arise from the protein or from its hydration water, with resolutions $\Delta E = 70\mu$eV and $\Delta E = 10\mu$eV. Furthermore, we especially want to separate self and distinct coherent scattering, in order to compare our results with the work of Arbe et al on MD simulations of coherent scattering of D_2O [156, 113]. Our collaboration already validated some results: an approximate 40% of hydration exchange in the D_2O layer is indeed required to explain static structure factors obtained from polarised neutrons. To compare this data with a more flexible protein, Tatsuhito Matsuo already proposed to share data of collective trajectories of a lysozyme protein obtained from MD simulations. Trajectories were analysed for total and incoherent scattering but not for coherent scattering, as published in Ref. [244].

Conclusion

It has always been admitted that proteins, due to their large amount of uniformly distributed hydrogen atoms, scatter neutrons with a dominant incoherent cross section for Q of the order of 1Å^{-1}. However, verifying this assumption has been impractical so far due to technical reasons: separation of incoherent and coherent dynamics requires a polarised neutron beam with adapted optics and detectors. Although polarised diffraction has been performed in the past and showed a non-negligible contribution of coherent scattering especially for $Q < 0.4\text{Å}^{-1}$ [33], its impact on dynamics has never been assessed before.
We propose a comparison study of a protonated (pGFP) and a deuterated (dGFP) powder-state proteins hydrated in D_2O with $h = 0.4$, which permits to clearly highlight new insights for neutron scattering applied to biomolecules.

First and foremost, we shed the light on the sub-second D/H exchange occurring in the deuterated hydration-layer of a protein when it is exposed to ambient air during sample preparation. We compared calculations to polarised diffraction data, and concluded that there is a robust 40% exchange occuring in the hydration layer of dGFP. Agreement between different techniques and dynamical ranges strongly support our findings, which are of paramount interest for experimenters: it calls for improving good practice during sample preparation. It clearly indicates that sample preparation requires careful handling in a glove box to avoid any contact to the air. To our knowledge based on scientific discussions and important research in literature, we reckon that it is an under-estimated phenomenon which adds up to labile atoms exchange. A reason for the under-estimation of this phenomenon is that a protonated protein hydration water might exchange on different timescales or to a lower extent, due to different surface interaction. Furthermore, no clear hint of the presence of H_2O appears in the diffraction pattern or the measured dynamics of a protonated protein. Eventually, a deuterated protein is usually used on purpose with H_2O for the study of its hydration water.

Although water and protein interactions are strongly entangled and occur both with similar relaxation times at the picosecond scale, we managed to single-out dynamics with polarised QENS. First and foremost, dGFP and pGFP incoherent contributions enables to assign the self-relaxation times for hydration water and internal protein dynamics, respectively. Hence, it permits to prove that coherent scattering in both proteins indeed arises

from very fast H-bond local dynamics and network rearrangement in the hydration layer, which contaminates standard experiments performed in the assumption of completely incoherent scattering. Furthermore, the Q-independent timescale found for coherent relaxation of hydration water is reminiscent of experimental and simulation findings in bulk D_2O [32, 156, 113] and other liquid, polymeric or supercooled systems [112, 239, 238]. It also gives a parameter-dependent quantitative estimation on the error made when assuming that scattering is fully incoherent.

All this study is performed with a 3-parameter model based on Fractional Brownian motion developed by Kneller et al [37, 38, 42, 40, 41, 39], describing the diffusion in a rugged harmonic potential of a Q-dependent dynamical variable, standing either for self or collective dynamics. Besides, it catches strong properties of protein relaxation processes: mathematically speaking, it is a convenient model for complex systems with self-similar behaviour. We show that this minimal model facilitates comparison between instruments, especially for the purpose of comparing polarised to non-polarised data. Obviously, it also avoids to overfit extremely noisy data due to the reduction by $\approx 2/3$ of a polarised flux with respect to a standard neutron flux. We further show that a quasi-analytical reduction of the model to 2 parameters, recently proposed by Kneller et al [75], improves the analysis when relaxation-times are very large compared to instrumental resolution.

To finish with, stemming from early reflexions in the frame of our initial project, we launch a discussion concerning elastic scattering in such complex systems. We show that zero-point fluctuations are clearly non-negligible in protein powders: a set of quantum harmonic oscillators models data very well and informs on the local environment of the protein (pGFP) and of hydration water (dGFP) at $T = 0$K. However, upon strong dependence of the analysis on the definition of the "elastic peak", we invoke the "pseudo-elastic" contribution proposed by Kneller et al [75] to quantify the impact of QENS in the experimenter-defined elastic peak. It appears that Q-dependent relaxation timescales typical of translational diffusion (e.g. self-diffusion of water in dGFP) imply that on the low Q range, long relaxation times compared to instrumental resolution greatly increases the non-elastic contribution in the "elastic peak". It artificially reduces the measured MSD. Finally, we propose a toy-model to explain that the dynamical transition in MSD as a function of temperature does not have to include instrumental resolution effects or a multi-minimal potential to raise a transition that shifts with change of the protein's

environment.

Bibliography

[1] Xiaohu Hu et al. "The dynamics of single protein molecules is non-equilibrium and self-similar over thirteen decades in time". In: *Nature Physics* 12.2 (2016), pp. 171–174. DOI: 10.1038/NPHYS3553.

[2] Anne V Goupil-Lamy et al. "High-resolution vibrational inelastic neutron scattering: a new spectroscopic tool for globular proteins". In: *Journal of the American Chemical Society* 119.39 (1997), pp. 9268–9273.

[3] Zhuo Liu et al. "Dynamical Transition of Collective Motions in Dry Proteins". In: *Physical Review Letters* 119.4 (July 2017). DOI: 10.1103/physrevlett.119.048101. URL: https://doi.org/10.1103/physrevlett.119.048101.

[4] Liang Hong, Nikolai Smolin, and Jeremy C Smith. "de Gennes narrowing describes the relative motion of protein domains". en. In: *Phys. Rev. Lett.* 112.15 (Apr. 2014), p. 158102.

[5] Kateri H. DuBay, Gregory R. Bowman, and Phillip L. Geissler. "Fluctuations within Folded Proteins: Implications for Thermodynamic and Allosteric Regulation". In: *Accounts of Chemical Research* 48.4 (Feb. 2015), pp. 1098–1105. DOI: 10.1021/ar500351b. URL: https://doi.org/10.1021/ar500351b.

[6] Daniele Di Bari et al. "Diffusive Dynamics of Bacterial Proteome as a Proxy of Cell Death". In: *ACS Central Science* 9.1 (Jan. 2023), pp. 93–102. DOI: 10.1021/acscentsci.2c01078. URL: https://doi.org/10.1021/acscentsci.2c01078.

[7] Maksym Golub et al. “The Effect of Crowding on Protein Stability, Rigidity, and High Pressure Sensitivity in Whole Cells”. In: *Langmuir* 34.35 (Aug. 2018), pp. 10419–10425. DOI: 10.1021/acs.langmuir.8b01240. URL: https://doi.org/10.1021/acs.langmuir.8b01240.

[8] Felix Roosen-Runge et al. “Protein self-diffusion in crowded solutions”. In: *Proceedings of the National Academy of Sciences* 108.29 (July 2011), pp. 11815–11820. DOI: 10.1073/pnas.1107287108. URL: https://doi.org/10.1073/pnas.1107287108.

[9] Mengting Wang et al. “Intracellular environment can change protein conformational dynamics in cells through weak interactions”. In: *Science Advances* 9.29 (2023), eadg9141.

[10] Joseph R. Lakowicz and Gregorio Weber. “Quenching of fluorescence by oxygen. Probe for structural fluctuations in macromolecules”. In: *Biochemistry* 12.21 (Oct. 1973), pp. 4161–4170. DOI: 10.1021/bi00745a020. URL: https://doi.org/10.1021/bi00745a020.

[11] Jeannine Yon-Kahn, Guy Hervé, and Jean-Luc Popot. *La structure des protéines*. fr. Mar. 2019.

[12] Kathleen L Grant and Judith P Klinman. “Evidence that both protium and deuterium undergo significant tunneling in the reaction catalyzed by bovine serum amine oxidase”. In: *Biochemistry* 28.16 (1989), pp. 6597–6605.

[13] Gregory S Engel et al. “Evidence for wavelike energy transfer through quantum coherence in photosynthetic systems”. In: *Nature* 446.7137 (2007), pp. 782–786.

[14] Jayendra N Bandyopadhyay, Tomasz Paterek, and Dagomir Kaszlikowski. “Quantum coherence and sensitivity of avian magnetoreception”. In: *Physical review letters* 109.11 (2012), p. 110502.

[15] Jennifer C. Brookes. “Quantum effects in biology: golden rule in enzymes, olfaction, photosynthesis and magnetodetection”. In: *Proceedings of the Royal Society A: Mathematical, Physical and Engineering Sciences* 473.2201 (May 2017), p. 20160822. DOI: 10.1098/rspa.2016.0822. URL: https://doi.org/10.1098/rspa.2016.0822.

[16] HD Middendorf, JT Randall, and HL Crespi. “Neutron Spectroscopy of hydrogenous and biosynthetically deuterated proteins”. In: *Neutrons in Biology* (1984), pp. 381–400.

[17] Gerald R. Kneller. “Franck–Condon picture of incoherent neutron scattering”. In: *Proceedings of the National Academy of Sciences* 115.38 (Aug. 2018), pp. 9450–9455. DOI: 10.1073/pnas.1718720115. URL: https://doi.org/10.1073/pnas.1718720115.

[18] Léon Van Hove. “Correlations in space and time and Born approximation scattering in systems of interacting particles”. In: *Physical Review* 95.1 (1954), p. 249.

[19] E. U. Condon. “The Franck-Condon Principle and Related Topics”. In: *American Journal of Physics* 15.5 (Sept. 1947), pp. 365–374. DOI: 10.1119/1.1990977. URL: https://doi.org/10.1119/1.1990977.

[20] Peters Judith et al. *Quantum effects investigated on the dynamics of a protein.* 2019. DOI: 10.5291/ILL-DATA.DIR-173. URL: https://doi.ill.fr/10.5291/ILL-DATA.DIR-173.

[21] Marc Bée. *Quasielastic neutron scattering, principles and applications in solid state chemistry, biology and materials science.* en. London, England: CRC Press, Jan. 1988.

[22] Peter L Hall and DK Ross. “Incoherent neutron scattering functions for random jump diffusion in bounded and infinite media”. In: *Molecular Physics* 42.3 (1981), pp. 673–682.

[23] Varley F Sears. “Neutron scattering lengths and cross sections”. In: *Neutron news* 3.3 (1992), pp. 26–37.

[24] Liang Hong et al. “Determination of functional collective motions in a protein at atomic resolution using coherent neutron scattering”. In: *Science advances* 2.10 (2016), e1600886. DOI: 10.1126/sciadv.1600886.

[25] Jonathan D Nickels et al. “Coherent neutron scattering and collective dynamics in the protein, GFP”. In: *Biophysical journal* 105.9 (2013), pp. 2182–2187. DOI: 10.1016/j.bpj.2013.09.029.

[26] MC Bellissent-Funel, A Filabozzi, and SH Chen. “Measurement of coherent Debye-Waller factor in in vivo deuterated C-phycocyanin by inelastic neutron scattering”. In: *Biophysical journal* 72.4 (1997), pp. 1792–1799.

[27] RM Moon, T Riste, and WC Koehler. “Polarization analysis of thermal-neutron scattering”. In: *Physical Review* 181.2 (1969), p. 920.

[28] Barbara J Gabrys, Wojciech Zajac, and Otto Schärpf. "QENS from "soft" systems: why use polarised neutrons?" In: *Physica B: Condensed Matter* 301.1-2 (2001), pp. 69–77. DOI: 10.1016/S0921-4526(01)00514-2.

[29] J. R. Stewart et al. "Disordered materials studied using neutron polarization analysis on the multi-detector spectrometer, D7". In: *Journal of Applied Crystallography* 42.1 (Dec. 2008), pp. 69–84. DOI: 10.1107/s0021889808039162. URL: https://doi.org/10.1107/s0021889808039162.

[30] Barbara J. Gabrys, Wojciech Zajac, and Otto Schärpf. "QENS from soft systems: why use polarised neutrons?" In: *Physica B: Condensed Matter* 301.1-2 (July 2001), pp. 69–77. DOI: 10.1016/s0921-4526(01)00514-2. URL: https://doi.org/10.1016/s0921-4526(01)00514-2.

[31] Tatsiana Burankova et al. "Linking Structure to Dynamics in Protic Ionic Liquids: A Neutron Scattering Study of Correlated and Single-Particle Motions". In: *Scientific Reports* 8.1 (Nov. 2018). DOI: 10.1038/s41598-018-34481-w. URL: https://doi.org/10.1038/s41598-018-34481-w.

[32] Arantxa Arbe et al. "Coherent structural relaxation of water from meso-to intermolecular scales measured using neutron spectroscopy with polarization analysis". In: *Physical Review Research* 2.2 (2020), p. 022015.

[33] A. M. Gaspar et al. "Dynamics of well-folded and natively disordered proteins in solution: a time-of-flight neutron scattering study". In: *European Biophysics Journal* 37.5 (Jan. 2008), pp. 573–582. DOI: 10.1007/s00249-008-0266-3. URL: https://doi.org/10.1007/s00249-008-0266-3.

[34] PETERS Judith et al. *Using polarization analysis to separate the coherent and incoherent scattering from protonated and deuterated protein samples.* 2021. DOI: 10.5291/ILL-DATA.8-05-468. URL: https://doi.ill.fr/10.5291/ILL-DATA.8-05-468.

[35] NIDRICHE Agathe, MANGIN-THRO Lucile, and PETERS Judith. *Use polarisation analysis to separate coherent from incoherent elastic scattering intensities with protonated and per-deuterated GFP.* 2021. DOI: 10.5291/ILL-DATA.EASY-1064. URL: https://doi.ill.fr/10.5291/ILL-DATA.EASY-1064.

[36] J. Peters. *Separate incoherent and coherent QENS of protonated and fully deuterated GFP with polarisation analysis, 10.5286/ISIS.E.RB2220225*. 2022. URL: https://doi.org/10.5286/ISIS.E.RB2220225.

[37] GR Kneller and Konrad Hinsen. "Fractional Brownian dynamics in proteins". In: *The Journal of chemical physics* 121.20 (2004), pp. 10278–10283.

[38] Gerald R Kneller. "Quasielastic neutron scattering and relaxation processes in proteins: analytical and simulation-based models". In: *Physical Chemistry Chemical Physics* 7.13 (2005), pp. 2641–2655.

[39] Melek Saouessi, Judith Peters, and Gerald R Kneller. "Asymptotic analysis of quasielastic neutron scattering data from human acetylcholinesterase reveals subtle dynamical changes upon ligand binding". In: *The Journal of chemical physics* 150.16 (2019), p. 161104.

[40] Abir N Hassani et al. "Multiscale relaxation dynamics and diffusion of myelin basic protein in solution studied by quasielastic neutron scattering". In: *The Journal of Chemical Physics* 156.2 (2022).

[41] Abir N. Hassani, Andreas M. Stadler, and Gerald R. Kneller. "Quasi-analytical resolution-correction of elastic neutron scattering from proteins". In: *The Journal of Chemical Physics* 157.13 (Oct. 2022), p. 134103. DOI: 10.1063/5.0103960. URL: https://doi.org/10.1063/5.0103960.

[42] Abir N. Hassani et al. "Signature of functional enzyme dynamics in quasielastic neutron scattering spectra: The case of Phosphoglycerate Kinase - to be published". In: *The Journal of Chemical Physics.* (2023). DOI: 10.1063/5.0166124.

[43] James Chadwick. "The existence of a neutron". In: *Proceedings of the Royal Society of London. Series A, Containing Papers of a Mathematical and Physical Character* 136.830 (1932), pp. 692–708.

[44] Tapan Chatterji. "Magnetic Neutron Scattering". In: *Neutron Scattering from Magnetic Materials*. Elsevier, 2006, pp. 1–24. DOI: 10.1016/b978-044451050-1/50002-1. URL: https://doi.org/10.1016/b978-044451050-1/50002-1.

[45] Stephen W Lovesey. *Theory of neutron scattering from condensed matter: Volume II: Polarization effects and magnetic scattering*. en. Theory of Neutron Scattering from Condensed Matter. Oxford, England: Clarendon Press, Oct. 1986.

[46] G. L. Squires. *Introduction to the Theory of Thermal Neutron Scattering*. Cambridge University Press, Mar. 2012. DOI: 10.1017/cbo9781139107808. URL: https://doi.org/10.1017/cbo9781139107808.

[47] M Blume. "Polarization effects in the magnetic elastic scattering of slow neutrons". In: *Physical Review* 130.5 (1963), p. 1670.

[48] E Fermi. "Motion of neutrons in hydrogenous substances". In: *Ricerca Scientifica* 7.2 (1936), pp. 13–52.

[49] Christopher R Gould and Eduard I Sharapov. "Fermi's favorite figure: the history of the pseudopotential concept in atomic physics and neutron physics". In: *The European Physical Journal H* 47.1 (2022), p. 10.

[50] Heinrich B Stuhrmann. "Unique aspects of neutron scattering for the study of biological systems". In: *Reports on Progress in Physics* 67.7 (June 2004), pp. 1073–1115. DOI: 10.1088/0034-4885/67/7/r02. URL: https://doi.org/10.1088/0034-4885/67/7/r02.

[51] B. van den Brandt et al. "Time-resolved nuclear spin-dependent small-angle neutron scattering from polarised proton domains in deuterated solutions". In: *The European Physical Journal B - Condensed Matter and Complex Systems* 49.2 (Jan. 2006), pp. 157–165. DOI: 10.1140/epjb/e2006-00037-9. URL: https://doi.org/10.1140/epjb/e2006-00037-9.

[52] G. L. Squires. *Introduction to the theory of thermal neutron scattering*. Mineola, N.Y: Dover Publications, 1996. ISBN: 048669447X.

[53] Madhusudan Tyagi. *Complementary Methods*. 2021.

[54] Axel Gomez et al. "Water Diffusion Proceeds via a Hydrogen-Bond Jump Exchange Mechanism". In: *The Journal of Physical Chemistry Letters* 13.21 (May 2022), pp. 4660–4666. DOI: 10.1021/acs.jpclett.2c00825. URL: https://doi.org/10.1021/acs.jpclett.2c00825.

[55] Gerald Kneller. *Energy landscape versus trajectory interpretation of neutron scattering spectra from complex systems*. June 2019. URL: http://dirac.cnrs-orleans.fr/~kneller/Talks/LANL-CNLS-June-2019.pdf.

[56] Damien Laage, Thomas Elsaesser, and James T. Hynes. "Water Dynamics in the Hydration Shells of Biomolecules". In: *Chemical Reviews* 117.16 (Mar. 2017), pp. 10694–10725. DOI: 10.1021/acs.chemrev.6b00765. URL: https://doi.org/10.1021/acs.chemrev.6b00765.

[57] Martin H Petersen et al. "Assessing Diffusion Relaxation of Interlayer Water in Clay Minerals Using a Minimalist Three-Parameter Model". In: *The Journal of Physical Chemistry C* 125.27 (2021), pp. 15085–15093.

[58] George E Uhlenbeck and Leonard S Ornstein. "On the theory of the Brownian motion". In: *Physical review* 36.5 (1930), p. 823.

[59] H. Risken. *The Fokker-Planck equation: methods of solution and applications*. 2nd ed. Springer series in synergetics. New York: Springer-Verlag, 1996. ISBN: 9783540615309.

[60] Crispin W. Gardiner. *Handbook of stochastic methods: for physics, chemistry and the natural sciences*. eng. Study ed., 2. ed., 6. print. Springer series in synergetics. Berlin Heidelberg: Springer, 2002. ISBN: 9783540616344.

[61] Gerald Kneller. *Fokker-Planck equations*. URL: http://dirac.cnrs-orleans.fr/~kneller/Lectures/EMSTU/Lecture3.pdf.

[62] Patrick Cheridito, Hideyuki Kawaguchi, and Makoto Maejima. "Fractional Ornstein-Uhlenbeck processes". In: *Electronic Journal of Probability* 8.none (Jan. 2003). DOI: 10.1214/ejp.v8-125. URL: https://doi.org/10.1214/ejp.v8-125.

[63] IUliia S. Mishura. *Stochastic calculus for fractional Brownian motion and related processes*. Lecture notes in mathematics. Berlin; New York: Springer-Verlag, 2008. ISBN: 9783540758723.

[64] Hans Frauenfelder, Fritz Parak, and Robert D Young. "Conformational substates in proteins". In: *Annual review of biophysics and biophysical chemistry* 17.1 (1988), pp. 451–479.

[65] Robert Zwanzig. "Diffusion in a rough potential." In: *Proceedings of the National Academy of Sciences* 85.7 (1988), pp. 2029–2030.

[66] H Frauenfelder, S G Sligar, and P G Wolynes. "The Energy Landscapes and Motions of Proteins." In: *Science* 254.5038 (1991), pp. 1598–1603. DOI: 10.1126/science.1749933.

[67] Sheila Khodadadi and Alexei P. Sokolov. “Atomistic details of protein dynamics and the role of hydration water”. In: *Biochimica et Biophysica Acta (BBA) - General Subjects* 1861.1 (Jan. 2017), pp. 3546–3552. DOI: 10.1016/j.bbagen.2016.04.028. URL: https://doi.org/10.1016/j.bbagen.2016.04.028.

[68] J. Sabatier, Om Prakash Agrawal, and J A Tenreiro Machado. *Advances in fractional calculus: theoretical developments and applications in physics and engineering*. eng. Dordrecht, The Netherlands: Springer Verlag, 2007. ISBN: 9781402060410.

[69] Rudolf Gorenflo et al., eds. *Mittag-Leffler Functions, Related Topics and Applications*. Springer Monographs in Mathematics. Heidelberg: Springer, 2014. ISBN: 978-3-662-43929-6 978-3-662-43930-2.

[70] Francesco Mainardi. “Why the Mittag-Leffler Function Can Be Considered the Queen Function of the Fractional Calculus?” In: *Entropy* 22.12 (Nov. 2020), p. 1359. DOI: 10.3390/e22121359. URL: https://doi.org/10.3390/e22121359.

[71] *NIST handbook of mathematical functions*. Cambridge; New York: Cambridge University Press: NIST, 2010. ISBN: 9780521192255.

[72] Melek Saouessi. “Modélisation de la dynamique fonctionnelle de l’Acétylcholinestérase humainevue par diffusion quasi-élastique de neutrons”. 2020ORLE3065. PhD thesis. 2020. URL: http://www.theses.fr/2020ORLE3065/document.

[73] Hazime Mori. “Transport, collective motion, and Brownian motion”. In: *Progress of theoretical physics* 33.3 (1965), pp. 423–455.

[74] Robert Zwanzig. *Nonequilibrium Statistical Mechanics*. Oxford ; New York: Oxford University Press, 2001. ISBN: 978-0-19-514018-7.

[75] Abir N Hassani, Andreas M Stadler, and Gerald R Kneller. “Quasi-analytical resolution-correction of elastic neutron scattering from proteins”. In: *The Journal of Chemical Physics* 157.13 (2022), p. 134103.

[76] I. E. T. Iben et al. “Glassy Behavior of a Protein.” In: *Phys Rev Lett* 62.16 (1989), pp. 1916–1919. DOI: 10.1103/PhysRevLett.62.1916.

[77] Walter G Glöckle and Theo F Nonnenmacher. “A fractional calculus approach to self-similar protein dynamics”. In: *Biophysical Journal* 68.1 (1995), pp. 46–53. DOI: 10.1016/S0006-3495(95)80157-8.

[78] Wei Min et al. “Observation of a Power-Law Memory Kernel for Fluctuations within a Single Protein Molecule”. In: *Physical Review Letters* 94.19 (May 2005). DOI: 10.1103/physrevlett.94.198302. URL: https://doi.org/10.1103/physrevlett.94.198302.

[79] J. Schlichter et al. “Protein dynamics at low temperatures”. In: *The Journal of Chemical Physics* 112.6 (Feb. 2000), pp. 3045–3050. DOI: 10.1063/1.480879. URL: https://doi.org/10.1063/1.480879.

[80] K. Kämpf, F. Klameth, and M. Vogel. “Power-law and logarithmic relaxations of hydrated proteins: A molecular dynamics simulations study”. In: *The Journal of Chemical Physics* 137.20 (Nov. 2012), p. 205105. DOI: 10.1063/1.4768046. URL: https://doi.org/10.1063/1.4768046.

[81] Aoife C. Fogarty and Damien Laage. “Water Dynamics in Protein Hydration Shells: The Molecular Origins of the Dynamical Perturbation”. In: *The Journal of Physical Chemistry B* 118.28 (Feb. 2014), pp. 7715–7729. DOI: 10.1021/jp409805p. URL: https://doi.org/10.1021/jp409805p.

[82] G.R. Kneller and M. Saouessi. “Mittag–Leffler Relaxation in the Light of Asymptotic Analysis”. In: *Acta Physica Polonica B* 53.2 (2022), p. 1. DOI: 10.5506/aphyspolb.53.2-a2. URL: https://doi.org/10.5506/aphyspolb.53.2-a2.

[83] Gerald R Kneller and Melek Saouessi. “Weak self-similarity of the Mittag–Leffler relaxation function”. In: *Journal of Physics A: Mathematical and Theoretical* 53.20 (May 2020), 20LT01. DOI: 10.1088/1751-8121/ab83c8. URL: https://doi.org/10.1088/1751-8121/ab83c8.

[84] Victoria Garcia Sakai. *Quasi-Elastic Neutron Scattering*. Sept. 2013.

[85] F. Natali et al. “Anomalous water dynamics in brain: a combined diffusion magnetic resonance imaging and neutron scattering investigation”. In: *Journal of The Royal Society Interface* 16.157 (Aug. 2019), p. 20190186. DOI: 10.1098/rsif.2019.0186. URL: https://doi.org/10.1098/rsif.2019.0186.

[86] F. Volino and A.J. Dianoux. “Neutron incoherent scattering law for diffusion in a potential of spherical symmetry: general formalism and application to diffusion inside a sphere”. In: *Molecular Physics* 41.2 (Oct. 1980), pp. 271–279. DOI: 10.1080/00268978000102761. URL: https://doi.org/10.1080/00268978000102761.

[87] M.-C. Bellissent-Funel et al. “Dynamics of hydration water in protein”. In: *Journal de Physique I* 2.6 (June 1992), pp. 995–1001. DOI: 10.1051/jp1:1992192. URL: https://doi.org/10.1051/jp1:1992192.

[88] M. Trapp et al. “Correlation of the dynamics of native ihuman/i acetylcholinesterase and its inhibited huperzine A counterpart from sub-picoseconds to nanoseconds”. In: *Journal of The Royal Society Interface* 11.97 (Aug. 2014), p. 20140372. DOI: 10.1098/rsif.2014.0372. URL: https://doi.org/10.1098/rsif.2014.0372.

[89] VF Sears. “Theory of cold neutron scattering by homonuclear diatomic liquids: I. Free rotation”. In: *Canadian Journal of Physics* 44.6 (1966), pp. 1279–1297.

[90] Maksym Golub et al. “Dynamics of a family of cyan fluorescent proteins probed by incoherent neutron scattering”. In: *Journal of The Royal Society Interface* 16.152 (Mar. 2019), p. 20180848. DOI: 10.1098/rsif.2018.0848. URL: https://doi.org/10.1098/rsif.2018.0848.

[91] Jonathan D Nickels, Victoria Garcıa Sakai, and Alexei P Sokolov. “Dynamics in protein powders on the nanosecond–picosecond time scale are dominated by localized motions”. In: *The Journal of Physical Chemistry B* 117.39 (2013), pp. 11548–11555. DOI: 10.1021/jp4058884.

[92] Graham Williams and David C. Watts. “Non-symmetrical dielectric relaxation behaviour arising from a simple empirical decay function”. In: *Transactions of the Faraday Society* 66 (1970), p. 80. DOI: 10.1039/tf9706600080. URL: https://doi.org/10.1039/tf9706600080.

[93] S-H Chen et al. “Observation of fragile-to-strong dynamic crossover in protein hydration water”. In: *Proceedings of the National Academy of Sciences* 103.24 (2006), pp. 9012–9016.

[94] Sverre Holm. “Time domain characterization of the Cole-Cole dielectric model”. In: *Journal of Electrical Bioimpedance* 11.1 (Jan. 2020), pp. 101–105. DOI: 10.2478/joeb-2020-0015. URL: https://doi.org/10.2478/joeb-2020-0015.

[95] VK Malinovsky, VN Novikov, and AP Sokolov. “Log-normal spectrum of low-energy vibrational excitations in glasses”. In: *Physics Letters A* 153.1 (1991), pp. 63–66.

[96] Hiroshi Nakagawa and Mikio Kataoka. "How can we derive hydration water dynamics with incoherent neutron scattering and molecular dynamics simulation?" In: *Biophysics and Physicobiology* 16.0 (2019), pp. 213–219. DOI: 10.2142/biophysico.16.0_213. URL: https://doi.org/10.2142/biophysico.16.0_213.

[97] Stefania Perticaroli et al. "Rigidity, Secondary Structure, and the Universality of the Boson Peak in Proteins". In: *Biophysical Journal* 106.12 (June 2014), pp. 2667–2674. DOI: 10.1016/j.bpj.2014.05.009. URL: https://doi.org/10.1016/j.bpj.2014.05.009.

[98] Kurt Sköld. "Small energy transfer scattering of cold neutrons from liquid argon". In: *Physical Review Letters* 19.18 (1967), p. 1023.

[99] D. Richter et al. "From Rouse dynamics to local relaxation: A neutron spin echo study on polyisobutylene melts". In: *The Journal of Chemical Physics* 111.13 (Oct. 1999), pp. 6107–6120. DOI: 10.1063/1.479907. URL: https://doi.org/10.1063/1.479907.

[100] Andreas M. Stadler et al. "Internal Nanosecond Dynamics in the Intrinsically Disordered Myelin Basic Protein". In: *Journal of the American Chemical Society* 136.19 (May 2014), pp. 6987–6994. DOI: 10.1021/ja502343b. URL: https://doi.org/10.1021/ja502343b.

[101] Ralf Biehl et al. "Direct Observation of Correlated Interdomain Motion in Alcohol Dehydrogenase". In: *Physical Review Letters* 101.13 (Sept. 2008). DOI: 10.1103/physrevlett.101.138102. URL: https://doi.org/10.1103/physrevlett.101.138102.

[102] Zimei Bu et al. "Coupled protein domain motion iniTaq/ipolymerase revealed by neutron spin-echo spectroscopy". In: *Proceedings of the National Academy of Sciences* 102.49 (Nov. 2005), pp. 17646–17651. DOI: 10.1073/pnas.0503388102. URL: https://doi.org/10.1073/pnas.0503388102.

[103] P.G. De Gennes. "Liquid dynamics and inelastic scattering of neutrons". In: *Physica* 25.7-12 (Jan. 1959), pp. 825–839. DOI: 10.1016/0031-8914(59)90006-0. URL: https://doi.org/10.1016/0031-8914(59)90006-0.

[104] George H Vineyard. "Scattering of slow neutrons by a liquid". In: *Physical Review* 110.5 (1958), p. 999. DOI: 10.1103/PhysRev.110.999.

[105] KS Singwi. "Coherent scattering of slow neutrons by a liquid". In: *Physical Review* 136.4A (1964), A969.

[106] Tatsiana Burankova et al. "Collective ion diffusion and localized single particle dynamics in pyridinium-based ionic liquids". In: *The journal of physical chemistry B* 118.49 (2014), pp. 14452–14460. DOI: https://doi.org/10.1021/jp5092416.

[107] Arantxa Arbe, Fernando Alvarez, and Juan Colmenero. "Insight into the Structure and Dynamics of Polymers by Neutron Scattering Combined with Atomistic Molecular Dynamics Simulations". In: *Polymers* 12.12 (Dec. 2020), p. 3067. DOI: 10.3390/polym12123067. URL: https://doi.org/10.3390/polym12123067.

[108] Juan Colmenero, Fernando Alvarez, and Arantxa Arbe. "Collective dynamics of glass-forming polymers at intermediate length scales". In: *EPJ Web of Conferences* 83 (2015). Ed. by B. Frick et al., p. 01001. DOI: 10.1051/epjconf/20158301001. URL: https://doi.org/10.1051/epjconf/20158301001.

[109] VN Novikov, Kenneth S Schweizer, and Alexei P Sokolov. "Coherent neutron scattering and collective dynamics on mesoscale". In: *The Journal of Chemical Physics* 138.16 (2013).

[110] P. Carlsson et al. "The segmental dynamics of a polymer electrolyte investigated by coherent quasielastic neutron scattering". In: *The Journal of Chemical Physics* 114.21 (June 2001), pp. 9645–9656. DOI: 10.1063/1.1370073. URL: https://doi.org/10.1063/1.1370073.

[111] Arantxa Arbe et al. "Dielectric susceptibility of liquid water: Microscopic insights from coherent and incoherent neutron scattering". In: *Physical review letters* 117.18 (2016), p. 185501.

[112] Arantxa Arbe et al. "Collective dynamics and self-motions in the van der Waals liquid tetrahydrofuran from meso-to inter-molecular scales disentangled by neutron spectroscopy with polarization analysis". In: *The Journal of Chemical Physics* 158.18 (2023).

[113] Fernando Alvarez, Arantxa Arbe, and Juan Colmenero. "Understanding the coherent dynamic structure factor of liquid water measured by neutron spectroscopy with polarization analysis: a Molecular Dynamics simulations study". In: *EPJ Web of Conferences*. Vol. 272. EDP Sciences. 2022, p. 01011.

[114] Fernando Alvarez, Arantxa Arbe, and Juan Colmenero. "Unraveling the coherent dynamic structure factor of liquid water at the mesoscale by molecular dynamics simulations". In: *The Journal of Chemical Physics* 155.24 (2021), p. 244509.

[115] Xavier Doligez et al. "Fundamentals of reactor physics with a view to the (possible) futures of nuclear energy". In: *Comptes Rendus Physique* 18.7-8 (Sept. 2017), pp. 372–380. DOI: 10.1016/j.crhy.2017.10.004. URL: https://doi.org/10.1016/j.crhy.2017.10.004.

[116] David Findlay et al. "Practical Guide to the ISIS Neutron and Muon Source". In: UKRI Creative Services.

[117] P. Courtois. "Neutron Optics". In: EIROforum School on Instrumentation, 2019.

[118] Ross Stewart. "Polarized Neutrons". In: Oxford School on Neutron Scattering, 2011.

[119] Kathryn Krycka. "Overview of Polarization Analysis for Neutron Scattering". In: National School on Neutron and X-Ray Scattering, 2020.

[120] Ferenc Mezei. "Neutron spin echo: A new concept in polarized thermal neutron techniques". In: *Zeitschrift für Physik A Hadrons and nuclei* 255 (1972), pp. 146–160.

[121] J. Ollivier and J.-M. Zanotti. "Diffusion inélastique de neutrons par temps de vol". In: *JDN 16 – Diffusion Inélastique des Neutrons pour l'Etude des Excitations dans la Matiére Condensée*. EDP Sciences, 2010. DOI: 10.1051/sfn/2010006. URL: https://doi.org/10.1051/sfn/2010006.

[122] Quentin Berrod et al. "Inelastic and quasi-elastic neutron scattering. Application to soft-matter". In: *EPJ Web of Conferences* 188 (2018). Ed. by M. Wolff and F. Cousin, p. 05001. DOI: 10.1051/epjconf/201818805001. URL: https://doi.org/10.1051/epjconf/201818805001.

[123] Ross Stewart. "Practical Neutron Scattering Course". In: Oxford School on Neutron Scattering (2019), 2019.

[124] R Zorn. "Multiple scattering correction of polarized neutron diffraction data". In: *Nuclear Instruments and Methods In Physics Research Section A: Accelerators, Spectrometers, Detectors and Associated Equipment* 479.2-3 (2002), pp. 568–584.

[125] R.I. Bewley, J.W. Taylor, and S.M. Bennington. "LET, a cold neutron multi-disk chopper spectrometer at ISIS". In: *Nuclear Instruments and Methods in Physics Research Section A: Accelerators, Spectrometers, Detectors and Associated Equipment* 637.1 (May 2011), pp. 128–134. DOI: 10.1016/j.nima.2011.01.173. URL: https://doi.org/10.1016/j.nima.2011.01.173.

[126] Karin Schmalzl et al. "The upgrade of the cold neutron three-axis spectrometer IN12 at the ILL". In: *Nuclear Instruments and Methods in Physics Research Section A: Accelerators, Spectrometers, Detectors and Associated Equipment* 819 (2016), pp. 89–98.

[127] Barbara Gabrýs and Otto Schärpf. "Scattering from polymers using polarised neutrons: a new development". In: *Physica B: Condensed Matter* 180-181 (June 1992), pp. 495–498. DOI: 10.1016/0921-4526(92)90803-z. URL: https://doi.org/10.1016/0921-4526(92)90803-z.

[128] Ann Maconnachie. "On the assessment of incoherent neutron scattering intensities from polymer systems". In: *Polymer* 25.8 (Aug. 1984), pp. 1068–1072. DOI: 10.1016/0032-3861(84)90340-9. URL: https://doi.org/10.1016/0032-3861(84)90340-9.

[129] W Zajac. "Structure of poly(ethylene oxide) (PEO and PEO·LiSO3CF3) studied with spin polarised neutrons". In: *Solid State Ionics* 147.3-4 (Apr. 2002), pp. 213–223. DOI: 10.1016/s0167-2738(02)00019-x. URL: https://doi.org/10.1016/s0167-2738(02)00019-x.

[130] G Cassella et al. "Polarization analysis on the LET cold neutron spectrometer using a sup3/supHe spin-filter: first results". In: *Journal of Physics: Conference Series* 1316.1 (Oct. 2019), p. 012007. DOI: 10.1088/1742-6596/1316/1/012007. URL: https://doi.org/10.1088/1742-6596/1316/1/012007.

[131] Wolfram Research Inc. *Mathematica, Version 13.2*. Champaign, IL, 2022. URL: https://www.wolfram.com/mathematica.

[132] D Richard, M Ferrand, and GJ Kearley. "Analysis and visualisation of neutron-scattering data". In: *Journal of Neutron Research* 4.1-4 (1996), pp. 33–39.

[133] Reiner Zorn. "Sample shape contribution to the resolution function of time-of-flight neutron scattering spectrometers". In: *Nuclear Instruments and Methods in Physics Research Section A: Accelerators, Spectrometers, Detectors and Associated*

Equipment 674 (May 2012), pp. 85–91. DOI: 10.1016/j.nima.2012.01.055. URL: https://doi.org/10.1016/j.nima.2012.01.055.

[134] Jonathan D Nickels et al. "Dynamics of protein and its hydration water: neutron scattering studies on fully deuterated GFP". In: *Biophysical journal* 103.7 (2012), pp. 1566–1575.

[135] Stefania Perticaroli et al. "Secondary structure and rigidity in model proteins". In: *Soft Matter* 9.40 (2013), p. 9548. DOI: 10.1039/c3sm50807b. URL: https://doi.org/10.1039/c3sm50807b.

[136] Osamu Shimomura, Frank H Johnson, and Yo Saiga. "Extraction, purification and properties of aequorin, a bioluminescent protein from the luminous hydromedusan, Aequorea". In: *Journal of cellular and comparative physiology* 59.3 (1962), pp. 223–239.

[137] Mark A. Hink et al. "Structural Dynamics of Green Fluorescent Protein Alone and Fused with a Single Chain Fv Protein". In: *Journal of Biological Chemistry* 275.23 (June 2000), pp. 17556–17560. DOI: 10.1074/jbc.m001348200. URL: https://doi.org/10.1074/jbc.m001348200.

[138] Marc Zimmer. "Green Fluorescent Protein (GFP): Applications, Structure, and Related Photophysical Behavior". In: *Chemical Reviews* 102.3 (Feb. 2002), pp. 759–782. DOI: 10.1021/cr010142r. URL: https://doi.org/10.1021/cr010142r.

[139] Michael Haertlein et al. "Biomolecular deuteration for neutron structural biology and dynamics". In: *Methods in enzymology*. Vol. 566. Elsevier, 2016, pp. 113–157. DOI: 10.1016/bs.mie.2015.11.001.

[140] Florent Bernaudat and Leif Bülow. "Combined hydrophobic-metal binding fusion tags for applications in aqueous two-phase partitioning". In: *Protein expression and purification* 46.2 (2006), pp. 438–445. DOI: 10.1016/j.pep.2005.09.026.

[141] Marcus Trapp et al. "Correlation of the dynamics of native human acetylcholinesterase and its inhibited huperzine A counterpart from sub-picoseconds to nanoseconds". In: *Journal of the Royal Society Interface* 11.97 (2014), p. 20140372.

[142] Y.M Efimova et al. "On the neutron scattering length density of proteins in H2O/D2O". In: *Physica B: Condensed Matter* 350.1-3 (July 2004), E877–E880. DOI: 10.1016/j.physb.2004.03.227. URL: https://doi.org/10.1016/j.physb.2004.03.227.

[143] Chie Shibazaki et al. “Direct Observation of the Protonation States in the Mutant Green Fluorescent Protein”. In: *The Journal of Physical Chemistry Letters* 11.2 (Dec. 2019), pp. 492–496. DOI: 10.1021/acs.jpclett.9b03252. URL: https://doi.org/10.1021/acs.jpclett.9b03252.

[144] M. Adachi et al. *Neutron crystal structure of the mutant green fluorescent protein (EGFP)*. Apr. 2020. DOI: 10.2210/pdb6l26/pdb. URL: https://doi.org/10.2210/pdb6l26/pdb.

[145] John J. Skinner et al. “Protein dynamics viewed by hydrogen exchange”. In: *Protein Science* 21.7 (June 2012), pp. 996–1005. DOI: 10.1002/pro.2081. URL: https://doi.org/10.1002/pro.2081.

[146] Jacob Arthur Brockerman. “Characterizing labile protons by NMR spectroscopy”. en. In: (2019). DOI: 10.14288/1.0376560. URL: https://doi.library.ubc.ca/10.14288/1.0376560.

[147] Sheena E. Radford et al. “Hydrogen exchange in native and denatured states of hen egg-white lysozyme”. In: *Proteins: Structure, Function, and Genetics* 14.2 (Oct. 1992), pp. 237–248. DOI: 10.1002/prot.340140210. URL: https://doi.org/10.1002/prot.340140210.

[148] Yoshitomo Hamuro et al. “Rapid analysis of protein structure and dynamics by hydrogen/deuterium exchange mass spectrometry”. en. In: *J. Biomol. Tech.* 14.3 (Sept. 2003), pp. 171–182.

[149] Benjamin T. Walters et al. “Minimizing Back Exchange in the Hydrogen Exchange-Mass Spectrometry Experiment”. In: *Journal of the American Society for Mass Spectrometry* 23.12 (Sept. 2012), pp. 2132–2139. DOI: 10.1007/s13361-012-0476-x. URL: https://doi.org/10.1007/s13361-012-0476-x.

[150] Yawen Bai et al. “Primary structure effects on peptide group hydrogen exchange”. In: *Proteins: Structure, Function, and Genetics* 17.1 (Sept. 1993), pp. 75–86. DOI: 10.1002/prot.340170110. URL: https://doi.org/10.1002/prot.340170110.

[151] Yury Kostyukevich et al. “Hydrogen/deuterium exchange in mass spectrometry”. In: *Mass Spectrometry Reviews* 37.6 (Mar. 2018), pp. 811–853. DOI: 10.1002/mas.21565. URL: https://doi.org/10.1002/mas.21565.

[152] Y. M. Efimova et al. “Stability of globular proteins in H2O and D2O”. In: *Biopolymers* 85.3 (2007), pp. 264–273. DOI: 10.1002/bip.20645. URL: https://doi.org/10.1002/bip.20645.

[153] Y M Efimova. *Proteins at Surfaces*. Amsterdam, NY: IOS Press, Mar. 2006.

[154] Giuseppe Maria Paternò et al. “Neutron polarisation analysis of Polymer:Fullerene blends for organic photovoltaics”. In: *Polymer* 105 (Nov. 2016), pp. 407–413. DOI: 10.1016/j.polymer.2016.07.079. URL: https://doi.org/10.1016/j.polymer.2016.07.079.

[155] M-C Bellissent-Funel et al. “Neutron structure factors of in-vivo deuterated amorphous protein C-phycocyanin”. In: *Biophysical journal* 64.5 (1993), pp. 1542–1549. DOI: 10.1016/S0006-3495(93)81523-6.

[156] Fernando Alvarez, Arantxa Arbe, and Juan Colmenero. “Unraveling the coherent dynamic structure factor of liquid water at the mesoscale by molecular dynamics simulations”. In: *The Journal of Chemical Physics* 155.24 (2021), p. 244509. DOI: 10.1063/5.0074588.

[157] Helmut Grubmüller, Theoretical Biophysics Group, Institut für Medizinische Optik, Ludwig-Maximilians-Universität München, München, Germany. *Solvate*. URL: https://www.mpinat.mpg.de/grubmueller/solvate.

[158] Maddalena Bin et al. “Wide-angle X-ray scattering and molecular dynamics simulations of supercooled protein hydration water”. In: *Physical Chemistry Chemical Physics* 23.34 (2021), pp. 18308–18313. DOI: 10.1039/d1cp02126e. URL: https://doi.org/10.1039/d1cp02126e.

[159] Sanchi Maithani, Abhijit Maity, and Manik Pradhan. “Probing the H–D isotopic exchange reaction in a liquid droplet ivia/i surface plasmon resonance”. In: *Journal of Analytical Atomic Spectrometry* 37.3 (2022), pp. 544–550. DOI: 10.1039/d1ja00350j. URL: https://doi.org/10.1039/d1ja00350j.

[160] B. Topley and H. Eyring. “The Separation of the Hydrogen Isotopes by Electrolysis. Part I”. In: *The Journal of Chemical Physics* 2.5 (May 1934), pp. 217–230. DOI: 10.1063/1.1749454. URL: https://doi.org/10.1063/1.1749454.

[161] Elizabeth A. Raymond et al. "Hydrogen-Bonding Interactions at the Vapor/Water Interface Investigated by Vibrational Sum-Frequency Spectroscopy of HOD/Hsub2/subO/Dsub2/ Mixtures and Molecular Dynamics Simulations". In: *The Journal of Physical Chemistry B* 107.2 (Dec. 2002), pp. 546–556. DOI: 10.1021/jp021366w. URL: https://doi.org/10.1021/jp021366w.

[162] Igor V. Stiopkin et al. "Hydrogen bonding at the water surface revealed by isotopic dilution spectroscopy". In: *Nature* 474.7350 (June 2011), pp. 192–195. DOI: 10.1038/nature10173. URL: https://doi.org/10.1038/nature10173.

[163] F A Deeney and J P O'Leary. "An experimental investigation of the process of isotope exchange that takes place when heavy water is exposed to the atmosphere". In: *European Journal of Physics* 30.4 (May 2009), pp. 871–876. DOI: 10.1088/0143-0807/30/4/019. URL: https://doi.org/10.1088/0143-0807/30/4/019.

[164] T.-S. Kim et al. "Laser-based sensor for a coolant leak detection in a nuclear reactor". In: *Applied Physics B* 100.2 (Mar. 2010), pp. 437–442. DOI: 10.1007/s00340-010-3947-4. URL: https://doi.org/10.1007/s00340-010-3947-4.

[165] Tadeja Gao et al. "Ion influence on surface water dynamics and proton exchange at protein surfaces – A unified model for transverse and longitudinal NMR relaxation dispersion". In: *Journal of Molecular Liquids* 367 (Dec. 2022), p. 120451. DOI: 10.1016/j.molliq.2022.120451. URL: https://doi.org/10.1016/j.molliq.2022.120451.

[166] Kathleen Wood et al. "Coincidence of dynamical transitions in a soluble protein and its hydration water: direct measurements by neutron scattering and MD simulations". In: *Journal of the American Chemical Society* 130.14 (2008), pp. 4586–4587. DOI: 10.1021/ja710526r.

[167] GJ Nilsen et al. "Polarisation analysis on the LET time-of-flight spectrometer". In: *Journal of Physics: Conference Series*. Vol. 862. 1. IOP Publishing. 2017, p. 012019. DOI: 10.1088/1742-6596/862/1/012019.

[168] Barbara J Gabrys. "Applications of polarized neutrons to non-magnetic materials". In: *Physica B: Condensed Matter* 267-268 (June 1999), pp. 122–130. DOI: 10.1016/s0921-4526(99)00009-5. URL: https://doi.org/10.1016/s0921-4526(99)00009-5.

[169] Kirill Nemkovski et al. “SHERPA: A Spectrometer with High Energy Resolution and Polarisation Analysis”. In: *EPJ Web of Conferences* 272 (2022). Ed. by A. Arbe and J. Colmenero, p. 02004. DOI: 10.1051/epjconf/202227202004. URL: https://doi.org/10.1051/epjconf/202227202004.

[170] Ron Milo and Rob Phillips. *Cell biology by the numbers*. New York, NY: Garland Science, Taylor Francis Group, 2016. ISBN: 9780815345374.

[171] Behzad Chahkandi, Mohammad Chahkandi, and Bentolhoda Ashrafi. “Conformational analysis of N- and C-terminally protected tripeptide model glycyl-isoleucine-glycyl: An ab initio and DFT study”. In: *Physical Chemistry Research* 2.1 (May 2014). DOI: 10.22036/pcr.2014.3858. URL: https://doi.org/10.22036/pcr.2014.3858.

[172] Hans Frauenfelder, Stephen G Sligar, and Peter G Wolynes. “The energy landscapes and motions of proteins”. In: *Science* 254.5038 (1991), pp. 1598–1603.

[173] Hans Frauenfelder, Paul W Fenimore, and Robert D Young. “Protein dynamics and function: insights from the energy landscape and solvent slaving”. In: *IUBMB life* 59.8-9 (2007), pp. 506–512.

[174] M. Siddiqui, Maulik Badmalia, and Trushar Patel. “Bioinformatic Analysis of Structure and Function of LIM Domains of Human Zyxin Family Proteins”. In: *International Journal of Molecular Sciences* 22.5 (Mar. 2021), p. 2647. DOI: 10.3390/ijms22052647. URL: https://doi.org/10.3390/ijms22052647.

[175] Giorgio Schirò and Martin Weik. “Role of hydration water in the onset of protein structural dynamics”. In: *Journal of Physics: Condensed Matter* 31.46 (Aug. 2019), p. 463002. DOI: 10.1088/1361-648x/ab388a. URL: https://doi.org/10.1088/1361-648x/ab388a.

[176] Markus H. J. Seifert et al. “Backbone Dynamics of Green Fluorescent Protein and the Effect of Histidine 148 Substitution”. In: *Biochemistry* 42.9 (Feb. 2003), pp. 2500–2512. DOI: 10.1021/bi026481b. URL: https://doi.org/10.1021/bi026481b.

[177] J. H. Roh et al. “Onsets of Anharmonicity in Protein Dynamics”. In: *Physical Review Letters* 95.3 (July 2005). DOI: 10.1103/physrevlett.95.038101. URL: https://doi.org/10.1103/physrevlett.95.038101.

[178] H. Jansson et al. “Dynamics of a protein and its surrounding environment: A quasielastic neutron scattering study of myoglobin in water and glycerol mixtures”. In: *The Journal of Chemical Physics* 130.20 (May 2009). DOI: 10.1063/1.3138765. URL: https://doi.org/10.1063/1.3138765.

[179] A.M. Stadler et al. “From Powder to Solution: Hydration Dependence of Human Hemoglobin Dynamics Correlated to Body Temperature”. In: *Biophysical Journal* 96.12 (June 2009), pp. 5073–5081. DOI: 10.1016/j.bpj.2009.03.043. URL: https://doi.org/10.1016/j.bpj.2009.03.043.

[180] Marion Jasnin et al. “Solvent isotope effect on macromolecular dynamics in E. coli”. In: *European Biophysics Journal* 37.5 (Feb. 2008), pp. 613–617. DOI: 10.1007/s00249-008-0281-4. URL: https://doi.org/10.1007/s00249-008-0281-4.

[181] Patrizia Cioni and Giovanni B Strambini. “Effect of heavy water on protein flexibility”. In: *Biophysical journal* 82.6 (2002), pp. 3246–3253.

[182] Sheh-Yi Sheu et al. “Molecular dynamics of hydrogen bonds in protein- D2O: the solvent isotope effect”. In: *The journal of physical chemistry A* 112.5 (2008), pp. 797–802.

[183] Chang-Hwei Chen, Fred Tow, and Donald S. Berns. “Solvent isotope effect on the differences in structure and stability between normal and deuterated proteins”. In: *Biopolymers* 23.5 (May 1984), pp. 887–896. DOI: 10.1002/bip.360230506. URL: https://doi.org/10.1002/bip.360230506.

[184] Setare Mostajabi Sarhangi and Dmitry V. Matyushov. “Effect of Water Deuteration on Protein Electron Transfer”. In: *The Journal of Physical Chemistry Letters* 14.3 (Jan. 2023), pp. 723–729. DOI: 10.1021/acs.jpclett.2c03690. URL: https://doi.org/10.1021/acs.jpclett.2c03690.

[185] Joao Ramos et al. “Structural insights into protein folding, stability and activity using in vivo perdeuteration of hen egg-white lysozyme”. In: *IUCrJ* 8.3 (Mar. 2021), pp. 372–386. DOI: 10.1107/s2052252521001299. URL: https://doi.org/10.1107/s2052252521001299.

[186] Yang Tai et al. “X-ray crystallographic studies on the hydrogen isotope effects of green fluorescent protein at sub-ångström resolutions”. In: *Acta Crystallographica*

Section D Structural Biology 75.12 (Nov. 2019), pp. 1096–1106. DOI: 10.1107/s2059798319014608. URL: https://doi.org/10.1107/s2059798319014608.

[187] Parker J. Nichols et al. "Deuteration of nonexchangeable protons on proteins affects their thermal stability, side-chain dynamics, and hydrophobicity". In: *Protein Science* 29.7 (May 2020), pp. 1641–1654. DOI: 10.1002/pro.3878. URL: https://doi.org/10.1002/pro.3878.

[188] Flora Meilleur et al. "Structural Stability and Dynamics of Hydrogenated and Perdeuterated Cytochrome P450cam (CYP101)". In: *Biochemistry* 43.27 (June 2004), pp. 8744–8753. DOI: 10.1021/bi049418q. URL: https://doi.org/10.1021/bi049418q.

[189] Ai Woon Yee et al. "Impact of Deuteration on the Assembly Kinetics of Transthyretin Monitored by Native Mass Spectrometry and Implications for Amyloidoses". In: *Angewandte Chemie International Edition* 55.32 (June 2016), pp. 9292–9296. DOI: 10.1002/anie.201602747. URL: https://doi.org/10.1002/anie.201602747.

[190] Liliya Vugmeyster et al. "Correlated motions of C$\prime$–N and C–C pairs in protonated and per-deuterated GB3". In: *Journal of Biomolecular NMR* 72.1-2 (Aug. 2018), pp. 39–54. DOI: 10.1007/s10858-018-0205-2. URL: https://doi.org/10.1007/s10858-018-0205-2.

[191] Anders Nilsson and Lars G. M. Pettersson. "The structural origin of anomalous properties of liquid water". In: *Nature Communications* 6.1 (Dec. 2015). DOI: 10.1038/ncomms9998. URL: https://doi.org/10.1038/ncomms9998.

[192] Antonio Cupane et al. "Experimental evidence for a liquid-liquid crossover in deeply cooled confined water". In: *Physical Review Letters* 113.21 (2014), p. 215701.

[193] J Teixeira and M-C Bellissent-Funel. "Dynamics of water studied by neutron scattering". In: *Journal of Physics: Condensed Matter* 2.S (1990), SA105.

[194] K. S. Singwi and Alf Sjölander. "Diffusive Motions in Water and Cold Neutron Scattering". In: *Physical Review* 119.3 (Aug. 1960), pp. 863–871. DOI: 10.1103/physrev.119.863. URL: https://doi.org/10.1103/physrev.119.863.

[195] Johan Qvist, Helmut Schober, and Bertil Halle. "Structural dynamics of supercooled water from quasielastic neutron scattering and molecular simulations". In: *The Journal of Chemical Physics* 134.14 (Apr. 2011). DOI: 10.1063/1.3578472. URL: https://doi.org/10.1063/1.3578472.

[196] SH Chen et al. “Model for single-particle dynamics in supercooled water”. In: *Physical Review E* 59.6 (1999), p. 6708.

[197] Martin H Petersen et al. “Revisiting the modeling of quasielastic neutron scattering from bulk water”. In: *EPJ Web of Conferences*. Vol. 272. EDP Sciences. 2022, p. 01012. DOI: 10.1051/epjconf/202227201012.

[198] Daniela Russo et al. “Pressure effects on collective density fluctuations in water and protein solutions”. In: *Proceedings of the National Academy of Sciences* 114.43 (Oct. 2017), pp. 11410–11415. DOI: 10.1073/pnas.1705279114. URL: https://doi.org/10.1073/pnas.1705279114.

[199] M-C Bellissent-Funel. “Status of experiments probing the dynamics of water in confinement”. In: *The European Physical Journal E* 12 (2003), pp. 83–92.

[200] Liang Hong et al. “Three Classes of Motion in the Dynamic Neutron-Scattering Susceptibility of a Globular Protein”. In: *Physical Review Letters* 107.14 (Sept. 2011). DOI: 10.1103/physrevlett.107.148102. URL: https://doi.org/10.1103/physrevlett.107.148102.

[201] Filip Persson, Pär Söderhjelm, and Bertil Halle. “The geometry of protein hydration”. In: *The Journal of Chemical Physics* 148.21 (June 2018). DOI: 10.1063/1.5026744. URL: https://doi.org/10.1063/1.5026744.

[202] Sudipta Kumar Sinha, Sudip Chakraborty, and Sanjoy Bandyopadhyay. “Thickness of the Hydration Layer of a Protein from Molecular Dynamics Simulation”. In: *The Journal of Physical Chemistry B* 112.27 (June 2008), pp. 8203–8209. DOI: 10.1021/jp8000724. URL: https://doi.org/10.1021/jp8000724.

[203] Stefania Perticaroli et al. “Description of Hydration Water in Protein (Green Fluorescent Protein) Solution”. In: *Journal of the American Chemical Society* 139.3 (Nov. 2016), pp. 1098–1105. DOI: 10.1021/jacs.6b08845. URL: https://doi.org/10.1021/jacs.6b08845.

[204] Stefania Perticaroli et al. “Description of hydration water in protein (green fluorescent protein) solution”. In: *Journal of the American Chemical Society* 139.3 (2017), pp. 1098–1105.

[205] Nicholas B. Rego, Erte Xi, and Amish J. Patel. "Identifying hydrophobic protein patches to inform protein interaction interfaces". In: *Proceedings of the National Academy of Sciences* 118.6 (Feb. 2021). DOI: 10.1073/pnas.2018234118. URL: https://doi.org/10.1073/pnas.2018234118.

[206] Daniela Russo et al. "Vibrational Density of States of Hydration Water at Biomolecular Sites: Hydrophobicity Promotes Low Density Amorphous Ice Behavior". In: *Journal of the American Chemical Society* 133.13 (Mar. 2011), pp. 4882–4888. DOI: 10.1021/ja109610f. URL: https://doi.org/10.1021/ja109610f.

[207] Tadeja Janc et al. "Multiscale Water Dynamics on Protein Surfaces: Protein-Specific Response to Surface Ions". In: *The Journal of Physical Chemistry B* 125.31 (Aug. 2021), pp. 8673–8681. DOI: 10.1021/acs.jpcb.1c02513. URL: https://doi.org/10.1021/acs.jpcb.1c02513.

[208] A. Paciaroni et al. "Fingerprints of Amorphous Icelike Behavior in the Vibrational Density of States of Protein Hydration Water". In: *Physical Review Letters* 101.14 (Oct. 2008). DOI: 10.1103/physrevlett.101.148104. URL: https://doi.org/10.1103/physrevlett.101.148104.

[209] Baofu Qiao et al. "Water follows polar and nonpolar protein surface domains". In: *Proceedings of the National Academy of Sciences* 116.39 (Sept. 2019), pp. 19274–19281. DOI: 10.1073/pnas.1910225116. URL: https://doi.org/10.1073/pnas.1910225116.

[210] Franci Merzel and Jeremy C Smith. "Is the first hydration shell of lysozyme of higher density than bulk water?" In: *Proceedings of the National Academy of Sciences* 99.8 (2002), pp. 5378–5383.

[211] Rui Shi. "The structural order of protein hydration water". In: *Communications in Theoretical Physics* 74.9 (2022), p. 095602.

[212] Manuela Maurer and Chris Oostenbrink. "Water in protein hydration and ligand recognition". In: *Journal of Molecular Recognition* 32.12 (Aug. 2019). DOI: 10.1002/jmr.2810. URL: https://doi.org/10.1002/jmr.2810.

[213] Antonino Caliò et al. "Unravelling the Adaptation Mechanisms to High Pressure in Proteins". In: *International Journal of Molecular Sciences* 23.15 (July 2022), p. 8469. DOI: 10.3390/ijms23158469. URL: https://doi.org/10.3390/ijms23158469.

[214] M-C Bellissent-Funel and J Teixeira. “Dynamics of water studied by coherent and incoherent inelastic neutron scattering”. In: *Journal of molecular structure* 250.2-4 (1991), pp. 213–230.

[215] Viren Pattni et al. “Distinct Protein Hydration Water Species Defined by Spatially Resolved Spectra of Intermolecular Vibrations”. In: *The Journal of Physical Chemistry B* 121.31 (July 2017), pp. 7431–7442. DOI: 10.1021/acs.jpcb.7b03966. URL: https://doi.org/10.1021/acs.jpcb.7b03966.

[216] Hiroshi Nakagawa and Naoki Yamamoto. “Incoherent Neutron Scattering and Terahertz Time-Domain Spectroscopy on Protein and Hydration Water”. In: *Life* 13.2 (Jan. 2023), p. 318. DOI: 10.3390/life13020318. URL: https://doi.org/10.3390/life13020318.

[217] Damien Laage and James T. Hynes. “A Molecular Jump Mechanism of Water Reorientation”. In: *Science* 311.5762 (Feb. 2006), pp. 832–835. DOI: 10.1126/science.1122154. URL: https://doi.org/10.1126/science.1122154.

[218] Z. F. Brotzakis et al. “Dynamics of Hydration Water around Native and Misfolded -Lactalbumin”. In: *The Journal of Physical Chemistry B* 120.21 (May 2016), pp. 4756–4766. DOI: 10.1021/acs.jpcb.6b02592. URL: https://doi.org/10.1021/acs.jpcb.6b02592.

[219] Samir Kumar Pal, Jorge Peon, and Ahmed H. Zewail. “Biological water at the protein surface: Dynamical solvation probed directly with femtosecond resolution”. In: *Proceedings of the National Academy of Sciences* 99.4 (Feb. 2002), pp. 1763–1768. DOI: 10.1073/pnas.042697899. URL: https://doi.org/10.1073/pnas.042697899.

[220] Tanping Li et al. “Hydration Dynamics and Time Scales of Coupled Water-Protein Fluctuations”. In: *Journal of the American Chemical Society* 129.11 (Feb. 2007), pp. 3376–3382. DOI: 10.1021/ja0685957. URL: https://doi.org/10.1021/ja0685957.

[221] Yangzhong Qin, Lijuan Wang, and Dongping Zhong. “Dynamics and mechanism of ultrafast water–protein interactions”. In: *Proceedings of the National Academy of Sciences* 113.30 (June 2016), pp. 8424–8429. DOI: 10.1073/pnas.1602916113. URL: https://doi.org/10.1073/pnas.1602916113.

[222] Giorgio Schirò et al. “Translational diffusion of hydration water correlates with functional motions in folded and intrinsically disordered proteins”. In: *Nature communications* 6.1 (2015), p. 6490.

[223] Luyuan Zhang et al. “Protein Hydration Dynamics and Molecular Mechanism of Coupled Water-Protein Fluctuations”. In: *Journal of the American Chemical Society* 131.30 (July 2009), pp. 10677–10691. DOI: 10.1021/ja902918p. URL: https://doi.org/10.1021/ja902918p.

[224] Yangzhong Qin, Lijuan Wang, and Dongping Zhong. “Dynamics and mechanism of ultrafast water–protein interactions”. In: *Proceedings of the National Academy of Sciences* 113.30 (2016), pp. 8424–8429. DOI: 10.1073/pnas.160291611.

[225] Anna Stefaniuk et al. “Isotope effects observed in diluted D2O/H2O mixtures identify HOD-induced low-density structures in D2O but not H2O”. In: *Scientific Reports* 12.1 (Nov. 2022). DOI: 10.1038/s41598-022-23551-9. URL: https://doi.org/10.1038/s41598-022-23551-9.

[226] FX Prielmeier et al. “The pressure dependence of self diffusion in supercooled light and heavy water”. In: *Berichte der Bunsengesellschaft für physikalische Chemie* 92.10 (1988), pp. 1111–1117.

[227] R Mills. “Self-diffusion in normal and heavy water in the range 1-45. deg.” In: *The Journal of Physical Chemistry* 77.5 (1973), pp. 685–688.

[228] Manfred Holz et al. “Experimental study of dynamic isotope effects in molecular liquids: Detection of translation-rotation coupling”. In: *The Journal of Chemical Physics* 104.2 (Jan. 1996), pp. 669–679. DOI: 10.1063/1.470863. URL: https://doi.org/10.1063/1.470863.

[229] J.H. Roh et al. “Influence of Hydration on the Dynamics of Lysozyme”. In: *Biophysical Journal* 91.7 (Oct. 2006), pp. 2573–2588. DOI: 10.1529/biophysj.106.082214. URL: https://doi.org/10.1529/biophysj.106.082214.

[230] Melek Saouessi, Judith Peters, and Gerald R. Kneller. “Asymptotic analysis of quasielastic neutron scattering data from human acetylcholinesterase reveals subtle dynamical changes upon ligand binding”. In: *The Journal of Chemical Physics* 150.16 (Apr. 2019), p. 161104. DOI: 10.1063/1.5094625. URL: https://doi.org/10.1063/1.5094625.

[231] S. Khodadadi et al. “The origin of the dynamic transition in proteins”. In: *The Journal of Chemical Physics* 128.19 (May 2008). DOI: 10.1063/1.2927871. URL: https://doi.org/10.1063/1.2927871.

[232] S. Khodadadi, S. Pawlus, and A. P. Sokolov. “Influence of Hydration on Protein Dynamics: Combining Dielectric and Neutron Scattering Spectroscopy Data”. In: *The Journal of Physical Chemistry B* 112.45 (Oct. 2008), pp. 14273–14280. DOI: 10.1021/jp8059807. URL: https://doi.org/10.1021/jp8059807.

[233] Amos M Tsai, Terrence J Udovic, and Dan A Neumann. “The inverse relationship between protein dynamics and thermal stability”. In: *Biophysical Journal* 81.4 (2001), pp. 2339–2343.

[234] S.-H. Chen et al. “Observation of fragile-to-strong dynamic crossover in protein hydration water”. In: *Proceedings of the National Academy of Sciences* 103.24 (June 2006), pp. 9012–9016. DOI: 10.1073/pnas.0602474103. URL: https://doi.org/10.1073/pnas.0602474103.

[235] Hiroshi Nakagawa and Mikio Kataoka. “How can we derive hydration water dynamics with incoherent neutron scattering and molecular dynamics simulation?” In: *Biophysics and Physicobiology* 16 (2019), pp. 213–219.

[236] Marco Grimaldo et al. “Dynamics of proteins in solution”. In: *Quarterly Reviews of Biophysics* 52 (2019), e7. DOI: 10.1017/S0033583519000027.

[237] Martin H. Petersen et al. “Assessing Diffusion Relaxation of Interlayer Water in Clay Minerals Using a Minimalist Three-Parameter Model”. In: *The Journal of Physical Chemistry C* 125.27 (July 2021), pp. 15085–15093. DOI: 10.1021/acs.jpcc.1c04322. URL: https://doi.org/10.1021/acs.jpcc.1c04322.

[238] Philip H. Handle, Lorenzo Rovigatti, and Francesco Sciortino. “Independent Slow Dynamics in Atomic and Molecular Systems”. In: *Physical Review Letters* 122.17 (May 2019). DOI: 10.1103/physrevlett.122.175501. URL: https://doi.org/10.1103/physrevlett.122.175501.

[239] Giovanni Nava et al. “Fluctuating Elasticity Mode in Transient Molecular Networks”. In: *Physical Review Letters* 119.7 (Aug. 2017). DOI: 10.1103/physrevlett.119.078002. URL: https://doi.org/10.1103/physrevlett.119.078002.

[240] C. Alba-Simionesco et al. *"de Gennes" narrowing in supercooled molecular liquids : Evidence for center-of-mass dominated slow dynamics*. 2001. DOI: 10.48550/ARXIV.COND-MAT/0103599. URL: https://arxiv.org/abs/cond-mat/0103599.

[241] Peng Luo et al. "Q-dependent collective relaxation dynamics of glass-forming liquid Ca0.4K0.6(NO3)1.4 investigated by wide-angle neutron spin-echo". In: *Nature Communications* 13.1 (Apr. 2022). DOI: 10.1038/s41467-022-29778-4. URL: https://doi.org/10.1038/s41467-022-29778-4.

[242] Peng Luo et al. "Q-dependent collective relaxation dynamics of glass-forming liquid Ca0. 4K0. 6 (NO3) 1.4 investigated by wide-angle neutron spin-echo". In: *Nature communications* 13.1 (2022), p. 2092.

[243] Barbara Gabrys, Julia S Higgins, and Otto Schärpf. "Contamination by coherent scattering of the elastic incoherent structure factor observed in neutron scattering experiments". In: *Journal of the Chemical Society, Faraday Transactions 1: Physical Chemistry in Condensed Phases* 82.6 (1986), pp. 1923–1927.

[244] Tatsuhito Matsuo. "Changes in protein dynamical parameters derived from quasi-elastic neutron scattering spectra induced by coherent scattering: A molecular dynamics simulation study". In: (Oct. 2022). DOI: 10.1101/2022.10.27.514007. URL: https://doi.org/10.1101/2022.10.27.514007.

[245] LLC Schrödinger and Warren DeLano. *PyMOL*. Version 2.4.0. May 20, 2020. URL: http://www.pymol.org/pymol.

[246] M. Krishnan, V. Kurkal-Siebert, and Jeremy C. Smith. "Methyl Group Dynamics and the Onset of Anharmonicity in Myoglobin". In: *The Journal of Physical Chemistry B* 112.17 (Apr. 2008), pp. 5522–5533. DOI: 10.1021/jp076641z. URL: https://doi.org/10.1021/jp076641z.

[247] M Tarek and DJ Tobias. "Role of protein-water hydrogen bond dynamics in the protein dynamical transition". In: *Physical review letters* 88.13 (2002), p. 138101.

[248] Giorgio Schirò et al. "Hydration dependent dynamics in sol–gel encapsulated myoglobin". In: *European Biophysics Journal* 37.5 (Feb. 2008), pp. 543–549. DOI: 10.1007/s00249-007-0249-9. URL: https://doi.org/10.1007/s00249-007-0249-9.

[249] Alessandro Paciaroni, Stefania Cinelli, and Giuseppe Onori. "Effect of the Environment on the Protein Dynamical Transition: A Neutron Scattering Study". In: *Biophysical Journal* 83.2 (Aug. 2002), pp. 1157–1164. DOI: 10.1016/s0006-3495(02)75239-9. URL: https://doi.org/10.1016/s0006-3495(02)75239-9.

[250] ZhaoRu Sun et al. "Liquid-liquid phase transition in water". In: *Science China Physics, Mechanics & Astronomy* 57 (2014), pp. 810–818.

[251] Yi Xue et al. "Methyl Rotation Barriers in Proteins from sup2/supH Relaxation Data. Implications for Protein Structure". In: *Journal of the American Chemical Society* 129.21 (May 2007), pp. 6827–6838. DOI: 10.1021/ja0702061. URL: https://doi.org/10.1021/ja0702061.

[252] Sheh-Yi Sheu et al. "Energetics of hydrogen bonds in peptides". In: *Proceedings of the National Academy of Sciences* 100.22 (Oct. 2003), pp. 12683–12687. DOI: 10.1073/pnas.2133366100. URL: https://doi.org/10.1073/pnas.2133366100.

[253] Zeke A. Piskulich and Ward H. Thompson. "Examining the Role of Different Molecular Interactions on Activation Energies and Activation Volumes in Liquid Water". In: *Journal of Chemical Theory and Computation* 17.5 (Apr. 2021), pp. 2659–2671. DOI: 10.1021/acs.jctc.0c01217. URL: https://doi.org/10.1021/acs.jctc.0c01217.

[254] Marco Lagi et al. "The Low-Temperature Dynamic Crossover Phenomenon in Protein Hydration Water: Simulations vs Experiments". In: *The Journal of Physical Chemistry B* 112.6 (Jan. 2008), pp. 1571–1575. DOI: 10.1021/jp710714j. URL: https://doi.org/10.1021/jp710714j.

[255] Andreas Neophytou, Dwaipayan Chakrabarti, and Francesco Sciortino. "Topological nature of the liquid–liquid phase transition in tetrahedral liquids". In: *Nature Physics* 18.10 (Aug. 2022), pp. 1248–1253. DOI: 10.1038/s41567-022-01698-6. URL: https://doi.org/10.1038/s41567-022-01698-6.

[256] Jean-Marc Zanotti et al. "Competing coexisting phases in 2D water". In: *Scientific Reports* 6.1 (May 2016). DOI: 10.1038/srep25938. URL: https://doi.org/10.1038/srep25938.

[257] AZMS Rahman, KS Singwi, and A Sjölander. "Theory of slow neutron scattering by liquids. I". In: *Physical Review* 126.3 (1962), p. 986.

[258] D Zeller et al. “Analysis of elastic incoherent neutron scattering data beyond the Gaussian approximation”. In: *The Journal of chemical physics* 149.23 (2018), p. 234908.

[259] Gerald R. Kneller and Konrad Hinsen. “Quantitative model for the heterogeneity of atomic position fluctuations in proteins: A simulation study”. In: *The Journal of Chemical Physics* 131.4 (July 2009). DOI: 10.1063/1.3170941. URL: https://doi.org/10.1063/1.3170941.

[260] Judith Peters and Gerald R. Kneller. “Motional heterogeneity in human acetylcholinesterase revealed by a non-Gaussian model for elastic incoherent neutron scattering”. In: *The Journal of Chemical Physics* 139.16 (Oct. 2013). DOI: 10.1063/1.4825199. URL: https://doi.org/10.1063/1.4825199.

[261] Prithwish K. Nandi and Niall J. English. “Role of Hydration Layer in Dynamical Transition in Proteins: Insights from Translational Self-Diffusivity”. In: *The Journal of Physical Chemistry B* 120.47 (Nov. 2016), pp. 12031–12039. DOI: 10.1021/acs.jpcb.6b06683. URL: https://doi.org/10.1021/acs.jpcb.6b06683.

[262] Giuseppe Zaccai. “How soft is a protein? A protein dynamics force constant measured by neutron scattering”. In: *Science* 288.5471 (2000), pp. 1604–1607.

[263] Lorenzo Cordone et al. “Harmonic behavior of trehalose-coated carbon-monoxy-myoglobin at high temperature”. In: *Biophysical Journal* 76.2 (1999), pp. 1043–1047.

[264] Claude Cohen-Tannoudji, Bernard Diu, and Franck Laloe. *Mecanique quantique*. fre. Nouvelle ed. Savoirs actuels. Les Ulis Paris: EDP sciences CNRS éditions, 2018. ISBN: 9782759822867.

[265] F Natali et al. “Myelin basic protein reduces molecular motions in DMPA, an elastic neutron scattering study”. In: *Physica B: Condensed Matter* 301.1-2 (July 2001), pp. 145–149. DOI: 10.1016/s0921-4526(01)00528-2. URL: https://doi.org/10.1016/s0921-4526(01)00528-2.

[266] Sophie Combet and Jean-Marc Zanotti. “Further evidence that interfacial water is the main “driving force” of protein dynamics: a neutron scattering study on perdeuterated C-phycocyanin”. In: *Physical Chemistry Chemical Physics* 14.14 (2012), pp. 4927–4934.

[267] Wolfgang Doster, Stephen Cusack, and Winfried Petry. "Dynamical transition of myoglobin revealed by inelastic neutron scattering". In: *Nature* 337.6209 (Feb. 1989), pp. 754–756. DOI: 10.1038/337754a0. URL: https://doi.org/10.1038/337754a0.

[268] Hans Frauenfelder et al. "A unified model of protein dynamics". In: *Proceedings of the National Academy of Sciences* 106.13 (Mar. 2009), pp. 5129–5134. DOI: 10.1073/pnas.0900336106. URL: https://doi.org/10.1073/pnas.0900336106.

[269] Alessandro Paciaroni, Stefania Cinelli, and Giuseppe Onori. "Effect of the environment on the protein dynamical transition: a neutron scattering study". In: *Biophysical journal* 83.2 (2002), pp. 1157–1164.

[270] Yinglong Miao et al. "Temperature-Dependent Dynamical Transitions of Different Classes of Amino Acid Residue in a Globular Protein". In: *Journal of the American Chemical Society* 134.48 (Nov. 2012), pp. 19576–19579. DOI: 10.1021/ja3097898. URL: https://doi.org/10.1021/ja3097898.

[271] M. Tarek and D. J. Tobias. "Role of Protein-Water Hydrogen Bond Dynamics in the Protein Dynamical Transition". In: *Physical Review Letters* 88.13 (Mar. 2002). DOI: 10.1103/physrevlett.88.138101. URL: https://doi.org/10.1103/physrevlett.88.138101.

[272] Torsten Becker et al. "Neutron Frequency Windows and the Protein Dynamical Transition". In: *Biophysical Journal* 87.3 (Sept. 2004), pp. 1436–1444. DOI: 10.1529/biophysj.104.042226. URL: https://doi.org/10.1529/biophysj.104.042226.

[273] Alexander L. Tournier and Jeremy C. Smith. "Principal Components of the Protein Dynamical Transition". In: *Physical Review Letters* 91.20 (Nov. 2003). DOI: 10.1103/physrevlett.91.208106. URL: https://doi.org/10.1103/physrevlett.91.208106.

[274] DJ Bicout and G Zaccai. "Protein flexibility from the dynamical transition: a force constant analysis". In: *Biophysical Journal* 80.3 (2001), pp. 1115–1123.

[275] Giorgio Schirò et al. "The "Protein Dynamical Transition" Does Not Require the Protein Polypeptide Chain". In: *The Journal of Physical Chemistry Letters* 2.18 (Aug. 2011), pp. 2275–2279. DOI: 10.1021/jz200797g. URL: https://doi.org/10.1021/jz200797g.

[276] Yunfen He et al. “Protein Dynamical Transition Does Not Require Protein Structure”. In: *Physical Review Letters* 101.17 (Oct. 2008). DOI: 10.1103/physrevlett.101.178103. URL: https://doi.org/10.1103/physrevlett.101.178103.

[277] L. Tavagnacco et al. “Proteinlike dynamical transition of hydrated polymer chains”. In: *Physical Review Research* 3.1 (Feb. 2021). DOI: 10.1103/physrevresearch.3.013191. URL: https://doi.org/10.1103/physrevresearch.3.013191.

[278] Marco Zanatta et al. “Evidence of a low-temperature dynamical transition in concentrated microgels”. In: *Science Advances* 4.9 (Sept. 2018). DOI: 10.1126/sciadv.aat5895. URL: https://doi.org/10.1126/sciadv.aat5895.

[279] Antonio Iorio, Gaia Camisasca, and Paola Gallo. “Slow dynamics of hydration water and the trehalose dynamical transition”. In: *Journal of Molecular Liquids* 282 (May 2019), pp. 617–625. DOI: 10.1016/j.molliq.2019.02.088. URL: https://doi.org/10.1016/j.molliq.2019.02.088.

[280] Aline Cisse et al. “Dynamics of Apolipoprotein B-100 in Interaction with Detergent Probed by Incoherent Neutron Scattering”. In: *The Journal of Physical Chemistry Letters* 12.51 (Dec. 2021), pp. 12402–12410. DOI: 10.1021/acs.jpclett.1c03141. URL: https://doi.org/10.1021/acs.jpclett.1c03141.

[281] Benedetta P. Rosi et al. “Impact of the Environment on the PNIPAM Dynamical Transition Probed by Elastic Neutron Scattering”. In: *Macromolecules* 55.11 (June 2022), pp. 4752–4765. DOI: 10.1021/acs.macromol.2c00177. URL: https://doi.org/10.1021/acs.macromol.2c00177.

[282] Philip M. Morse. “Diatomic Molecules According to the Wave Mechanics. II. Vibrational Levels”. In: *Physical Review* 34.1 (July 1929), pp. 57–64. DOI: 10.1103/physrev.34.57. URL: https://doi.org/10.1103/physrev.34.57.

[283] A Matsumoto. “Generalised matrix elements in discrete and continuum states for the Morse potential”. In: *Journal of Physics B: Atomic, Molecular and Optical Physics* 21.16 (1988), p. 2863.

[284] Catalin Gainaru et al. “Anomalously large isotope effect in the glass transition of water”. In: *Proceedings of the National Academy of Sciences* 111.49 (Nov. 2014), pp. 17402–17407. DOI: 10.1073/pnas.1411620111. URL: https://doi.org/10.1073/pnas.1411620111.

[285] Mikio Kataoka et al. “Neutron inelastic scattering as a high-resolution vibrational spectroscopy: New tool for the study of protein dynamics”. In: *Spectroscopy* 17.2-3 (2003), pp. 529–535.

[286] Juergen Eckert. “Computational study of inelastic neutron scattering vibrational spectra of water clusters and their relevance to hydration water in proteins”. In: *Biochimica et Biophysica Acta (BBA)-General Subjects* 1861.1 (2017), pp. 3564–3572.

[287] Julien Gonthier et al. “BerILL: The ultimate humidity chamber for neutron scattering”. In: *Journal of Neutron Research* 21.1-2 (2019), pp. 65–76.

Appendices

Theory

Theory: Fermi's Golden Rule

Fermi's Golden rule yields the rate of transition from an initial state i to a continuum of final states f, considering that the transition is induced by a pertubative Hamiltionian $\hat{H}_c$ which is time independent and weakly coupled. It is obtained from first order perturbation of the system's eigenstates [61]. It requires a few assumptions :

-It holds for very long times, ensuring that only transitions corresponding to E_i to E_f take place.

-Hamiltonian matrix elements and the final density of states vary slowly with the final system's energy.

let us denote the initial state $i \equiv m \otimes k$ and the final state $f \equiv m' \otimes \mathbf{k'}$. Fermi Golden Rule yields

$$W_{i\to f} = \frac{2\pi}{\hbar} |\langle f| \hat{H}_c |i\rangle|^2 \rho(E_f) dE_f \delta(E_f - E_i). \tag{A-1}$$

Such that $E_f = E_{k'} + E_{m'}$ and $E_i = E_k + E_m$, denoting energy conservation of the whole system for very long times.

Equation 1-1 yields the following equivalence :

$$dE_f \rho(E_f) = d\mathbf{k'}\rho(\mathbf{k'}). \tag{A-2}$$

That is, the final density of energy for the final state can be expressed from the density of vectorial momentum transfers of the neutron probe.

We consider that the initial and final quantum states of the neutron probe are plane wavefunctions, due to the long distance from the sample to the detectors. This implies that we are considering transitions between free states, which are not normalised and prevent a calculation of the density of momentum states. Thus, we normalise them using a cubic volume $V = L^3$ containing both the neutron and the scattering system, so that the continuum is retrieved for $L \to \infty$. This method is called the "box normalisation".

$$\begin{aligned} |k\rangle = \langle r|\phi_k\rangle &= \frac{1}{\sqrt{L^3}} \exp(i\mathbf{kr}), \\ |k'\rangle = \langle r|\phi_{k'}\rangle &= \frac{1}{\sqrt{L^3}} \exp(i\mathbf{k'r}). \end{aligned} \tag{A-3}$$

Therefore, $\langle k|k\rangle = \langle k'|k'\rangle = 1$.

This imposes boundary conditions on wavefunctions, so that they vanish outside the box: $\phi_k(\mathbf{r}) = \phi_k(\mathbf{r} + \mathbf{L})$ with $\mathbf{L} = \{L, L, L\}$ in cartesian coordinates. Consequently, $\mathbf{k} = \frac{2\pi}{L^3}\{k_1, k_2, k_3\}$, k_i being integers.

Thus each wavevector occupies a volume of $V_k = \left(\frac{2\pi}{L}\right)^3$, defining the density of momentum states

$$\rho(\mathbf{k}) = \left(\frac{L}{2\pi}\right)^3. \tag{A-4}$$

On the other hand, the volume element for the final wavevector $d\mathbf{k'}$ in solid angle $\mathbf{d\Omega}$ writes $d\mathbf{k'}^3 = dk'k'^2\mathbf{d\Omega}$ such that k' is the norm of momentum $\mathbf{k'}$, yielding :

$$\begin{aligned} \rho(\mathbf{k})d\mathbf{k'} &= \left(\frac{L}{2\pi}\right)^3 d\mathbf{k'}^3 \\ &\underset{dk=\frac{dEm}{\hbar k'},}{=} \left(\frac{L}{2\pi}\right)^3 \frac{mk'}{\hbar^2} dEd\mathbf{\Omega}. \end{aligned} \tag{A-5}$$

Therefore, the transition rate in Equation A-1 finally writes from Equation A-5 :

$$W_{i\to f} \underset{L\to\infty}{=} \frac{L^3}{\hbar^3}\frac{mk'}{(2\pi)^2} dEd\mathbf{\Omega} |\langle f|\, \hat{H}_c\, |i\rangle\,|^2 \delta(E_f - E_i). \tag{A-6}$$

Theory: Express the coupling Hamiltonian H_c

Another way of calculating the double-differential cross section involves the use of the Lippmann-Schwinger equation. This equation expresses the scattered neutron as the sum of the incident neutron wavefunction and the application of the Green propagator $\hat{G_0}$ and the transition operator $\hat{T}$ to the incident neutron wavefunction:

$$|k'\rangle = |k\rangle + \hat{T}\hat{G_0}\,|k\rangle\,. \tag{A-7}$$

The transition operator $\hat{T}$ is an infinite sum of operators involving the potential of interaction $\hat{H_c}$ between the neutron and the probe.

$$\hat{T} = \sum_{n=1}^{n=\infty} \hat{G_0}^{\,n-1} \hat{H_c}^{\,n}. \tag{A-8}$$

A pseudo-potential $\hat{V_f}$ was introduced by Fermi in 1936 [48, 49], such that $\hat{T} = \hat{V_f}$ for the scattering of a single nucleus.

Considering the first-order truncation of the series yields $\hat{T} = \hat{H_c}$ (Born approximation,

implying that attenuation effects vanish). Therefore, we use $\hat{V_f}$ as an expression for the interaction potential $\hat{H_c}$ in the Golden Rule, in the frame of the first-order perturbation. $\hat{V_f}$ writes, for the interaction of the neutron with a nucleus denoted j :

$$\hat{V}_{f,j} = \frac{2\pi\hbar^2}{m} b_j \delta(\hat{r} - \hat{R}_j). \tag{A-9}$$

Such that $\hat{H_c}$ for the total system composed of N nuclei equals :

$$\boxed{\hat{H_c} = \sum_j^N \frac{2\pi\hbar^2}{m} b_j \delta(\hat{r} - \hat{R}_j)}. \tag{A-10}$$

$\hat{R}_j$ is the position operator of nucleus j at time t_0, and b_j is a complex value, the bound scattering length of nucleus j, holding for the case of a fixed nucleus. Rigorously, b_j should to be treated as an operator dependent on the system's spin, as explained in subsection 1.3.1.

Fermi pseudo-potential is empirical by definition, and expresses the strong interaction of the neutron with the nucleus compared to the neutron's wavelength such that the interaction potential is simply an impulse. It also expresses the spherical symmetry of scattering. The interaction is point-like, and the bound-scattering length is evaluated experimentally. b_j is a measure of the amplitude of interaction. A positive value for b denotes a repulsive interaction. The real part of the scattering length implies scattering of the neutron, while its imaginary part denotes the absorption of the neutron.

Now we can express the matrix element $\langle f| \hat{H_c} |i\rangle$, using the neutron wavefunctions introduced in Equation A-3:

$$\begin{aligned}
&\langle f| \hat{H_c} |i\rangle = \langle m' \otimes k'| \hat{H_c} |k \otimes m\rangle \\
&= \langle m'| \int \frac{1}{\sqrt{L^3}} \exp(-i\mathbf{kr}) \sum_j \frac{2\pi\hbar^2}{m} b_j \delta(\mathbf{r} - \hat{R}_j) \frac{1}{\sqrt{L^3}} \exp(i\mathbf{k'r}) d\mathbf{r} \, |m\rangle \\
&= \frac{2\pi\hbar^2}{mL^3} \langle m'| \, b_j \exp\Big(i\mathbf{Q}\hat{R}_j\Big) \, |m\rangle \, .
\end{aligned}$$

With $\mathbf{Q} = \mathbf{k'} - \mathbf{k}$ the momentum transfer of the neutron probe, such that the norm of the

matrix element equals :

$$\begin{aligned} &|\langle f|\,\hat{H}_c\,|i\rangle\,|^2 = \langle m'\otimes k'|\,\hat{H}_c\,|k\otimes m\rangle^*\,\langle m'\otimes k'|\,\hat{H}_c\,|k\otimes m\rangle \\ &= \left(\frac{2\pi\hbar^2}{mL^3}\right)^2 \sum_j \sum_l \langle m|\,b_j^*\exp\left(-i\mathbf{Q}\hat{R}_j\right)|m'\rangle\,\langle m'|\,b_l\exp\left(i\mathbf{Q}\hat{R}_l\right)|m\rangle\,. \end{aligned} \tag{A-11}$$

Therefore, using Equation A-11 and Equation 1-7 boils down to :

$$W_{i\to f} \underset{L\to\infty}{=} \left(\frac{\hbar k'}{mL^3}\right) \sum_j \sum_l \langle m|\,b_j^*\exp\left(-i\mathbf{Q}\hat{R}_j\right)|m'\rangle\,\langle m'|\,b_l\exp\left(i\mathbf{Q}\hat{R}_l\right)|m\rangle\,\delta(E_f - E_i)d\mathbf{\Omega}dE. \tag{A-12}$$

Calculate the double differential scattering function The flux of incoming neutrons Φ_0 in the volume $V = L^3$ is the product of the neutron's velocity Equation 1-1 and its density $\rho_n = \frac{1}{L^3}$ (the box is defined to contain 1 neutron).

$$\Phi_0 = \frac{\hbar k}{L^3 m}. \tag{A-13}$$

We replace terms in expression Equation 1-4 using Equation A-5 and Equation A-13

$$\begin{aligned} &\left(\frac{d\sigma^2}{\mathbf{d\Omega}dE}\right)_{m,m'} = \frac{W_{i\to f}}{\Phi_0 d\mathbf{\Omega}dE} \\ &= \frac{k'}{k}\sum_j \sum_l \langle m|\,b_j^*\exp\left(-i\mathbf{Q}\hat{R}_j\right)|m'\rangle\,\langle m'|\,b_l\exp\left(i\mathbf{Q}\hat{R}_l\right)|m\rangle\,\delta(E_f - E_i). \end{aligned} \tag{A-14}$$

Theory: Sum over all sample accessible states

Therefore, we have access to the double differential cross section corresponding to fixed initial and final sample states, as denoted from subscript $(...)_{m,m'}$. However we want to express this value for all accessible initial and final states, referring to [Equation 1-5. This requires to introduce $P_m = \frac{\exp(-\beta E_m)}{Z_m}$ with $Z_m = \sum_n \exp(-\beta E_n)$ the partition function of the sample system at equilibrium following the Boltzmann law. This implies that

$$\begin{aligned} &\left(\frac{d\sigma^2}{\mathbf{d\Omega}dE}\right) = \\ &\sum_j \sum_l \frac{k'}{k} \sum_m \sum_{m'} \frac{\exp(-\beta E_m)}{Z_m} \langle m|\,b_j^*\exp\left(-i\mathbf{Q}\hat{R}_j\right)|m'\rangle\,\langle m'|\,b_l\exp\left(i\mathbf{Q}\hat{R}_l\right)|m\rangle\,\delta(E_f - E_i). \end{aligned} \tag{A-15}$$

We use then the following relationships :

1. We introduce the integral notation of the Dirac function of energy conservation (E and t are non-commutative variables connected by Heisenberg uncertainty principle). This is how the time dependence of position operators is introduced :

$$\begin{aligned}\delta(E_f - E_i) &= \delta((E_{m'} - E_m) - \underbrace{E_{k'} - E_k)}_{\boxed{\hbar\omega}} \\ &= \frac{1}{2\pi\hbar}\int_{-\infty}^{\infty} \exp\left(i\frac{E_{m'}t}{\hbar}\right)\exp\left(-i\frac{E_m t}{\hbar}\right)\exp(-i\omega t)dt.\end{aligned} \tag{A-16}$$

   Such that $\hbar\omega$ is the energy transfer of the neutron, and therefore :

$$\begin{aligned}&\langle m|\, b_j^* \exp\left(-i\mathbf{Q}\hat{R}_j\right)|m'\rangle\,\langle m'|\, b_l \exp\left(i\mathbf{Q}\hat{R}_l\right)|m\rangle\,\delta(E_f - E_i) \\ &= \frac{1}{2\pi\hbar}\int_{-\infty}^{\infty}\langle m|\, b_j^* \exp\left(-i\mathbf{Q}\hat{R}_j\right)|m'\rangle\,\langle m'|\, b_l \exp\left(i\frac{E_{m'}t}{\hbar}\right)\exp\left(i\mathbf{Q}\hat{R}_l\right)\exp\left(-i\frac{E_m t}{\hbar}\right)|m'\rangle\exp(-i\omega t)dt \\ &= \frac{1}{2\pi\hbar}\int_{-\infty}^{\infty}\langle m|\, b_j^* \exp\left(-i\mathbf{Q}\hat{R}_j(0)\right)|m'\rangle\,\langle m'|\, b_l \exp\left(i\mathbf{Q}\hat{R}_l(t)\right)|m'\rangle\exp(-i\omega t)dt.\end{aligned}$$

   Using Heisenberg representation to express $\hat{R}_j$ operator as a function of t

$$\hat{R}_j(t) = \exp\left(i\frac{\hat{H}_m t}{\hbar}\right)\exp\left(i\mathbf{Q}\hat{R}_j\right)\exp\left(-i\frac{\hat{H}_m t}{\hbar}\right). \tag{A-17}$$

   .

2. The closure relationship ensures that term $\sum'_m |m'\rangle\langle m'| = 1$ makes the final states vanish, due to the orthonormality of eigenfunctions.

3. The thermal average of a given observable at equilibrium $\hat{A}$ is given by formula $\langle A\rangle = \sum_m \langle m|\,\hat{\rho}_m\hat{A}\,|m\rangle = Tr(\hat{\rho}_m A)$.
   $|m\rangle$ are H_m eigenvalues, Tr(..) is the trace operator and $\hat{\rho_m} = \frac{\exp(-\beta H_m)}{Tr(\exp(-\beta H_m))}$ is the density operator for a canonical ensemble. The thermal average is denoted $\langle..\rangle$
   The thermal average is applied using that $\frac{\exp(-\beta E_m)}{Z_m}|m\rangle = \hat{\rho}_m|m\rangle$.

All previous remarks lead to :

$$\left(\frac{d\sigma^2}{\mathbf{d\Omega}dE}\right) = \frac{1}{2\pi\hbar}\frac{k'}{k}\int_{-\infty}^{\infty}\sum_j\sum_l\langle b_j^* bl\exp\left(-i\mathbf{Q}\hat{R}_j(0)\right)\exp\left(i\mathbf{Q}\hat{R}_l(t)\right)\rangle\exp(-i\omega t)dt. \tag{A-18}$$

Each nucleus j or l can belong to any isotope present in the sample.

Thus, for further considerations, it is interesting to separate contributions into sums cor-

responding to the N isotopes represented in the sample. Each matrix element corresponds to the position operators $R_{\alpha,j}(R_{\beta,l})$ of two nuclei of type α or β, denoted j and l such that $j(l)$ is one of the $N_\alpha(N_\beta)$ nuclei of their respective type.

$$\left(\frac{d\sigma^2}{\mathbf{d\Omega}dE}\right) = \frac{1}{2\pi\hbar}\frac{k'}{k}\sum_{\alpha=1}^{N}\sum_{\beta=1}^{N} \int_{-\infty}^{\infty}\left(\sum_{j=1}^{N_\alpha}\sum_{l=1}^{N_\beta}\langle b^*_{\alpha,j}b_{\alpha,l}exp\left(-i\mathbf{Q}\hat{R}_{\alpha,j}(0)\right)\exp\left(i\mathbf{Q}\hat{R}_{\beta,l}(t)\right)\rangle\right)\exp(-i\omega t)dt. \tag{A-19}$$

Now we have an expression for the partial double-differential cross section for any initial and final sample state. This is expressed from the momentum exchange of the neutron $\mathbf{Q}$ and its energy exchange $\hbar\omega$ which are the observables of a neutron experiment.

Theory: the relaxation function

Replacing the particle density operator with $\hat{\rho}_j(\mathbf{Q},\mathbf{t}) = \delta\hat{\rho}_j(\mathbf{Q},\mathbf{t}) + \langle\hat{\rho}_j(\mathbf{Q})\rangle$ and normalizing the relaxation function in Equation 1-61 leads to

$$\begin{aligned} F(\mathbf{Q},t) &= \frac{1}{N}\sum_{j,k}\langle b^*_j b_k \hat{\rho}^\dagger_j(\mathbf{Q},0)\hat{\rho}_k(\mathbf{Q},t)\rangle \\ &\underbrace{=}_{\substack{\hat{\rho}_j(\mathbf{Q},t)= \\ \delta\hat{\rho}_j(\mathbf{Q},t)+\langle\hat{\rho}_j(\mathbf{Q})\rangle}} \underbrace{\frac{1}{N}\sum_{j,k}\langle b^*_j b_k \delta\hat{\rho}^\dagger_j(\mathbf{Q},0)\delta\hat{\rho}_k(\mathbf{Q},0)\rangle}_{A} \underbrace{\frac{\frac{1}{N}\sum_{j,k}\langle b^*_j b_k \delta\hat{\rho}^\dagger_j(\mathbf{Q},0)\delta\hat{\rho}_k(\mathbf{Q},t)\rangle}{\frac{1}{N}\sum_{j,k}\langle b^*_j b_k \delta\hat{\rho}^\dagger_j(\mathbf{Q},0)\delta\hat{\rho}_k(\mathbf{Q},0)\rangle}}_{\phi(\mathbf{Q},t)} \\ &+ \underbrace{\frac{1}{N}\sum_{j,k}\langle b^*_j\hat{\rho}_j(\mathbf{Q})\rangle\langle b_k\hat{\rho}_k(\mathbf{Q})\rangle}_{ESF(\mathbf{Q})}. \end{aligned} \tag{A-20}$$

$$\text{With } A = \underbrace{\frac{1}{N}\sum_{j,k}\langle b^*_j b_k \hat{\rho}^\dagger_j(\mathbf{Q},0)\hat{\rho}_k(\mathbf{Q},0)\rangle}_{I(\mathbf{Q},0)} - \underbrace{\frac{1}{N}\sum_{j,k}\langle b^*_j\hat{\rho}^\dagger_j(\mathbf{Q},0)\rangle\langle b_k\hat{\rho}_k(\mathbf{Q})\rangle}_{ESF(\mathbf{Q})}$$

$$- \underbrace{\frac{1}{N}\sum_{j,k}\langle b^*_j\hat{\rho}^\dagger_j(\mathbf{Q})\rangle\langle b_k\hat{\rho}_k(\mathbf{Q},0)\rangle}_{ESF(\mathbf{Q})} + \underbrace{\frac{1}{N}\sum_{j,k}\langle b^*_j\hat{\rho}^\dagger_j(\mathbf{Q})\rangle\langle b_k\hat{\rho}_k(\mathbf{Q})\rangle}_{ESF(\mathbf{Q})}.$$

Therefore, $F(\mathbf{Q},t) = (F(\mathbf{Q},0) - ESF(\mathbf{Q}))\,\phi(\mathbf{Q},t) + ESF(\mathbf{Q})$.

A-1 Calculations of $S_{\mathbf{coh}}(Q)$ in an isotropic powder

In powder state the static structure factor is averaged over θ and ϕ in spherical coordinates due to the isotropy of the sample. It yields :

$$S(Q) = \frac{1}{4\pi} \int_{\theta=0}^{\theta=\pi} \int_{\phi=0}^{\phi=2\pi} \sin(\theta) d\theta d\phi \frac{1}{N} \sum b_i, b_j \exp(iqr_{ij}cos(\theta)). \tag{A-21}$$

Replacing $\cos(\theta)$ with the variable u raises :

$$\begin{aligned} S(Q) =& \frac{1}{4\pi} 2\pi \int_{u=-1}^{1} \sin(\theta) \frac{-du}{\sin(\theta)} \frac{1}{N} \sum b_i, b_j \exp(iqr_{ij}u) \\ &= \frac{1}{2} \frac{1}{N} \sum b_i, b_j \left[\frac{\exp(iqr_{ij}u)}{iqr_{ij}} \right]_{-1}^{1} \\ &= \frac{1}{N} \sum b_i, b_j \frac{\exp(iqr_{ij}) - \exp(-iqr_{ij})}{2iqr_{ij}} \\ &= \frac{1}{N} \sum b_i, b_j \frac{\sin(qr_{ij})}{qr_{ij}}. \end{aligned} \tag{A-22}$$

Experiments

Labile atoms exchange

Amino Acid	Category	Side Chains, nb of exch. H (Pk_x)	Backbone, nb of exch. h
Arg	Charged +	3 (12.48)	1
His	Charged +	1 (6)	1
Lys	Charged +	3 (10.53)	1
Asp	Charged -	0 (3.65)	1
Glu	Charged -	0 (4.25)	1
Ser	Polar	1	1
Thr	Polar	1	1
Asn	Polar	2	1
Gln	Polar	0	1
Ala	Hydrophobic	0	1
Val	Hydrophobic	0	1
Ile	Hydrophobic	0	1
Leu	Hydrophobic	0	1
Met	Hydrophobic	0	1
Phe	Hydrophobic	0	1
Tyr	Hydrophobic	1 (10.07)	1
Trp	Hydrophobic	1	1
Cys	Others	1 (8.08)	1
Gly	Others	0	1
Pro	Others	0	0

Table A-I: Chart of exchangeable hydrogen atoms depending on the amino-acid's category, Pk_x values were obtained on www.sigmaaldrich.com.

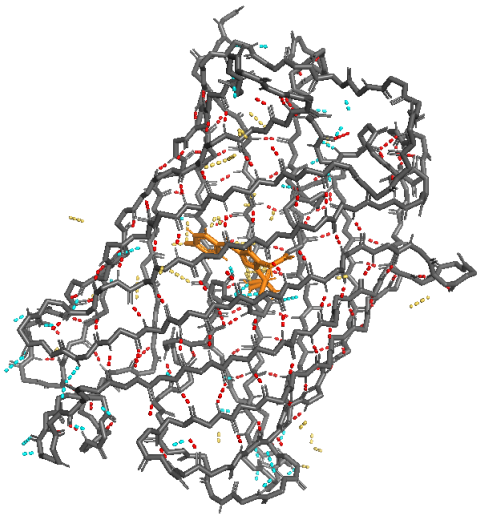

Figure A-1: Internal H-bond network estimated with Pymol software. Red distances correspond to backbone-backbone Hbonds, yellow distances to backbone-side chains ($\approx$ 39), blue distances to side chains-side chains H-bonds ($\approx$ 35). Polar bounds are calculated with a cutoff distance of 3.2Å.

A-2 Data reduction and analysis of quasielastic neutron elastic on IN5

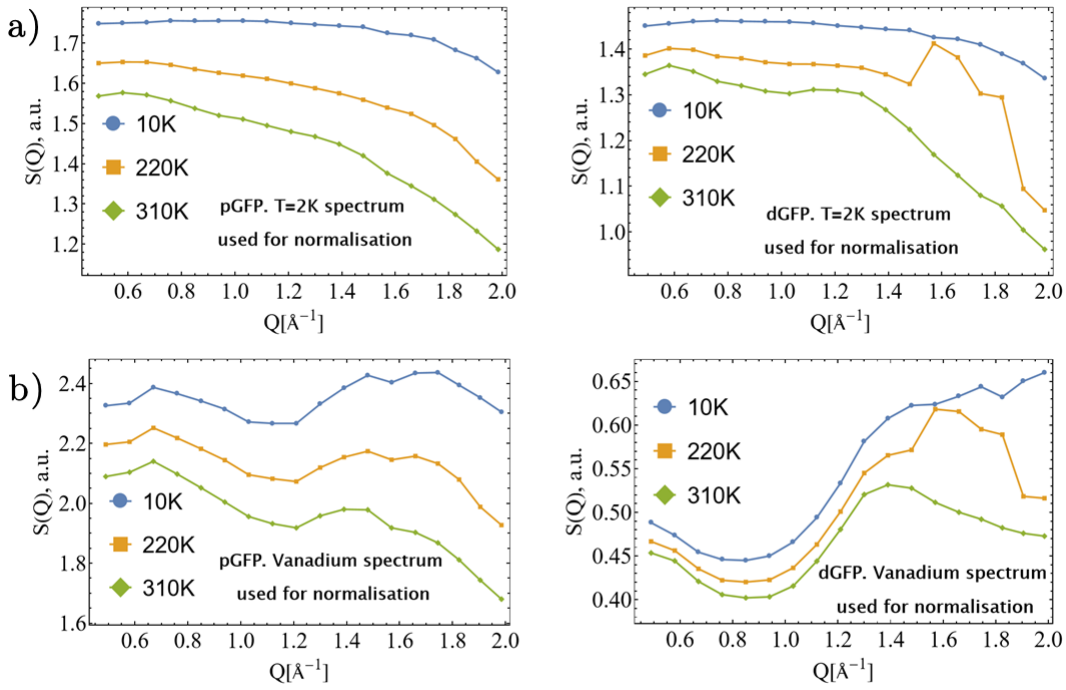

Figure A-2: a) Static structure factor $S(Q)$ measured on IN5 for $E \in [-2.5, 2]$ meV. Normalization performed with the spectrum of the respective sample at low temperature ($T = 2$ K). b) Static structure factor $S(Q)$ measured on IN5. Normalization performed with a spectrum of a vanadium incoherent scatterer. Lines are meant as a guide.

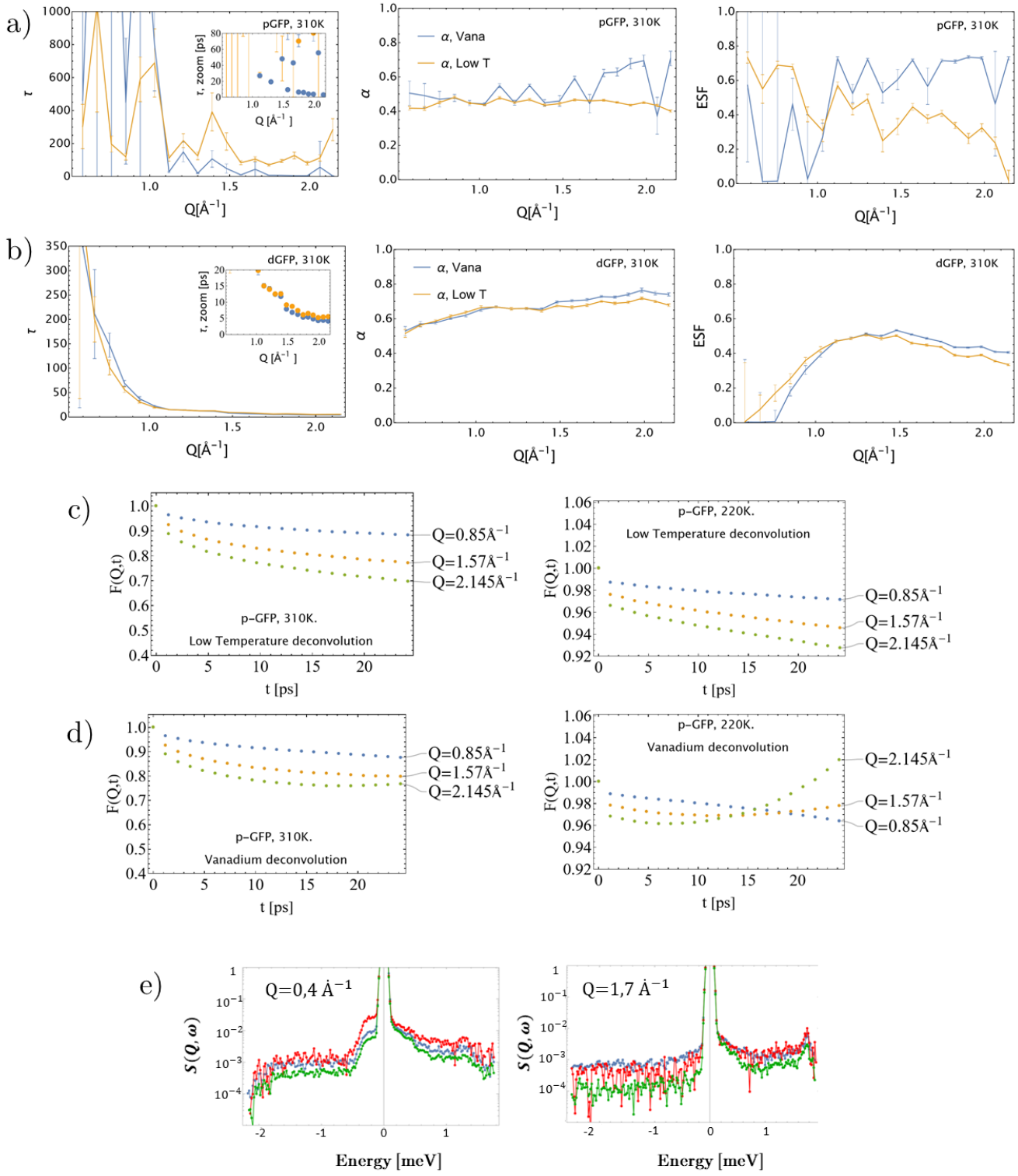

Figure A-3: (a) and (b): Parameters τ, α and ESF obtained for pGFP and dGFP respectively, at T=310K. Blue joined dots correspond to deconvolution performed with Vanadium, and orange to deconvolution performed with a low temperature spectrum of the said sample. Lines are meant as a guide. c) F(Q,t), intermediate scattering function of pGFP deconvolved with the low temperature spectrum ($T = 2$ K) of pGFP. On the right-hand side, $T = 310$ K, on the left hand-side: $T = 220$ K. d) Same for F(Q,t) deconvolved with Vanadium, pGFP. d) Comparison of Vanadium with pGFP and dGFP low temperature spectra for $Q = 0.4$ Å^{-1} and $Q = 1.7$ Å^{-1}. Blue lines correspond to Vanadium, red lines to dGFP, and green lines to pGFP.

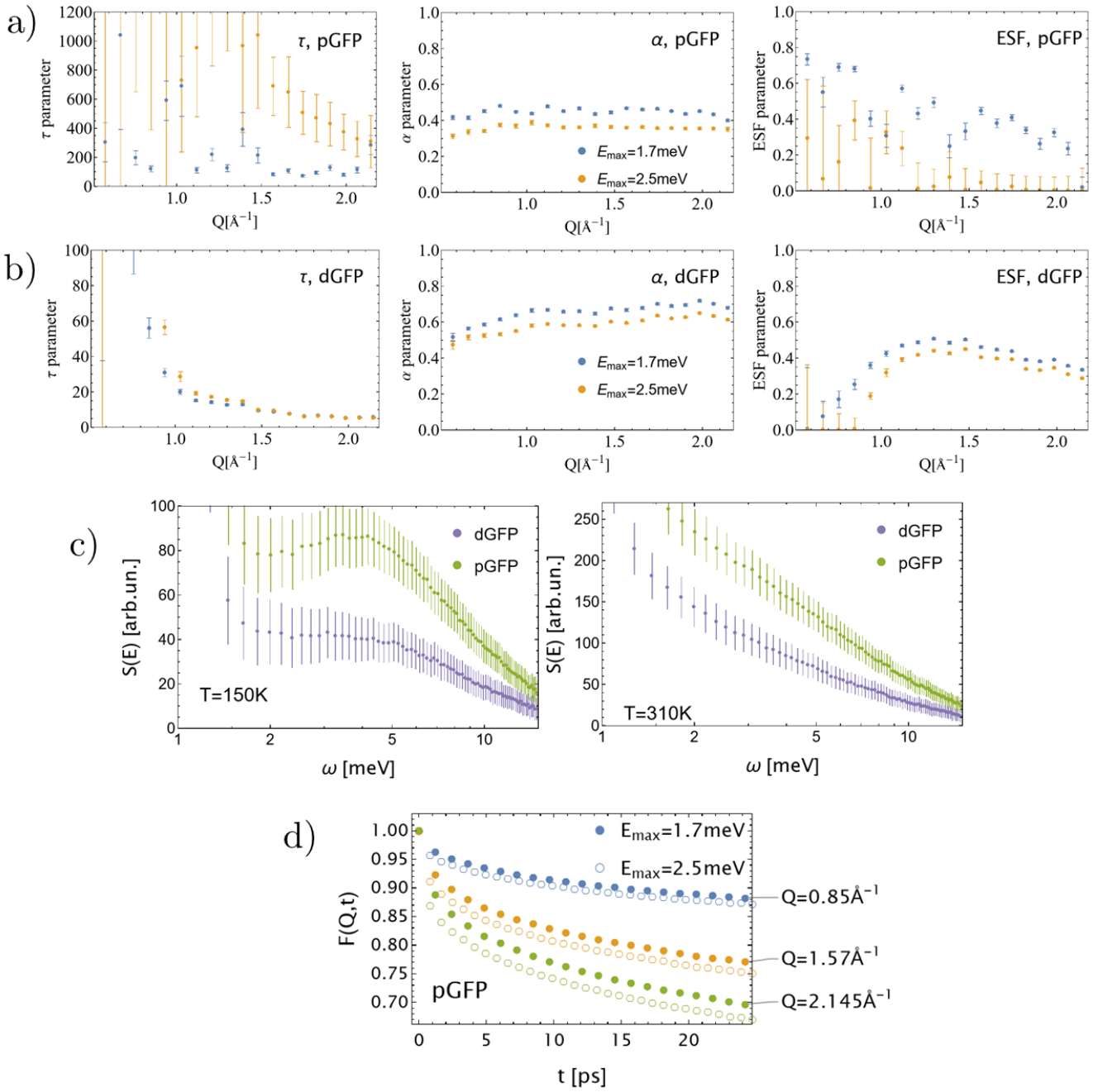

Figure A-4: (a) and (b): Parameters τ, α and ESF obtained for pGFP and dGFP respectively, at T=310K. Blue dots correspond to a cut dynamical range of $E_{\max} = 1.7$ meV, and orange dots correspond to a full dynamical range of $E_{\max} = 2.5$ meV. Lines are meant as a guide.
c) $S(Q, \omega)$ summed over accessible Q values in $[0.02, 3]$ Å^{-1} for $E_i = 19$ meV, measured on Panther. On the left hand-side this corresponds to $T = 150$ K and on the right hand-side this corresponds to $T = 310$ K. dGFP is in purple and pGFP in green.
d) $T = 310$ K. Comparison of intermediate scattering functions corresponding to $E_{\max} = 1.7$ meV (full dots) and $E_{\max} = 2.5$ meV (empty dots) for pGFP.

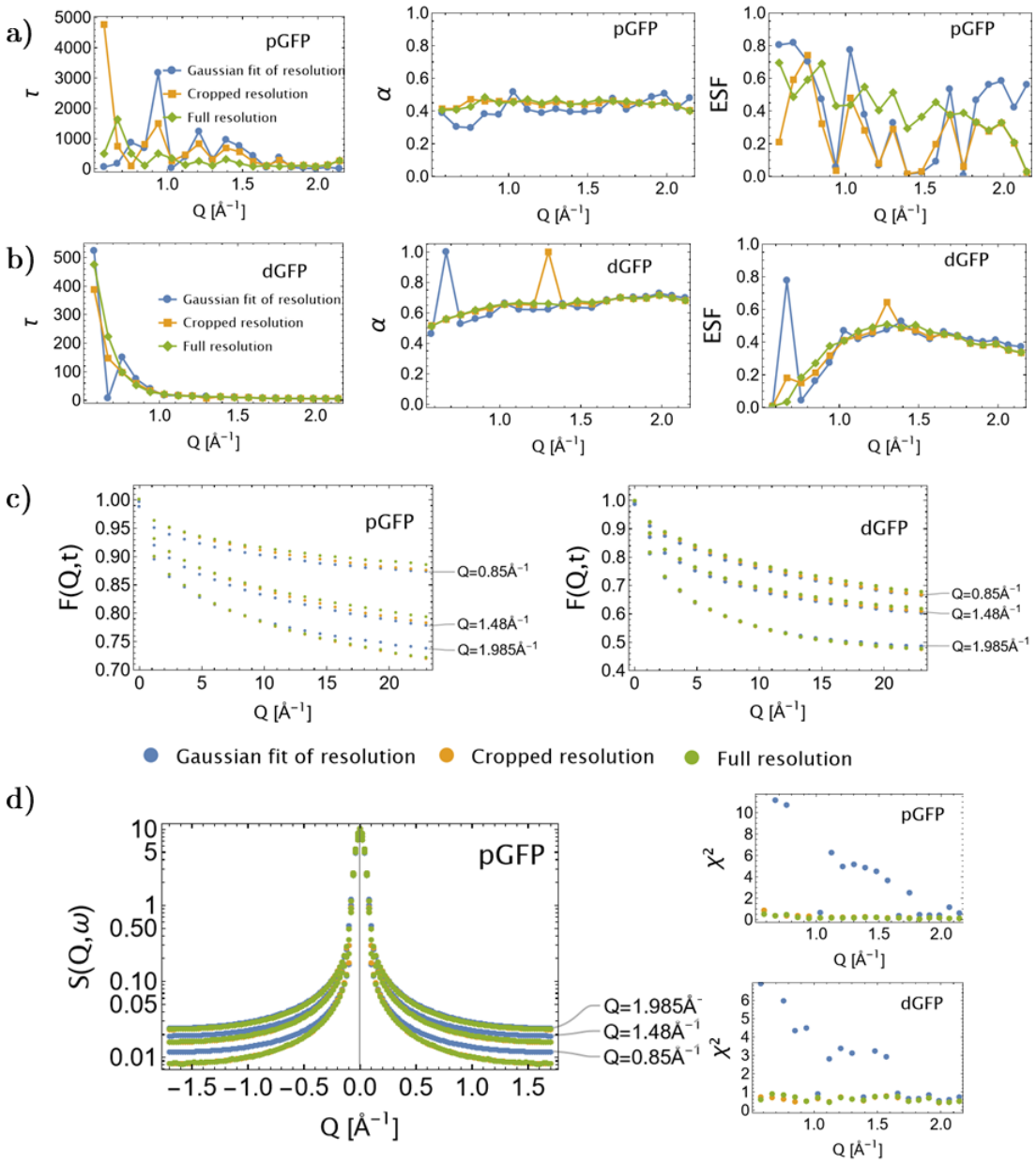

Figure A-5: Study of the deconvolution method for IN5. T=310K. a) and b) display parameters τ, α and ESF for dGFP and pGFP respectively, deconvoluting either with a fitted Gaussian resolution function (blue), a cropped resolution function corresponding to the low-temperature spectrum (orange) or the total low-temperature spectrum (blue). c) Shows the corresponding deconvolved F(Q,t) for $Q = 0.85$ Å^{-1},$Q = 1.48$ Å^{-1} and $Q = 1.985$ Å^{-1}. The colour code is the same. d) Shows the same results for pGFP but in the energy transfer domain. χ^2 are calculated for pGFP and dGFP with the 3 deconvolution methods.

A-3 Data analysis of quasielastic neutron elastic on LET

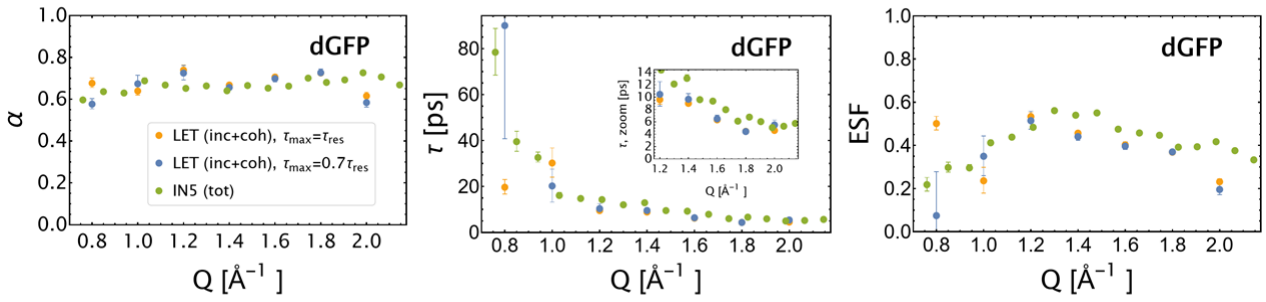

Figure A-6: dGFP, T=310K. Comparison of parameters τ, α and ESF obtained from cutting the deconvoluted function in time for $t_{\max} = t_{\text{res}}$ (orange dots), or $t_{\max} = 0.7t_{\text{res}}$ (blue dots). IN5 parameters obtained in similar experimental conditions for $t_{\max} = t_{\text{res}}$ are displayed in green dots.

	$t_{\max} = 0.7\ t_{t\text{res}}$	$t_{\max} = t_{\text{res}}$
τ	0.41 ± 0.1	0.32 ± 0.5
α	0.10 ± 0.03	0.08 ± 0.04
ESF	0.34 ± 0.08	0.30 ± 0.11

Table A-II: Relative gaps defined by $(\text{param}_{\text{LET}} - \text{param}_{\text{IN5}})/\text{param}_{\text{LET}}$ obtained for $t_{\max} = t_{\text{res}}$ and $t_{\max} = 0.7\ t_{\text{res}}$, for τ α and ESF.

Detailed atomic contributions to the distinct structure factor of hydrated dGFP, 40% D→H exchange

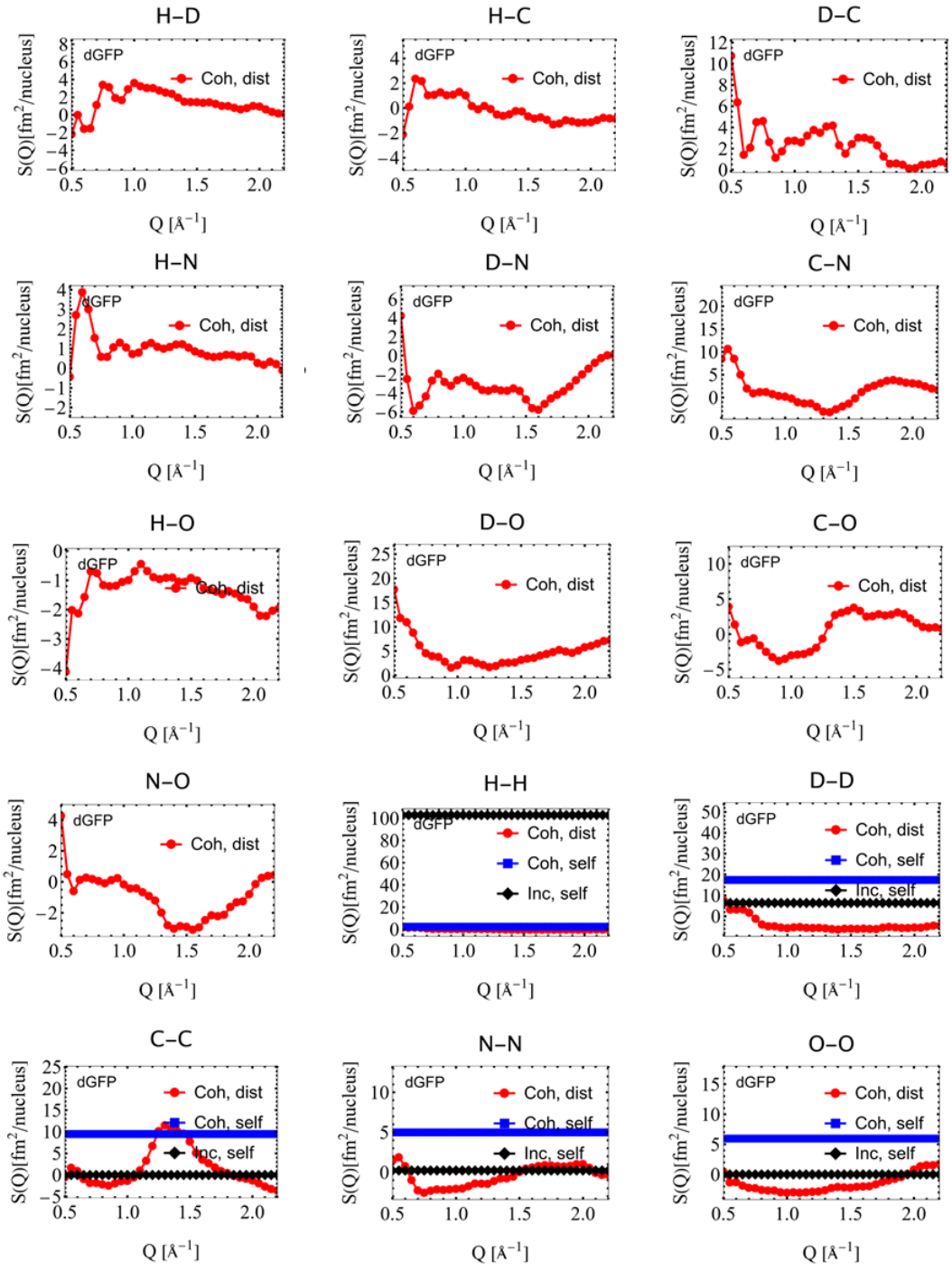

Figure A-7: Comparison of all partial structure factors (divided into incoherent, coherent self and coherent distinct structure factors) in the deuterated GFP protein in the case of full labile atoms exchange (configuration B) + 40% hydration water exchange (a). D-D and O-O partial structure factors are isolated for pGFP b), displaying a compensation of self and distinct coherent partial structure factors over a large range of Q.